Universiteit Gent
Faculteit Ingenieurswetenschappen
Vakgroep Informatietechnologie

Compacte ’on-chip’ optische interconnecties op silicium door heterogene integratie van III-V microbronnen en detectoren

Compact on-chip Optical Interconnects on Silicon by Heterogeneous Integration of III-V Microsources and Detectors

---

Thijs Spuesens

Proefschrift tot het bekomen van de graad van
Doctor in de Ingenieurswetenschappen:
Fotonica
Academiejaar 2013-2014

Promotoren:

Prof. Dr. Ir. Dries Van Thourhout

Examencommissie:

Prof. Dr. Ir. Luc Taerwe (voorzitter)	Universiteit Gent, CMSE
Prof. Dr. Ir. Dries Van Thourhout (promotor)	Universiteit Gent, INTEC
Prof. Dr. Ir. Geert Morthier (secretaris)	Universiteit Gent, INTEC
Prof. Dr. Ir. Johan Bauwelinck	Universiteit Gent, INTEC
Prof. Dr. Ir. Erwin Bosman	Universiteit Gent, ELIS
Prof. Dr. Ir. Oded Raz	Technische Universiteit Eindhoven
Prof. Dr. Ir. Pedro Rojo Romeo	Ecole Centrale de Lyon, INL

Universiteit Gent
Faculteit Ingenieurswetenschappen en Architectuur

Vakgroep Informatietechnologie
Sint-Pietersnieuwstraat 41, B-9000 Gent, België

Tel.: +32-9-264.33.39
Fax.: +32-9-331.35.93

Dit werk kwam tot stand in het kader van een specialisatiebeurs van het IWT-Vlaanderen (Instituut voor de aanmoediging van Innovatie door Wetenschap en Technologie in Vlaanderen).

Dankwoord

Het was 30 april 2008. Een mooie lente dag, een prachtige dag om Koninginnedag te vieren. Maar eerst even snel naar Gent voor een sollicitatiegesprek. Even. Tegen de tijd dat ik terug aangekomen was in Nederland, stonden mijn vrienden al zo'n beetje op tafel te dansen. Ik denk niet dat ik dit ooit van mijn leven nog ga vergeten. Desalniettemin was ik blij op 6 mei (mijn verjaardag) te vernemen dat ik aangenomen was (ik weet eigenlijk nog steeds niet of dit louter toeval was of een zeer attent verjaardagscadeau). Op de eerste plaats wil ik dan ook graag Roel en Dries bedanken die mij de mogelijkheid hebben geboden om in deze groep, die wereldwijd erkenning geniet, onderzoek te doen. Roel, niet alleen een getalenteerd wetenschapper, maar ook een uitmuntend 'people-manager'. Dries, ik weet niet of je thuis met je kinderen ook wel eens verstoppertje speelt, maar wat ben jij daar ongelooflijk goed in! Werkelijk onvindbaar en soms dagenlang! Gelukkig waren er de project vergaderingen van WADIMOS, waardoor je met enige regelmaat met mij opgesloten zat in het vliegtuig of in de trein, waar ik dan weer dankbaar gebruik van heb gemaakt. I should also thank dr. Liu Liu who teached me relevant skills in simulation, fabrication and measurements in a short period of time.

En dan zijn er natuurlijk de bureaugenoten (kantoorgenoten voor de Nederlandse lezer). Allereerst Diedrik (den didi), een bureaugenoot van het eerste uur. Jouw streken zijn ongeëvenaard en hebben voor heel wat onvergetelijke momenten gezorgd. Den Peter, een party animal pur sang; beneden in de Grand Canyon geslapen, cruisen met de Dodge door de woestijn, dat was echt een geweldige trip. Eva, altijd met een grote glimlach die nog groter wordt wanneer ze een potje chocomousse aan het leeglepelen is. Thomas, mijn steun en toeverlaat bij (Pythonscript) problemen en altijd een weloverwogen eigen mening. Martijn, bedankt voor de vele discussies over fabricage problemen en de mogelijke oplossingen. Raphaël, -de advocaat- je brede interesse en je frisse blik gaan je vast nog ver brengen. Rajesh, thanks for the endless discussions on microdisk laser issues. Sukumar, yet another party animal! Honghui, our martial arts expert catching flies with his bare hands! And of course the next generation PhD students: Amin, Pijush, Haolan and Andreas, I wish you all the best in the exciting years to come.

Naast de bureaugenoten zijn er natuurlijk nog de andere collega's, ondanks dat dit er te veel zijn om bij naam te noemen en ik ze allemaal evenveel wil bedanken, wil ik er toch een aantal vernoemen: Bart, fantastisch gevoel voor humor en

altijd van alles op de hoogte (jij zou echt een part-time job bij de Story moeten overwegen). Yannick, gozer! Een enthousiasme dat naar oneindig gaat, fanatiek op het werk en op de fiets. De fiets brengt ons dan bij Sam: ik hoop dat we met z'n drieën nog veel mooie tochten mogen maken (of Geert, ga je ook nog eens mee een tochtje maken)! Pauline, thanks for your helpfulness and time to discuss fabrication and measurements issues. De andere koppeltjes (Sam en Pauline zijn een koppel): Elewout en Cristina, Wout en Marie, thanks for spreading the love. Martin, de mastermind achter het Caphe simulatie programma, ik was nog niet klaar met het debuggen van de installer vx.0 en v(x+1).0 werd alweer gelanceerd. Koen, bedankt voor de snelcurcus Vlaams voor gevorderden. Kristof en Jan-Willem, is het nu 'Gruyere' of toch 'Heryere' kaas? Joris, een Baantjer-fan van het eerste uur. Pieter W. als we nog eens samen in een team zitten met AoE, dan zal ik zorgen dat ik geoefend heb. Nannicha, thanks for sharing your happiness and being a 'buddy' during the evenings in the clean room. Stevan, for sharing your bonding expertise with the highest possible level of precision. Shahram, you are really a funny guy. My advice to you (and Gunay): start writing your thesis and get it over with, it will feel great I can tell. Wim en Pieter D., om mij de mogelijkheid te geven in deze fijne groep te blijven werken.

Uiteraard ook een welgemeend woord van dank voor de mensen die mij op verschillende manieren geholpen hebben met praktische zaken. Steven, wat zouden we zonder jou moeten in de clean room? Zoveel kennis en altijd rustig en relativerend: 'Weet je wat het probleem is met jullie? Jullie denken teveel na! Je moet het gewoon proberen!' Kasia en Liesbet voor alle uren die we aan de FIB gezeten hebben. Liesbet nog een extra merci, voor de overuren die je gemaakt hebt tijdens het einde van mijn doctoraat toen de druk er echt goed op zat. Jeroen en Michael, voor jullie verwoede pogingen om de meetkamer en de simulatie pc's op orde te houden. Ilse vR. en Ilse M. om achter mij aan te zitten om administratieve zaken af te handelen. Kristien -'dat zou moeten werken'-, bedankt voor (bijna) alle ICT problemen op te lossen. Peter G. om supersnel custom componenten te maken voor de meetsetups.

Aangezien inspanning ook ontspanning vereist, moet ik hier nog een aantal mensen bedanken. Laat ik beginnen met de vrienden aan de thuisbasis, die zorgen voor de nodige ontspanning in het weekend: Thomas, Steven, Gerlinde, Ronald, Marieke, Gert-Jan, Esther, Alexander en Elske. We hebben echt een gezellig clubje en ik hoop dat dat nog lang zo blijft. Lees dit boek en je zult erachter komen dat coaxiale kabels zooo 20^{e} eeuw zijn Gert-Jan. Steven, na mijn uitleg tot 3 uur 's nachts tijdens het weekendje in het pittoreske Ermelo (of was het nu Elst?), moet dit boek voor jou al gesneden koek zijn. Marco en Eefje, bedankt voor jullie interesse in mijn werk en hopelijk gaat het nu eindelijk eens echt lukken met ons uit-eten project. En dan nog mijn roomies uit Eindhoven voor de legendarische tijd in de Bennekel. Mijn fietsmaatjes van 'TC de Supapkus', ik hoop dat we nog veel epische tochten mogen maken.

Natuurlijk wil ik ook mijn familie bedanken. Opa's en oma's -en hoe is het op school?-. Bart en Annabel; een extra broer en zus. Myrthe en Ruben die altijd een glimlach op mijn gezicht kunnen toveren. Fred en Leen, bedankt om altijd

interesse te tonen in wat ik doe en natuurlijk voor het zorgen van een 2e thuis voor Fajah tijdens de werkdagen.

Pa en ma, bedankt om mij altijd mijn eigen ding te laten doen en mij daar onvoorwaardelijk in te steunen. Maartje en Liselotte, het was een leuke tijd in de Vrijstraat.

Evelien, wat ben ik ongelooflijk blij met jou! Altijd zo vrolijk en stralend, echt een zonnetje in huis! Zonder jou zou dit boek waarschijnlijk nooit geschreven zijn. Ik weet zeker dat ons nog mooie tijden te wachten staan...

Gent, Februari 2014
Thijs Spuesens

Table of Contents

Dankwoord **i**

Nederlandse samenvatting **xv**
Referenties xxi

English summary **xxiii**
References xxviii

1 Introduction **1**
1.1 The information revolution 1
1.2 Photonics 6
1.2.1 Integrated Photonics 6
1.3 Silicon Photonics 8
1.4 Heterogeneous integration 10
1.4.1 Germanium on silicon 10
1.4.2 III-V on silicon 11
1.5 Optical interconnects 14
1.5.1 Architectures 15
1.6 Optical Network-on-Chip 15
1.7 Electro-photonic integration 19
1.8 Rationale and goal 21
1.8.1 Contributions by third parties 23
1.9 Outline of the thesis 24
References 26

2 Optical modes in a microdisk and their interaction with an access waveguide **33**
2.1 Microdisk cavities 33
2.1.1 Mathematical description of Whispering Gallery Modes . 34
2.1.2 Microdisk parameters 36
2.2 Layout of a III-V microdisk laser on Silicon 37
2.2.1 Mode profiles in a microdisk 38
2.3 Loss contributions 39
2.3.1 Bend losses 40
2.3.2 Metal losses 40

2.3.3 Scattering losses 45
2.4 Microdisk-Waveguide evanescent coupling 46
2.4.1 Simulation using CMT 48
2.4.2 Simulation using FDTD 53
2.4.3 Experimental results 57
2.5 Conclusions 63
References 64

3 Microdisk laser design and simulation 67
3.1 Lasers on Silicon 67
3.1.1 Micro lasers 68
3.1.2 Microlasers on silicon 69
3.2 Semiconductor laser theory 71
3.2.1 Laser rate equations 72
3.2.2 Internal optical loss 74
3.2.3 Optical gain 75
3.3 Structure of the microdisk laser 77
3.4 Electrical behavior of the microdisk laser 80
3.4.1 Current injection into the semiconductor 80
3.4.2 Carrier transport 80
3.4.3 Carrier mobility 82
3.4.4 Tunnel junction 83
3.4.5 2D axi-symmetric simulation of electrical behavior 84
3.5 Full laser simulation 87
3.5.1 Bandgap 87
3.5.2 Gain spectrum 89
3.5.3 Static laser performance 92
3.6 Fabrication 100
3.7 Conclusions 101
References 102

4 Characterization of microdisk lasers 105
4.1 Run 1 results: First generation CMOS 105
4.1.1 7.5 μm diameter microdisk lasers 106
4.1.2 20 μm diameter microdisk lasers 107
4.1.3 40 μm diameter microdisk lasers 109
4.2 Run 2 results: Second generation CMOS 112
4.2.1 Burn-in treatment 114
4.2.2 Pulsed measurements 114
4.2.3 CW performance 115
4.2.4 Self heating 120
4.2.5 Small-signal behavior 123
4.2.6 Multi-wavelength lasers 124
4.3 Run 3 results: UGent clean room 129
4.3.1 Pulsed performance 130

4.3.2 CW performance . . . 131
4.3.3 Temperature dependence . . . 134
4.3.4 Multi-wavelength laser . . . 136
4.4 Comparison between generations . . . 139
4.5 Conclusions . . . 140
References . . . 141

5 Integrated photodetectors: Design and fabrication **143**
5.1 Detectors on Silicon . . . 143
5.1.1 State-of-the-art . . . 144
5.1.2 Proposed integration scheme . . . 145
5.2 Design and simulations . . . 145
5.2.1 Epitaxial structure . . . 146
5.2.2 Optical modes . . . 146
5.2.3 Optical absorption versus length . . . 149
5.2.4 Bandwidth . . . 152
5.3 Fabrication process for microdisk lasers with detectors . . . 154
5.3.1 CMOS pilot line process . . . 154
5.3.2 UGent process . . . 158
5.4 Characterization of photodetectors . . . 164
5.4.1 Run 1: CMOS pilot line . . . 164
5.4.2 Run 2: UGent clean room . . . 168
5.5 Conclusions . . . 172
References . . . 174

6 Optical Interconnects on Silicon **177**
6.1 State-of-the-art on-chip optical links on silicon . . . 177
6.2 Compact integration of microdisk lasers and detectors . . . 179
6.2.1 Compact single optical link . . . 179
6.2.2 Optical interconnect design for integration with CMOS . . . 187
6.3 Towards Optical Networks on Chip . . . 191
6.3.1 ONoC demonstrators circuits . . . 193
6.4 Conclusions . . . 195
References . . . 199

7 Conclusions and outlook **201**
7.1 Conclusions . . . 201
7.2 Outlook . . . 203

A List of publications **205**
A.1 Publications in International Journals . . . 205
A.2 Publications in International Conferences . . . 207
A.3 Publications in National Conferences . . . 211

B Process flow **213**
B.1 Bonding . . . 213
B.1.1 III-V preparation . . . 213
B.1.2 SOI preparation . . . 214
B.1.3 Bonding . . . 214
B.1.4 InP substrate removal . . . 214
B.2 Detector mesa . . . 215
B.3 Disk definition . . . 215
B.4 Metal contacts . . . 216
B.5 Island . . . 216
B.6 Passivation and planarization . . . 217
B.7 Open contacts . . . 217
B.8 Contact metal . . . 217

C Mask layouts **219**
C.1 Layouts run 1 . . . 219
C.2 Layouts run 2 . . . 219
C.3 Layouts run 3 . . . 220

List of Acronyms

A

AFM	Atomic Force Microscope
APD	Avalanche Photodiode
AWG	Arrayed Waveguide Grating

B

BEOL	Back-end-of-line
BOX	Buried Oxide

C

CMOS	Complementary Metal Oxide Semiconductor
CMP	Chemical-Mechanical Polishing
CMT	Coupled Mode Theory
CW	Continuous Wave

D

DBBA	Direct Band-to-Band Absorption
DMSO	Dimethyl Sulfoxide
DVS-BCB	divinylsiloxane-bis-benzocyclobutene

E

ELOG	Epitaxial Lateral Overgrowth
EMI	Electromagnetic Interference

F

FC	Fiber Coupler
FCA	Free Carrier Absorption
FDM	Finite Difference Method
FEM	Finite Element Method
FEOL	Front-end-of-line
FIB	Focused Ion Beam
FLOPS	Floating Point Operations per Second
FMM	Film Mode Matching
FP7	European Framework Program 7
FSR	Free Spectral Range
FTTH	Fiber-to-the-Home
FWHM	Full Width Half Maximum

G

GSG	Ground-Signal-Ground

I

IC	Integrated Circuit
ICP	Inductively Coupled Plasma
I/O	input/output
ITRS	International Technology Roadmap for Semiconductors
IVBA	Intervalence Band Absorption

L

LCA	Lightwave Component Analyzer

M

MPW	Multi Project Wafer
MQW	Multiple Quantum Well
MSM	Metal-Semiconductor-Metal
MWL	Multi-Wavelength Laser
MZI	Mach-Zehnder Interferometer

O

ONoC	Optical Network-on-Chip
OSA	Optical Spectrum Analyzer

P

PCB	Printed Circuit Board
PECVD	Plasma Enhanced Chemical Vapor Deposition
PIC	Photonic Integrated Circuit
PL	Photoluminescence
PML	Perfectly Matched Layer
PNA	Performance Network Analyzer

R

RIE	Reactive Ion Etching

S

SCL	Separate Confinement Layer
SEM	Scanning Electron Microscope
SG	Signal-Ground
SMSR	Side Mode Suppression Ratio
SOI	Silicon-on-Insulator
SSMBE	Solid Source Molecular Beam Epitaxy

T

TIA	Transimpedance Amplifier
TIR	Total Internal Reflection
TL	Tunable Laser
TSV	Through Silicon Via

V

VCSEL	Vertical Cavity Surface Emitting Laser

W

WDM	Wavelength Division Multiplexing
WGM	Whispering Gallery Mode

Nederlandse samenvatting –Summary in Dutch–

De evolutie van moderne digitale electronica is het resultaat van de mogelijkheid om meerdere transistoren te integreren op een enkele chip. Dit heeft het niet alleen mogelijk gemaakt om de complexiteit van de circuits te vergroten, maar gaf ook toegang tot massaproductie, wat resulteerde in goedkope transistoren. Gedurende de laatste decennia is er veel moeite gedaan om de fabricageprocessen te verbeteren en zo de dimensies van de transistoren te kunnen verkleinen. Dit verkleinen heeft een aantal voordelen; de schakelsnelheid van de transistoren wordt bijvoorbeeld groter en de prijs per transistor daalt omdat er meer op hetzelfde oppervlak geplaatst kunnen worden. De elektrische interconnecties tussen de transistoren ondervinden echter geen voordeel van deze miniaturisatie. Omdat het aantal transistoren op een chip toeneemt, blijft de grootte van de chip min of meer gelijk en de globale elektrische interconnecties blijven dus even lang. Aangezien elektrische interconnecties een bandbreedte/lengte beperking kennen komt er een moment waarop ze de bandbreedte niet meer aankunnen. Bovendien neemt ook de vermogensdissipatie toe, omdat de diameter van de interconnectie wel afneemt. Deze problemen zijn samen bekend als de interconnectie flessenhals.

Optische interconnecties hebben geen beperking voor wat betreft de lengte/-bandbreedte verhouding. Daarom werden begin jaren tachtig de lange elektrische verbindingen in telecommunicatienetwerken vervangen door optische verbindingen. Door de constant toenemende vraag naar bandbreedte, wordt de afstand waarbij het economisch haalbaar wordt om bestaande elektrische verbindingen te vervangen door optische verbindingen steeds korter. Als we ons baseren op transities van elektrische naar optische verbindingen in het verleden, dan blijkt er steeds een overgang plaats te vinden bij een bandbreedte-lengte product van 100 Gb/s x m. Globale interconnecties op een chip hebben een lengte in de orde van enkele centimeters en dus wordt er een transitie verwacht op het moment dat de datasnelheid rond de 10 Tb/s ligt. Op basis van voorspellingen in de ITRS roadmap, worden deze snelheden binnen enkele jaren verwacht.

Voor het vervangen van elektrische interconnecties op een chip door optische interconnecties zijn er fotonische geïntegreerde circuits (PICs) nodig. Het silicium-op-insulator materiaalsysteem is een aantrekkelijk platform voor deze PICs. Dit materiaalsysteem heeft een groot indexcontrast, wat het mogelijk maakt om een grote integratiedichtheid te bekomen. Bovendien kan bestaande CMOS technologie gebruikt worden voor het fabriceren van deze circuits. Een groot pro-

bleem is echter de indirecte bandkloof van silicium, waardoor het moeilijk is een efficiënte lichtbron te maken. Alternatieve oplossingen worden onderzocht en een veelbelovende route is een heterogene integratie techniek waarbij III-V materiaal geïntegreerd wordt met silicium door middel van een verbindingsproces. III-V materiaal is superieur wanneer het gaat om het vervaardigen van actieve photonische componenten. Het integreren van dit materiaal met silicium combineert het beste van twee werelden. Het is van groot belang dat de vermogensdissipatie van de interconnecties niet toeneemt op het moment dat er gemigreert wordt naar optische interconnecties. Daarom zijn zogenaamde microlasers nodig als lichtbronnen, die significant kleiner zijn dan conventionele lasers. De vermogensdissipatie in deze microlasers is lager, hetgeen ten koste gaat van uitgangsvermogen, maar ook minder belangrijk is gezien de korte afstanden. Voor bidirectionele optische verbindingen is het bovendien nodig om compacte integratie van efficiënte microlasers en detectoren mogelijk te maken. Wanneer het aantal benodigde verbindingen groot wordt, zijn conventionele punt-naar-punt verbindingen vermoedelijk niet meer de meest efficiënte aanpak.

Het doel van dit werk was het onderzoeken van compacte 'on-chip' optische interconnecties op silicium met behulp van heterogeen geïntegreerde microbronnen en detectoren. Ook de mogelijkheid tot het realiseren van Optische Netwerken-on-Chip (ONoCs) door passieve golflengte gevoelige elementen en multi-golflengte lasers te integreren is onderzocht. Voor de microbronnen bouwen we verder op het III-V gebaseerde microschijflaserontwerp ontwikkelt door Van Campenhout en anderen [1]. Het is reeds aangetoond dat multigolflengte lasers gemaakt kunnen worden met behulp van deze microschijflasers, dit door meerdere schijven met een kleine variatie in straal, en dus in golflengte, te integreren op een enkele golfgeleider [2]. Het integreren van efficiënte III-V lasers en detectoren die direct naast elkaar staan is niet triviaal, aangezien er doorgaans een andere epitaxiale structuur benodigd is voor beide componenten. Wanneer dezelfde epitaxiale structuur gebruikt wordt voor beide componenten is compacte integratie mogelijk, maar dit gaat ten koste van de performantie van een van de twee componenten. Het gebruik van twee verschillende epitaxiale structuren resulteert in spatiële restricties. In dit werk maken we gebruik van een nieuwe epitaxiale structuur waarbij er voordeel wordt gehaald uit het feit dat er een dunne film gebruikt wordt voor de microschijflaser. Deze epitaxiale structuur bevat aparte lagen voor de laser en detector. Deze nieuwe aanpak laat het toe om microschijflasers en detectoren compact te integreren, waardoor het mogelijk wordt om bidirectionele optische verbindingen te realiseren op silicium. Het gepresenteerde werk werd uitgevoerd in het raamwerk van het EU FP7 project WADIMOS.

In [1] werd de wereldwijd eerste elektrisch geïnjecteerde microschijflaser op silicium gedemonstreerd. Er werd echter ook gerapporteerd dat er nog ruimte voor verdere verbetering is voor wat betreft de performantie. Ook de opbrengst in aantallen werkende lasers was niet erg hoog. De epitaxiale groei van de III-V stapel werd uitgevoerd door onze projectpartners van INL. Ze hebben het groeiproces verder geoptimaliseerd en konden daardoor een dunnere stapel groeien met een tunneljunctie boven de actieve laag in plaats van eronder, zoals in voorgaande ont-

werpen. Tijdens dit onderzoek hebben we simulaties uitgevoerd gebaseerd op deze nieuwe stapel om de geometrie van de microschijflaser te optimaliseren, zodat de optische verliezen geminimaliseerd kunnen worden.

Uit metingen is gebleken dat in een multi-golflengte laser, gebaseerd op een rij van microschijflasers, er sterke koppeling was naar hogere orde modi van de naastliggende microschijven waardoor de performantie sterk verminderd werd. Simulaties van de koppeling tussen een microschijflaser en een golfgeleider zijn uitgevoerd, zodat de gewenste koppeling tussen de fundamentele modi van de microschijf en golfgeleider gemaximaliseerd wordt, terwijl de koppeling tussen andere modi juist geminimaliseerd wordt.

Een rigoreuze 2.5D axi-symmetrische electro-optische simulatie werd uitgevoerd op de microschijflaser structuur om inzicht te krijgen in het transport van ladingsdragers en andere kritische parameters. Om de betrouwbaarheid te vergroten zijn de parameters aangepast op basis van experimentele resultaten.

Een ontwerp voor de detector werd gemaakt op basis van de nieuwe epitaxiale structuur en optische simulaties werden uitgevoerd om de koppeling tussen de golfgeleider en de absorptielaag van de detector te vergroten. Uit de resultaten bleek dat de ongewenste absorptie in de laserquantumvallen te verwaarlozen is, maar dat de invloed van het top metaal contact significant is.

In totaal zijn er 3 verschillende fabricage cycli uitgevoerd; twee in een CMOS proeflijn en één in de stofvrije ruimte van de Universiteit Gent. Het CMOS fabricageproces voor de microschijflaser en -detector werd ontwikkeld en geoptimaliseerd door onze project partners bij CEA-Leti. Alle fabricagestappen voor de microschijflaser en -detector werden hier uitgevoerd op een 200 mm waferschaal in een CMOS proeflijn.

In de eerste CMOS ronde werden zowel microschijflasers als detectoren gefabriceerd. Alleen de microschijflasers met een diameter groter dan 20 μm toonden laserwerking. Van dwarsdoorsnede SEM foto's werd het duidelijk dat er een Titanium ring residu lag rond de microschijf caviteit. Dit resulteerde in grote optische absorptie en weerhield de kleinere microschijflasers van het vertonen van laserwerking. De detectoren hadden een responsiviteit tot maximum 0.97 A/W voor 80 μm lange structuren. Relatief hoge donkerstromen werden gemeten met waarden tussen een paar honderd nano-Ampere tot enkele micro-Ampere. Dit werd mogelijk veroorzaakt door het niet tijdig passiveren van de structuren. Klein-signaal bandbreedtes tot 16 GHz werden gemeten voor structuren met een lengte van 20 μm.

De tweede CMOS ronde bevatte meer complexe ontwerpen met 8x8 ONoCs en ook 2x2 ONoCs, welke speciaal ontworpen waren om geïntegreerd te kunnen worden met CMOS electronica door middel van een flip-chip integratie. Echter, door verschillende problemen tijdens de processing en design fase, werden geen werkende detectoren gerealiseerd in deze ronde en daardoor konden deze circuits enkel gedeeltelijk gekarakteriseerd worden. Het chipontwerp bevatte ook op zichzelf staande microschijflasers met diameters tussen de 5 en 40 μm en CW laserwerking werd geregistreerd voor structuren met een diameter groter dan 6 μm. De beste performantie werd gemeten op structuren met een diameter van 7 μm met

drempelstromen van 0.6 mA en een maximaal uitgangsvermogen van 31 μW in de silicium golfgeleider. Sterke oscillaties tussen de linker en rechter uitgang van de laser werden waargenomen in de LI figuren. Dit werd veroorzaakt door externe reflecties van onder andere de vezelkoppelaars. Uit klein-signaal metingen werd een maximale 3 dB bandbreedte van 7.8 GHz gevonden. De golflengtespatiëring in multigolflengte lasers was niet uniform en dit werd mogelijk veroorzaakt door de 5 nm grid van het masker en bijkomende afrondingsfouten. De MWLs lieten een dalend uitgangsvermogen zien naarmate de betreffende microschijf verder van de uitgang verwijderd stond. Dit kan toegeschreven worden aan de koppeling naar hogere orde modi van naastliggende microschijven in de rij. Dit resultaat was de aanleiding voor de simulaties die werden uitgevoerd omtrent de koppeling. Geoptimaliseerde ontwerpen werden gemaakt op basis van deze simulaties. Deze ontwerpen zijn gebruikt in de fabricageronde in de clean room van de Universiteit Gent.

In het fabricageproces uitgevoerd aan de Universiteit Gent werd gebruik gemaakt van een aangepaste adhesieve verbindingsmethode welke het toelaat een betere controle te hebben over de verbindingslaagdikte vergeleken met het standaard adhesieve verbindingsproces. Verder werd er ook een zelf-gealigneerde aanpak ontworpen voor de fabricage van het kritieke topcontact van de microschijflaser. In deze ronde werden zowel microschijflasers als detectoren succesvol gefabriceerd op een enkele chip. Een compacte optische link op deze silicium chip werd gerealiseerd door de mirscoschijflaser en de detector met elkaar te verbinden via een silicium golfgeleider. Een microscoop opname van deze link is weergegeven in Figuur 1. De detectoren hadden een responsiviteit tot 0.69 A/W voor een 60 μm lange structuur en de donkerstroom was 20 nA voor 40 μm lange structuren. Een bandbreedte van 18 GHz was gemeten voor de detectoren bij een spervoorspanning van 1 V. De microschijflasers lieten CW operatie zien met drempelstromen van 220 μA en een maximale hellingefficiëntie van 57 $\mu W/mA$ gemeten aan 1 uitgang. De stroom-versus-stroom karakteristiek van de gehele optische link is weergegeven in Figuur 2. Een klein-signaal metingen werd uitgevoerd over de complete verbinding en een bandbreedte van 7.6 GHz werd gemeten bij een laserinstelspanning van 1.9 V en een detector instelspanning van 1 V. De klein-signaal responsie karakteristiek versus de instelspanning van de laser is weergegeven in Figuur 3. De bandbreedte van de link is dus gelimiteerd door de bandbreedte van de microschijflaser. Multi-golflengte lasers met geoptimaliseerde koppeling condities werden ook in deze fabricageronde opgenomen en de metingen gaven aan dat het uitgangsvermogen van de microschijflaser in de rij niet langer afhangt van de positie in de rij.

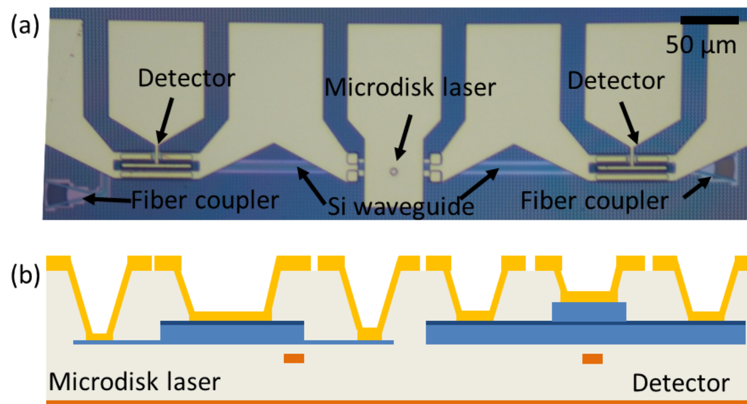

Figuur 1: (a) Microscoop beeld van de complete optische link, waarbij detectoren aan beide zijden van de microschijf laser verbonden zijn via een silicium golfgeleider. (b) Schematische weergave van de doorsnede van de microschijf laser en de detector.

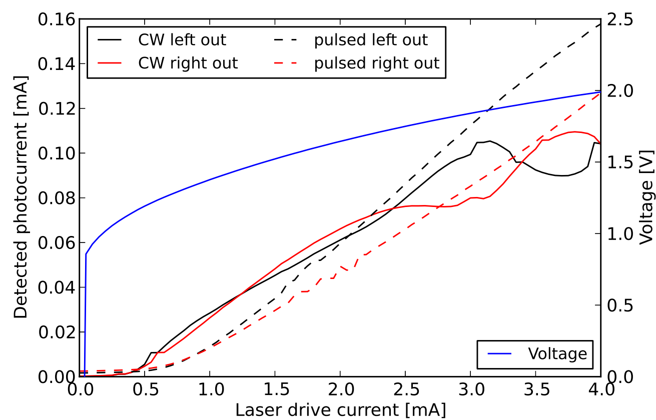

Figuur 2: Stroom versus stroom plot van de optische link. De zwarte en rode lijn komen overeen met respectievelijk de linker- en rechterdetector. Doorgetrokken lijnen representeren CW metingen en onderbroken lijnen gepulste metingen. De IV curve is aangeduid met de blauwe lijn.

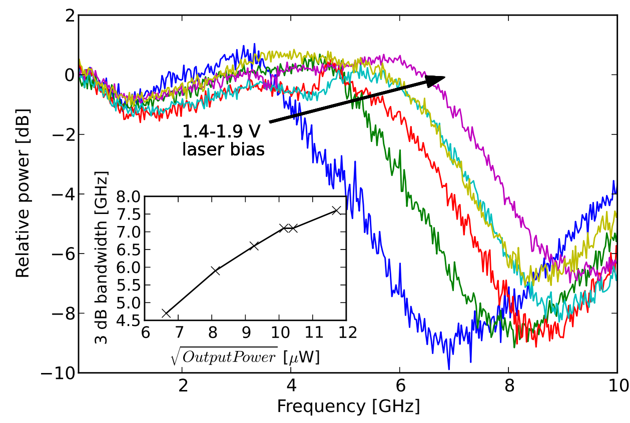

Figuur 3: Klein-signaal respontie van de volledige optische link voor verschillende instelspanningen en de 3 dB bandbreedte versus de wortel van het uitgangsvermogen van de laser (inzet).

Referenties

[1] Joris Van Campenhout. *Thin-Film Microlasers for the Integration of Electronic and Photonic Integrated Circuits*. PhD thesis, Ghent University, 2007.

[2] Joris Van Campenhout, Liu Liu, Pedro Rojo Romeo, Dries Van Thourhout, Christian Seassal, Philippe Regreny, Lea Di Cioccio, Jean-Marc Fedeli, and Roel Baets. *A Compact SOI-Integrated Multiwavelength Laser Source Based on Cascaded InP Microdisks*. IEEE Photonics Technology Letters, 20(16):1345–1347, August 2008.

English summary

The evolution of modern digital electronics is the result of the ability to integrate multiple transistors on a single chip. This made it possible to increase the complexity of the circuits but also allowed for mass fabrication, resulting in low cost transistors. Over the last decades lots of efforts have been put in improving the fabrication technology to scale down the dimensions of the transistors. Down scaling in size has several advantages, the switching speed of the transistors increases, while the price of a chip decreases. However, the electrical interconnects between the transistors do not benefit from this down scaling. In fact, the performance of these electrical interconnects becomes worse as the dimensions decrease. That is, by decreasing the cross-sectional dimensions of the wire, its bandwidth capacity is reduced. Decreasing the length of the interconnect has a positive effect on the bandwidth, but because of the increasing number of transistors on the chip, the size of the chip remains constant and hence, the length of the interconnect remains the same. At the same time, also the power dissipation increases. This is known as the interconnect bottleneck.

Optical interconnects do not suffer from this bandwidth length trade-off. As a result, optical interconnects started to replace electrical interconnects in the long-haul connections in the early 80's. Because of the ever increasing bandwidth, the length at which it becomes economically feasible to replace electrical interconnects by optical interconnects becomes shorter and shorter. Based on transitions from electrical to optical interconnects that have taken place in the past, the cross-over point lies around 100 Gb/s x m. Global electrical interconnects on chip are on a cm scale and thus have an expected transition point around 10 Tb/s, which is soon going to be reached according to the ITRS roadmap.

Replacing electrical interconnects on a chip requires photonic integrated circuits (PICs). The Silicon-on-Insulator (SOI) material system has received a lot of attention as a platform for these PICs. It has a large index contrast, which allows for a high integration density and existing CMOS technology can be used for the fabrication of these circuits. However, a major issue is the difficulty of achieving light emission in silicon due to its indirect bandgap. Alternative solutions are being investigated and a promising route is a heterogeneous integration technique where III-V materials are integrated with silicon through a bonding approach. III-V material is a superior material when it comes to active photonic devices and integrating these materials with silicon allows to combine the best of both worlds. It also important that the power dissipation by the interconnects does not increase when migrating to optical interconnects, therefore so called micro lasers are re-

quired which are an order of magnitude smaller than conventional laser designs. The power dissipation in these micro lasers is lower, at the cost of lower output power. For bidirectional optical links, compact integration of efficient micro lasers and detectors is required, which has not yet been achieved. Furthermore, when the number of links is large, conventional point-to-point links might not be the most efficient approach.

The goal of this work was to investigate compact on-chip optical interconnects on silicon based on heterogeneously integrated microsources and detectors. Also the possibility of realizing Optical Networks-on-Chip (ONoCs) by integrating passive wavelength selective elements and multi-wavelength lasers was explored. For the microsources we build upon the III-V based microdisk laser design developed by Van Campenhout et al. [1]. It was also shown that a multi-wavelength laser can be made using these microdisk lasers, by cascading multiple disks with slightly different radius and thus slightly different resonant wavelengths, on a single access waveguide [2]. Integrating efficient III-V lasers and detectors next to each other is not trivial as typically a different epitaxial structure is required. Using the same epitaxy for both devices leads to inefficient operation of one of the two, while using separate epitaxial structures results in spatial restrictions. In the latter case, no bidirectional optical links can be achieved. Here we use a new epitaxial structure that relies on the fact that a thin film is used for the microdisk laser. This epitaxial structure contains the layers for both the laser and the detector. This new approach allows for the compact integration of microdisk lasers and detectors, thereby making it possible to realize bidirectional optical links on silicon. The work presented here was performed in the framework of the EU FP7 project WADIMOS.

In [1] the worlds first electrically injected microdisk laser on silicon was demonstrated. However, it was also reported that there was still room for further improvement in the performance of the device and also the yield was not very high. The epitaxial growth of the III-V stack was performed by our project partners at INL. They optimized the growth process and were therefore able to grow a thinner stack with a tunnel junction above the active layer, instead of below in previous devices. In this work, we performed simulations based on this improved stack to optimize the microdisk laser geometry to reduce optical losses.

From measurements it was found that in a multi-wavelength laser based on an array of microdisk lasers there was strong coupling to higher order modes of subsequent disks which detoriates the performance significantly. Simulations on the coupling between a microdisk laser and the access waveguide have been performed to optimize the coupling between the desired fundamental disk mode, while minimizing coupling to other higher order modes.

A rigorous 2.5 D axi-symmetric electro-optic simulation was performed on the microdisk laser structure in order to get insight into the charge carrier transport and critical parameters. To increase the reliability of the model, it was fitted to obtained experimental results.

A detector design was made based on the new epitaxial structure and optical simulations were performed to optimize the coupling between the fundamental

waveguide mode and the absorption layer of the detector. Undesired absorption at the laser quantum wells was found to be negligible, but the influence of the top metal contact cannot be neglected.

In total 3 different fabrication runs were performed, two in a CMOS pilot line and one in the clean room of Ghent University. The CMOS fabrication process for the III-V microdisk laser and detector was developed by our project partners at CEA Leti. All fabrication steps for the microdisk laser and detector were carried out 200 mm waferscale in a CMOS pilot line.

In the first CMOS run both microdisk lasers and detectors were fabricated. Only the microdisk lasers with radii larger than 20 μm diameter showed lasing behavior. Cross-section SEM images revealed that a titanium ring residue was present close to the microdisk cavity resulting in strong optical absorption and withholds the small microdisk cavities from lasing. The detectors had responsivities up to 0.97 A/W for 80 μm long devices. Relatively high dark currents with values between a few hundred nano amperes to micro amperes were obtained and most likely caused by not timely passivating the devices. Small-signal bandwidths up to 16 GHz were obtained for 20 μm long detectors.

The second CMOS run contained more complex designs with 8x8 Optical Networks-on-chip (ONoCs) and also 2x2 ONoCs that were made in such a way that they allowed for flip-chip integration with CMOS electronics. However, due to several processing and design issues, no working detectors were obtained in this run and therefore these circuits could only be partially characterized. The designs also contained stand-alone microdisk lasers with diameters ranging from 5 to 40 μm and CW lasing was obtained for devices with a diameter of 6 μm or larger. The best performance was obtained for 7 μm diameter devices with threshold currents of 0.6 mA and a maximum output power of 31 μW in the silicon waveguide. Strong oscillations between the left and right output of the laser was observed in the LI curves and this is caused by external reflections from e.g. the fiber couplers. From small-signal measurements a maxmimum 3 dB bandwidth of 7.8 GHz was obtained. The wavelength grid of the multi-wavelength lasers was not uniform and this can is most likely caused by the 5 nm grid of the mask and rounding errors. The MWLs also suffered from a decreasing output power for disks further away from the output and this can be attributed to the coupling to higher order modes of subsequent disks in the array. This was the trigger for the simulations performed on the coupling and optimized designs were made based on these simulations. These designs were included in the process run at Ghent University.

for the fabrication process in Ghent a modified adhesive bonding approach was used that allows for better control of the bonding layer thickness, compared to the standard adhesive bonding approach. Also, a self-aligned approach was developed for the fabrication of the critical top contact of the microdisk laser. In this run both microdisk lasers and detectors were successfully fabricated on a single chip. A compact optical link on this silicon chip was realized by interconnecting the microdisk laser and the detector through a silicon waveguide. A microscope image of this link is shown in Figure 4. The detectors had responsivities up to 0.69 A/W for 60 μm long devices and dark currents down to 20 nA for 40 μm long devices.

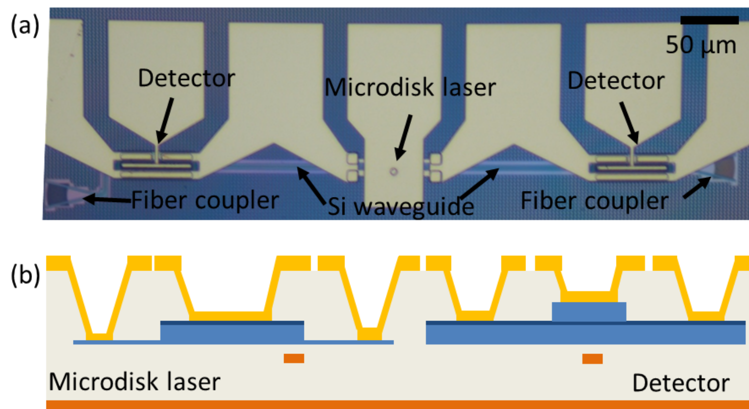

Figure 4: (a) Microscope image of the full optical link, where detectors on both sides of the microdisk laser are connected via a silicon waveguide and (b) schematic representation of the cross-section of the microdisk laser and detector.

A bandwidth of 18 GHz was measured for the detectors at a reverse bias of 1V. The microdisk lasers showed CW operation with threshold currents as low as 220 μA and a maximum single sided slope efficiency of 57 $\mu W/mA$ was obtained. A current versus current characteristic of the optical link is shown in Figure 5 A small-signal measurement was performed on the complete optical link, where a bandwidth of 6.7 GHz was obtained for a laser bias of 1.9 V and a dtector bias of 1 V. The small-signal response versus laser bias is shown in Figure 6. The bandwidth of this link is limited by the microdisk laser. Multi-wavelength lasers with optimized coupling conditions were included in this run and measurements showed that the output power of the microdisks in the array no longer depend on the position in the array.

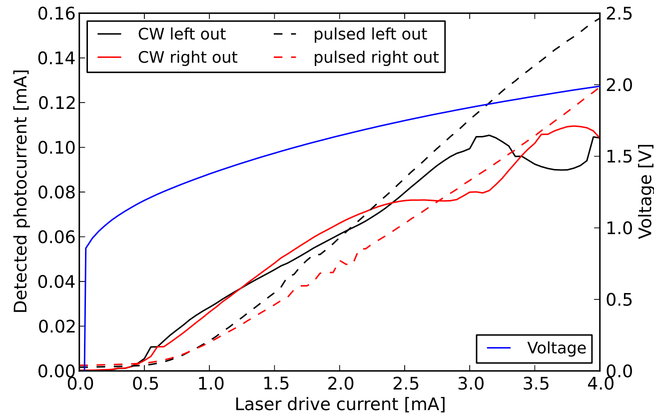

Figure 5: Current versus current plot of the optical link. The black and red curves correspond with the left and right detector, respectively. Solid lines represent CW measurements, while dashed lines represent pulsed measurements. The IV curve is indicated by the blue curve.

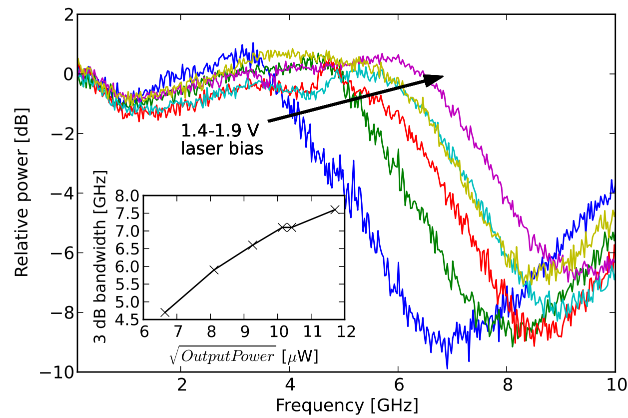

Figure 6: Small signal response of the full optical link versus laser bias and the 3dB bandwidth versus the square root of the laser output power (inset).

References

[1] Joris Van Campenhout. *Thin-Film Microlasers for the Integration of Electronic and Photonic Integrated Circuits*. PhD thesis, Ghent University, 2007.

[2] Joris Van Campenhout, Liu Liu, Pedro Rojo Romeo, Dries Van Thourhout, Christian Seassal, Philippe Regreny, Lea Di Cioccio, Jean-Marc Fedeli, and Roel Baets. *A Compact SOI-Integrated Multiwavelength Laser Source Based on Cascaded InP Microdisks*. IEEE Photonics Technology Letters, 20(16):1345–1347, August 2008.

1 Introduction

1.1 The information revolution

Without a doubt the invention of the transistor, which was the lead-in for modern digital electronics, and the Internet can be named in one breath with other important life changing inventions like e.g. the steam engine and the printing press. The numerous devices and equipment available today relying on this transistor, like smartphones, televisions and medical scanners to name a few, cover to whole range from consumer products to medical and communication products. Nowadays, it is hard to imagine a live without all these electronic devices and communication networks. The key to realizing modern digital electronics was the ability to integrate multiple transistors on a single chip. This not only made it possible to increase the complexity of the circuits on the chip, but also allowed for mass-fabrication resulting in extremely low cost transistors. Over the last decades lots of efforts have been put in improving the semiconductor fabrication technology to scale down the dimensions of the transistors. This has led to a steady increase in integration density and also the switching speed of the transistors improved with decreasing dimensions, thereby increasing the computational power. This trend was predicted by Gordon Moore in 1965 when he stated that 'the number of components in an integrated circuit will double every 18 to 24 months'. Up until today this law still holds, albeit somewhat as a self fulfilling prophecy of the semiconductor industry.

Keeping up with Moore's law is not without hurdles. The transistor count on a state-of-the-art processor today, already exceeds the number of 1 billion per square

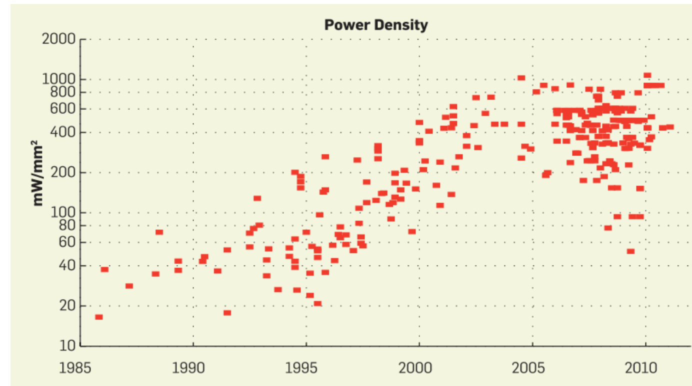

Figure 1.1: Evolution of power density in microprocessors [1].

centimeter. This large integration density lowers the cost, but also has a downside as the power dissipation density in microprocessors is reaching values of hundreds of W/cm^2, which is about the power density in a nuclear reactor! It is clear that the trend shown in Figure 1.1 up to 2005 could not continue, which is obvious from the saturation beyond 2005. The power dissipation and the heat generation associated with it are proportional to the clock frequency. Therefore, instead of further increasing the clock frequency, around 2005 the focus was shifted to parallel computing where multiple processor cores working at clock speeds up to 3 GHz are interconnected. This way the computational power can still increase without increasing clock speed. Today, these multi-core processors are mainstream. However, large amounts of data needs to be transferred between these cores and this puts stringent demands on the electrical interconnects. What is more, electrical interconnects do not benefit from the downscaling in size as transistors do. Major concerns at this point in time are the chip-to-chip interconnects and the so-called 'global interconnects' on chip which are responsible for conducting information across the chip over longer distances.

The main problems with metal wires, serving as electrical interconnects, is that they suffer from loss and signal delay which are caused by the finite resistance and the capacitance to e.g. other wires. The signal delay is proportional to the RC time constant and in turn this is proportional to the square of the length of the interconnect (because both R and C are proportional to the length). Although the dimensions of the components go down with improved fabrication processes, the number of transistors on a chip still increases to improve the computational power. The net result is that the chip area remains more or less constant over time, as is shown for several generations of Intel processors in Figure 1.2, and the length of the interconnects thereby stays the same. The width and the spacing of the interconnects become smaller when scaling down, reducing the available bandwidth of

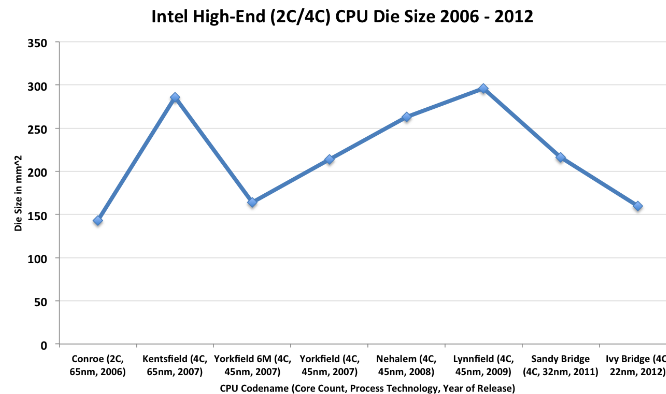

Figure 1.2: Die size of several generations of Intel's microprocessors [4].

the interconnects. Keeping in mind that the bandwidth requirements increase with increasing computational power, it becomes clear from predictions in the International Technology Roadmap for Semiconductors (ITRS) [2] that electrical interconnects cannot keep up with the data processing capabilities on the chip. This ITRS roadmap is an important reference for the semiconductor industry and is a cooperative effort of semiconductor manufacturers, academics and government organizations. The main objective of the ITRS roadmap is to identify technological challenges that are expected in both the near and longer term future, while at the same time possible solutions are discussed and analyzed.

Next to these limitations for on-chip interconnects, the same reasoning holds for off chip input/output (I/O) connections and because the lengths of these interchip interconnects are even longer, the available bandwidth per interconnect is smaller. Realizing that according to the ITRS roadmap the total I/O bandwidth requirement is in the order of several hundreds of Tb/s by 2022 and that current bandwidths for off-chip interconnects are in the order of a few tens of Tb/s [3], it is clear that this is a burden that will not be easy to overcome.

Next to the bandwidth problem, there also exists a major issue concerning the energy consumption. The power dissipation in modern microprocessors is reaching a value of 200 W, which is about the maximum amount of power that can be dissipated such that generated heat can still be removed from the chip in a cost effective manner. In microprocessors made with the 130 nm technology node (the technology of 10 years ago), the interconnects consumed about 50% of the total dissipated power. Today's interconnects are more power efficient, but at the same time, required bandwidth grows faster resulting in even larger power dissipation by the interconnects. To stretch this issue, consider the expected I/O bandwidth required in 2022 of 230 Tb/s as predicted in the ITRS roadmap and assume a

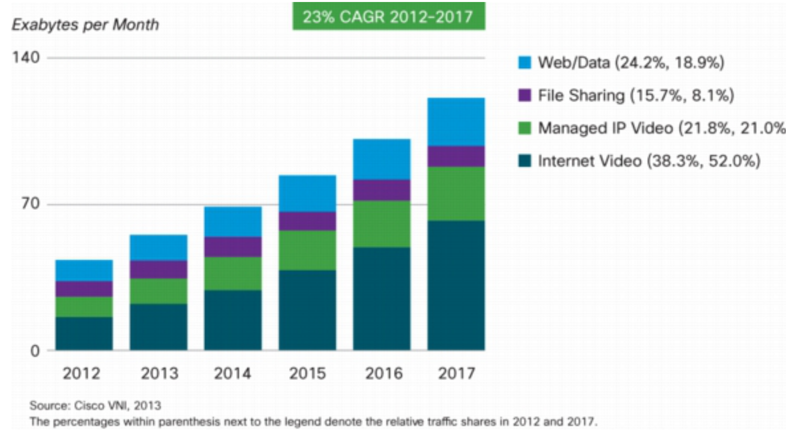

Figure 1.3: Prediction of the global IP traffic per month in coming years. The colors indicate the percentages of different types of data [5].

power dissipation plateau of 200 W, this means only 170 fJ/bit is available for the I/O interconnects [3].

Also when looking at a larger scale the energy consumption problem becomes obvious. Applications like Facebook, YouTube and more recently Netflix are immensely popular and used by hundreds of million people. Huge numbers of pictures and videos are send over the network through these applications. According to Cisco annual global IP traffic will pass the zettabyte threshold by the end of 2015, and will reach 1.4 zettabytes per year by 2017 [5]. The expected trend of global IP traffic is shown in Figure 1.3 and also indicates the percentages of different types of data. Clearly, huge amounts of data need to be transferred and stored, resulting in more and bigger data centers around the globe. As these data centers contain racks full with microprocessors, one can imagine that the energy consumption of such a data center is enormous. It is estimated that currently about 2% of the electrical power worldwide is dissipated by these data centers. About 15 to 30 % of this power consumption is spent on interconnects [3, 6].

These issues all together are known in semiconductor industry as the interconnect bottleneck. The ITRS roadmap describes several possible solutions to this problem both for short and long term.

As the dimensions of the components scale down in integrated electronics, the interconnect wires come closer together. The parasitic capacitance between the interconnect wires thereby increases. To be able to keep on scaling according to Moore's law, semiconductor industry started looking in the late nineties to reduce the dielectric constant of the insulating material, the so-called low-κ dielectrics, to reduce the capacitance. Since then, several 'materials' with a lower κ value compared to pure silicon dioxide, have been implemented in integrated

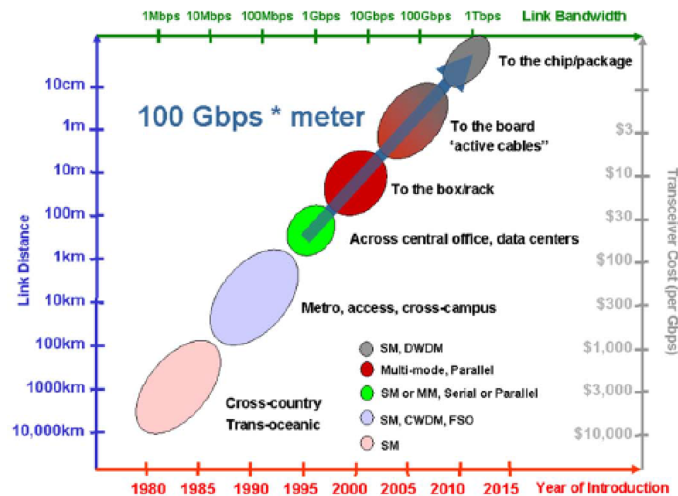

Figure 1.4: Evolution of optical links in communication systems. Taken from [7].

circuits (ICs). As it becomes increasingly more difficult to fabricate materials with lower κ, this approach cannot continue forever and especially for the global interconnects new solutions are required. New emerging interconnect solutions are discussed in the ITRS roadmap. Potential solutions for global interconnects are 3D integration, which allows for shorter interconnects by stacking ICs in the vertical direction, and optical interconnects, where the metal wires are replaced with dielectric waveguides that guide light. Next, to the replacement of electrical global interconnects, optical interconnects have also been proposed for I/O. The cross-over point where optical interconnects outperform electrical interconnects depends on the bandwidth-length product. The bandwidth-length product is an important figure of merit in communication systems, indicating the maximum bandwidth that a link can support for a given length. Electrical interconnects typically have a maximum bandwidth-length product of $10Mb/s \times km = 10Gb/s \times m$, whereas for optical interconnects this is orders of magnitude higher with values of $10Pb/s \times m$. Based on the transitions from electrical to optical interconnects that have taken place in the past the cross-over point seems to lie around $100Gb/s \times m$ as can be seen in Figure 1.4 [7]. Based on this projection, a transition for chip level I/O from electrical to optical interconnects is expected somewhere in the next few years. Obviously, this requires the development of CMOS compatible optical components.

1.2 Photonics

The field of photonics studies the generation, detection, and other manipulations of light. The name 'photonics' comes from the analogy with electronics, the field that is based on manipulation of electrons, whereas photonics focuses on the manipulation of photons, the elementary 'particle' of light. It was realized already in the 1950s that using an optical instead of an electrical carrier signal could improve the capacity of a communication link by several orders of magnitude. However, in absence of coherent light sources and optical media to transfer light, such systems could not be realized [8]. It took till 1970 when a breakthrough occurred and both compact optical sources and low-loss optical fibers were demonstrated [8]. This was the kick-start for worldwide research in optical communication systems. Later on, when photonics technology matured, next to communication other applications came up, such as laser printing, optical data recording, displays, etc.

Next to the larger capacity, optical links have some other advantages over electrical links. The loss in optical fiber links is almost two orders of magnitude lower compared to coaxial links and they are immune to electromagnetic interference (EMI). Optical links started to replace electrical, coaxial links in long-haul networks, because of their larger bandwidth-length product, which made them more cost efficient as less repeaters were needed in these links. Later on when the bandwidth requirements grew larger, the distances at which optical links became economically feasible, became shorter and shorter. This trend, illustrated in Figure 1.4, is still going on where optical fiber is currently reaching into the access networks through a Fiber-to-the-home (FTTH) network architecture [9] and also data centers are heavily making use of optical fiber connections for rack-to-rack connections [10].

As already pointed out in the previous section, electrical interconnects are also starting to form a bottleneck in inter- and intrachip level connections. Obviously, if one would want to include optical links on this scale, integrated photonics circuits are required.

1.2.1 Integrated Photonics

Following the successful road of miniaturization and integration in electronics, also in photonics it is desirable to include all kinds of optical functions on a single chip, resulting in a so-called Photonic Integrated Circuit (PIC). Next to the obvious advantages of lower cost and compactness, it also avoids a significant amount of alignment constraints. In contrast to electrical circuits, where it is sufficient to simply make contact between components through a conductor, in photonics accurate alignment of the optical fiber with the optical component is required. In case of bulk optical components mirrors and lenses need to be properly aligned, which is a daunting task. If multiple optical components can be integrated on a single

chip, this reduces the assembly cost of an optical system considerably.

Several material systems can be used for PICs. An important requirement in choosing a material system is obviously that the material should be transparent for the desired wavelength range. On a PIC, light is guided by a dielectric waveguide that is surrounded by a material with a lower refractive index than that of the waveguide core. As a result light can be guided by total internal reflection (TIR), similar to optical fibers. The refractive index contrast between the core and the cladding of the waveguide determines the integration density that can be achieved. A high refractive index contrast means that small bend radii can be used without causing excessive bend losses. Also, the crosstalk between waveguides for a given pitch is lower when using a higher index contrast. A downside when using high contrast material systems is that fabrication tolerances are smaller and also surface roughness will have a stronger impact.

Besides the transparency and the index contrast of the material system used, it can also be important, depending on the application, that strong non-linear effects are present or that active components can be efficiently integrated.

The most common integration platforms for PICs are:

- *Silica-on-silicon*: this approach uses doped and undoped silica as core and cladding material on a silicon substrate, respectively. It is a very mature and robust technology with low waveguide losses and high thermal stability. However, the low refractive index contrast makes this platform not suitable for high integration densities as very large bend radii are needed. Furthermore, this material system is not suited for circuits requiring active components.

- *Silicon-on-insulator (SOI)*: a silicon layer is isolated from the silicon substrate through a underlying buried oxide layer (BOX). The cladding material is thus either air or SiO_2 resulting in a very high index contrast both horizontally and vertically. Therefore, very high integration density can be obtained. At the same time, this also sets high demands for the fabrication as e.g. small variations in device structures can detoriate the performance significantly. However, the fabrication process is CMOS compatible in the sense that the SOI wafers can be processed using standard CMOS tools and recipes. As this is a very mature processing technology it allows for the fabrication of high quality PICs. SOI is therefore one of the most popular platforms for PICs at the moment and famous under the name of Silicon Photonics. However, due to the indirect bandgap of silicon, it is difficult to make light emitters in this material system.

- *III-V materials*: Materials from group III and V are epitaxially grown in different compositions on mostly GaAs and InP based substrates. This makes it

possible to have direct bandgaps in a wide wavelength range and in combination with the good electrical properties, this is the material system of choice for fabricating high quality semiconductor lasers and other active components. A major advantage is that all kinds of passive and active devices can be integrated monolithically. However, the index contrast in the vertical direction is low, limiting the integration density. Furthermore, these materials are more expensive than e.g. silicon and the processing technology is less mature compared to the CMOS technology. Although this material system is traditionally used for stand-alone high-end components for the long-haul, the trend is to also realize more complex integrated circuits [11].

- *TriPlex (SiO_2/Si_3N_4)*: uses alternating Si_3N_4 and SiO_2 layers on a silicon substrate. By changing the thickness of the layers the index contrast can be engineered from medium to high and very low waveguide losses of 0.1 dB/cm can be reached. It also has a broad wavelength range of 400 nm to 2.35 μm. The fabrication process itself is compatible with CMOS technology, but to make e.g. a waveguide structure more processing steps are required compared to the SOI material system. As for the SOI platform, also in TriPlex it is not possible to fabricate active components.

- *Lithium Niobate ($LiNbO_3$)*: Lithium Niobate is a ferroelectric material with excellent electro-optic, non-linear and piezoelectric properties. It is mostly used for high-performance stand-alone electro-optic modulators, acousto-optic devices and other non-linear applications. It is less suited for complex integrated circuits because of its complex and expensive fabrication process.

- *Polymers*: a material system based on polymers can offer a low cost solution as both the materials and fabrication are cheap. The index contrast is typically very low, which makes this material system not suitable for dense integration of complex photonic circuits. The thermo-optic effect is large resulting in low-power, but also slow thermo-optic switches.

As for the purpose of I/O and global optical interconnects in CMOS electronics, the SOI platform is currently receiving a lot of attention. The main reasons for this are the possibility to reach a high integration density and the fact that the same infrastructure as for CMOS electronics can be used. A more detailed description including strengths and weaknesses of this platform are the content of the next section.

1.3 Silicon Photonics

Silicon is transparent for light with wavelengths in the telecommunication range (1300 nm and 1550 nm windows). Silicon also has a high refractive index of 3.48,

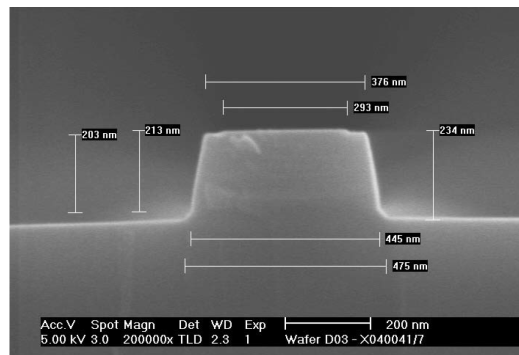

Figure 1.5: SEM image of a cross-section of a single mode waveguide in silicon. The width of the waveguide is 450 nm and the height is 220 nm. Picture from [12]

while its native oxide (SiO_2) has a refractive index of 1.44 (both for wavelengths around 1550 nm). Therefore, the SOI platform has as a very high refractive index contrast allowing for very compact integration of photonic circuits. A scanning electron microscope (SEM) image of a cross-section of a single mode waveguide in silicon with dimensions as small as 450 x 220 nm is shown in Figure 1.5. The fact that this material system is also used for electronic ICs leads us to the next major advantage of silicon photonics: PICs can be fabricated using the standard CMOS fabrication technology used in electronics. This is a very mature processing technology that allows for fabrication of structures with very small feature sizes. Existing CMOS infrastructures can be used to fabricate these PICs, which makes it a very cost-effective approach. Furthermore, the cost of silicon itself is much lower compared to e.g. III-V based materials and it can be grown with very high crystal quality.

The downside of a high index contrast is that the effect of light scattering from imperfections at the interfaces is quite strong, resulting in additional losses and back reflections. However, it has already been shown that by using more recent and advanced CMOS technology this can effectively be reduced [13].

A large amount of highly compact passive photonic components, like waveguides, crossings, filters, fiber couplers, etc., have already been successfully demonstrated since the 1990s and their performance has been improved ever since [14–16]. More recently, also several configurations of high-speed silicon modulators based on the plasma dispersion effect have been shown experimentally [17] with speeds up to 40 Gb/s [18]. Realization of other key active components in silicon such as lasers and detectors is more difficult. Silicon has an indirect bandgap which makes it extremely difficult to make an efficient light source. The most successful attempt is probably the demonstration of a silicon Raman laser [19]. A major drawback however, is that this laser needs to be pumped optically, which

makes it less suitable for efficient integration. Another promising approach is the use of rare-earth-doped silicon for achieving lasing [20]. However, realization of an efficient laser using this technique is not to be expected for the near future. As a result, researchers also started looking at possibilities to combine other materials with the SOI material system and the most important results are discussed below.

1.4 Heterogeneous integration

1.4.1 Germanium on silicon

Germanium has been and is still used as a highly sensitive detector material for the near infrared. However, these high sensitivity detectors are cooled to 77 K to reduce the dark current, which makes them expensive and only suited for some niche applications [21]. This has changed during the last decade when it became possible to epitaxially grow germanium on silicon. This reduced the cost of these detectors considerably and also opened up the possibility to use these detectors in optical communications. Epitaxial growth of germanium on silicon is not trivial due to the large lattice mismatch of 4.2%, resulting in high surface roughness and a high density of threading dislocations degrading the performance [21]. These problems were overcome by improved growth techniques using e.g. SiGe buffer layers [22], two step growth processes [23] and H_2 annealing [24].

Several germanium detectors, both for normal incidence [25, 26] and waveguide approaches [27, 28], have been successfully demonstrated on silicon. Especially the waveguide type detectors attract a lot of attention because they do not suffer from a bandwidth-responsivity trade-off as normal incidence detectors do. In terms of bandwidth and responsivity, the performance of these detectors is similar to InGaAs based detectors, which are the reference for high performance detectors in the near infrared. The main drawback at the moment is the high dark current (around 100 nA @ -1V), which degrades the signal-to-noise ratio and makes them less attractive for the use in low-power consumption circuits.

Recently, there has also been an increasing interest in the realization of germanium/silicon avalanche photodiodes (APD). APDs are mostly used in receivers for long-haul communication systems because their internal gain offers an increased sensitivity over normal pin detectors. The reason for pursuing Si/Ge APDs is that the ionization ratio k, an important figure of merit in APDs, is much smaller in silicon than in typical III-V multiplication materials such as InP [29] and thus could potentially outperform the III-V APDs.

Next to detectors also lasers based on germanium are being investigated. Although in principle germanium is considered an indirect bandgap semiconductor, it can be engineered to behave like a direct bandgap semiconductor by applying tensile strain and n-type doping. An optically pumped Ge-on-Si laser was demonstra-

ted [30] and later on also an electrically pumped version was demonstrated [31] which could be operated just below room temperature (15 °C) and had a maximum output power of 1 mW, though in a multimode regime. Furthermore, a very high threshold current density of 280 kA/cm^2 is required to achieve lasing. Although it is an encouraging result, it is doubtful whether this technology can provide low power consumption devices.

1.4.2 III-V on silicon

As discussed above it is possible to make efficient detectors on silicon by selective growth of germanium. Although also a laser on silicon has been demonstrated using germanium, it is far from efficient and thus another material system is required. It is well known that III-V materials are very well suited for making efficient laser devices and this material system is heavily used to make high performance standalone components for optical communication systems. It is obvious that it would be highly desirable to be able to combine this superior performance of III-V materials for lasers (and other active devices) with the silicon platform that has excellent performance regarding passive components. However, the lattice mismatch between silicon and direct bandgap III-V material compositions is large, which makes it not trivial to achieve this integration. In the following, we will discuss the most important techniques to achieve integration of III-V materials with silicon.

Hetero-epitaxial growth of III-V

Epitaxial growth of III-V layers on silicon can be considered as the most desirable solution as it allows for a high integration density, efficient use of expensive III-V materials and it does not involve any critical alignment procedures. However, the lattice mismatch between silicon and III-V materials with a direct bandgap suitable for telecommunication wavelengths is very large. On top of this there is also a mismatch in the thermal expansion coefficients. These issues result in a very high threading dislocation density and anti-phase boundaries which makes it difficult to grow thin III-V layers of high quality. Several III-V materials have been grown, with moderate success, on a silicon[001] substrate that is slightly misoriented. However, this approach is not compatible with CMOS as standard wafers have a [001] orientation. Another approach involves the use of buffer layers which are grown on the silicon substrate before the other III-V layers are grown and filter out the structural defects. This is mostly done by growing GaAs buffer layers, as these have the smallest lattice mismatch with silicon (4.1%) [32]. A major problem with this approach is that these buffer layers are quite thick (1-2 μm) and therefore prevent efficient evanescent coupling between the active device and the silicon waveguide. A technique that received a lot of attention in recent years is the so called epitaxial lateral overgrowth (ELOG) technique. Here first a seed layer is

grown on the silicon after which a mask is deposited on the grown layer. Then, a material lattice matched to the seed layer is grown. By carefully choosing the size of the mask openings, threading dislocations in the layer above the mask are avoided. The growth of InGaAs/InP layers on a SOI substrate is already demonstrated using this approach [33]. Furthermore, an integration scheme allowing for evanescent coupling between a silicon waveguide and III-V layers grown using the ELOG technique has been proposed [34]. However, the photoluminescence achieved using the ELOG technique is still lower compared to the values seen in materials grown on III-V substrates. Although epitaxial growth based on ELOG is promising, there are still some hurdles that need to be overcome to make efficient active components. Main concerns are a smooth surface morphology allowing the growth of quantum wells, reducing the number of threading dislocations and using waferscale compatible lithographic techniques. Therefore, epitaxial growth is mostly considered as a technique that might become useful in the longer term.

Flip-chipping

Flip-chipping is a very mature process where individually fabricated devices are mounted on a common substrate that can contain a circuit through which individual components can be interconnected. This technique is frequently used in electronics to mount ICs or stand-alone electro-optic components on a printed circuit board (PCB). The individual components often contain special contact pads, such that by using gold or gold-tin alloy solder bumps for attaching the component to the substrate, an electrical connection is established at the same time. When a relatively small number of lasers need to be integrated on a certain chip, a flip-chip approach with vertical cavity surface emitting lasers (VCSELS) can be used such that the light can be coupled to the underlying waveguide via a grating coupler. This technique is demonstrated e.g. by Krishnamoorthy and co-workers [35]. A major advantage of this approach is that all devices can be tested separately before integration, resulting in a high yield. On the other hand, the alignment tolerance for flip-chipping active photonic components is typically smaller than 1 μm to achieve efficient light coupling between the active component and the grating coupler. It should also be noted that it is a sequential process limiting the throughput during processing and that the integration density is limited by the contact pads and solder bumps, making it less suitable for compact integration of lasers on silicon.

Bonding

Bonding is a technique where (possibly different) materials are permanently attached to each other. A wide range of bonding technologies exist which all have their specific characteristics. A good overview can be found in [36]. The optimum technology depends on the application. For the purpose of integrating III-V

material with silicon it is important that the intermediate material is transparent in the desired wavelength range and that this intermediate layer is sufficiently thin to allow for efficient evanescent coupling. Based on these requirements two bonding methods exist that could be used to combine III-V material with silicon: molecular bonding and adhesive bonding.

Molecular bonding, or plasma-activated direct wafer bonding, requires two ultra-clean and flat SiO_2 surfaces. These surfaces are then plasma-activated to remove possible remaining contaminants and to improve the quality of the bond through e.g. an increase in the number of silanol (Si-OH) groups. Next, the surfaces are brought into contact and are bonded through Van der Waals attraction. This is followed by a curing process at 300 °C where the O-H bonds are replaced by Si-O-Si bonds. To use this process for bonding III-V on silicon a few nanometer thin layer of SiO_2 is deposited on the III-V wafer or die. Successful bondings of III-V on silicon have been reported [37, 38], where bonding layers as thin as a few tens of nanometers have been achieved. The main advantages of molecular bonding are the CMOS-compatible fabrication process and the ultra-thin bonding layer thicknesses that can be achieved. The disadvantages are obviously the requirements for ultra flat and clean bonding surfaces. Surface roughness or particle contamination can reduce the bonding strength considerably and result in unbonded areas.

Adhesive bonding uses an intermediate material, typically a polymer, that is spread out over the interfaces that need to be bonded. The adhesive material is typically applied to the wafer in a liquid state. When the to be bonded interfaces are now brought into contact, an intimate contact between the adhesive and the interfaces is established. Possible voids in the interfaces are filled by the adhesive material. In order to achieve a permanent bond the molecules of the adhesive need to be crosslinked, which can be done by a curing treatment at around 250 °C and leads to solidification of the adhesive. An adhesive bonding process for integration of III-V material on silicon based on a polymer called divinylsiloxane-bis-benzocyclobutene (DVS-BCB) was developed by Roelkens and co-workers [39] and later on further improved [36, 40]. Bonding layers thicknesses as thin as a few tens of nanometers can be achieved using this approach. The main advantages of this approach is the tolerance to imperfections in the to be bonded interfaces and particle contamination as well as the simple process flow and low processing temperatures. Some important drawbacks of this approach are the possible non-uniformity over a larger area and the low thermal conductivity of adhesive polymers resulting in a high thermal impedance which can have detrimental effects for active components such as lasers.

Both bonding approaches discussed above allow for efficient integration of active III-V materials with silicon. It should also be noted that no critical alignment step is involved in the bonding process, as the III-V devices can be fabricated using

CMOS tools after the bonding process. Also, a high integration density can be achieved making bonding the preferred option for integrating III-V with silicon enabling active devices such as lasers and detectors on the silicon platform.

1.5 Optical interconnects

For optical interconnects to become feasible at a given length scale, they have to perform equally well or better than their electrical counterpart. We have already seen in Section 1.1 that there is a bandwidth length trade off for communication links and that when the bandwidth increases further, the length at which optical interconnects perform better compared to electrical interconnects decreases. Rack-to-rack optical interconnects are already being deployed in data centers since a few years and even board-to-board optical interconnects, with lengths in the order of a few tens of centimeters found their way to the market. Research is now focusing on realizing optical interconnects for chip-to-chip and on-chip communication.

To set targets for optical interconnects on this short distance scale we need to distinguish between the inter-chip and intra-chip optical interconnects, where typical lengths are in the order of several centimeters for inter-chip and below 2 centimeter for intra-chip interconnects. For inter-chip optical interconnects the energy efficiency should be <1pJ/bit to be competitive with the current state-of-of-the-art electrical interconnects and even around 100 fJ/bit in order to offer an energy advantage over electrical interconnects.

An important performance measure for a processor is the number of floating point operations per second (FLOPS). The targeted bandwidth is typically 1 byte per FLOP. Considering that modern processors can execute several TFLOP/s, I/O bandwidths should be in the order of TB/s. If the number of bytes/FLOP is to remain constant after 2022, then based on the predictions in the ITRS roadmap only 50 fJ/bit will be available [3]. For intra-chip global optical interconnects the energy efficiency should be <50-200 fJ/bit to be able to compete with near future electrical interconnects. Based on the ITRS predictions, only 30 fJ/bit will be available for global interconnects around 2022 and for the number of bytes/FLOP to sustain this reduces to 10 fJ/bit [3].

To realize intra- and interchip optical interconnects it is important that the fabrication process is compatible with existing fabrication processes used in the semiconductor industry. This obviously points in the direction of silicon photonics as it also relies on the same SOI technology platform as electronic ICs. A second requirement is the availability of active building blocks to construct an optical interconnect link. Through heterogeneous integration of germanium and III-V materials with silicon, it becomes possible to realize these active building blocks on an SOI platform and opens up the possibility to construct optical links on chip using a CMOS compatible platform.

1.5.1 Architectures

There are three main alternatives for realizing intra- and interchip optical interconnects that all differ at the transmitter side and these are schematically depicted in Figure 1.6. First, there is the possibility to use an off-chip laser and an on-chip modulator. Continuous wave (CW) light from the laser is coupled to a waveguide on the chip via an optical fiber. Light then enters the on-chip modulator, where the modulated light is subsequently coupled to another waveguide and collected at the other end by a photodetector. In this approach a conventional III-V based laser, which has a high efficiency, can be used. Because the laser is not on the chip it does not contribute to the power consumption on the chip. Also, the laser signal can be divided over multiple channels on the chip. On the other hand, additional coupling losses from fiber to chip have to be taken into account as well as splitting losses, putting an upper limit on the maximum number of channels that can be fed from a single laser. Also, if nearly all the channels are idle, the power consumption of the laser will still be the same. On the chip compact, fast and efficient modulators are required to modulate the data on the optical signals at the different channels.

A second approach uses both an on-chip laser and on-chip modulator. The CW light from the laser is coupled to a waveguide and enters the on-chip modulator after which the light path is the same as for the off-chip laser approach. Also in this approach the laser signal can be split over multiple channels. Chip coupling losses can be avoided in this way, but this comes at the cost of higher power consumption on the chip as both the laser and the modulator need to be driven. Therefore, this approach is less suited for intra-chip optical interconnects that set high demands for power consumption.

The last approach makes use of an on-chip laser that is directly modulated. The modulated light from the laser is then coupled to a waveguide and collected at the other end by a photodetector. Because of the direct modulation the output of the laser cannot be divided over multiple channels. Also, because high modulation speeds are required the laser cavity has to be small. Therefore, this approach requires so called microlasers. These microlasers typically have a lower output power compared to conventional laser designs, but the threshold current is also much smaller and they can be modulated at higher speeds.

1.6 Optical Network-on-Chip

As many-core architectures with hundreds of cores are foreseen to keep on improving the chip performance [41], the communication among these different cores is seen as one of the critical issues. Although optical interconnects can improve the bandwidth density, conventional point-to-point links will involve a large number of waveguide crossings as the complexity increases. This asks for a more efficient

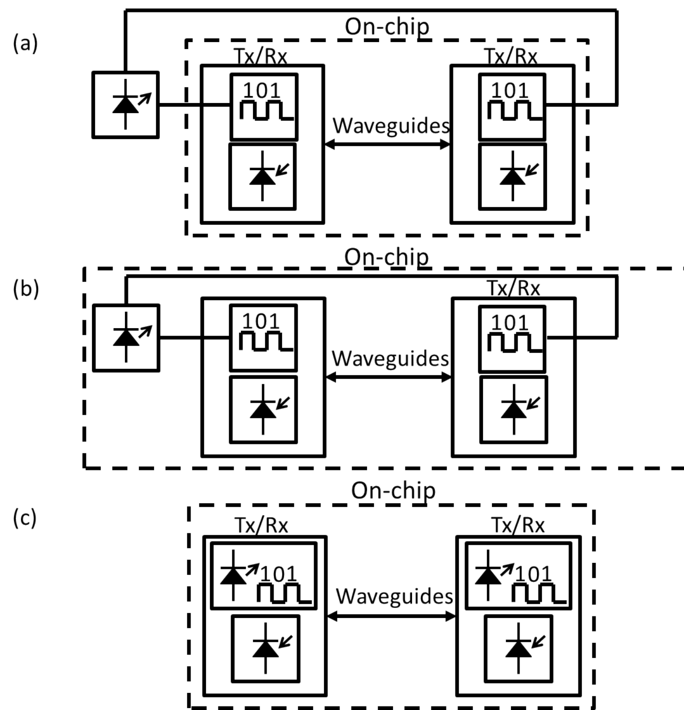

Figure 1.6: Schematic overview of 3 different architectures for realizing optical interconnects. (a) Off-chip CW lasers with on-chip modulators and detectors, (b) On-chip CW lasers, modulators and detectors and (c) On-chip directly modulated microlasers and detectors.

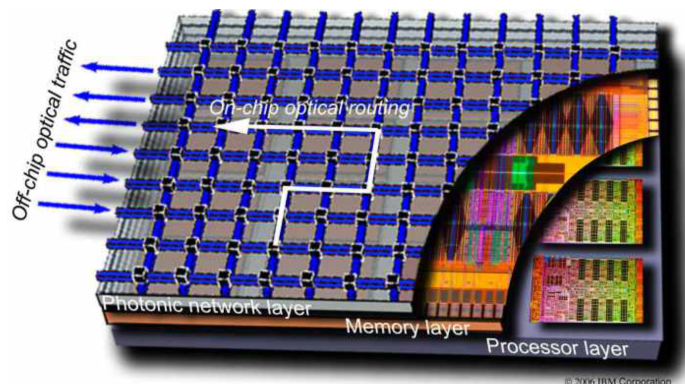

Figure 1.7: Impression by IBM of a future chip with an optical network through which the datastream is routed. Reproduced from [42].

Network-on-Chip design, through which the data can be routed to the appropriate destination without significant latency and excessive power consumption. The direct optical links discussed in the previous section can be extended to an Optical Network-on-Chip (ONoC) by e.g. exploiting the wavelength routing capabilities in optical networks. This principle is illustrated in figure 1.7. The recent advances in silicon photonics have resulted in a large toolbox of photonic components that are required for constructing these ONoCs, such as modulators, wavelength routers, receivers and so on. Although, further improvement of these components is required for efficient networks, it does already allow for proof-of-principle experiments of the concept.

Now there is more consensus that optical interconnects can potentially enhance bandwidth density, energy efficiency and latency of intra-chip and inter-chip communication links, this resulted in research efforts studying ONoCs from a system architectural perspective. The proposed architectures are similar to the ones used in electronic NoCs, but have an additional degree of freedom through wavelength division multiplexing. Most architectures are based on 4 different topologies which are briefly discussed below and are schematically depicted in Figure 1.8.

The first one shown in Figure 1.8(a), also being the simplest one, is the bus waveguide. N input terminals can communicate with the $N-1$ output terminals via this central bus waveguide. The number of waveguides required in such an approach is limited and the bus can also be used for broadcasting, where one initiator needs to send information to all targets. However, as the number of terminals increases a bus waveguide can suffer from bandwidth and latency issues. Some examples of bus waveguide designs can be found in [44, 45].

The crossbar topology is shown in Figure 1.8(b). Here each terminal has a

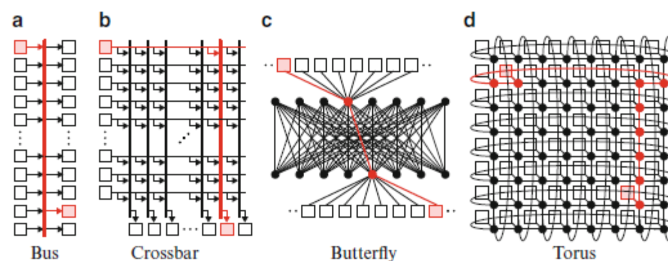

Figure 1.8: Schematic overview of 4 basic network topologies with (a) a bus, (b) a crossbar, (c) a butterfly and (d) a torus topology. Taken from [43].

dedicated bus and the switches are often organized in a matrix fashion. A crossbar has a larger aggregate bandwidth compared to the single bus waveguide approach and the predictability of latency improves. This comes at the cost of a much larger number of waveguides and increased arbitration delays. A significant amount of research on crossbar topologies has been performed and can be found in [46, 47].

The butterfly topology avoids global buses and arbitration as can be seen in Figure 1.8(c). It is a multi-stage approach, where each router is connected to a fixed number of other routers or terminals. The hop count is higher compared to a crossbar approach, but because of the more localized nature of the router this can be implemented more efficiently compared to a global crossbar. However, the latency in case of a low load will generally be higher than bus or crossbar topologies. Butterfly topology designs are proposed by e.g. [48, 49].

Finally, a torus topology is shown in Figure 1.8(d). Each terminal is associated with a router and these routers are organized in an N-dimensional array. For on-chip interconnects this is in principle a 2D array as this matches with the planar layout of the chip. A disadvantage is that low dimensional torus networks have a large hop count which increases the latency and energy consumption. When the number of dimensions are increased the hop counts are decreased but results in longer channels when mapped on a 2D planar structure. Increasing the number of dimensions also increases the complexity of the router. An example of a torus based topology can be found in [50].

The optimal topology depends on the application and the number of terminals that need to be connected and requires research on a system level. Some physical implementations of these architectures will be discussed in chapter 6 and a good general overview of the performance on system level as well as other physical implementations can be found in [43].

Next to optimizing the performance in terms of bandwidth and latency, another advantage of using system level design of on-chip networks is that the energy efficiency can be increased. The laser is one of the biggest consumers of power in op-

tical links. Although significant effort is put in optimizing the energy efficiency of the laser itself, interesting research is also performed to reduce the power dissipation of lasers by using algorithms to reduce the on-time of the lasers. Recently, an interesting result is obtained by [51], where a token-based weighted time-division multiplexing scheme is used. Based on the bandwidth requirements in the NoC for a certain application, the bandwidth multiplexing weights are adjusted for minimum aggregate bandwidth without compromising for application performance. In case of significant changes in required bandwidth, laser sources are switched on or off.

1.7 Electro-photonic integration

One other aspect that has to be addressed is the electro-photonic integration. To reach the targets for bandwidth density and energy efficiency the optical and electrical devices should be tightly integrated. In principle one can distinguish three approaches for electro-photonic integration in intra-chip and inter-chip interconnections: monolithic front-end-of-line (FEOL) integration, monolithic back-end-of-line (BEOL) integration and hybrid integration. These three approaches will be briefly discussed here.

- *Monolithic FEOL integration*: in this approach photonic devices are fabricated in the same layer as the electrical components, thus at transistor level as shown in Figure 1.9. This approach offers the highest possible level of integration with CMOS. As a result, ultra-low power optical interconnects can be formed. It is also considered a cost effective approach in terms of fabrication as the same mask set can be used for processing the electronic and photonic components and the same design environment can be used. On the other hand, it consumes valuable area for electronic circuits and it requires modification of the FEOL process. Additional processing steps might be required to reduce waveguide sidewall roughness and for integration of detectors Germanium needs to be incorporated. Another major difference is the thickness of the BOX which is typically 2 μm for photonic circuits to reduce substrate leakage, while in electronics the standard BOX thickness is only 145 nm. This approach does also not allow for integration of III-V materials and therefore requires off-chip laser sources. Monolithic FEOL integration of electronic and photonic components has been demonstrated by [52, 53] and it is also the integration scheme envisioned by IBM (as shown in Figure 1.7).
- *Monolithic BEOL integration*: Here photonic devices are deposited on top of the metal interconnect layers of the CMOS stack as is indicated in Figure 1.10. It requires deposition of different materials such as e.g. silicon nitride,

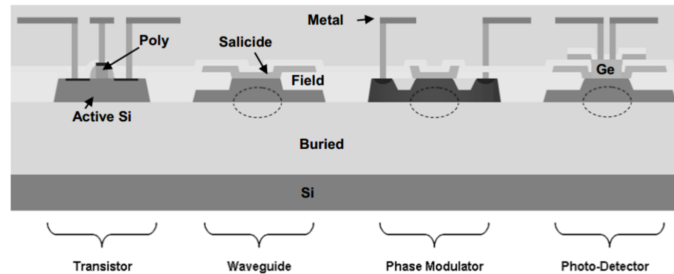

Figure 1.9: Schematic representation of a FEOL integration approach with the photonic components at the transistor level. Taken from [54].

silicon oxide, poly-silicon and germanium. With these materials one can make nitride or poly-silicon waveguides together with germanium detectors. In principle it also allows for the integration of III-V through bonding. It does not reach the high level of integration reached in the FEOL approach, but on the other hand it does not require modification of the FEOL process and it does not consume valuable area for electronic circuits. In principle this approach also allows for multilevel photonic circuits. A disadvantage is that only a limited thermal budget can be used for processing and some modifications to the final metal interconnects are required. The integration density is limited as nitride waveguides have a lower index contrast as compared to crystalline silicon. Demonstrations of this approach can be found in [55, 56].

- *hybrid integration*: The electronic ICs as well as the photonic ICs are fabricated separately in this approach. As a dedicated process can be used for photonics this leads to the best performing photonic components. The electronic and photonic chip are then interconnected through either package level integration [58], flip-chip bonding or 3D integration with through silicon vias (TSVs). It does not require modification of the electronic and photonic fabrication processes and can therefore be used already for near future solutions. A disadvantage is that micro-bumps in case of flip-chipping and TSVs in case of 3D integration are required, which will have a negative impact on the energy efficiency and the bandwidth density. It should be noted that there is also an interesting hybrid integration approach, that comes very close to monolithic BEOL integration and is shown in Figure 1.11. In this approach the PIC is fabricated using a silicon photonics platform where in the last step the whole wafer is covered by a top oxide that is subsequently planarized. Then, using molecular bonding, the wafer containing the PICs is placed upside down on the CMOS wafer and the silicon substrate of the PIC wafer is removed. If needed, additional III-V devices can now also be

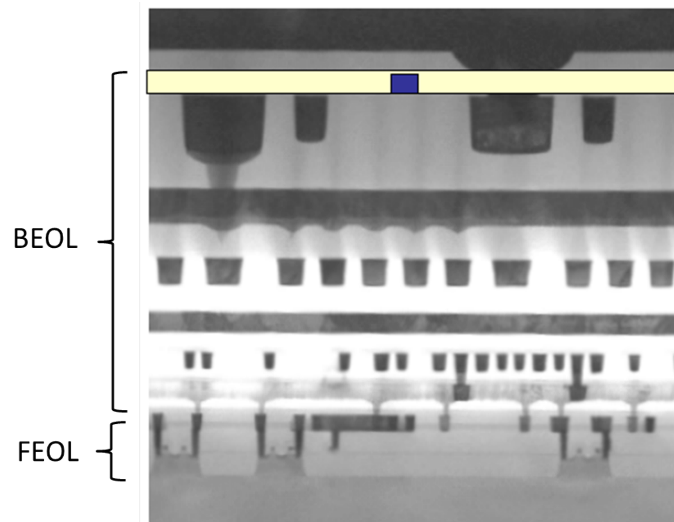

Figure 1.10: SEM image of a CMOS stack with FEOL and BEOL layers in which the position of the photonic layer is indicated for BEOL integration approach [57].

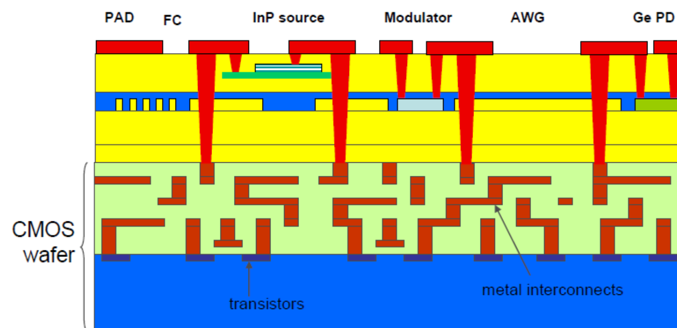

Figure 1.11: Schematic representation of a hybrid integration approach that is very similar to monolithic BEOL integration [57].

bonded on top again using molecular bonding.

1.8 Rationale and goal

Following the trend of ever increasing data rates and the predictions in the ITRS roadmap for inter- and intra-chip communication, it is clear that interconnects on these length scales are about to form a major bottleneck. Research efforts investigating alternatives point in the direction of 3D integration and on-chip optical

interconnects. There is a common believe that silicon photonics is a good option because of the high integration density and the ability to use the mature CMOS processes, which makes it cost effective and better suited for integration with electronics. Up until now most research efforts related to silicon photonics were focusing on the integration of individual active components such as lasers, modulators and detectors required for realizing optical interconnect circuits. Besides the work reported in [59] and [60], not much work has been done on the physical implementation of complete on-chip interconnect circuits or the more complex optical networks on chip. Furthermore, it would be desirable to reduce the number of processing steps, and hence the cost, by e.g. fabricating the lasers and detectors (or modulators and detectors depending on the integration approach) simultaneously.

Therefore, the goal of this work is to develop and investigate the potential of optical networks on a silicon chip. This includes the design, fabrication and characterization of optical interconnect circuits and networks on chip. For the realization of on-chip optical interconnects and optical networks we will rely on a heterogeneous integration approach of III-V on silicon, through adhesive and molecular bonding. By using III-V material for the active devices, lasers can be integrated on the chip offering additional spatial flexibility which is especially an advantage in the more complex ONoCs.

As a source we will make use of a heterogeneously integrated III-V microdisk laser developed in the framework of the EU FP6 PICMOS project [61–63]. An electrically pumped microdisk laser coupled to a silicon waveguide was experimentally demonstrated in 2007, but still with a limited output power and modulation bandwidth. Here we rely on this design and investigate this microdisk laser further to improve its performance. Based on system level calculations performed in the EU FP6 PICMOS project, new goals were set for the microdisk laser and a detector in the EU FP7 WADIMOS project.

The aim is to reach a threshold current below 100 μA, a maximum output power of 1 mW, a slope efficiency of 0.2 W/A and direct modulation at a rate of 10 Gb/s. Furthermore, it also has been shown that by cascading four microdisk lasers on a silicon waveguide a multi-wavelength laser can be realized [64], which is an attractive feature for WDM purposes and ONoCs. Here, we will investigate the possibility to increase the number of microdisks on one waveguide to eight.

For the detector we will investigate the possibility to combine additional InGaAs layers with the III-V epitaxial layers of the microdisk laser. This will allow for very compact integration of lasers and detectors and thereby opens up the possibility of realizing bidirectional links. We aim for a detector responsivity of 1 A/W and a dark current in the order of a few nA.

Apart from the microdisk laser, the detector and the waveguide, also additional passive components need to be integrated in case of an ONoC. These passive components will consist mostly of wavelength filters and routers, such as microrings

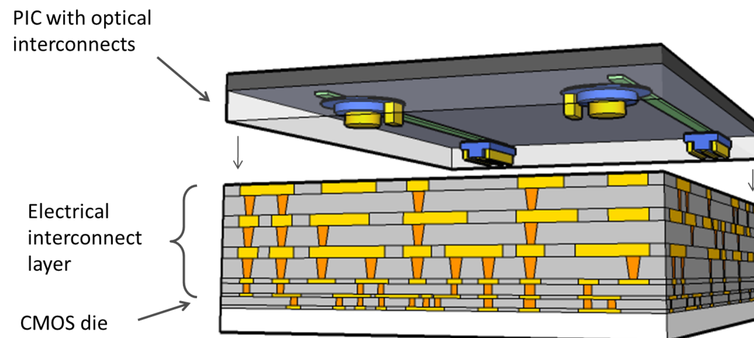

Figure 1.12: Schematic representation of a CMOS chip where a silicon PIC is going to be flip-chipped on top of it.

and Mach-Zehnder interferometers.

Next to the design of the optical interconnects, also the fabrication process will be considered. This includes optimization of the current fabrication process of the microdisk laser and the development of a fabrication process for a detector compatible with the microdisk laser process. Next to this, it is also targeted to fabricate these optical interconnects and networks completely in a CMOS pilot line. This requires special process development as the process should be compatible with waferscale fabrication and it should comply with CMOS standards which e.g. requires gold free contacts. This CMOS compatible process development was carried by our partner CEA Leti, in a collaboration through the European FP7 project WADIMOS. After fabrication, both the individual components and the interconnect circuits need to be carefully characterized.

Finally, we target a demonstrator consisting of an Optical Network-on-Chip with 4 transceivers integrated with CMOS. The optical circuits will be integrated with a CMOS chip through flip-chipping as schematically shown in Figure 1.12. The CMOS chip will contain a digital part for the generation of data as well as drivers and transimpedance amplifiers (TIAs) for the lasers and detectors, respectively.

1.8.1 Contributions by third parties

Because the work presented here is performed in the framework of the EU FP7 project WADIMOS and involves quite some collaborations, we will here briefly summarize the work performed by third parties.

- The microdisk laser design is based on the work performed in the EU FP6 project PICMOS. The original design consists of an epitaxial layer structure of 1 μm thick and has the tunnel junction located below the active region. Standard 500 nm wide silicon access waveguides are used. Detailed parameters can be found in [63].
- The material stack of the microdisk laser used in this work was optimized by our project partners from INL.
- The idea to combine the epitaxial structure of the microdisk laser with that of a detector was conceived during a WADIMOS project meeting and is filed under a joint patent of CEA Leti, INL and imec.
- Epitaxial growth of the III-V stacks was performed by INL.
- A CMOS compatible fabrication process for the microdisk laser and detector was developed and carried out by CEA Leti, Grenoble, France.
- The design of the CMOS chip to control the ONoC circuits was developed by ST microelectronics and INL.

1.9 Outline of the thesis

The outline of this thesis is as follows, first in Chapter 2 we will have a closer look at the optical modes in microdisk resonators. Then the effect of different loss mechanisms on these optical modes will be analyzed. The last part of this chapter deals with the analysis of efficient coupling of light between a microdisk resonator and an access waveguide, both through simulation and experiment.

Chapter 3 deals with the electro-optic behavior of the microdisk laser. Fully coupled electro-optic simulations are used to obtain realistic models which are fitted to experiments where possible.

Experimental results obtained on microdisk lasers are discussed in Chapter 4. First, the results from two different fabrication runs in a CMOS pilot line will be presented, followed by the results obtained from a fabrication run in the clean room of Ghent University.

In Chapter 5 a III-V detector will be presented. A special epitaxial structure for the detector that is compatible with the microdisk laser will be presented, followed by the design of the detector together with simulation results. Then, the fabrication process for fabricating both the microdisk laser and the detector will be explained. Finally, experimental results obtained of detectors fabricated in the CMOS pilot line runs as well as in a run in the clean room of Ghent University are presented.

Optical interconnects on silicon based on microdisk lasers and detector are presented in Chapter 6. First the designs of the optical interconnect circuits are

given and then the obtained experimental results are discussed. Next, some early results on optical networks on chip are presented.

Finally, in Chapter 7 conclusions and a future outlook will be given.

References

[1] Andrew Danowitz, Kyle Kelley, and James Mao. *CPU DB: recording microprocessor history*. Communications of the ACM, 55(4):55–63, 2012.

[2] ITRS. *INTERNATIONAL TECHNOLOGY ROADMAP FOR SEMICONDUCTORS*. Technical report, ITRS, 2011.

[3] D. Miller. *Device requirements for optical interconnects to silicon chips*. Proceedings of the IEEE, 97(7):1166–1185, 2009.

[4] Anand Lal Shimpi and Ryan Smith. *The Intel Ivy Bridge (Core i7 3770K) Review*, 2012.

[5] Cisco. *Cisco Virtual Networking Index*, 2013.

[6] MJR Heck, HW Chen, Alexander W. Fang, Brian R Koch, Di Liang, Hyundai Park, Matthew N Sysak, and John E Bowers. *Hybrid silicon photonics for optical interconnects*. IEEE Journal of Selected Topics in Quantum Electronics, 17(2):333–346, 2011.

[7] AV Krishnamoorthy, Keith W Goossen, William Jan, and Xuezhe Zheng. *Progress in low-power switched optical interconnects*. Selected Topics in Quantum Electronics, 17(2):357–376, 2011.

[8] Govind P. Agrawal. *Fiber-Optic Communication Systems(Google eBook)*. John Wiley & Sons, 2010.

[9] T. Koonen. *Fiber to the Home/Fiber to the Premises: What, Where, and When?* Proceedings of the IEEE, 94(5):911–934, May 2006.

[10] P. Pepeljugoski, J. Kash, F. Doany, D. Kuchta, L. Schares, C. Schow, M. Taubenblatt, B.J. Offrein, and A. Benner. *Low power and high density optical interconnects for future supercomputers*. In Optical Fiber Communication (OFC), collocated National Fiber Optic Engineers Conference, 2010 Conference on (OFC/NFOEC), pages 1–3. IEEE, 2010.

[11] R Nagarajan, M Kato, J Pleumeekers, P Evans, S Corzine, S Hurtt, A Dentai, S Murthy, M Missey, R Muthiah, R A Salvatore, C Joyner, Richard Schneider, M Ziari, F Kish, and D Welch. *InP Photonic Integrated Circuits*. IEEE Journal of Selected Topics in Quantum Electronics, 16(5):1113–1125, September 2010.

[12] Pieter Dumon. *Ultra-Compact Integrated Optical Filters in Silicon-on-insulator by Means of Wafer-Scale Technology*. PhD thesis, Ghent University, 2007.

[13] Jie Sun, Erman Timurdogan, Ami Yaacobi, Ehsan Shah Hosseini, and Michael R Watts. *Large-scale nanophotonic phased array.* Nature, 493(7431):195–9, January 2013.

[14] W. Bogaerts, R. Baets, P. Dumon, V. Wiaux, S. Beckx, D. Taillaert, B. Luyssaert, J. Van Campenhout, P. Bienstman, and D. Van Thourhout. *Nanophotonic waveguides in silicon-on-insulator fabricated with CMOS technology*. Lightwave Technology, Journal of, 23(1):401–412, January 2005.

[15] Richard Soref. *The Past, Present, and Future of Silicon Photonics*. IEEE Journal of Selected Topics in Quantum Electronics, 12(6):1678–1687, November 2006.

[16] Dirk Taillaert, Frederik Van Laere, Melanie Ayre, Wim Bogaerts, Dries Van Thourhout, Peter Bienstman, and Roel Baets. *Grating Couplers for Coupling between Optical Fibers and Nanophotonic Waveguides*. Japanese Journal of Applied Physics, 45(No. 8A):6071–6077, August 2006.

[17] G. T. Reed, G. Mashanovich, F. Y. Gardes, and D. J. Thomson. *Silicon optical modulators*. Nature Photonics, 4(8):518–526, July 2010.

[18] L Liao, A Liu, J Basak, and H Nguyen. *40 Gbit/s silicon optical modulator for highspeed applications*. Electronics Letters, 43(22), 2007.

[19] Haisheng Rong, Richard Jones, Ansheng Liu, Oded Cohen, and Dani Hak. *A continuous-wave Raman silicon laser*. Nature, 433(7027):725–728, 2005.

[20] O Jambois, F Gourbilleau, AJ Kenyon, J Montserrat, R Rizk, and B Garrido. *Towards population inversion of electrically pumped Er ions sensitized by Si nanoclusters*, February 2010.

[21] Jurgen Michel, Jifeng Liu, and Lionel C. Kimerling. *High-performance Ge-on-Si photodetectors*. Nature Photonics, 4(8):527–534, July 2010.

[22] S. B. Samavedam, M. T. Currie, T. A. Langdo, and E. A. Fitzgerald. *High-quality germanium photodiodes integrated on silicon substrates using optimized relaxed graded buffers*. Applied Physics Letters, 73(15):2125, October 1998.

[23] Hsin-Chiao H.C. Luan, D.R. Desmond R. Lim, K.K. Kevin K. Lee, Kevin M. K.M. Chen, J.G. Jessica G. Sandland, Kazumi Wada, and Lionel C. L.C. Kimerling. *High-quality Ge epilayers on Si with low threading-dislocation densities*. Applied Physics Letters, 75(19):2909, November 1999.

[24] Ammar Nayfeh, Chi On Chui, Krishna C. Saraswat, and Takao Yonehara. *Effects of hydrogen annealing on heteroepitaxial-Ge layers on Si: Surface*

roughness and electrical quality. Applied Physics Letters, 85(14):2815, October 2004.

[25] Jifeng Liu, Jurgen Michel, Wojciech Giziewicz, Dong Pan, Kazumi Wada, Douglas D. Cannon, Samerkhae Jongthammanurak, David T. Danielson, Lionel C. Kimerling, Jian Chen, F. Omer Ilday, Franz X. Kartner, and John Yasaitis. *High-performance, tensile-strained Ge p-i-n photodetectors on a Si platform*. Applied Physics Letters, 87(10):103501, September 2005.

[26] T. H. Loh, H. S. Nguyen, R. Murthy, M. B. Yu, W. Y. Loh, G. Q. Lo, N. Balasubramanian, D. L. Kwong, J. Wang, and S. J. Lee. *Selective epitaxial germanium on silicon-on-insulator high speed photodetectors using low-temperature ultrathin Si[sub 0.8]Ge[sub 0.2] buffer*. Applied Physics Letters, 91(7):073503, August 2007.

[27] Gianlorenzo Masini, Subal Sahni, Giovanni Capellini, Jeremy Witzens, and Cary Gunn. *High-Speed Near Infrared Optical Receivers Based on Ge Waveguide Photodetectors Integrated in a CMOS Process*. Advances in Optical Technologies, 2008:1–5, 2008.

[28] Dazeng Feng, Shirong Liao, Po Dong, Ning-Ning Feng, Hong Liang, Dawei Zheng, Cheng-Chih Kung, Joan Fong, Roshanak Shafiiha, Jack Cunningham, Ashok V. Krishnamoorthy, and Mehdi Asghari. *High-speed Ge photodetector monolithically integrated with large cross-section silicon-on-insulator waveguide*. Applied Physics Letters, 95(26):261105, 2009.

[29] Ning Duan, TY Liow, and AE Lim. *High speed waveguide-integrated Ge/Si avalanche photodetector*. In Optical Fiber Communication Conference/National Fiber Optic Engineers Conference, pages 3–5, 2013.

[30] Jifeng Liu, X. Sun, R. Camacho-Aguilera, L.C. Kimerling, and Jurgen Michel. *A Ge-on-Si laser operating at room temperature*. Optics letters, 35(5):679–681, 2010.

[31] Rodolfo E Camacho-Aguilera, Yan Cai, Neil Patel, Jonathan T Bessette, Marco Romagnoli, Lionel C Kimerling, and Jurgen Michel. *An electrically pumped germanium laser.* Optics express, 20(10):11316–20, May 2012.

[32] Jun Yang, Pallab Bhattacharya, and Zetian Mi. *Lasers on Silicon With Multiple-Layer Quantum-Dot Dislocation Filters*. IEEE Transactions on Electron Devices, 54(11):2849–2855, November 2007.

[33] Fredrik K. Olsson, Amandine Aubert, Manuel Avella, Juan Jimenez, Carlos A. Barrios, Jesper Berggren, and Sebastian Lourdudoss. *Heteroepitaxy of InP on Silicon-on-Insulator for Optoelectronic Integration*. In ECS Transactions, volume 3, pages 23–29. ECS, September 2007.

[34] Zhechao Wang, Carl Junesand, Wondwosen Metaferia, Chen Hu, Lech Wosinski, and Sebastian Lourdudoss. *IIIVs on Si for photonic applicationsA monolithic approach*. Materials Science and Engineering: B, 177(17):1551–1557, October 2012.

[35] A.V. Krishnamoorthy, L.M.F. Chirovsky, W.S. Hobson, R.E. Leibengath, S.P. Hui, G.J. Zydzik, K.W. Goossen, J.D. Wynn, B.J. Tseng, J. Lopata, J.A. Walker, J.E. Cunningham, and L.A. D'Asaro. *Vertical-cavity surface-emitting lasers flip-chip bonded to gigabit-per-second CMOS circuits*. IEEE Photonics Technology Letters, 11(1):128–130, January 1999.

[36] Stevan Stankovic. *Hybrid III-V / Si DFB Lasers Based on Polymer Bonding Technology*. PhD thesis, Ghent University, 2013.

[37] Di Liang, Alexander W. Fang, Hyundai Park, Tom E. Reynolds, Keith Warner, Douglas C. Oakley, and John E. Bowers. *Low-Temperature, Strong SiO2-SiO2 Covalent Wafer Bonding for IIIV Compound Semiconductors-to-Silicon Photonic Integrated Circuits*. Journal of Electronic Materials, 37(10):1552–1559, June 2008.

[38] M. Kostrzewa, L. Di Cioccio, M. Zussy, J.C. Roussin, J.M. Fedeli, N. Kernevez, P. Regreny, Ch. Lagahe-Blanchard, and B. Aspar. *InP dies transferred onto silicon substrate for optical interconnects application*. Sensors and Actuators A: Physical, 125(2):411–414, January 2006.

[39] G Roelkens. *Heterogeneous III-V/silicon photonics: bonding technology and integrated devices*. PhD thesis, Ghent University, 2007.

[40] S Keyvaninia and M Muneeb. *Ultra-thin DVS-BCB adhesive bonding of III-V wafers, dies and multiple dies to a patterned silicon-on-insulator substrate*. Optical Materials Express, 34(18):1047–1056, 2013.

[41] Shekhar Borkar. *Thousand core chips*. In Proceedings of the 44th annual conference on Design automation - DAC '07, page 746, New York, New York, USA, June 2007. ACM Press.

[42] Y Vlasov. *Silicon integrated nanophotonics: Road from scientific explorations to practical applications*. Proceedings of CLEO/QELS, San Jose, CA, USA, 2012.

[43] Christopher Batten, Ajay Joshi, Vladimir Stojanovć, and Krste Asanović. *Designing chip-level nanophotonic interconnection networks*. In Integrated Optical Interconnect Architectures for Embedded Systems, pages 81–134. 2013.

[44] Scott Beamer, Chen Sun, Yong-Jin Kwon, Ajay Joshi, Christopher Batten, Vladimir Stojanović, and Krste Asanović. *Re-architecting DRAM memory systems with monolithically integrated silicon photonics*. In Proceedings of the 37th annual international symposium on Computer architecture - ISCA '10, volume 38, page 129, New York, New York, USA, June 2010. ACM Press.

[45] Amit Hadke, Tony Benavides, S.J. Ben Yoo, Rajeevan Amirtharajah, and Venkatesh Akella. *OCDIMM: Scaling the DRAM Memory Wall Using WDM Based Optical Interconnects*. In 2008 16th IEEE Symposium on High Performance Interconnects, pages 57–63. IEEE, 2008.

[46] Sudeep Pasricha and Nikil Dutt. *Trends in emerging on-chip interconnect technologies*. Transaction on System LSI Design Methodology, 1:2–17, 2008.

[47] Michele Petracca, Benjamin G. Lee, Keren Bergman, and Luca P. Carloni. *Photonic NoCs: System-Level Design Exploration*. IEEE Micro, 29(4):74–85, July 2009.

[48] Christopher Batten, Ajay Joshi, Jason Orcutt, Anatol Khilo, Benjamin Moss, Charles W. Holzwarth, Miloš A. Popovic, Hanqing Li, Henry I. Smith, Judy L. Hoyt, Franz X. Kartner, Rajeev J. Ram, Vladimir Stojanovic, and Krste Asanovic. *Building Many-Core Processor-to-DRAM Networks with Monolithic CMOS Silicon Photonics*. IEEE Micro, 29(4):8–21, July 2009.

[49] Pranay Koka, Michael O. McCracken, Herb Schwetman, Xuezhe Zheng, Ron Ho, and Ashok V. Krishnamoorthy. *Silicon-photonic network architectures for scalable, power-efficient multi-chip systems*. ACM SIGARCH Computer Architecture News, 38(3):117, June 2010.

[50] Assaf Shacham, Keren Bergman, and L.P Luca P. Carloni. *Photonic networks-on-chip for future generations of chip multiprocessors*. IEEE Transactions on computers, 57(9):1246–1260, September 2008.

[51] Chao Chen and Ajay Joshi. *Runtime Management of Laser Power in Silicon-Photonic Multibus NoC Architecture*. Selected Topics in Quantum Electronics, 19(2), 2013.

[52] Michael Georgas, Jason Orcutt, Rajeev J. Ram, and Vladimir Stojanovic. *A Monolithically-Integrated Optical Receiver in Standard 45-nm SOI*. IEEE Journal of Solid-State Circuits, 47(7):1693–1702, July 2012.

[53] Cary Gunn. *CMOS photonics for high-speed interconnects*. Micro, IEEE, pages 58–66, 2006.

[54] Drew Guckenberger and Sherif Abdalla. *Advantages of CMOS photonics for future transceiver applications*. In European Conference on Optical Communications (ECOC), pages 19–23, 2010.

[55] Ian A. Young, Edris Mohammed, Jason T. S. Liao, Alexandra M. Kern, Samuel Palermo, Bruce A. Block, Miriam R. Reshotko, and Peter L.D. Chang. *Optical I/O Technology for Tera-Scale Computing*. IEEE Journal of Solid-State Circuits, 45(1):235–248, January 2010.

[56] Kyle Preston, Sasikanth Manipatruni, Alexander Gondarenko, Carl B. Poitras, and Michal Lipson. *Deposited silicon high-speed integrated electro-optic modulator*. Optics Express, 17(7):5118, March 2009.

[57] J-M Fedeli. *CMOS Photonics Winter school: Integration*, 2009.

[58] Andrew Alduino, Ling Liao, Richard Jones, Michael Morse, Brian Kim, Wei-Zen Lo, Juthika Basak, Brian Koch, Hai-Feng Liu, Haisheng Rong, Matthew Sysak, Christine Krause, Rushdy Saba, Dror Lazar, Lior Horwitz, Roi Bar, Stas Litski, Ansheng Liu, Kevin Sullivan, Olufemi Dosunmu, Neil Na, Tao Yin, Frederick Haubensack, I-wei Hsieh, John Heck, Robert Beatty, Hyundai Park, Jock Bovington, Simon Lee, Hat Nguyen, Hinmeng Au, Katie Nguyen, Priya Merani, Mahtab Hakami, and Mario Paniccia. *Demonstration of a High Speed 4-Channel Integrated Silicon Photonics WDM Link with Hybrid Silicon Lasers*. In Integrated Photonics Research, Silicon and Nanophotonics and Photonics in Switching, page PDIWI5, Washington, D.C., 2010. OSA.

[59] Jens Hofrichter, Thomas Morf, Antonio La Porta, Oded Raz, Harm J S Dorren, and Bert J Offrein. *A single InP-on-SOI microdisk for high-speed half-duplex on-chip optical links.* Optics express, 20(26):B365–70, December 2012.

[60] Noam Ophir, Kishore Padmaraju, Aleksandr Biberman, Long Chen, Kyle Preston, Michal Lipson, and Keren Bergman. *First Demonstration of Error-Free Operation of a Full Silicon On-Chip Photonic Link*. Optical Fiber Communication Conference/National Fiber Optic Engineers Conference 2011, page OWZ3, 2011.

[61] H T Hattori, C Seassal, E Touraille, X Letartre, G Hollinger, P Viktorovitch, L Di Cioccio, M Zussy, L El Melhaoui, and J M Fedeli. *Heterogeneous Integration of Microdisk Lasers on Silicon Strip Waveguides for Optical Interconnects*. Technology, 18(1):2005–2007, 2006.

[62] P Rojo Romeo, J Van Campenhout, P Regreny, a Kazmierczak, C Seassal, X Letartre, G Hollinger, D Van Thourhout, R Baets, J M Fedeli, and L Di Cioccio. *Heterogeneous integration of electrically driven microdisk based*

laser sources for optical interconnects and photonic ICs. Optics express, 14(9):3864–71, May 2006.

[63] J Van Campenhout, P Rojo Romeo, P Regreny, C Seassal, D Van Thourhout, S Verstuyft, L Di Cioccio, J-M Fedeli, C Lagahe, and R Baets. *Electrically pumped InP-based microdisk lasers integrated with a nanophotonic silicon-on-insulator waveguide circuit.* Optics express, 15(11):6744–9, May 2007.

[64] Joris Van Campenhout, Liu Liu, Pedro Rojo Romeo, Dries Van Thourhout, Christian Seassal, Philippe Regreny, Lea Di Cioccio, Jean-Marc Fedeli, and Roel Baets. *A Compact SOI-Integrated Multiwavelength Laser Source Based on Cascaded InP Microdisks*. IEEE Photonics Technology Letters, 20(16):1345–1347, August 2008.

2

Optical modes in a microdisk and their interaction with an access waveguide

This chapter deals with the optical design of a microdisk cavity. First, the modal solutions in a microdisk cavity are described and some important design parameters are given. Then, the geometry of the microdisk laser for which we want to optimize the cavity and the coupling conditions is presented. Section 2.3 deals with different optical loss mechanisms in microdisk cavities. Finally, in Section 2.4 we will analyze the coupling between a microdisk resonator and an access waveguide.

2.1 Microdisk cavities

Gain and feedback are the key aspects behind lasers. Gain can be generated by population inversion of carriers, which will be discussed in more detail in the next chapter. In order to generate feedback a cavity needs to be formed. In a semiconductor stripe laser, which is the most common type of lasers in telecommunications, mirrors are used to form a resonant cavity. Another approach is to use a ring or a disk geometry as shown in Figure 2.1. In this case the light bounces at the interfaces and interferes with itself after a roundtrip thereby also forming a cavity without the need for mirrors as shown in Figure 2.1(c).

When designing microlasers, the active region supplying gain is obviously very small and therefore the cavity loss needs to be sufficiently low such that the lasing

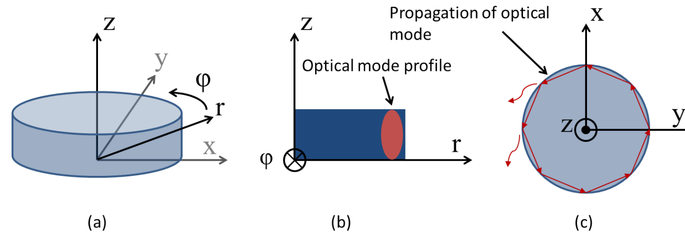

Figure 2.1: Geometry of a microdisk cavity.

action can be sustained. In case of stripe lasers, this means highly reflective mirrors are required, which is challenging from a processing point of view. In case of ring or disk cavities, no mirrors are required thereby avoiding this problem. However, some other loss factors need to be taken into account. While optical modes in a straight waveguide have a flat phase response, modes in a ring or disk have a phase front that is rotating around the center of the disk or ring. Given a bend waveguide with a fixed radius, the separation between the phase fronts increases with increasing radius and likewise the group velocity increases. As the group velocity cannot exceed the speed of light, there is a certain point where the phase front bends and results in radiation loss. This radiation or bend loss is a fundamental loss that depends on the radius of the ring or disk and the refractive indices of the materials. The higher the refractive index contrast, the smaller the acceptable bend radius. Other loss factors that can play an important role are loss induced by metal contacts and scattering loss at interfaces between materials with different refractive index. The losses will be studied in more detail in Section 2.3. We will now first have a closer look at the modal solutions in a microdisk cavity.

2.1.1 Mathematical description of Whispering Gallery Modes

Microdisk structures support whispering gallery modes (WGM) which are solutions of the Helmholtz equation in a cylindrical (or spherical) geometry as shown in Figure 2.1(b-c). As a microdisk possesses azimuthal symmetry, the refractive index $n(\mathbf{r})$ is constant in the azimuthal direction and only depends on the radial and axial coordinates. Assuming a piecewise homogeneous medium, the Helmholtz equation in cylindrical coordinates reads

$$\nabla^2 \mathbf{F}(\mathbf{r}) + k_0^2 n^2(r,z)\mathbf{F}(\mathbf{r}) = 0 \tag{2.1}$$

Where F represents the electric (E) or magnetic (H) field, k_0 is the wavenumber and $n(r,z)$ is the piecewise constant refractive index. An analytical solution to this equation does not exist and rigorous numerical methods are required to

find the solutions. However, for a qualitative understanding we can further simplify this equation through some approximations [1, 2]. Since the thickness of the microdisk is small compared to the radius, we can assume that there are two dominant polarizations labeled as quasi-TE and quasi-TM. Quasi-TE(TM) means that the $\{E_r, H_\phi, H_z\}$ ($\{H_r, E_\phi, E_z\}$) field components are still dominant, but the other field components are not strictly zero as would be the case in a 1D slab configuration. Under this assumption Equation 2.1 becomes scalar in the z direction and by using the effective index method it can be simplified to the following equation with an appropriate effective index $\bar{n}(r)$

$$\left(\frac{\partial^2}{\partial r^2} + \frac{\partial}{r\partial r} + \frac{\partial^2}{r^2\partial\phi^2} + k^2\bar{n}^2(r)\right) F_z(r,\phi) = 0. \tag{2.2}$$

Through separation of variables, equation 2.2 can be rewritten into two separate equations for the azimuthal and radial dependence

$$\left(\frac{\partial^2}{\partial\phi^2} + m^2\right) F_z(\phi) = 0 \tag{2.3}$$

$$\left(\frac{\partial^2}{\partial r^2} + \frac{\partial}{r\partial r} + k^2\bar{n}^2(r) - \frac{m^2}{r^2}\right) F_z(r) = 0, \tag{2.4}$$

The solution to Equation 2.3 describing azimuthal dependence can be written as $F_z(\phi) = e^{-im\phi}$. This solution makes sense because the structure is invariant in the ϕ direction and therefore the shape of the field will not change as it travels around the disk; only its phase will change. The second equation describing the radial dependence can be recognized as a Bessel equation. The solutions to this equation are Bessel functions of the first kind inside the disk $J_m(k_0\bar{n_d}R)$ and a superposition of the Bessel function of the first and second kind outside the disk, resulting in a Hankel function of the first kind $H_m(k_0\bar{n_0}R)$ [2], where $\bar{n_d}$ and $\bar{n_0}$ are the effective refractive indices of the microdisk slab and the cladding, respectively.

By requiring the tangential components of the field to be continuous across the edge of the microdisk structure (r=R), one finds the transcendental dispersion relation

$$k_0\bar{n_d}(k_0)J_{m+1}(k_0\bar{n_d}R) = (\frac{m}{R} + \eta k_0\sqrt{\bar{n_d}^2 - \bar{n_0}^2})J_m(k_0\bar{n_d}R). \tag{2.5}$$

Where $\eta = \frac{\bar{n_d}^2}{\bar{n_0}^2}$ for TE modes and $\eta = 1$ for TM modes. In order to calculate the propagation constant β for particular modes, the dispersion relation needs to be solved. The dispersion relation has eigensolutions with complex propagation constants, from which it follows that the mode solutions are inherently leaky. It implies that the frequency needs to be complex if an ideal passive resonator is

assumed. The complex frequency can be written as $\tilde{\omega} - i\gamma/2$ where γ is the temporal decay rate which accounts for the bend loss. The quality of a resonator is described by the number of optical cycles before confined energy leaks away and is given by the intrinsic quality factor $Q = \omega/\gamma$. For a fixed value of 'm' different solutions exist, having a different number of nodes in the radial direction. The different solutions (or modes) can thus be labeled with an azimuthal and radial mode number. For a sufficiently thick disk additional nodes in the vertical direction are present, as we will see later. Therefore, the different solutions that can exist inside a disk are designated by 3 modenumbers: m, l and k indicating the number of nodes in the azimuthal, radial and vertical direction, respectively.

2.1.2 Microdisk parameters

In this section some important microdisk parameters, that will be used throughout this thesis, are summarized.

Resonance wavelength

In order to build up power in the cavity the optical field needs to interfere with itself in a constructive manner. Therefore, the round-trip phase needs to be an integer multiple of 2π, which leads to the condition

$$2\pi R\beta = 2\pi M \tag{2.6}$$

Here β is the propagation constant, R is the radius of the microdisk and M is an integer value. By using $\beta = 2\pi n_{eff}/\lambda$, the resonant wavelengths can be found

$$\lambda_0 = \frac{2\pi R n_{eff}}{M}, \tag{2.7}$$

where n_{eff} is the effective index of the mode defined at the edge of the microdisk cavity.

Free Spectral Range

The Free Spectral Range (FSR) is defined as the wavelength spacing between the resonant modes in a cavity and is given by

$$\Delta\lambda = \frac{\lambda^2}{2\pi R n_g}, \tag{2.8}$$

where n_g is the group index. From this equation it is clear that the FSR increases, for decreasing microdisk radius. A single-mode laser, i.e. single mode in the azimuthal direction, can thus be obtained by decreasing the radius of the microdisk such that the FSR becomes larger and only one mode falls within the optical gain spectrum.

Quality factor and optical loss

As already briefly touched upon in the previous section, the quality factor of a resonator is defined as the ratio between the energy stored in the resonator and the energy dissipated per roundtrip

$$Q = 2\pi \frac{E_{stored}}{\Delta E_{dissipated}} = \frac{\omega}{\gamma} \tag{2.9}$$

The Q factor can be measured spectrally through the relation

$$Q = \frac{\omega_0}{\delta\omega}, \tag{2.10}$$

where $\delta\omega$ is the full width half maximum (FWHM) of the resonance. The resonance linewidth is related to the photon lifetime τ_p in the cavity through

$$\delta\omega = \frac{1}{\tau_p}. \tag{2.11}$$

As τ_p can also be expressed as

$$\tau_p = \frac{n_g}{c\alpha}, \tag{2.12}$$

the Q-factor can be related to the absorption coefficient α by

$$Q = \frac{\omega n_g}{c\alpha} = \frac{2\pi n_g}{\lambda_0 \alpha} \tag{2.13}$$

2.2 Layout of a III-V microdisk laser on Silicon

In the previous section we looked at WGM in general. Now we will take a closer look at the microdisk laser structure that was originally developed by Van Campenhout, et al. [3] and is schematically shown in Figure 2.2. We would like to optimize the performance of this laser for optical interconnect circuits on silicon. The original designs proposed by Van Campenhout had a 500 or 1000 nm thickness and a tunnel junction below the active region. The tunnel junction is added to reduce the amount of p-doped regions, thereby reducing the amount of free carrier loss. Next to this, the tunnel junction also ensures uniform injection across the microdisk. At the beginning of the current work an optimized epitaxial structure was provided by INL. In this optimized epitaxial structure the tunnel junction is located above the active region and should result in lower free carrier loss. This optimized 580 nm thin InP-based film is bonded on a silicon-on-insulator sample (see Section 5.3 on fabrication). The SOI sample can contain all kinds of passive circuits which can be very compact because of the high refractive index contrast of silicon to silicon dioxide or air. The microdisk is not completely etched through

Figure 2.2: Impression of a microdisk laser, 3D impression (a) and 2D cross-section (b).

the III-V, such that a thin bottom contact layer of 100 nm remains for electrical injection. The top contact of the laser is placed in the center of the disk such that the overlap with the optical WGM modes is limited. This is to avoid optical absorption induced by the metal. A bottom metal contact is placed around the disk to ensure uniform injection. A fraction of the generated light is coupled to an underlying silicon waveguide and this is the effective output of the laser. Some important geometrical design parameters are indicated in Figure 2.2(b).

2.2.1 Mode profiles in a microdisk

While the approximate analytical solution from the previous section is convenient for e.g. a quick and qualitative understanding of the distribution of the optical field in the radial direction, it cannot be used to calculate bend and metal losses or coupling to an access waveguide. Therefore, purely numerical tools are required to get more insight in optical losses and coupling conditions. Different simulation methods exist to obtain the optical mode profiles such as Film Mode Matching (FMM), the Finite Difference Method (FDM) and the Finite Element Method (FEM), which all have there (dis)advantages. A good overview and comparison can be found in [4]. The simulation results described in this section are obtained using the FDM solver from Phoenix Software B.V. and the FEM solver

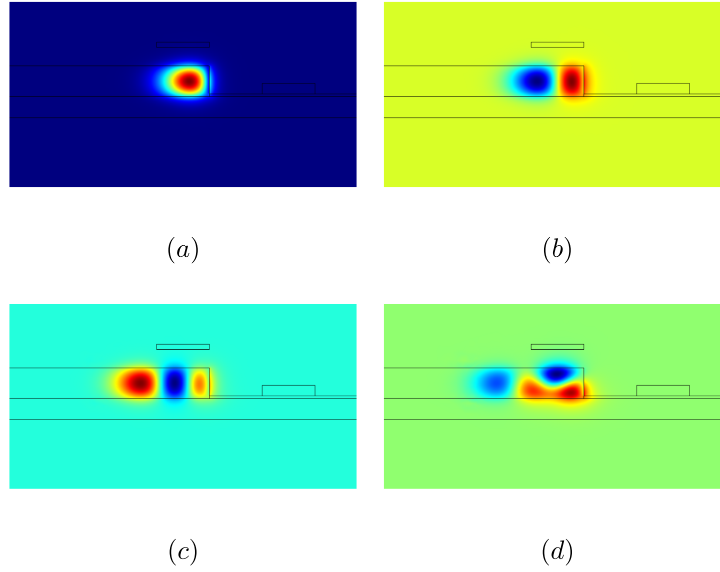

Figure 2.3: Mode profiles of the microdisk laser structure. Fundamental mode (a), first order radial mode (b), second order radial mode (c) and first order vertical mode (d).

from COMSOL. The mode profiles of the 4 highest order TE modes with a wavelength close to 1.55 μm obtained through a simulation with the FEM solver are shown in Figure 2.3. These mode solutions can be designated by their nodes in the azimuthal, radial and vertical direction (m,l,k) and are referred to as the fundamental mode with azimuthal mode order 40 (40,0,0) (Figure 2.3(a)), the first order radial mode (35,1,0) (Figure 2.3(b)), the second order radial mode (33,2,0) (Figure 2.3(c)) and the first order vertical mode (33,0,1) (Figure 2.3(d)). Clearly, due to the relatively thin stack of 580 nm, the first order vertical mode is almost in cutoff.

2.3 Loss contributions

In order to have an efficient laser it is important to keep the optical losses as low as possible. In this section we will evaluate losses that are dependent on the geometry of the structure, i.e. the bend loss, scattering loss and metal loss. Although coupling loss to a neighboring waveguide is also geometry dependent, it will be covered separately in Section 2.4 because it requires a more extensive analysis. Optical loss due to free carriers will be covered in the next chapter.

2.3.1 Bend losses

Bend loss is a fundamental loss in curved waveguide structures. The amount of loss depends on the radius of the curvature and the refractive index contrast. The microdisk structure is based on InP related materials (n= 3.2 @ 1.55 μm) and the cladding material is either BCB (n=1.54 @ 1.55 μm) or silicon oxide (n=1.44 @ 1.55 μm), which both have a similar refractive index. The refractive index contrast is therefore fixed and the minimum radius has to be determined to keep the bend loss sufficiently small. However, the microdisk structure also has a thin slab around the disk cavity for electrical injection, and the thickness of the slab will have an influence on the confinement of the optical modes and thus on the bend loss. To analyze the bend loss we used a 2.5D axi-symmetric finite element method (FEM) described in [5] that is capable of simulating 3D axi-symmetric resonator structures in an efficient way by exploiting the propagation invariance in the ϕ direction and thereby reducing it to a 2D problem. The original model by [5] does not include perfectly matched layers (PMLs) which is required to be able to determine the bend loss. The implementation of PMLs in such a 2D axi-symmetric finite element model is described in [6]. Both models were implemented in the commercially available finite element solver COMSOL.

Figure 2.4 shows the bend loss versus disk radius for both the fundamental TE and first order radial TE modes, which are the two modes with the highest confinement. The analysis was performed for slab thicknesses of 50 and 100 nm. If we arbitrarily set the limit for acceptable bend loss to a value of 1 cm^{-1}, the minimum disk radius is about 3.4 μm in case of a 100 nm thin slab while for a 50 nm thin slab it can be as small as 2.1 μm. The thickness of the slab clearly has a significant influence and should be well controlled during fabrication. It should also be noted that a trade-off has to be made concerning the slab thickness because although a thinner slab results in lower optical loss it also has a higher electrical resistance. As expected, the first order radial TE mode has much higher bend losses compared to the fundamental mode. In both the cases of 50 and 100 nm slab thickness the bend loss of the first order radial mode is around three orders of magnitude higher compared to the fundamental mode. For larger disks it can be advantageous to use a thicker slab layer as in this case the slab acts as an additional loss mechanism for undesired higher order modes and the electrical resistance does not need to be compromised.

2.3.2 Metal losses

For efficient current injection it is important to place the metal contacts as close as possible to the area where the light is propagating. On the other hand, they should be sufficiently far away from the optical mode as otherwise it will result in excessive optical absorption. The amount of absorption is proportional to the

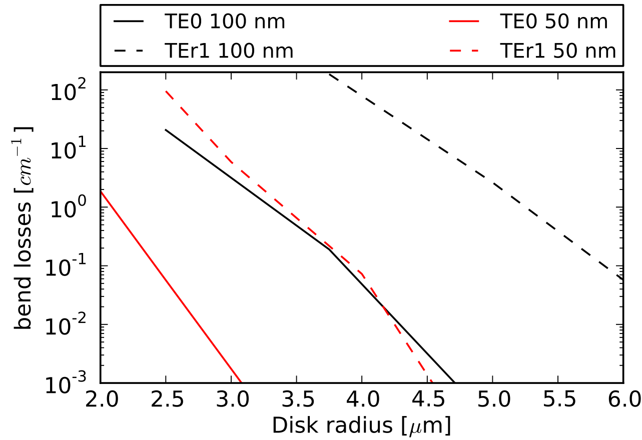

Figure 2.4: Bend losses of the fundamental and first order radial mode for a 50 and 100 nm thin bottom contact slab.

real part times the imaginary part of the refractive index. Au based contacts cause relatively low optical absorption as it is a noble metal with a small real part of the refractive index and a large imaginary part. However, conventional alloyed metal contacts like AuGe/Ni/Au cannot be used in thin film structures because the Au/InP intermixing is very violent and gold spikes might short-circuit the pn-junction. Therefore, we use non-alloyed Ti/Pt/Au contacts instead, where the Platinum acts as diffusion barrier for the gold. Typical metal thicknesses for such a stack are 20/50/100 nm, where especially the Platinum layer should be thick enough to avoid Au/InP intermixing. Both Titanium and Platinum cause similar but stronger optical absorption compared to gold. In the following analysis we used a single metal layer with a thickness of 200 nm and a complex refractive index of 4.04-3.82i corresponding to Titanium. Therefore, the impact of the metal will be slightly overestimated. Obviously, because of the thin film InP structure the metal contact at the top of the microdisk cavity cannot be placed at the periphery as this will lead to high optical absorption. As indicated in Figure 2.2(b) 3 distances between the optical mode and metal layers need to be analyzed, the contact metal (indicated by nr. 1), the top metal (indicated by nr. 2) and the bottom metal (indicated by nr. 3) layer distance.

We again use the 2.5D axi-symmetric finite element method as described in Section 2.2.1 to determine losses induced by the metal. For the top metal contact it is important to know the modewidth of the fundamental mode as function of the radius as this determines the area at the periphery of the microdisk where metal is to be avoided. The modewidth is defined arbitrarily as the distance between the

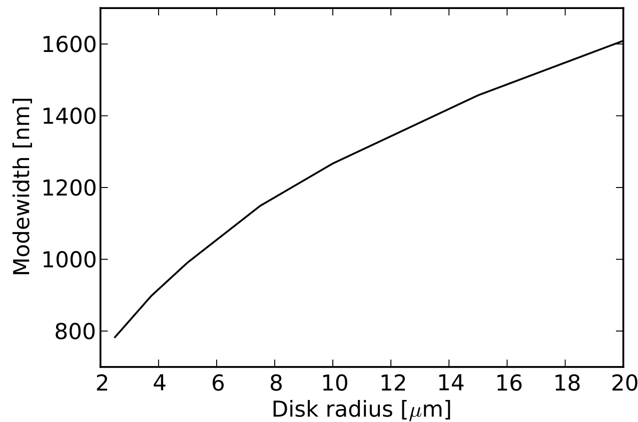

Figure 2.5: Modewidth of the fundamental mode versus the microdisk radius.

edge and the point where the electric field is 1% of its maximum value. Figure 2.5 shows the modewidth as a function of radius.

Based on the analysis in the previous section it is clear that microdisks with a radius of 2.5 μm are very challenging in terms of processing as this requires a slab thickness of 50 nm. As we will see in the next section also the scattering loss has a significant influence when the radius decreases. Therefore, we focus here on microdisks with a slightly larger radius, which are expected to be more feasible in terms of processing. If we consider a microdisk with a radius of 3.75 μm we can see from Figure 2.5 that the modewidth is around 900 nm. The metal free area at the top of the microdisk should be of the same order. Figure 2.6(a) shows the simulation result for a microdisk with 3.75 μm radius where the metal free area is sweeped from 600 to 1400 nm. The solid line represents the losses for the fundamental TE mode while the dashed line represents the first order radial TE mode. In order to have less than 1 cm^{-1} loss for the fundamental mode, the metal free area should be at least 1000 nm wide. This is slightly larger than the arbitrarily defined modewidth of 900 nm. Obviously, because the first order radial TE mode has a larger modewidth the overlap with the metal is larger and thus so are the losses. Therefore, the top metal can be used to suppress higher order modes by choosing the size of the top contact carefully. If the metal free area is increased to 1200 nm, the loss for the first order radial TE mode also drops below 1 cm^{-1} eliminating the effect of suppression for this mode. The margin on the radius of the top contact is therefore smaller than 200 nm in this case. Next to a small margin on the size, any misalignment of the top contact will result in an increase in optical loss. In Chapter 5 we will present an effective fabrication process achieving

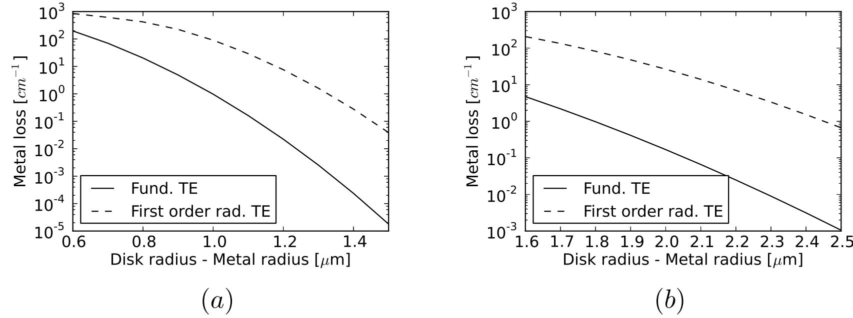

Figure 2.6: Optical loss induced by the top metal versus the size of the microdisk minus the size of the top metal contact for a 3.75 μm (a) and 20 μm (b) radius microdisk.

perfect alignment for the top contact.

The same analysis is performed for a 20 μm radius microdisk and the results are shown in Figure 2.6(b). A metal free area of 1.8 μm is required and also in this case this is slightly larger than the defined modewidth. However, the margin of metal free area to suppress higher order modes is larger in this case as the difference in size between the modewidths also increases with increasing modewidth.

The contact metal layer for electrical probing goes over the area where the light is propagating. Therefore, the vertical distance between the metal and the microdisk, as indicated in Figure 2.2(b), should be sufficiently large. From a processing point of view it is desirable to keep this distance small, because this eases the process for opening the contacts. The relation between the loss induced by the contact metal and the vertical distance to the microdisk is shown in Figure 2.7 for a microdisk with a radius of 3.75 μm. The cladding material is BCB in this case. The vertical distance should be at least 400 nm to keep the losses sufficiently low.

In order to keep the electrical resistance caused by the thin bottom slab low, the bottom metal contact should be placed as close as possible to the disk without causing excessive optical losses. For optimization of the bottom metal contact position the bend loss is an important parameter as this determines how much the mode extends in the bottom slab. Therefore, the optimum position depends on the bend radius of the microdisk, the bottom slab thickness and the refractive index of the cladding material. For small bend radii the mode extends more in the slab and the losses will be higher, therefore the simulation for a 3.75 μm radius microdisk with BCB as cladding layer can be seen as a worst case scenario. Figure 2.8 shows the optical loss induced by the bottom metal contact versus distance to the edge of the microdisk. In order to achieve a loss smaller than 1 cm^{-1} the metal should be positioned at least 750 nm away from the microdisk edge.

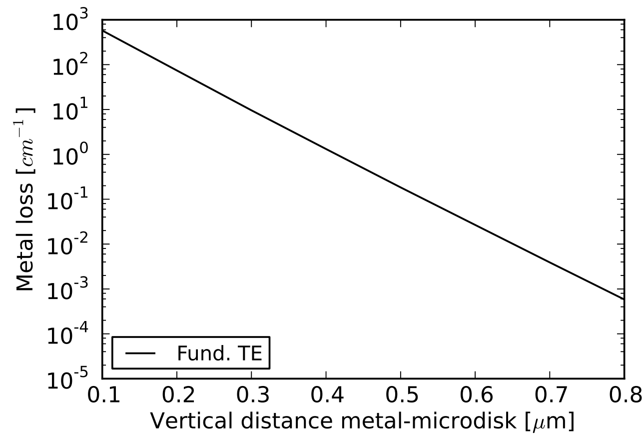

Figure 2.7: Optical loss induced by the contact metal versus the vertical distance between the contact metal and the microdisk.

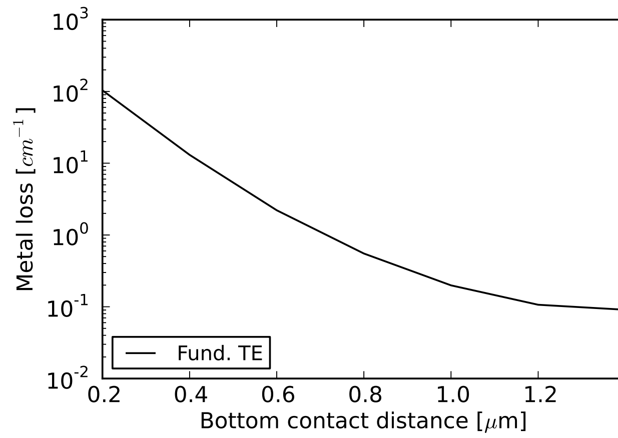

Figure 2.8: Optical loss induced by the bottom metal contact versus the distance between the bottom contact metal and the microdisk.

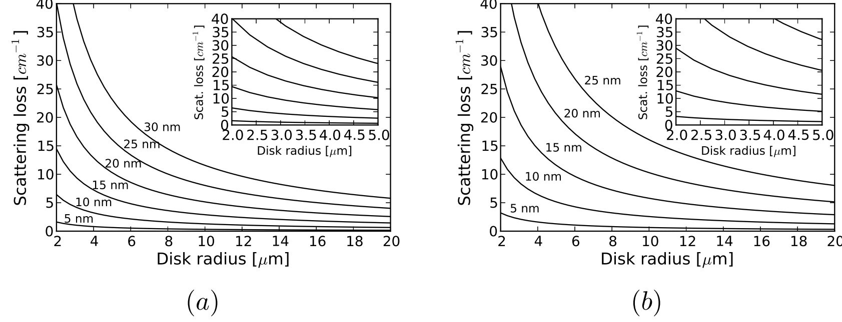

Figure 2.9: Calculated scattering loss due to sidewall roughness of the microdisk versus disk radius and RMS roughness based on a model proposed by [2]. In (a) a correlation length L_c of 50 nm is assumed and in (b) L_c is set to 100 nm. Insets show a close up for microdisk radii in the range of 2 to 5 μm.Replotted from [3]

2.3.3 Scattering losses

Another important loss factor in microdisk structures is scattering loss. Light propagating in the microdisk scatters at imperfections at the sidewalls. In order to determine the amount of scattering loss, one needs to determine the amount of surface roughness. Typically this is done be scanning the sidewall profile using an Atomic Force Microscope (AFM) probe [7]. The surface roughness is statistically quantified by the root mean square (RMS) value of the roughness σ and its correlation length L_c. Values strongly depend on the processing conditions but typical values are in the range of 3-20 nm for σ and 30-500 nm for L_c [7, 8].

Several models exist to deduce the amount of scattering loss based on the roughness parameters for microrings and microdisks [2, 9, 10] and show good agreement with experiments. Here we use the model proposed by [2] which was also used by [3] to get an estimate of the scattering loss. According to this model the scattering loss is given by

$$\alpha s = \frac{16\pi^3}{3R}(1 - \frac{n_2^2}{n_1^2})^2(\frac{n_1\sigma}{\lambda})^2\frac{n_1 L_c}{\lambda}\frac{\Gamma_z t}{\lambda}, \tag{2.14}$$

where R is the radius and t the thickness of the microdisk. Γ_z is the vertical confinement factor and n_1 and n_2 represent the refractive index of the microdisk and the cladding material, respectively. The result is plotted in Figure 2.9 for different values of σ versus the radius of the microdisk. The height is fixed to 580 nm. in Figure 2.9(a) a correlation length of 50 nm is assumed, while in Figure 2.9(b) 100 nm is assumed. From these plots it is obvious that scattering loss can have a significant impact on the optical loss.

2.4 Microdisk-Waveguide evanescent coupling

In the previous section we looked at optical losses of the microdisk structure. Another loss factor that requires special attention is the coupling loss to a neighboring waveguide. Obviously, part of the light should escape the cavity in a controlled way and serve as output of the laser. The coupling loss in a ring or disk laser is thereby the equivalent of mirror loss in a stripe laser. Therefore, the coupling between the access waveguide and the microdisk is an important parameter as it affects both the threshold current and slope efficiency of the laser. However, in case of microdisks, optimization of the coupling efficiency is not trivial as microdisks are inherently multimodal in the radial direction. In active microdisk structures this can become even worse when additional vertical modes come into play due to the increased thickness resulting from the extra layers required for electrical injection. Especially in more complex configurations when multiple disks are coupled to the same waveguide, such as e.g. a microdisk based multiwavelength laser, it is important to minimize the coupling to undesired higher order modes as otherwise the performance might severely degrade.

In other work [11, 12] simulations on the vertical coupling between III-V microdisks and silicon waveguides have been performed. However, only the coupling to single mode waveguides was investigated and the phase matching between the fundamental microdisk and waveguide mode is expected to be poor in this case.

The underlying mechanism for the coupling of light between the microdisk and the waveguide is known as evanescent coupling. This coupling effect occurs when two waveguides are in close proximity such that the evanescent mode tail of one waveguide overlaps with the neighboring waveguide, and as a result power is transferred from one waveguide to the other.

A convenient model to describe evanescent coupling is Coupled Mode Theory (CMT). It assumes that the field solution of the permittivity structure in the coupling section can be written as a linear combination of known electromagnetic fields of similar, but simplified, permittivity structures. As these similar permittivity structures can be chosen arbitrarily it is convenient to use the permittivity structures of the single unperturbed waveguides, i.e. the waveguide and the microdisk in this case. Due to the coupling these known electromagnetic fields are modulated in amplitude as function of the propagation direction. It can be shown that, see e.g. [13, 14], the coupling strength is a function of:

- the degree of phase matching
- the amount of overlap between the disk and waveguide mode
- the interaction length

Therefore, if one wants to optimize the coupling conditions the 3 parameters above need to be tuned. However, in case of microdisks the interaction length will be

very small due to the curvature of the microdisk. The degree of phase matching can be engineered by changing the dimensions of the disk and the waveguide, but as the dimensions of the disk will also directly influence the laser performance, we restrict ourselves here to only change the waveguide dimensions. To tune the amount of overlap both the vertical gap and the lateral offset of the waveguide with respect to the microdisk can be altered.

Phase matching

To optimize the coupling between the fundamental disk mode and the waveguide mode, the propagation constants of these modes need to match. Mode solver software can be used to find the eigenmodes and their propagation constant, or effective index. For the silicon waveguide the height is fixed to 220 nm, while the width can be changed according to our needs. A standard single mode TE waveguide has a width of 450 nm. Figure 2.10(a) shows the effective index versus waveguide width, where BCB is used as cladding material. The effective index ranges from 2.38 for a 450 nm width to 2.83 for a waveguide width of 2 μm.

Determining the effective index of a microdisk mode is less straightforward. As the microdisk is invariant in the azimuthal direction, the field only undergoes a phase change as it travels around the microdisk. As shown in Section 2.1.1 the field in a microdisk can be written as

$$\mathbf{E}(\mathbf{r}) = \mathbf{E}(r, z)e^{-im\phi} \tag{2.15}$$

This can be generalized to the case of a bend mode, where the azimuthal mode number m does not need to be an integer and is often written as γR, where R represents the bend radius and γ can be seen as the propagation constant. The behavior of the field in the azimuthal direction is thus described by the product γR. However, the definition of R is arbitrary. In other words, depending on the choice of R the propagation constant will change, but it will still describe the same physical system. As a result the phase matching argument used in e.g. directional couplers does not directly apply in the case of coupling between a disk and a waveguide, because of the arbitrary nature of the effective index of bend modes. An initial guess can be made by choosing an appropriate value for R by setting it e.g. equal to the disk perimeter or the maximum intensity of the field profile. Here we choose to use the disk perimeter as the definition of R and hence the effective indices found are a lower limit. Figure 2.10(b) shows the effective index as function of radius for the microdisk structure. If we compare figure 2.10(a) and (b) it is clear that phase matching between the waveguide mode and the fundamental disk mode cannot be achieved for microdisks with a radius larger than 10 μm as we here already used a lower limit for the microdisk mode effective index, while the effective index of the waveguide mode saturates around this point.

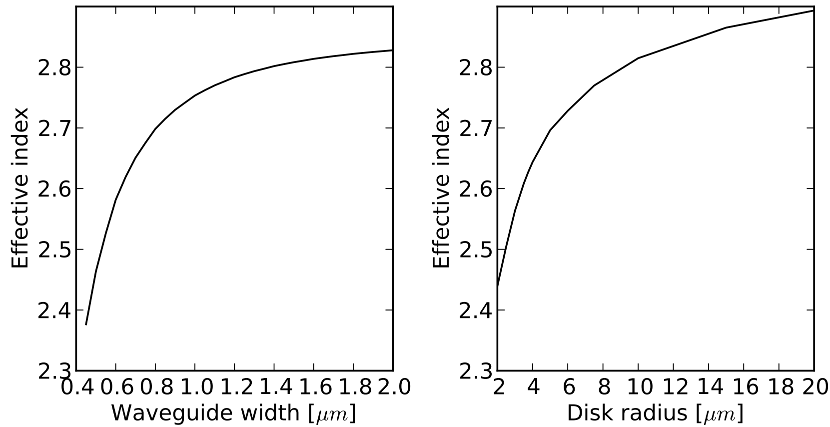

Figure 2.10: (a) Effective index of the fundamental mode in a silicon waveguide with 220 nm height versus waveguide width. (b) Effective index of the fundamental mode in a microdisk with 580 nm height versus disk radius.

The information on effective indices found above can be used as a starting point for simulations where parameters are sweeped to find the optimum coupling conditions. Simulation of vertical coupling between a bend and a straight structure is computationally intensive as it requires 3D simulation. We here used two different methods. First, a 3D CMT method was used to get a quick indication of the coupling conditions. Then, around the optimum coupling points more computationally intensive 3D FDTD simulations were performed to verify the results.

2.4.1 Simulation using CMT

We investigate the coupling between a microdisk structure and a silicon waveguide as shown in Figure 2.2. For computational efficiency the microdisk is modeled as a disk with a uniform refractive index of 3.2. The refractive indices of the silicon waveguide and the cladding material (BCB) are set to 3.48 and 1.54, respectively. The height of the microdisk is 580 nm. The 100 nm thin layer around the disk used for contacting the laser is also taken into account not only for calculating the mode profile of the whispering gallery modes in the disk but also for calculating the mode in the silicon waveguide. This is done because the optical mode in the access waveguide will be influenced by the presence of this layer when the vertical gap between the waveguide and this InP layer is small.

For the CMT simulation the commercial software tool FieldDesigner from Phoenix was used. A 3D CMT module is available in this package which makes it possible to simulate vertical coupling rather efficient.

Modename	*Modenumbers*	*Effective index*
Fundamental	(40,0,0)	$2.627 + 1.909e - 6i$
First order radial	(35,1,0)	$2.314 + 1.653e - 3i$
Second order radial	(33,2,0)	$2.177 + 1.083e - 2i$
First order vertical	(33,0,1)	$2.155 + 2.529e - 3i$

Table 2.1: Effective indices of the 4 highest order TE modes in a 3.75 μm radius microdisk structure with 580 nm height and a 100 nm thin bottom slab.

The first step in determining the coupling is to find the basis fields corresponding to the constituting permittivity profiles. That is, in this case the basis fields of the microdisk and the waveguide without the presence of the other. This is quite trivial for the silicon waveguide, but a little tricky for the microdisk structure as it supports multiple modes. The effective index of the fundamental TE mode in a 450 nm wide standard single mode waveguide is 2.38. If we would use this value as an effective index target for the fundamental mode of the microdisk in order to have proper phase matching, the radius should be smaller than 2.5 μm. This would lead to very high bend losses and therefore the dimensions of the waveguide should also be altered. As we already found in the previous section a bend radius larger than 3.4 μm is required if a slab thickness of 100 nm is used and bend losses lower than 1 cm^{-1} are desired. Therefore, we focus here on microdisks with a radius of 3.75 μm.

If we assume nearly vertical sidewalls of the microdisk the hybridness of the modes is negligible and the interaction between modes of different polarizations is expected to be low. From simulations it is found that this assumption is even valid for sidewall angles up to 60 degrees, which is well within in reach of what can be achieved in standard fabrication technology. Therefore, we will only take the TE modes into account in this simulation. The mode profiles of the lowest order TE modes supported by the microdisk are already shown in Figure 2.3. The corresponding effective indices of these modes at a wavelength of 1.55 μm are given in Table 2.1.

From Table 2.1 it can be seen that the fundamental mode has the highest real part of the effective index and the lowest imaginary part indicating that this mode has the highest confinement and lowest loss. In the following we would like to optimize the coupling to the fundamental mode while minimizing it for the other supported modes.

In the simulations the coupling gap and lateral waveguide position are varied to influence the overlap between the microdisk modes and the waveguide modes. Furthermore, different waveguide widths are used to change the effective index of the waveguide mode. The coupling gap is defined as the distance between the bottom of the microdisk and the top of the waveguide. The lateral offset is

assumed to be zero when the center of the waveguide is in line with the edge of the microdisk. Negative lateral offset then corresponds with a shift of the waveguide towards the center of the disk, while a positive offset is away from the center. This is schematically indicated in Figure 2.2(b).

Depending on the dimensions of the waveguide either one or two waveguide modes are taken into account in the simulation. For the microdisk modes we focus on the fundamental and first order radial mode. The reason for this is that the other higher order modes in Table 2.1 were too lossy to be used in the CMT model as it resulted in strong non -reciprocal coupling, which is obviously an unphysical result. Thus, in the simulations scattering matrices with a maximum size of 4x4 are generated. More higher order modes are taken into account in the FDTD model that will be discussed in the next section.

Based on the effective index plots we can make an initial guess for the width of the waveguide in order to have acceptable phase matching and thus efficient coupling. From Table 2.1 we find an effective index of 2.62 for the fundamental mode and thus a waveguide width of 600 nm is used as initial guess. Figure 2.11 shows the power coupling through the complete coupling section as function of a lateral waveguide sweep where the gap is fixed to 100 nm. For clarity the scattering coefficients have subscripts that denote a certain basis mode. Here $wg0$ and $wg1$ stand for the fundamental and first order TE waveguide mode, while $d0$ and $d1$ stand for the fundamental and first order radial disk mode. The different scattering coefficients are divided over three plots. The diagonal elements of the scattering matrix, corresponding with the transmission of each mode, are shown in the left plot. The plot in the middle shows the coupling between disk and waveguides modes and finally the right plot shows the coupling between disk modes. Furthermore, the dashed lines of a certain color correspond with the reciprocal of the solid line with the same color. It should be noted that in some cases the difference between these two lines became quite large and in a few cases for higher order modes even the shape of the curves was different. Therefore, we decided to verify the obtained results from this model through FDTD simulations and this will be further discussed in the next section.

Ideally, the transmission of the waveguide mode should equal the transmission of the fundamental disk mode, indicating that there is no coupling to other modes. From Figure 2.11(a) we see however, that for this configuration it is not the case and that the transmission in the waveguide equals the sum of the transmission of the two disk modes, in the area between -400 and 100 nm offset.

From Figure 2.11(b) it can be seen that the coupling between the fundamental disk mode and the fundamental waveguide mode reaches a maximum of 30% coupling at a waveguide offset of -300 nm. This optimum offset point is what one would expect as in this case the center of the waveguide is more or less positioned at the point where the radial electric field component reaches a maximum and thus

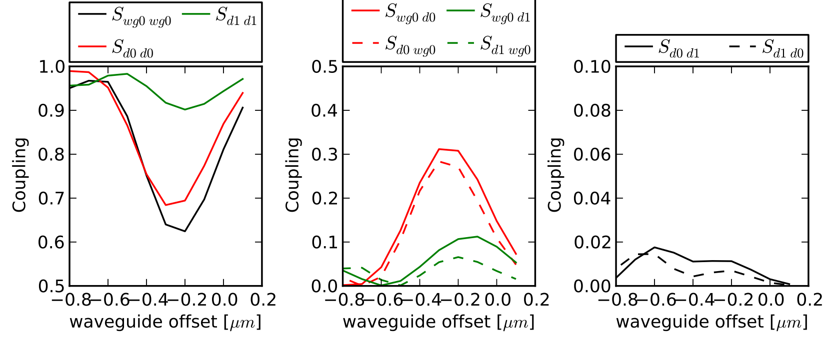

Figure 2.11: Power coupling between modes through the complete coupling section as a function of lateral waveguide offset for a waveguide width of 600 nm and a gap of 100 nm. (a) The power transmission of the fundamental waveguide mode S_{wg0wg0} and the two highest order disk modes S_{d0d0} and S_{d1d1}, (b) coupling between the fundamental waveguide mode and fundamental or first order radial disk mode S_{wg0d0}, S_{wg0d1} and (c) intermodal coupling between the fundamental and first order radial disk mode S_{d0d1}.

large overlap exists between the waveguide and fundamental disk mode. As also seen in Figure 2.11(a), there is also significant coupling to the first order radial mode which is not desired. We based our first initial guess on the effective index of the fundamental mode defined at the edge of the disk. As discussed before, the effective index of bend mode depends on the radius. By using the edge of the disk as radius for effective index calculation this results in a lower limit. Therefore, the next step would be to simulate the effect of a waveguide mode with a higher effective index.

Finally, from Figure 2.11(c) it can be seen that there is also some intermodal coupling between the two disk modes, which is caused by the disturbance of the field in the disk by the presence of the waveguide. By increasing the gap size an exponential decrease in coupling efficiency is expected due to the reduced overlap of the modes. The disturbance of the disk modes should also become less with increasing gap, resulting in lower intermodal coupling.

Now, let us first consider a wider waveguide of 800 nm, still with a gap of 100 nm. The results are shown in Figure 2.12. The transmission curves of the waveguide mode and the fundamental disk mode show good overlap at the optimum coupling point, indicating that in this region power exchange is mainly between these modes. The maximum amount of coupling at the optimum coupling point is slightly higher compared to the previous case with a 600 nm wide waveguide. Coupling between the waveguide and the first order radial mode is now negligible in the optimum coupling point, while for larger negative offset the coupling starts to increase due to the increasing overlap with the second node of the first order

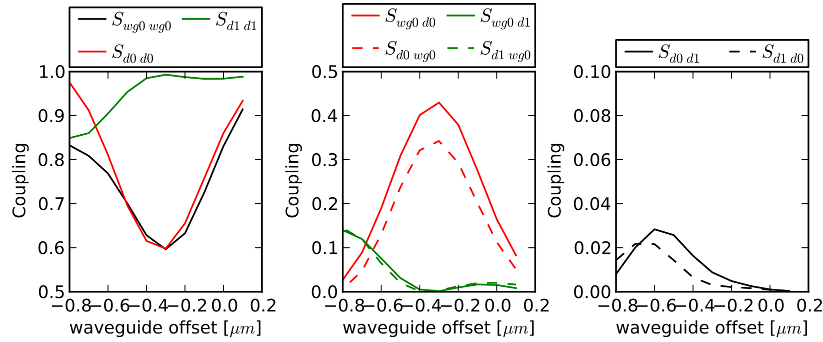

Figure 2.12: Power coupling between modes through the complete coupling section as a function of lateral waveguide offset for a waveguide width of 800 nm and a gap of 100 nm. (a) The power transmission of the fundamental waveguide mode S_{wg0wg0} and the two highest order disk modes S_{d0d0} and S_{d1d1}, (b) coupling between the fundamental waveguide mode and fundamental or first order radial disk mode S_{wg0d0}, S_{wg0d1} and (c) intermodal coupling between the fundamental and first order radial disk mode S_{d0d1}.

radial mode. The intermodal coupling is similar as in the case of a 600 nm wide waveguide. Based on these results a waveguide width of 800 nm seems better suited for 7.5 μm diameter microdisks. However, the first order waveguide mode cannot be neglected anymore, as the effective index of this mode is 2.18. In the following, we compare the coupling for slightly different waveguide widths where we take into account the first two TE waveguide modes and again the fundamental and first order radial disk mode.

The red, green and blue curves in Figure 2.13 correspond with waveguide widths of 700, 800 and 900 nm, respectively. The gap was set to 150 nm for these simulations. The goal here is to optimize the coupling between the fundamental waveguide mode and the fundamental disk mode (Fig. 2.13(a)), while undesired coupling between other modes is minimized (Fig. 2.13(b-c)). Figure 2.13(a) shows the coupling between the fundamental disk mode and the fundamental waveguide mode. Clearly, there is no major difference in coupling between these modes for the waveguide widths. The wider waveguides are a little bit more tolerant in terms of lateral offset. The coupling between the fundamental waveguide mode and the first order radial disk mode is shown in Figure 2.13(b). Again, we find similar results for the different waveguide widths, although the coupling for the 700 nm wide waveguide is slightly worse compared to the others. This is because at the optimum offset of -300 nm there is some coupling, between the fundamental waveguide mode and the first order radial disk mode. This is an undesired situation in a configuration with multiple disks coupled to one waveguide as the output from one disk might couple into a higher order mode of another disk. On the other hand,

from Figure 2.13(c) we find that a 700 nm wide waveguide performs slightly better, as there is almost no coupling between the fundamental disk mode and the first order waveguide mode. For the 900 nm wide waveguide however, there is already 5% coupling between these modes. This coupling can be seen as an extra loss factor for the lasing mode and thus should be avoided. For completeness the coupling between the first order radial disk mode and first order waveguide mode is also displayed in Figure 2.13(d), however this is not a concern for our structures. From the above analysis we find that a waveguide width between 700 and 800 nm is optimal for a 7.5 μm diameter microdisk.

The last step in optimizing the coupling conditions is to tune the actual amount of coupling. The amount of power coupling at the optimum waveguide position found in the simulations discussed above, is already too high for our microdisk lasers as for these small lasers typically only about 1 to 10% coupling is targeted. The optimum amount of coupling depends on other laser parameters and will be discussed in Chapter 3. To lower the power coupling one could change the lateral offset of the waveguide, but this is not preferred as due to the steep slope away from the optimal coupling point, any misalignment during processing will have a large effect on the coupling. Furthermore, coupling to undesired modes might be enhanced. By increasing the gap between the waveguide and the microdisk, the overlap between the modes is reduced and thus also the coupling will be reduced. However, because of the exponentially decaying mode tails the coupling also has an exponential dependence on the gap. This is shown in Figure 2.14 for a 7.5 μm diameter microdisk with a 750 nm wide waveguide and -300 nm lateral offset. Coupling in the order of 1 to 10 % requires a gap between 200 and 300 nm. It is obvious that accurate control of the gap is crucial in order to get reproducibale results. An accurate bonding approach to control the gap thickness will be presented in Section 5.3.

In some situations it might be advantageous to use bend waveguide structures to optimize the beat length for a certain mode, while decreasing it for other modes. However, this complicates the alignment procedure during processing. As in this case the desired coupling conditions could be met by using straight waveguides, bend waveguides were not considered here.

2.4.2 Simulation using FDTD

The CMT method can give quick insight into the coupling conditions, but in some situations e.g. when analyzing relatively lossy microdisk modes, the CMT algorithm gave unphysical results as already mentioned in the previous section. Therefore, we also performed FDTD simulations to get more accurate results near the coupling points of interest found by CMT. First we will verify the coupling between the fundamental disk mode and the waveguide mode. Then, the amount of

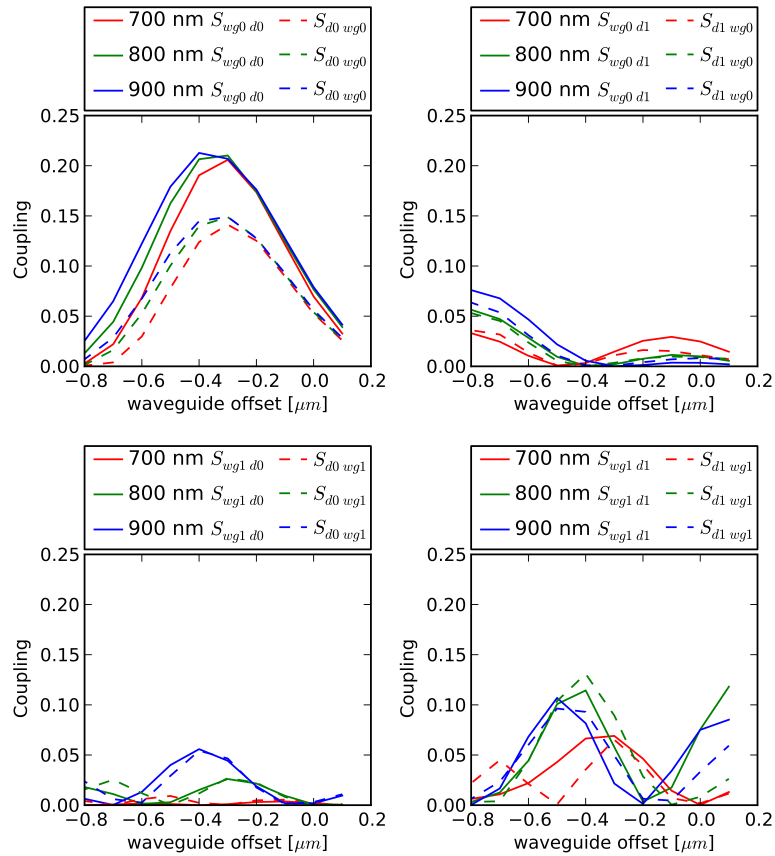

Figure 2.13: Comparison of power coupling for waveguide widths of 700, 800 and 900 nm. (a) Desired power coupling between fundamental waveguide and fundamental disk mode, (b)undesired power coupling between the fundamental waveguide mode and first order radial disk mode, (c) undesired coupling between the first order waveguide mode and fundamental disk mode and (d) undesired coupling between the first order waveguide mode and the first order radial disk mode.

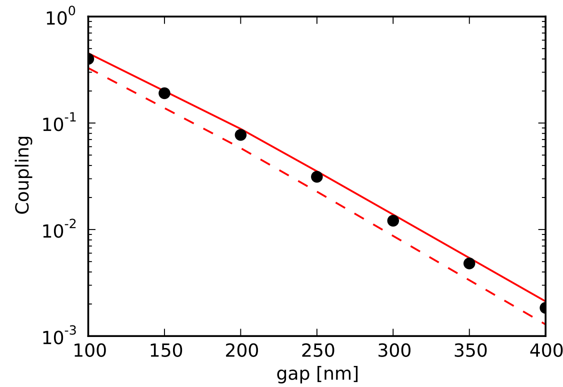

Figure 2.14: Power coupling between the fundamental waveguide mode and the fundamental disk mode versus gap. The waveguide width is set to 750 nm and the lateral offset is fixed to -300 nm. Some results obtained from FDTD simulations, which will be discussed in the next section, are also included in the plot and indicated by the black dots. Good agreement is obtained between the CMT and FDTD simulations.

reflection and intermodal coupling is investigated.

As we are here investigating the coupling between the microdisk laser and the waveguide and are at this point not interested in the resonant behavior of the microdisk, we use a simulation setup where a Perfectly Matched Layer (PML) is placed inside the disk cavity. Such a PML is an artificial absorbing layer that is often used to simulate problems with open boundaries to truncate the computational region and can in this case be used to avoid resonant behavior. This substantially shortens the simulation time. A schematic representation of the simulation setup is shown in Figure 2.15. The simulation relies on modal expansion of the detected fields at certain points in the structure. First several modal solutions for the microdisk and waveguide are calculated. Then, a source having an appropriate mode profile is excited either in the waveguide or in the disk in front of the coupling section. The fields are analyzed in cross-sectional planes of the microdisk and waveguide after the coupling section. Because of the orthogonality of the modes the detected fields can be written as a superposition of modes. Therefore, the fraction of power in a certain mode can be found by calculating the overlap of the field with this mode. The results discussed here are for a wavelength of 1.55 μm. Although each mode in the disk cavity has a different resonance wavelength and the coupling is wavelength dependent, using single wavelength results can be justified by the fact that the wavelength dependence will be very small, because of the short interaction length between the microdisk and the waveguide. In fact, the simulations were performed in a wavelength range of 1.5 to 1.6 μm and very little variation in coupling efficiency was observed over this wavelength range.

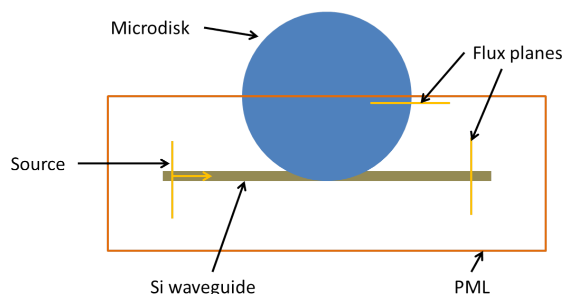

Figure 2.15: Top view of the FDTD simulation setup. The PML runs through the center of the microdisk to avoid any resonance behavior. An optical mode is injected in the silicon waveguide and the resulting fields are analyzed at the end of the waveguide and in the microdisk just before the PML.

We start by analyzing a similar configuration as the first one described in the previous section; a microdisk with a diameter of 7.5 μm and a waveguide width of 600 nm. The lateral waveguide offset is varied around the point that gave maximum coupling for the fundamental disk mode in the CMT analysis. Furthermore, the gap is adjusted to 200 nm in order to get power coupling in the desired 1-10 % order. Figure 2.16 shows the fraction of power coupled to the 4 highest order TE microdisk modes (i.e. fundamental, first order radial, second order radial and first order vertical) when the fundamental TE waveguide mode is excited. The results of the two highest order modes are in good qualitative agreement with the CMT analysis as, apart from the lower power coupling due to the larger gap, the curves show the same behavior. However, from the FDTD simulation it is clear that coupling to the second order radial and first order vertical mode cannot be neglected, while it leaded to unphysical results in the CMT analysis. The coupling to the TM modes was found to be negligible. The black dashed line shows the power through the flux plane originating from the 4 highest order TE and TM modes, while the black solid line represents the total power through this flux plane. The discrepancy between these two indicates there is still a few percent of power that is coupled to even higher order modes or radiating modes. The discrepancy decreases when the lateral offset is towards the edge of the disk, while for offsets towards the center of the disk it increases. This can be explained by the fact that for larger negative waveguide offsets the coupling from waveguide to disk can be seen as coupling to a slab with a large number of modes. Finally, by analyzing the total power through the flux plane in the disk cavity and the flux plane through the waveguide after the coupling section, one can find that the scattered power is just above 1% in this configuration.

Figure 2.17 shows the FDTD simulation results for a 800 nm wide waveguide as discussed in the previous section. Again, the results are in good agreement

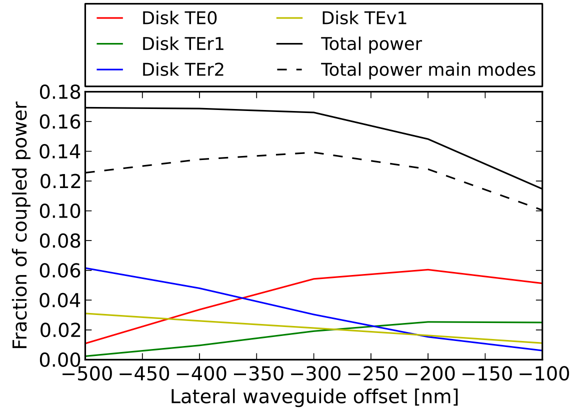

Figure 2.16: Power coupled between the fundamental waveguide mode and the 4 highest order TE modes in the microdisk versus lateral waveguide offset. The width of the waveguide is 600 nm and the gap is 200 nm. The black solid line represents the total power through the flux plane and the dashed black line represents the power through this flux plane of the four highest order TE and TM modes.

with the CMT analysis showing efficient coupling between the fundamental disk and waveguide mode and almost no coupling to the first order radial disk mode. However, from the FDTD simulation it is found that the highest undesired coupling is to the second order radial mode and is around 1% at the optimum coupling point for the fundamental mode. The scattering loss in this case was found to be lower than 1%.

The results obtained with the CMT and FDTD simulations are in good agreement and it is therefore expected that these models can provide a good prediction of the coupling conditions between microdisks and access waveguides. Experimental verification of the coupling conditions will be discussed in the next section.

2.4.3 Experimental results

In the previous section we studied the coupling between the microdisk and a waveguide using simulations. Here we will focus on experimental verification of the simulation results. In a ring or disk laser the coupling coefficient can be deduced from transmission measurements as described in [15] and also in [16] for evanescently coupled photonic crystal lasers. In this approach, a probe signal that is sweeped in wavelength is injected in the access waveguide of the resonator and collected on the other side where the output spectrum will show a resonance dip. By pumping the resonator, the losses in the resonator cavity can be changed and thus also the coupling regime. Under the critical coupling condition, the amount of coupling can be deduced by fitting a Lorentzian to the resonance dip.

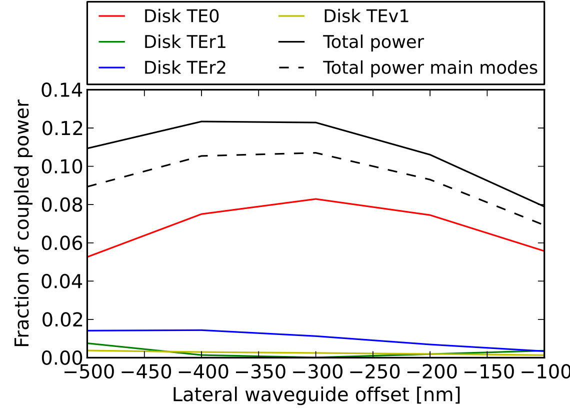

Figure 2.17: Power coupled between the fundamental waveguide mode and the 4 highest order TE modes in the microdisk versus lateral waveguide offset. The width of the waveguide is 800 nm and the gap is 200 nm. The black solid line represents the total power through the flux plane and the dashed black line represents the power through this flux plane of the four highest order TE and TM modes.

The theory is briefly described below. For a more extensive explanation we refer to [15].

Theory

In an active microdisk the time evolution of the amplitude A(t) in the cavity can be written as:

$$\frac{dA}{dt} = \left(j\omega_R - \frac{1}{\tau_0} - \frac{1}{\tau_c} + \frac{1}{\tau_g} \right) A + \sqrt{\frac{2}{\tau_c}} S_{in}, \tag{2.16}$$

where ω_R is the resonance frequency, S_{in} the input amplitude from the waveguide and $\tau_{0,c,g}$ are the time constants for the internal losses, coupling losses and gain, respectively. Assuming the input signal S_{in} has an $e^{j\omega t}$ time dependence the power transmission in the the steady state regime can be written as:

$$T = \left| 1 - \frac{\frac{2}{\tau_c}}{\left(j\left(\omega - \omega_R\right) + \frac{1}{\tau_0} + \frac{1}{\tau_c} - \frac{1}{\tau_g} \right)} \right|^2, \tag{2.17}$$

When no pumping is applied to the disk, the active region absorbs and adds up to the total losses in the cavity. $1/\tau_g$ takes on a negative value in this case and this can be identified as a microdisk in the undercoupled regime. By pumping the microdisk, losses in the active region will go down and at a certain point $1/\tau_g$ becomes positive and starts compensating for the intrinsic and coupling losses. When

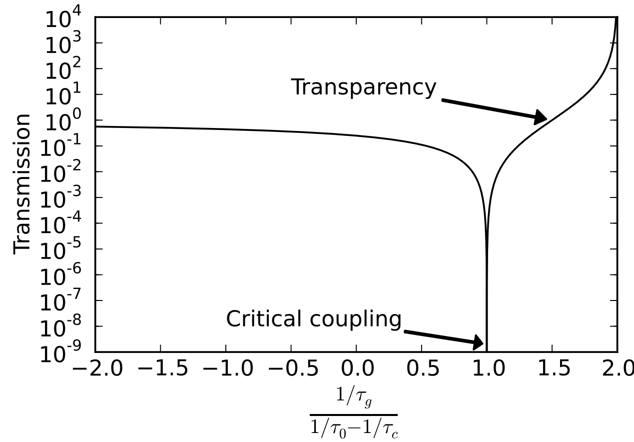

Figure 2.18: Calculated transmission at the resonance frequency versus the ratio of gain over intrinsic and coupling losses. By increasing the gain the coupling condition changes from the undercoupled regime to the critically coupled regime and finally enters the overcoupled regime.

$1/\tau_g = 1/\tau_0 - 1/\tau_c$ all the losses are compensated which corresponds to critical coupling. By increasing the pump further $1/\tau_g > 1/\tau_0 - 1/\tau_c$ and the overcoupled regime is entered. Finally, when the gain is high enough the microdisk will work as a wavelength selective amplifier. With a single transmission measurement without changing the losses in the cavity one would not be able to distinguish between the different coupling regimes. When the losses in the cavity are changed, the transmission at the resonance frequency will also change and reach a minimum value when the critical coupling condition is met and hence the other regimes can be identified as well. This evolution of the transmitted power at the resonance frequency is shown in Figure 2.18 as a function of $\left(1/\tau_0 - 1/\tau_c\right)/\tau_g$.

The time constant τ_c can be related to the coupling quality factor of the disk resonator as $Q_c = \omega_R \tau_c/2$ and the time constants τ_0 and τ_g can be related to the intrinsic quality factor as $Q_i = \omega_R(\tau_0 + \tau_g)/2$. The loaded or total quality factor Q_t follows then from $1/Q_t = 1/Q_i + 1/Q_c$ and can be found by measuring the FWHM and resonance frequency (conform Equation 2.10). When the critical coupling condition is met, Q_c equals Q_i and thus Q_c can be determined from Q_t. As described above, the critical coupling point can be found by sweeping τ_g and looking for the point with minimal transmission.

Measurement setup

In order the measure the coupling efficiency we use an Agilent tunable laser (TL) 8164B as a probe signal. The output of the laser is then injected into the silicon waveguide through a fiber coupler (FC). A polarization rotator is included to adjust the polarization state. The microdisk laser is electrically pumped through a Keithley 2400 current source and the current is varied to change the losses in the microdisk cavity. The transmitted light is then collected at the other side of the access waveguide via another FC by the integrated detector of the Agilent TL. By using this integrated detector it is possible to sweep the wavelength fast at high resolution. The wavelength was swept around 1550 nm within a range of a few tens of nanometer with a 10 pm resolution. The output power of the TL should be carefully chosen, it should be low enough such that no strong non-linear effects occur in the disk cavity, but also high enough such that it not drowns in the spontaneous emission generated in the microdisk. The current range depends on the threshold and thus on the radius of the microdisk, but ranges from 0 to 1 mA.

Results

Figure 2.19 shows the transmission spectra for different pump currents for a 7.5 μm diameter microdisk laser. Due to the carrier injection in the microdisk the resonance wavelength first shifts towards shorter wavelengths. At a certain point thermal effects come into play and start compensating for this blue shift. As the current is increased further a red shift is observed. The FWHM of the resonance decreases with increasing pump level. It is also clear that by increasing the pump the transmitted power at resonance first decreases, reaches the critical coupling point, increases again and finally gets amplified. If the transmission at the resonance wavelength is plotted versus pump power it results in a curve as shown in Figure 2.20. Indeed, this curve shows a similar evolution as the calculated curve based on theory which was shown in Figure 2.18. By determining the Q factor of the resonance at the critical coupling point, the coupling efficiency can be found. The experimentally determined coupling efficiencies for coupling between the fundamental waveguide mode and fundamental microdisk mode are given in Table 2.2 for different devices, together with the predicted values based on the simulation results. Cross-sections of several structures were made using a Focused Ion Beam (FIB) after which a Scanning Electron Microscope (SEM) was used to measure the geometrical parameters. These geometrical parameters were then used in the simulations. Deviations between simulation and measurement can be caused by small variations in the actual gap, thickness of the microdisk, misalignment, etc. Also, in the simulation a uniform refractive index of 3.2 was assumed for the microdisk stack. In general however, good agreement is obtained between the simulation and measurement results.

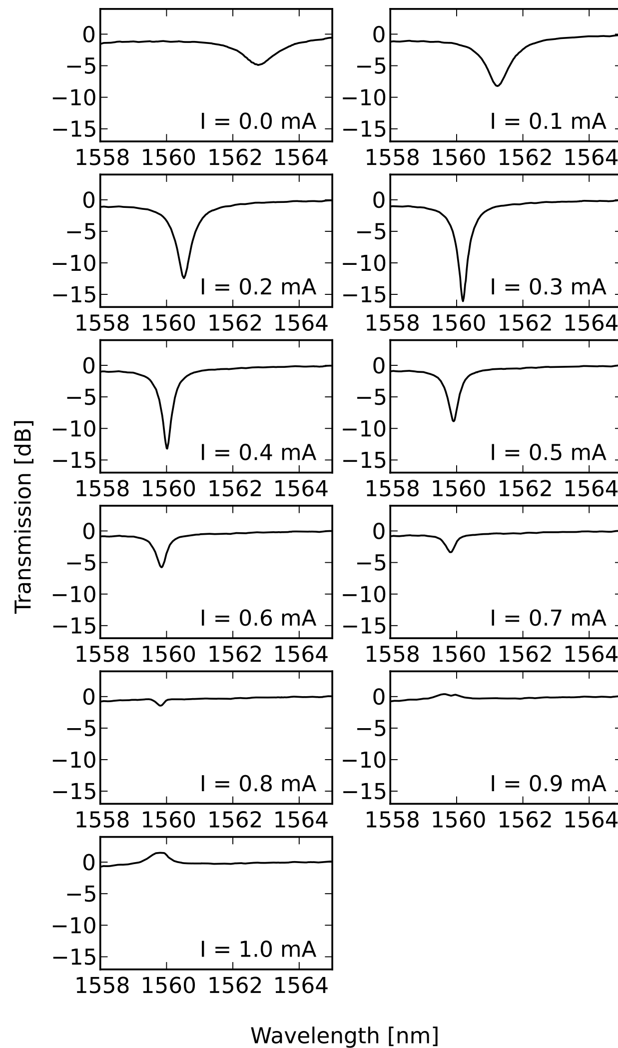

Figure 2.19: Transmission spectra of a 7.5 μm diameter microdisk laser versus injected current. First the transmission at the resonance frequency decreases until the critical coupling condition is met after which the transmission increases again and results in selective gain in the last plots. Besides the change in transmitted power also a wavelength change is observed; first a blue shift due to the injection of carriers and at higher currents a red shift due to thermal effects.

Disk radius μm	*Waveguide width* nm	*Waveguide offset* nm	*gap* nm	*Simulated coupling* %	*Measured coupling* %
3.75	560	-170	260	2.1	3.4 (2.8-5.0)
3.75	710	-430	260	2.3	2.9 (2.6-3.8)
3.75	710	-170	260	2.3	1.8 (1.0-2.8)
3.75	710	-230	260	2.1	1.7 (1.0-2.1)
3.75	710	-70	260	1.4	1.6 (0.9-2.7)
3.75	600	-225	130	10.5	11.9 (10.3-13.8)
5	810	-170	260	2.2	2.2 (1.9-3.1)
5	810	-70	260	2.4	3.6 (3.3-4.6)
5	1160	-270	260	3.1	2.6 (2.4-3.2)
5	1160	-330	260	3.3	1.3 (1.2-1.9)
5	750	-300	130	15.9	12.4 (10.5-15.1)

Table 2.2: Experimentally obtained coupling efficiencies for several microdisk laser structures together with the values predicted by the simulations. Good agreement is obtained between simulation and measurement results. The values between brackets in the last column follow from the quality factors from points adjacent to the minimum transmission point and are therefore measured lower and upper limits for the coupling efficiency.

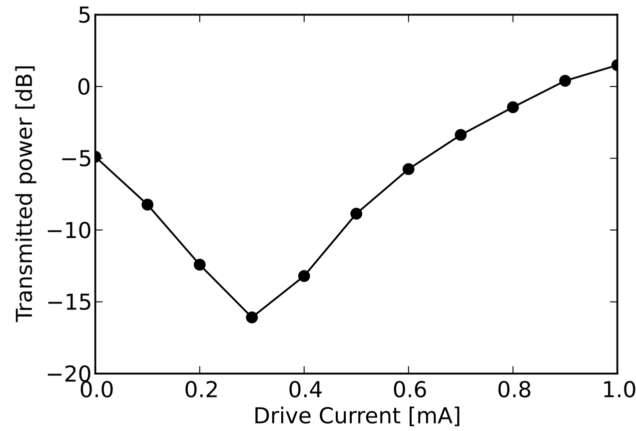

Figure 2.20: Transmitted power at the resonance frequency versus injected current. The curve shows a similar evolution as the calculated curve based on theory shown in Figure 2.18.

2.5 Conclusions

In this chapter we evaluated several loss mechanisms in microdisk cavities and the coupling between optical modes in a microdisk and an access waveguide. The thickness of the bottom contact layer can be used to increase the bend loss of undesired higher order modes. Only in case of microdisks with very small bend radii ($\leq 2.5\mu m$), the bottom contact layer should be made thinner as otherwise the fundamental mode becomes too lossy. Optimum conditions for the metal contact positions and sizes are found and especially the top contact metal should be controlled very well in size and position to avoid excessive optical loss.

Coupling simulations based on CMT and FDTD approaches have been performed and show good agreement. These simulations were not only used to optimize the coupling between the fundamental modes in the microdisk and the waveguide, but also to reduce undesired coupling between higher order modes present in the microdisk. This is especially of concern in multi-wavelength laser designs, where multiple microdisk lasers are coupled to the same waveguide. Measurements were performed on fabricated microdisk lasers to deduce the coupling efficiency and the results show good agreement with the simulation results.

References

[1] Matthew Borselli. *High-Q microresonators as lasing elements for silicon photonics*. PhD thesis, California Insitute of Technology, 2006.

[2] John E Heebner, Tiziana C Bond, and Jeff S Kallman. *Generalized formulation for performance degradations due to bending and edge scattering loss in microdisk resonators.* Optics express, 15(8):4452–73, April 2007.

[3] J Van Campenhout, P Rojo Romeo, P Regreny, C Seassal, D Van Thourhout, S Verstuyft, L Di Cioccio, J-M Fedeli, C Lagahe, and R Baets. *Electrically pumped InP-based microdisk lasers integrated with a nanophotonic silicon-on-insulator waveguide circuit.* Optics express, 15(11):6744–9, May 2007.

[4] *Waveguide Mode Solvers Feature List - FIMMWAVE.*

[5] Mark Oxborrow. *Traceable 2D finite-element simulation of the whispering-gallery modes of axisymmetric electromagnetic resonators*. IEEE Transactions on Microwave Theory and Techniques, 55(6):1209–1218, 2007.

[6] M Imran Cheema and Andrew G Kirk. *Implementation of the Perfectly Matched Layer to Determine the Quality Factor of Axisymmetric Resonators in COMSOL.* In Proceedings of the COMSOL Conference 2010 Boston, pages 2–4, 2010.

[7] J. H. Jang, W. Zhao, J. W. Bae, D. Selvanathan, S. L. Rommel, I. Adesida, a. Lepore, M. Kwakernaak, and J. H. Abeles. *Direct measurement of nanoscale sidewall roughness of optical waveguides using an atomic force microscope*. Applied Physics Letters, 83(20):4116, 2003.

[8] Akihiro Matsutani, Fumio Koyama, and Kenichi Iga. *Three-dimensional electron probe roughness analysis of InP sidewalls processed by reactive ion beam etching*. Applied physics letters, 66(1):64–66, 1994.

[9] B E Little, J P Laine, and S T Chu. *Surface-roughness-induced contradirectional coupling in ring and disk resonators.* Optics letters, 22(1):4–6, January 1997.

[10] Matthew Borselli, Thomas Johnson, and Oskar Painter. *Beyond the Rayleigh scattering limit in high-Q silicon microdisks: theory and experiment.* Optics express, 13(5):1515–30, March 2005.

[11] F Mandorlo, P Rojo-Romeo, J-M Fedeli, H. MD Sohrab, and R Orobtchouk. *Mode density reduction and coupling in microdisk LASERs processed on a 200 mm CMOS pilot line*. IEEE Photonics Journal, 23(17):1183–1185, 2011.

[12] Jens Hofrichter. *InP microdisks for optical signal processing and data transmission*. PhD thesis, Eindhoven University of Technology, 2012.

[13] C Manolatou, MJ Khan, and Shanhui Fan. *Coupling of modes analysis of resonant channel add-drop filters*. IEEE Journal of Quantum Electronics, 35(9):1322–1331, 1999.

[14] Remco Stoffer, KR Hiremath, and Manfred Hammer. *Cylindrical integrated optical microresonators: Modeling by 3-D vectorial coupled mode theory*. Optics Communications, 256(1):1–20, 2005.

[15] Yannick Dumeige, Stéphane Trebaol, L Ghisa, T.K Ngan Nguyen, Hervé Tavernier, and P Feron. *Determination of coupling regime of high-Q resonators and optical gain of highly selective amplifiers*. Journal of Optical Society of America B, 25(12):2073–2080, 2008.

[16] Y Halioua, A Bazin, P Monnier, T J Karle, G Roelkens, I Sagnes, R Raj, and F Raineri. *Hybrid III-V semiconductor/silicon nanolaser.* Optics express, 19(10):9221–31, May 2011.

3

Microdisk laser design and simulation

While the previous chapter dealt with the optical cavity formed by a microdisk, this chapter will give a more detailed analsysis of the electro-optic behavior of a microdisk laser. First we will give a brief overview of the state-of-the-art in micro laser design. Then, some important laser physics will be briefly explained, after which the microdisk laser structure that we would like to investigate is presented. Next, simulation results on the electrical behavior of the microdisk laser will be given and finally, results from fully coupled electro-optic simulations will be given.

3.1 Lasers on Silicon

In Chapter 1 we already briefly discussed the difficulty of realizing efficient lasers in silicon. As a result researchers focused on methods to integrate other materials with silicon to make lasers on this platform. If a large number of lasers is required, which is the case for on-chip optical interconnects, the most successful approach so far is that of heterogeneous integration. In recent years several heterogeneously integrated lasers have already been demonstrated [1–4]. However, these lasers are typically large devices and have threshold currents of several tens of mA. The energy efficiency and footprint of these lasers is therefore considered too high for on-chip optical interconnects. Therefore, we focus here on the integration of microlasers on silicon. First we will give a brief overview of recent advances in the development of microlasers in general, followed by the progress made on micro lasers integrated on silicon.

3.1.1 Micro lasers

Quite a number of micro lasers have been reported in literature of which most of them are based on microdisk and photonic crystal cavities and more recently also metal cavity nanolasers [5]. Here we will briefly discuss the most recent advances in micro laser development.

Metal nanocavity lasers are in most cases surface emitting lasers and are considered less suitable for coupling to in plane waveguides. However, in [6] lasing in a metal-insulator-metal plasmonic waveguide has been demonstrated. The waveguide has a width of only 130 nm and a length of 3 μm. A lasing threshold of 40 μA has been obtained at a temperature of 78 K and also pulsed operation at room temperature has been demonstrated. An advantage of these devices is that it is relatively straightforward to use an electrical injection scheme, although low specific contact resistances are essential because of the small dimensions. On the other hand, coupling schemes to standard waveguides still need to be developed and also the efficiency is still low due to the metal losses.

In 2010 an optically pumped photonic crystal laser was demonstrated on an InP platform [7]. The laser operates in continuous wave regime at room temperature and has a single mode fiber output power of 0.44 μW. The 3 dB modulation bandwidth is 5.5 GHz and an ultra high energy efficiency under direct modulation is obtained as it is estimated that the required energy for transmitting one bit is only 13 fJ. However, fabrication of this laser is difficult as a regrowth process is needed for the buried heterostructure while at the same time a flat top surface is required for a high Q cavity.

An electrically pumped photonic crystal laser in GaAs was demonstrated by Ellis and coworkers [8]. A lateral p-i-n junction is formed by ion implantation and the active region consists of three layers of InAs quantum dots. Ultra low threshold currents of 181 nA @ 50 K and 287 nA @ 150 K were demonstrated. However, no lasing was achieved at room temperature and the output power was rather low with sub pW values. It should also be noted that the design of the laser allows for heterogeneous integration with silicon through a bonding approach.

More recently, an electrically pumped photonic crystal laser based on the design of Matsuo has been developed in the same research group (NTT) [9]. The laser operates at room temperature and has a threshold current as low as 4.8 μA. The output power is in the μW level and CW operation up to 95 °C is demonstrated. Furthermore, direct modulation at 10 Gb/s is demonstrated with an efficiency of 4.4 fJ/bit. For the electrical injection a lateral p-i-n junction is used similar as the approach demonstrated by Ellis et al. Current blocking trenches and an InAlAs sacrificial layer were used to reduce the current leakage. A heterogeneous integration approach is proposed to fabricate these lasers on a silicon platform, but this has not been demonstrated for these lasers so far. This also does not seem to be trivial as a regrowth step is required to fabricate these lasers and thus the alignment

tolerance for the bonding process will be very small.

In [10] lasing was demonstrated in compact microdisks with InAs quantum dots in a well structure (DWELL). These DWELL structures have a quantum well layer underneath the quantum dots to enhance the carrier injection efficiency. The microdisks have diameters between 1.7 and 1.83 μm and emit around a wavelength of 1300 nm. A pulsed optical injection scheme was used and a threshold power of 0.6 mW was obtained. The output was collected via a 100X objective lens and a multimode fiber.

Realizing efficient electrical contacts, without affecting the optical properties of the laser, is difficult. Recently, microdisk lasers with transparent graphene electrodes have been demonstrated [11]. Because few layer graphene is not 100% transparent a dielectric layer was still used at the periphery of the microdisk to separate the graphene from the optical mode. Lasing was achieved at room temperature with threshold currents of 300 μA under pulsed conditions. The output light was collected via a 50X objective lens. The series resistance of the microdisk laser was 5.8 kΩ and this high value prevented lasing in CW.

3.1.2 Microlasers on silicon

Realizing micro lasers on silicon involves an extra challenge as we already have seen that silicon is not suitable as a light emitter and that it is difficult to grow III-V materials on silicon. However, in 2011 InGaAs nanolasers directly grown on silicon have been demonstrated by using a novel growth scheme [12]. The nanopillars are defined using contact lithography and have a radius in the order of a few hundred nanometer. The hexagonal cross-section of the pillars results from the single-crystal wurtzite structure and forms a natural optical cavity. The nanopillars support helically propagating cavity modes resulting in strong confinement of the light. Room temperature lasing was achieved under optical pumping. Electrically injected LEDs based on these nanopillars have also already been demonstrated [13]

More recently, InP nanowire lasers grown on prepatterned silicon substrates have been demonstrated [14]. In order to obtain high quality InP nanowires, a nano-trench assisted defect-trapping effect in combination with an epitaxial lateral overgrowth process is used. This results in similar hexagonal structures as described above but under an angle of 35 degrees with respect to the silicon plane. The diameter of the nanowire is about 400 nm and the length of the cavity is 1.4 μm. Lasing at room temperatures has been achieved under pulsed optical pumping conditions with a threshold of 6.7 $\mu J/cm^2$. The laser peak was located at a wavelength around 851 nm.

Several photonic crystal lasers on silicon have been demonstrated [15–17] but in these cases the light was not yet coupled to a silicon waveguide. Coupling to a silicon access waveguide from a heterogeneously integrated photonic crystal

laser has been demonstrated in [18]. The laser was optically pumped at room temperature but under pulsed conditions. A threshold power of 17 μW has been obtained.

Recently, a new type of microcavity laser has been developed by De Koninck and coworkers [19]. In this design the mirrors to form the laser cavity are actually resonating cavities themselves. As a result high narrowband reflection can be obtained and if the laser cavity itself is made short enough, only one longitudinal mode will lie in the reflection bandwidth of the mirrors, yielding an intrinsically single mode laser. The resonant mirrors are formed by etching gratings in the silicon while optical gain is generated by a III-V wire. Laser operation has been demonstrated under optical pumping at room temperature with pulsed drive conditions. CW operation has not yet been demonstrated and is said to be hindered by self heating effects.

The worlds first electrically injected microlaser on silicon was demonstrated by Van Campenhout and coworkers in 2007 [20]. Here a disk cavity is etched in an InP-based thin film that is bonded on silicon. The diameter of the microdisks was in the order of 7.5 μm. CW operation was obtained at room temperature with a threshold current of 0.5 mA. The maximum output power was limited to 10 μW in the silicon waveguide. The work presented here builds upon this microlaser design.

In [21] a III-V microring laser on top of a silicon microdisk has been demonstrated. The diameter of these rings is in the order of 50 μm and the center part is not completely etched through such that a bottom contact layer remains for electrical injection. A threshold current of 5.4 mA has been demonstrated at room temperature under CW operation. A maximum output power of 230 μW has been obtained, although for devices with higher threshold currents of 8 mA.

Although a few monolithically integrated III-V lasers on silicon have been demonstrated and show promising results, electrically injected lasers with reasonable efficiency are not expected for the near future.

Also photonic crystal lasers on silicon have been demonstrated by heterogeneous integration of III-V, but also in this case no lasers with electrical injection schemes have been demonstrated so far. An electrically injected photonic crystal laser on InP shows record low energy efficiency, but in this case the heterogeneous integration with silicon does not seem trivial.

Thus far, the only electrically injected micro lasers on silicon are based on microdisk cavities. Therefore, we will here focus on microdisk laser structures and build further upon the work performed in the framework of the EU FP6 project PICMOS.

3.2 Semiconductor laser theory

Electro-optic components such as lasers and detectors convert electrical current into light or vice versa. This requires materials that can manipulate both light and electric current; the so called semiconductor materials. The interaction between light and electrons results from the transition of an electron between the valence band and conduction band in the semiconductor material. When the system is in thermal equilibrium, most electrons are located in the valence band. An incoming photon can be absorbed by an electron in the valence band, which is thereby excited to the conduction band and results in the generation of an electron-hole pair. Another possibility, though less likely under thermal equilibrium, is that an incoming photon stimulates the recombination of an electron in the conduction band with a hole in the valence band. This recombination results in an identical photon which has exactly the same wavelength and phase as the incoming photon and thus the amplitude of the monochromatic wave is doubled. Repetition of this process results in strong amplification. This stimulated recombination by an incoming photon is, next to optical feedback, one of the key physical aspects of lasing. The absorption and stimulated recombination are two competing processes. When more electrons are present at the conduction band level then at the valence band level, stimulated emission will dominate. This situation is known as population inversion and is a first requirement for lasing. In semiconductors it can be reached by adding either optical or electrical energy to the system.

As discussed in Chapter 2, a microdisk cavity is used here to provide optical feedback. The photon round trip gain is then given by

$$G_{rt} = (1 - C)e^{(\Gamma g - \alpha)2\pi R} = e^{(\Gamma g - \alpha - \alpha_c)2\pi R} \tag{3.1}$$

where C is the power coupling from the microdisk to the waveguide, g the material optical gain, R the radius of the microdisk, Γ the optical confinement factor of the optical mode within the gain region and α the optical loss. The coupling losses can also be written as a distributed loss denoted as α_c in the equation above and equals

$$\alpha_c = \frac{1}{2\pi R} ln(\frac{1}{1 - C}). \tag{3.2}$$

The material optical gain is proportional to the stimulated emission and thus rises with increasing concentration of electrons and holes. When the modal gain Γg compensates all the losses including the coupling loss, the round trip gain is unity and lasing threshold is reached.

3.2.1 Laser rate equations

Not all injected carriers will result in stimulated recombination and generate photons. Other carrier recombination effects need to be taken into account and also optical losses have an impact on the laser behavior. A widely used method to describe the interplay between carriers and photons is to make use of laser rate equations. The equations can be used to model both the static and dynamic behavior of laser.

The spatially dependent rate equations can be written as

$$\begin{aligned}\frac{\partial N(\mathbf{r},t)}{\partial t} =& \frac{\eta_i j(\mathbf{r},t)}{q t_a} - AN(\mathbf{r},t) - BN^2(\mathbf{r},t) - CN^3(\mathbf{r},t) \\ & - v_g \sum_m G_m(N,S_m)S_m \end{aligned} \tag{3.3}$$

$$\frac{\partial S_m(\mathbf{r},t)}{\partial t} = \left(\Gamma_m v_g G_m(N,S_m) - \frac{1}{\tau_{ph,m}}\right) S_m + \beta m \Gamma_m B N^2(\mathbf{r},t), \tag{3.4}$$

where N represents the carrier density and S_m the photon density for mode m. The first term in Equation 3.3 represents the injection of carriers in the active region. Here η_i gives the fraction of terminal current that generates carriers in the active region and therefore accounts for carrier leakage effects. $j(\mathbf{r},t)$ is the current density, q the elementary charge and t_a the thickness of the active region.

The next term AN accounts for non-radiative recombination of carriers through defect and surface states. These recombination effects involve single carriers and are thus linearly dependent on N. Recombination through defects is known as Shockley-Read-Hall (SRH) recombination and is often modeled through SRH lifetimes, which can be different for electrons and holes. Typical values are in the nanosecond to microsecond range. At the semiconductor surfaces dangling bonds are present due to the abrupt termination of the lattice. Such dangling bonds occur in very high densities and form a miniband within the bandgap region of the semiconductor material. Surface recombination tends to be more of a problem when the surface to volume ratio is large, i.e. when device dimensions are decreased. Surface recombination only occurs at the interfaces and therefore instead of a carrier lifetime, a capture rate of carriers located within a certain capture length of the surface is defined. Thus, the surface recombination parameter v_s has dimensions of velocity. Surface recombination is often stronger in short-wavelength material systems compared to long-wavelength material systems. Typical values for InGaAsP are in the order of 1e4 cm/s or lower.

When an electron spontaneously recombines with a hole, a photon can be emitted. This process is known as spontaneous radiative recombination and is represented by the third term in Equation 3.3. It has a quadratic dependence on N as

the process involves two carriers. B depends on the used materials and is typically in the order of 1e-10 cm^3/s for InGaAsP based materials. In device simulations a representative value for B is often used for less important semiconductor layers of the device, while in the active region the spontaneous emission spectrum is calculated self-consistently from the band parameters, the Fermi distribution and the bound state energies in the case of quantum well structures.

The term CN^3 accounts for Auger recombination. In this process 3 carriers are involved and thus there is a cubic dependence on N. Different types of Auger recombination exist, but basically it is a collision between two electrons of which one electron recombines with a hole in the valence band, while the other electron is excited to a higher energy state in the conduction band and eventually loses its energy by emitting phonons. A similar process exists for holes in the valence band. In practice C is experimentally obtained by polynomial fits to carrier lifetime measurements. In device simulations a model is often used that can distinguish between Auger recombination effects caused by electrons or holes and can be written as

$$R_{aug} = (C_n n + C_p p)(np - n_0 p_0). \tag{3.5}$$

It is known that this model slightly overestimates the Auger recombination in case of degenerate carrier densities ($\geq 10^{18} cm^{-3}$) [22]. The Auger coefficients are also temperature dependent and this is often modeled as

$$C(T) = C_0 exp(-\frac{E_a}{k_B T}), \tag{3.6}$$

where E_a is the activation energy, which is 64 meV for long wavelength materials. Typical values for C are in the range of 1e-29 - 1e-28 cm^6/s for long wavelength materials at room temperature.

The last term accounts for the stimulated recombination of carriers. Here v_g is the group velocity, $G_m(N, S_m)$ the material gain and S_m the photon density of cavity mode m. A more detailed description of the gain parameter will be given later in this chapter.

Equation 3.4 describes the evolution of photon density for a particular mode within the active region. The first term describes the modal gain for cavity mode m. Here Γ_m is the confinement factor of the optical mode within the active region and $G_m(N, S_m)$ the material gain. The second term describes the photon losses through the photon lifetime parameter $\tau_{p,m}$. The last term accounts for spontaneous emission that is coupled into cavity mode m. Here β_m is the spontaneous emission factor giving the fraction of spontaneous emission that is coupled into cavity mode m.

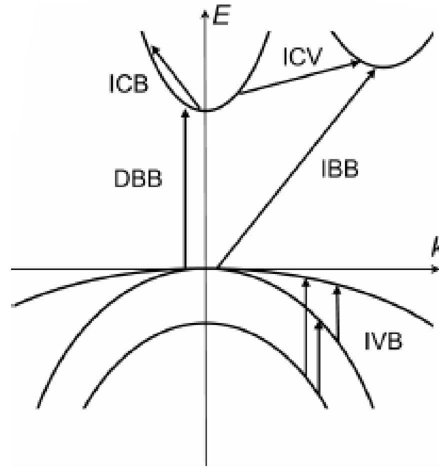

Figure 3.1: Different absorption processes within the energy bands. DBB = direct band-to-band absorption, IVB = intervalence band absorption, IBB = indirect band-to-band absorption, ICB = intraconduction band absorption and ICV = interconduction valley absorption. [23]

3.2.2 Internal optical loss

In the previous chapter we discussed several important loss mechanisms in microdisk cavities and optimized the geometry of the microdisk structure to reduce the optical loss where possible. However, one more loss mechanism needs to be taken into account: loss due to free carrier absorption (FCA). We already briefly touched upon the principle of direct band-to-band absorption (DBBA), where an incoming photon is absorbed by an electron in the valence band, which is then excited to the conduction band. DBBA is typically the strongest absorption effect in semiconductors, but obviously it can only occur if the energy of the photon is larger than the bandgap. If the energy of the photon is lower, FCA will dominate. FCA can be caused by several transitions which are indicated in Figure 3.1. The intervalence band transitions are the most important when using III-V materials in the 1.3-1.6 μm range, because the energy separation between the different valence bands is lower or matches these wavelengths.

Obviously, FCA depends on the carrier concentration and in general a linear dependence is assumed

$$\alpha_i = k_n n + k_p p. \tag{3.7}$$

For bulk InGaAsP typical values at 1.55 μm are $1 \times 10^{-18} cm^2$ for k_n and $20 - 60 \times 10^{-18} cm^2$ for k_p. For quantum well structures it is difficult to measure

this parameter accurately and also the impact of strain is unclear, resulting in a wide range of values for k_p. Often it is assumed that k_p decreases with compressive strain. However, because of the uncertainty this parameter should be used as a fitting parameter in device simulations.

3.2.3 Optical gain

Optical gain describes the ratio between stimulated emission and direct band-to-band absorption and can be written as

$$g_{ij}(h\nu) = \left(\frac{q^2 h}{2m_0^2 \epsilon_0 n_r c}\right) \frac{1}{h\nu} \left|M(E_{ij})\right|^2 \rho_r(E_{ij})(f_j - f_i). \tag{3.8}$$

As discussed above, population inversion is required for stimulated emission to become stronger than band-to-band absorption and this is described by the last part of the equation $(f_j - f_i)$ also known as the Fermi factor. Here f_j and f_i are the Fermi functions and give the probability that the energy level E_j in the conduction band and E_i in the valence band are occupied by an electron. Maximum population inversion and thus maximum gain is obtained when $f_j = 1$ and f_i=0.

Next to the probability of finding an electron in the valence or conduction band, the actual concentration of electrons depends on the available electron states in the bands. In bulk material it is often justified to treat the electrons as free particles such that their energy can be approximated by a parabolic function in k-space. In this case the reduced density of states can be written as

$$\rho_r^{3D}(E) = \frac{1}{2\pi^2} \left(\frac{2m_r}{\hbar^2}\right)^{3/2} \sqrt{E - E_g}, \tag{3.9}$$

where m_r represents a reduced mass depending on the electron and hole effective masses.

The transition strength between two states is determined by the transition matrix element $\left|M(E_{ij})\right|^2$ and depends on the wavefunctions that describe these two electron states. In case of quantum wells it gives the allowed and forbidden transitions between subbands. In principle the transition strength depends on the angle between the electron wave vector and the polarization of the electric field of the optical mode. However, in bulk materials a large variety of k-vectors exist and results in an isotropic transition matrix element. This bulk momentum matrix element M_b^2 is a constant for a given material. This does not hold for quantum wells as we will see below.

Quantum wells

In a quantum well carriers are confined in a very thin region. The well thickness is in the order of the de Broglie wavelength of the carriers and this quantum confine-

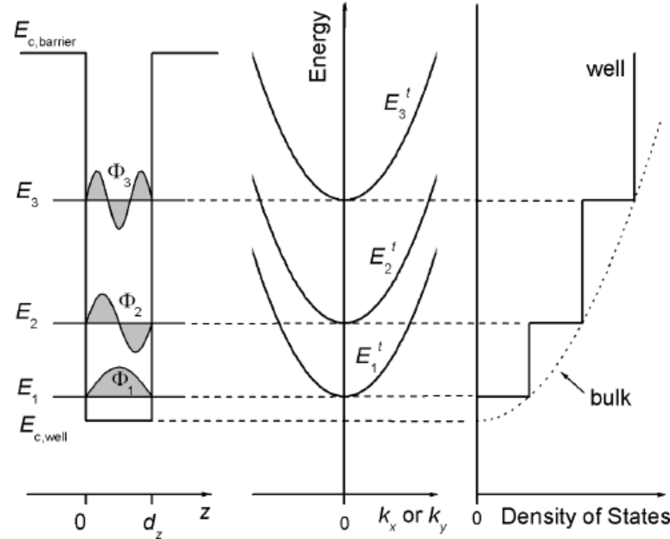

Figure 3.2: Schematic showing the discrete energy levels in quantum well structures, the in-plane energy dispersion and the difference between the 2D and 3D density of states in quantum wells and bulk, respectively. [23]

ment makes that carriers can only have discrete energy levels, or subbands, in the direction perpendicular to the potential well. This has strong implications for both the reduced DOS and the transition matrix element.

Because of the discrete subbands, the reduced DOS now contains a summation over all possible subbands pairs. That is, allowed subband pairs that have the same quantum number. The 2D reduced DOS can be written as

$$\rho_r^{2D}(E) = \frac{1}{d_z} \sum_{n_z} \frac{m_r}{\pi\hbar^2} H(E - E_{n_z}), \tag{3.10}$$

where d_z is the thickness of the quantum well, n_z is the quantum number and H is the Heaviside unit step function. The difference between the reduced DOS for bulk and quantum wells is shown in Figure 3.2. Because of the staircase like shape of the 2D DOS, the number of states to be filled for a certain energy level is lower.

If we distinguish between TE and TM optical modes, then either the electric field or the magnetic field lies within the plane of the quantum well. Because the transition matrix element depends on the angle between the electron wave vector and the polarization of the electric field of the optical mode, the transition matrix element becomes anisotropic. These transition strengths are also different for heavy and light holes, where heavy holes favor TE polarized light, while light

holes favor TM polarized light.

Strain can be applied to a quantum well by deliberately changing its material composition such that it has a slightly different lattice constant compared to the substrate. This strain can either be compressive or tensile. Under the influence of strain two things tend to happen, the bandgap changes and the energy bands become non-parabolic. Under compressive strain the bandgap tends to increase while it decreases for tensile strain. At the same time the degeneracy of the light and heavy holes is lifted at the Γ point, where the heavy hole band is lifted above the light hole band in case of compressive strain, while it is the other way around for tensile strain. Because the transition between the conduction band and heavy hole band favors TE polarization, TE gain is enhanced under compressive strain.

Next to the change of the bandgap, also the energy dispersion of the valence bands is affected. The curvature of the bands increases whereby the effective mass of the light and heavy holes is reduced.

Linewidth broadening

Until now, we have assumed distinct energy levels for the electrons in the conduction and valence bands. However, because of the interaction of electrons and holes with other carriers and phonons, their energy slightly changes within the bands. These scatter events result in an uncertainty of the electron energy. To account for this, a linewidth broadening function can be included into the gain formula

$$g(h\nu) = \int dE_{ij} g_{ij}(E_{ij}) L(h\nu - E_{ij}). \tag{3.11}$$

The gain spectrum is smoothened by this lineshape broadening and this becomes especially apparent in gain spectra of structures with high quantum confinement that theoretically show sharp peaks. The peak gain also becomes lower. In most cases a Lorentzian lineshape function is used, which is written as

$$L(h\nu - E_{ij}) = \frac{1}{\pi} \frac{\Gamma_0}{(h\nu - E_{ij})^2 + \Gamma_0^2}. \tag{3.12}$$

A typical value for the linewidth broadening factor Γ_0 is 6.5 meV.

3.3 Structure of the microdisk laser

The geometrical design of the microdisk laser was presented in Chapter 2. For the simulations discussed in Chapter 2 a uniform III-V structure was assumed, which was sufficient for an assessment of the optical losses and the coupling efficiency. Here, the goal is to get a better understanding of the electro-optic properties of the microdisk laser and how it can be optimized. Therefore, a more detailed laser structure is required that takes into account the epitaxial layers of the microdisk

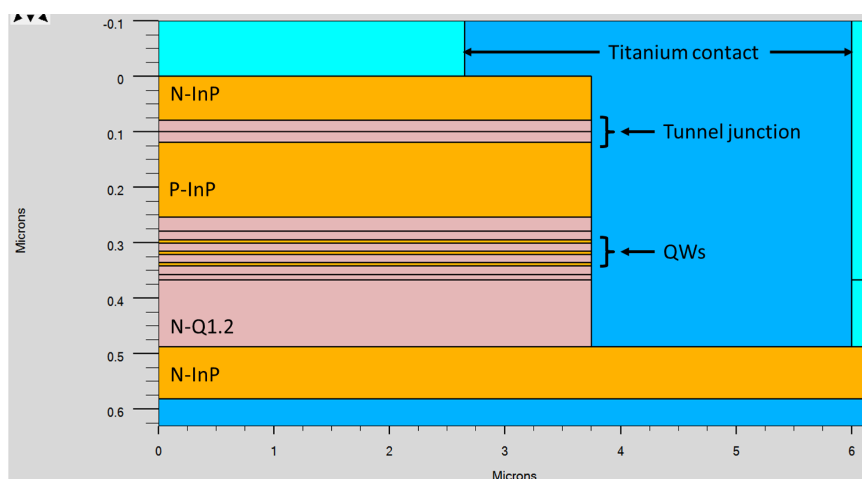

Figure 3.3: Detailed layer structure used for the microdisk laser.

laser. The cross-section of the microdisk laser including the layer structure is shown in Figure 3.3.

At the heart of the microdisk laser lies a multiple quantum well (MQW) structure. This active region consists of 3 compressively strained InAsP quantum wells with a thickness of 6 nm which are separated by InGaAsP (1.2 μm) barrier layers with a thickness of 15 nm. At the p-doped side of the stack a tunnel junction is included to avoid the need for small bandgap materials for achieving ohmic contacts at the p-side. The tunnel junction will be explained in more detail in Section 3.4.4. The active region itself is sandwiched between InGaAsP (1.2 μm) separate confinement layers (SCL) to confine the optical mode to the active region. These SCL layers are asymmetric around the active region such that the overlap with the underlying waveguide is large to have efficient coupling, while the overlap with the tunnel junction is minimized to reduce optical losses. The confinement of the optical mode within the active region is 6.7% and the confinement within the p-doped layer of the tunnel junction is 2.3%. The lower part of the bottom SCL layer is n-doped and forms, together with a p-doped InP layer above the top SCL layer, the laser p-i-n structure. An n-doped InP layer at the bottom is used as interface layer to achieve an ohmic metal contact. Ohmic contacts to p-InP are difficult to obtain because of the higher barrier height. Often low bandgap semiconductors, such as e.g. InAs or InGaAs, are used as intermediate layers to make ohmic contacts at the p-side. However, these layers cause strong optical absorption and because the total film thickness is low for the device discussed here the optical loss would be too high. Therefore, a tunnel junction is used instead which consists of two 20 nm thin layers of InGaAsP (1.3 μm) of which one is heavily p-doped and the other heavily

Layer	*Composition*	*Doping* cm^{-3}	*Refr. index*	*e mobility* cm^2/Vs	*h mobility* cm^2/Vs
Laser N	InP	N+ 5×10^{18}	3.17	1400	40
Tunnel junction	$In_{0.7}Ga_{0.3}As_{0.65}P_{0.35}$	N++ 1×10^{19}	3.4	700	35
Tunnel junction	$In_{0.7}Ga_{0.3}As_{0.65}P_{0.35}$	P++ 2×10^{19}	3.43	550	25
Laser diode P	InP	P+ 1×10^{18}	3.17	2200	75
SCH	$In_{0.8}Ga_{0.2}As_{0.44}P_{0.56}$	nid	3.32	5200	100
3x barrier	$In_{0.8}Ga_{0.2}As_{0.44}P_{0.56}$	nid	3.32	5200	100
3x QW	$InAs_{0.65}P_{0.35}$	nid	3.41	7000	160
SCH	$In_{0.8}Ga_{0.2}As_{0.44}P_{0.56}$	nid	3.32	5200	100
SCH Laser diode N	$In_{0.8}Ga_{0.2}As_{0.44}P_{0.56}$	N+ 1×10^{18}	3.32	1400	50
Laser N contact	InP	N+ 5×10^{18}	3.17	1400	40

Table 3.1: Parameters of the microdisk laser materials used in the simulation.

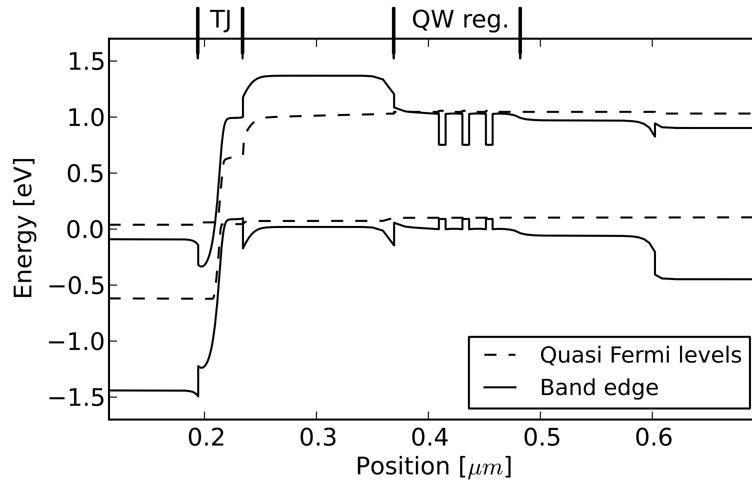

Figure 3.4: Banddiagram of the microdisk laser around threshold. The solid lines represent the conduction and valence band edges and the dashed lines the quasi-Fermi levels. The position of the tunnel junction is indicated by 'TJ' and the laser quantum well region by 'QW reg.'

n-doped. This allows electrons to tunnel from the valence band to the conduction band through which electron-hole pairs are created. On top of the tunnel junction again an n-doped layer can be used to make an ohmic contact with the metal for which an n-doped InP layer is used here. This material stack was developed in the framework of the EU FP7 project WADIMOS by our project partners from INL.

In the next sections we will analyze the electro-optic behavior of the microdisk laser for which we use the semiconductor device simulation software Atlas from Silvaco. Important material parameters used in the simulation are given in Table 3.1 and the banddiagram of the microdisk laser stack is shown in Figure 3.4.

3.4 Electrical behavior of the microdisk laser

Running a full electro-optic laser simulation can be very time consuming. Therefore, we first performed purely electrical simulations to make sure that the IV curves are representative for real devices.

3.4.1 Current injection into the semiconductor

Obviously an important aspect when using semiconductor devices is to inject current into the device in an efficient way and this is determined by the properties at the metal-semiconductor interface. For many devices, and also for lasers, so called ohmic contacts are desired. An ohmic contact has a linear current-voltage relationship and a contact resistance that is very small compared to the bulk or spreading resistance of the semiconductor.

Different mechanisms can govern the current flow at metal-semiconductor interfaces, but the most important one when using heavily doped semiconductors is field emission. In this case the depletion region is very narrow and electrons can tunnel from the metal to the semiconductor. Ideally the contact resistance is determined by the barrier height which depends on the difference in the work function of the metal and the semiconductor. In reality, a large number of surface states exist at the semiconductor interface and the Fermi level is pinned. In this case the barrier height does no longer depend on the metal work function, but depends on the bandgap and the surface state density. Surface treatment prior to metal deposition is therefore very important to achieve low-resistance ohmic contacts. The Fermi level pinning is also said to be dependent on the chemical reaction between the metal and the semiconductor.

Titanium based contacts are often used to achieve ohmic contacts with III-V materials and can be used for both n- and p-type contacts. Reported values for Ti/Pt/Au contacts are 8e-6 Ωcm^2 for 1e18 n-doped InP and 6e-7 Ωcm^2 for 5e18 p-doped InGaAs after annealing for 30s at 450 $^\circ C$ [24]. The annealing procedure can have a large influence and reduce the contact resistance by two orders of magnitude compared to the as-deposited values. The platinum layer acts as a diffusion barrier for the gold, because gold-InP intermixing can be very strong and result in short circuits after annealing. For the simulations we assume a contact resistance between 1e-4 and 1e-6, which is representative for the contact resistance typically obtained in the clean room of Ghent University.

3.4.2 Carrier transport

Carriers need to be injected into the active region of the laser in order to achieve population inversion. When simulating a laser, it is therefore of prime importance to have a realistic model of the transport of carriers. Electrical current flow in

semiconductors is mainly dominated by drift and diffusion of electrons and holes. The so-called drift-diffusion model is therefore the most widely used model for simulating charge transport for these type of devices and will also be used here.

Drift-diffusion

The basic set of equations that need to be solved are the poisson equation and the carrier continuity equations. The poisson equation relates the electrostatic potential to the space charge density and reads

$$\nabla \cdot (\epsilon \nabla \psi) = -\rho \tag{3.13}$$

where ψ is the electrostatic potential, ϵ is the dielectric permittivity and ρ is the local space charge density, which includes the sum of all mobile and fixed charges.

If there is a change in local carrier concentration over time it has to be accompanied by a change in current flow or by the generation or recombination of electron-hole pairs. This is described by the the continuity equations which can be written as

$$\frac{\partial n}{\partial t} = \frac{1}{q} \nabla \cdot \mathbf{J_n} + G_n - R_n \tag{3.14}$$

$$\frac{\partial p}{\partial t} = \frac{1}{q} \nabla \cdot \mathbf{J_p} + G_p - R_p \tag{3.15}$$

where $\mathbf{J_n}$ and $\mathbf{J_p}$ denote the electron and hole current densities, G_n and G_p the generation rates and R_n and R_p the recombination rates.

In the drift-diffusion model it is assumed that the total current densities can be completely determined by a drift current due to the presence of an electric field and a diffusion current that depends on the concentration gradient of electrons and holes. The total current density of electrons and holes can then be written as

$$\mathbf{j_n} = q\mu_n n\mathbf{F} + qD_n \nabla n \tag{3.16}$$

$$\mathbf{j_p} = q\mu_p p\mathbf{F} + qD_p \nabla p. \tag{3.17}$$

where μ_n and μ_p are the electron and hole mobilities and D_n and D_p the diffusion coefficients. Both the mobility parameters and the diffusion coefficients are important paramaters for realistic current flow modeling. The mobility parameters depend on material, doping and temperature and will be discussed in more detail further on. The diffusion coefficients are calculated through Boltzmann statistics or Fermi-Dirac statistics in case of highly doped materials.

Carrier transport across heterojunctions

Different materials are used in the microdisk laser stack to confine both carriers and the optical mode. As a result several heterojunctions appear in the stack. An important heterojunction parameter is the conduction band offset ΔE_c which determines how the bands of different semiconductor materials line up. In literature this is value is commonly given as a fraction of the difference in bandgap of two adjacent materials. Current flow across a heterojunction can be limited by drift-diffusion or by thermionic emission, which describes the heat induced flow of charge carriers over a potential energy barrier. The dominant transport mechanism at heterobarriers depends on the barrier height and the thermal energy given of the carriers. It can therefore be important to also include thermionic emission effects when simulating heterojunctions, especially when simulations at elevated temperatures are required.

As the lattice temperature increases, thermionic emission will have a larger impact and will result in an increased vertical leakage current. Electrons have mobilities that are significantly larger then hole mobilities. Electrons can therefore move more easily across the quantum well regions. To confine the electrons in the active region the conduction band offset should be large, to avoid electron overflow. The conduction band offset of InGaAsP/InP heterostructures is typically around 0.4ΔE_g and this rather low conduction band offset limits the performance of this material system. Here we use InAsP quantum wells with InGaAsP barrier layers of which it is reported in literature that it has a conduction band offset in the order of 0.5-0.6ΔE_g [25, 26]. This higher conduction band offset should result in lower threshold currents and better performance at higher temperatures.

3.4.3 Carrier mobility

The conductivity of electrons $\sigma_n = q\mu_n n$ and holes $\sigma_p = q\mu_p p$ is obviously not the same for every material and depends on the carrier mobility. Collisions of electrons and holes with e.g. other carriers and crystal defects limit this carrier mobility. As a result the mobilities are functions of the electric field, lattice temperature and doping concentrations. Mobility modeling is often divided in low-field and high-field behavior. The low-field mobility depends upon doping concentrations and lattice temperature and as long as the electric field is low enough, this model is sufficient. In this case, the current density is proportional to the electric field. At high electric fields, the carriers gain energy and can take part in a wider range of scattering processes. As a result the mean drift velocity of carriers will increase more slowly and eventually saturates at a constant velocity.

In practical device simulation, empirical models that are fitted to experiments are often used. A large amount of data is available for silicon and germanium, while for III-V compounds fewer data is available. The standard models available

in most device simulation tools are optimized for silicon and germanium. However, Sotoodeh et al. have developed a general low-field mobility model for III-V compounds in combination with fitting parameters based on published data [27] which takes into account both lattice temperature and doping concentrations. In the work presented here, we rely on the model and material parameters given in [27].

In this model the low-field mobility is expressed as

$$\mu(N,T) = \mu_{min} + \frac{\mu_{max}(300K)(300K/T)^{\theta_1} - \mu_{min})}{1 + \left(\frac{N}{N_{ref}(300K)(T/300K)^{\theta_2}}\right)^{\lambda}}, \quad (3.18)$$

with $\mu_{min}, \mu_{max}(300K), N_{ref}(300K), \lambda, \theta_1 and \theta_2$ as fitting parameters that are all functions of material composition.

For ternary and quaternary materials, the simplest possible interpolation schemes are used that fit the data and are also given in [27] for some important materials. For the fitting parameters of InAsP we used the interpolation schemes of InGaAsP with the x-composition set to zero. The mobility parameters for electrons and holes obtained using this model for the structure used here are given in Table 3.1.

High-field mobility effects are modeled using one of the standard models available in Silvaco Atlas and can be expressed as

$$\mu(F) = \frac{\mu_{low}}{\sqrt[\beta]{1 + (\mu_{low}F/v_s)^{\beta}}}, \quad (3.19)$$

where μ_{low} is the low-field mobility obtained using the model described above, v_s the saturation velocity and β as fitting parameter. The saturation velocity is a material parameter and can be different for electrons and holes. A very limited amount of data is available for InGaAsP and InAsP and therefore a constant saturation velocity of 9 $10^6 cm/s$ is assumed for these materials. For InP a value of 7 $10^6 cm/s$ is used.

3.4.4 Tunnel junction

Achieving ohmic contacts on p-type InP is difficult because of the high barrier height. Therefore, typically low bandgap heavily p-doped layers are used as interface layer between the p-InP layer and the metal. However, because of this low bandgap, direct band-to-band absorption can have a significant impact on device performance. Overlap of the optical mode with this layer should thus be minimized or preferably avoided. In a thin film structure as used here in the microdisk laser, this is very difficult. In [20] the use of a tunnel junction was suggested and used to avoid this band-to-band absorption.

In a tunnel junction under reverse bias electrons can tunnel from the valence band to the conduction band. This way holes are created while an n-type instead of a p-type contact layer to the metal can be used. In order to have a finite probability

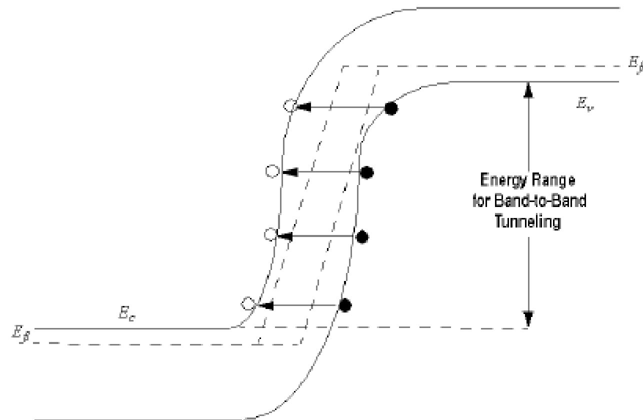

Figure 3.5: Schematic of the banddiagram of a tunnel junction in reverse bias, showing large band bending enabling band-to-band tunneling.

for the tunneling process to occur the depletion region has to be very small. A tunnel junction therefore consists of a degenerately doped p-n junction, where the Fermi levels penetrate into the bands. If the electric field over the junction is sufficiently high, strong local bending of the bands will occur as is shown in Figure 3.5. As can be seen there is now a region where the valence and conduction band energies are equal and electrons can tunnel to the conduction band. This region can also be identified in the banddiagram of the microdisk laser as displayed in Figure 3.4.

The tunnel junction can be made of material with a large bandgap, such that direct band-to-band absorption can be avoided. However, because of the high doping levels required for the tunnel junction there will still be strong intervalence band absorption and thus the overlap of the optical mode with the p-doped layer of the tunnel junction should be minimized.

3.4.5 2D axi-symmetric simulation of electrical behavior

Based on the models and device structure discussed above, we will now analyze the electrical behavior of the microdisk laser. Before analyzing the electrical behavior of the complete laser diode the tunnel junction is tested separately to confirm correct tunneling behavior. In this simulation we only consider the heavily doped InGaAsP layers that form the tunnel junction. Ideal electrodes are placed at the top and the bottom of the InGaAsP layers. A voltage is applied to the anode contact and the resulting IV curve is shown in Figure 3.6.

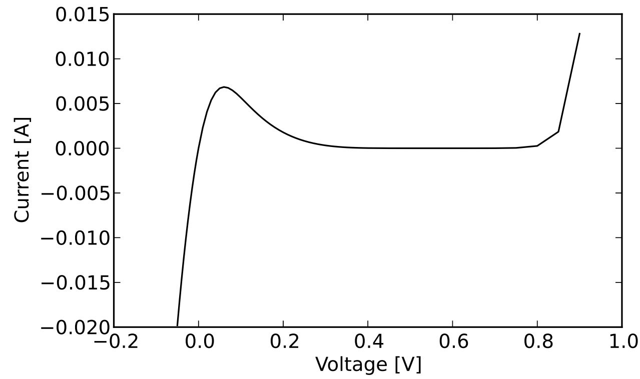

Figure 3.6: Simulated IV curve of the tunnel junction under reverse and forward bias.

It can be seen that the expected tunneling behavior is obtained. At forward bias we first find a steep increase in current flow, while around a voltage of 0.06 a maximum current of 7 mA is obtained. After this point the tunneling current decreases resulting in a region with negative resistance. By increasing the voltage further a normal diode is formed, which is evident by the large increase of current. When a reverse bias is applied, which is the desired operating regime for the microdisk laser, immediately a large current is flowing showing that indeed a relatively low resistance is obtained.

As we cannot directly measure the tunnel junction behavior in fabricated devices, we will now incorporate this tunnel junction model into the model for the complete microdisk laser diode which can then be fitted to measurement results.

In the following we analyze the current-voltage behavior of the microdisk laser, where we perform parameter sweeps that are expected to have an influence on this behavior. Note that if the total microdisk laser structure is under forward bias, the tunnel junction is under reverse bias. Let us first consider the influence of the p-type doping level in the tunnel junction on the laser diode. The doping level should be as low as possible to minimize optical losses, while at the same time it should be high enough to have efficient tunneling for low series resistance. The device structure for these simulations is as illustrated in Figure 3.3. The radius of the microdisk laser is set to 3.75 μm and a cylindrical coordinate system is used with symmetry around x=0. The bottom contact layer is fixed to a thickness of 95 nm. Again ideal electrodes are used to apply a voltage over the diode. The IV curves of the laser diode for 4 different p-type doping levels are shown in Figure 3.7.

The impact of the p-type doping level on the tunnel junction performance is quite strong as was also observed in [20, 28] and the lowest resistance is obtained

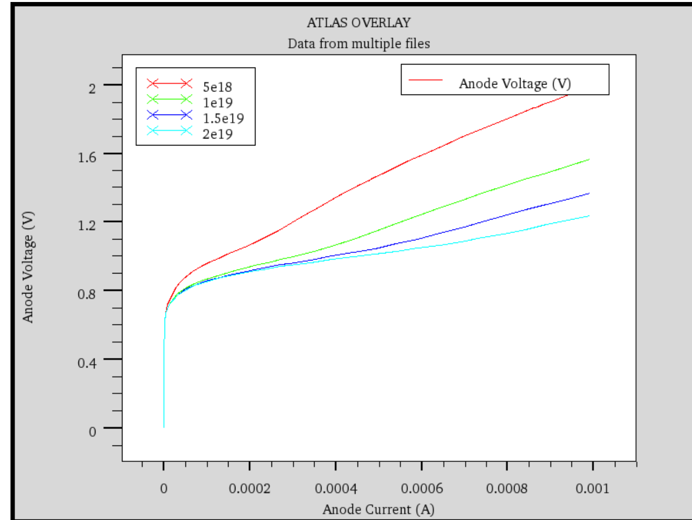

Figure 3.7: Influence of the p-type doping level in the tunnel junction on the IV curve of the microdisk laser.

for the highest doping level. The total series resistance is $110\ \Omega$ in this case, which is already significant. If the p-type doping level is reduced to $1e19$, the series resistance increases to $130\ \Omega$. For low doping levels also a clear kink in the LI curve can be observed, showing that the total IV curve of the microdisk laser is limited by the resistance of the tunnel junction.

Next, we look at the influence of the thickness of the bottom contact layer. The epitaxial structure is designed with a 95 nm bottom contact layer, but during processing it is difficult to control the etch depth as a dry etch step is required to define the circular disk structure. As a result, the bottom contact thickness will deviate from the targeted 95 nm. The effect of over etching the bottom contact on the electrical performance is found to be very small as can be seen in Figure 3.8. Even for a bottom contact layer as thin as 25 nm the IV curve hardly changes. However, it is questionable whether this will also be the case for a fabricated device. If the etching is slightly non-uniform, it might result in open circuits and making a good ohmic contact to such a thin layer might also be problematic. Nevertheless, we can conclude that slightly over etching the bottom contact layer should have no disastrous effect on the electrical performance.

The impact of contact resistance is shown in Figure 3.9. Here the contact resistance is assumed to be the same for the top and bottom contact and the p-type doping level is set to $2 \times 10^{19} cm^3$. Furthermore, it is also assumed that the contact is ohmic. In order for the contact resistance to be negligible with respect to the resistance of the semiconductor stack, it should be smaller than $10^{-5}\Omega cm^2$.

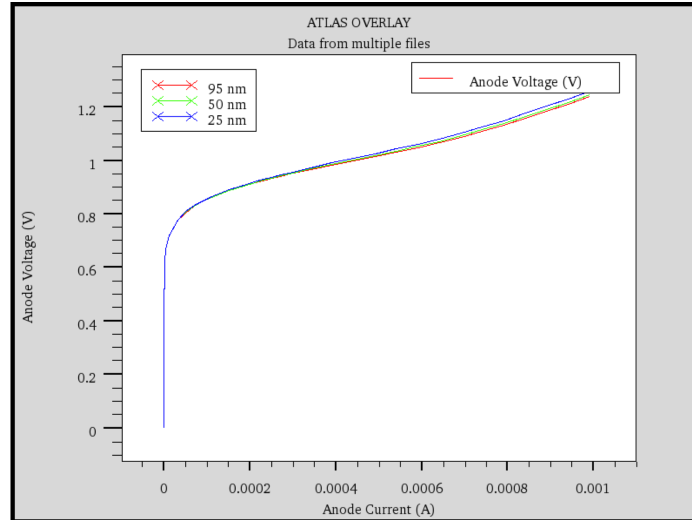

Figure 3.8: Influence of the thickness of the bottom contact slab on the IV curve of the microdisk laser.

It is also clear that the total series resistance increases rapidly for higher contact resistances which is due to the small contact areas.

3.5 Full laser simulation

Now that we have a model for the electrical behavior of the microdisk laser, we can move on to the full laser simulation. As we are considering quantum wells that are compressively strained, we can no longer assume that the energy bands are parabolic within the plane of the quantum well. Therefore, the effective mass approximation assuming parabolic energy bands can no longer be used to calculate the gain. In order to calculate the correct energy dispersion in these cases the $k \cdot \mathbf{p}$ method is often used [23, 29]. Here we will also rely on this model which has been implemented in Silvaco Atlas on our request.

3.5.1 Bandgap

In order to have gain in the correct wavelength region, we need to make sure that the bandgap of the InAsP active region is correct. For modeling material parameters of ternary and quaternary alloys often interpolation schemes based on known values of binary materials are used. In most cases linear interpolation schemes are sufficient, but in some cases an empirical bowing parameter needs to be included. In case of bandgap calculations strong bowing is often observed. In [30] it

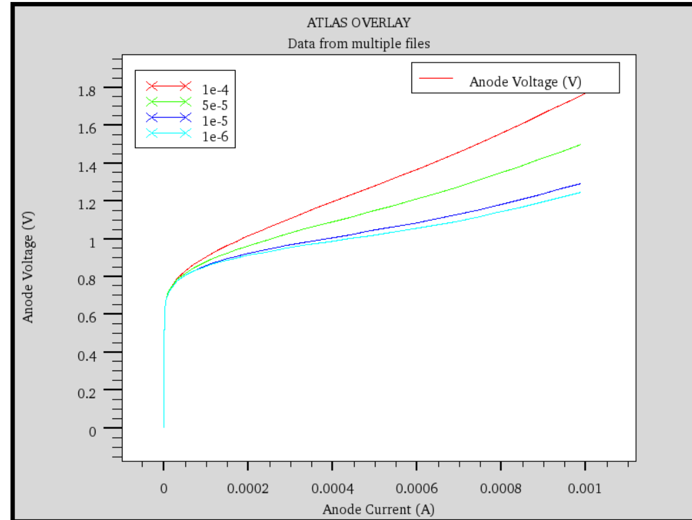

Figure 3.9: Influence of the contact resistance on the IV curve of the microdisk laser.

is reported that for InAsP a bowing parameter of 0.1 eV gives the best fit to experimental results. For the composition used here (x=0.65), this yields an unstrained bandgap of 0.678 eV at 300 K for bulk layers. In quantum wells the discrete subbands need to be taken into account to find the lowest possible transition energy. Furthermore, under the influence of compressive strain the bandgap will increase and also the degeneracy of the heavy- and light-hole band will be lifted. The barrier layers in the material stack are lattice matched to InP. By comparing the lattice constant of InP with that of InAsP with x=0.65, we find a compressive strain of 2.1%.

The energy dispersion of the valence subbands is calculated using the two-band $k \cdot \mathbf{p}$ model. The conduction subbands are still assumed to be parabolic. The lowest allowed transition is now between the first conduction subband and the first heavy-hole subband (C1-HH1) with an energy of 0.778 eV at the Γ point.

The spontaneous emission spectrum is calculated self-consistently from the Fermi distributions, the reduced DOS and the transition matrix element. In order to verify if the model is representative, a comparison with the obtained spectrum of a photoluminescence (PL) measurement should be made. In Figure 3.10 both the simulated as well as the experimentally obtained spontaneous emission spectrum are shown. The measured PL spectrum has a global peak at 1532 nm and another peak at 1630 nm. This last peak is caused by an InGaAs sacrificial layer that protects the epitaxial structure and is normally removed before processing. The global peak is from spontaneous emission from the active region of the laser stack. The peak of the simulated spontaneous emission spectrum lies at 1535 nm and thus

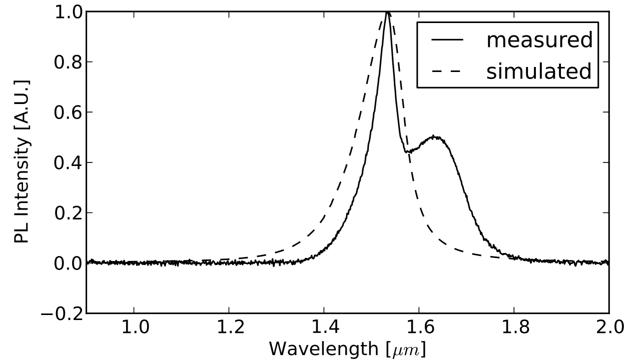

Figure 3.10: Measured and simulated PL spectrum of the epitaxial structure of the microdisk laser.

differs by only 3 nm from the measured peak. This corresponds to a difference less than 2 meV and can be explained by small differences in the material composition or the quantum well width. Taken this shift into account, it can be seen that at longer wavelengths there is a good match between the simulated and measured spectrum. At shorter wavelengths however, the simulated spectrum is broader than the measured spectrum indicating that the transitions away from the Γ point and between higher subbands are overestimated in the simulation.

The bandgap is also temperature dependent and decreases with increasing temperature. This is modeled using the Varshni approximation which is a standard model in Silvaco Atlas and can be written as

$$E_g(T) = E_g(0) - \frac{\alpha T^2}{\beta + T}, \tag{3.20}$$

where α and β are fitting parameters. We here used a linear interpolation scheme to determine these values for InAsP based on data from [23]. In order to obtain more accurate data on the bandgap shrinkage due to increasing temperature, one could measure the spontaneous emission spectrum versus temperature, which will reveal the red-shift of the spectrum.

3.5.2 Gain spectrum

Now the simulated spontaneous emission spectrum is found to be in reasonable agreement with the measured spontaneous emission spectrum, we can evaluate the gain spectrum. Lorentzian gain broadening is included to account for the uncertainty of the electron energy due to scatter events. A Lorentzian linewidth Γ_s of

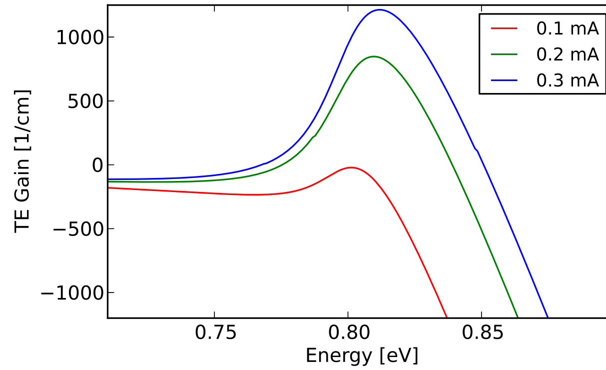

Figure 3.11: Simulated gain spectrum for different injection levels.

6.6 meV is used. The gain spectrum for different pumping levels is shown in Figure 3.11. At a drive current just above 0.1 mA the gain becomes positive and we find a transparency carrier density of $2.95e18cm^{-3}$. This is a rather high value, as it is well known that under the influence of compressive strain in quantum wells the transparency carrier density is reduced and values between $1 - 2e18cm^{-3}$ are more common [22].

The influence of the lattice temperature on the gain is shown in Figure 3.12. The gain peaks at a wavelength of 1554 nm at room temperature, while at 70 $^{\circ}C$ the peak lies at 1590 nm, giving a red shift of 0.72 nm/K . Also the peak gain reduces significantly with increasing temperature and is caused by the wider spreading of the Fermi distribution of carriers [23]. As a result a higher carrier concentration is required to achieve the same amount of gain at elevated temperatures. This also leads to increased intervalence band absorption and an increase of non-radiative recombination effects through which the threshold current increases considerably. The conduction band offset at the active region will also play an important role at higher temperatures. Electrons can move more easily across the quantum wells compared to holes and therefore it is important to have a large conduction band offset to confine the electrons in the quantum wells. Due to the wider spreading of the Fermi distribution at higher temperatures carriers, and particularly electrons, can leak out of the quantum wells and the amount of this vertical carrier leakage depends strongly on the conduction band offset.

In order to have an idea of the gain spectrum in experimental devices we performed a Hakki-Paoli measurement [31]. From this measurement gain spectra can be obtained by measuring the modulation depth of the resonances in the emission spectrum. The Hakki-Paoli method was originally developed for Fabry-Perot cavities, but can also be used in ring or disk cavities provided that the diameter of the

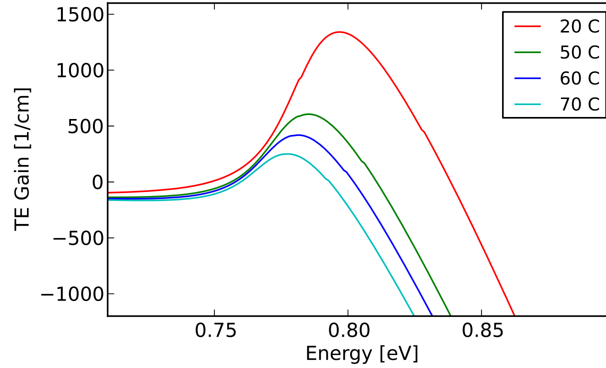

Figure 3.12: Simulated gain spectrum for different lattice temperatures.

ring or disk is within certain limits. If the radius is too small, the FSR of the modes will become too large to have sufficient data points within the gain spectrum. On the other hand, very large radii will result in small FSRs and this makes it increasingly difficult to resolve the minimum values especially when an optical spectrum analyzer (OSA) is used due to its limited resolution. However, a high resolution OSA or a spectrometer could be used to alleviate this problem.

We used a microdisk laser with a radius of 20 μm, resulting in an FSR in the order of 5 nm. the optical spectrum was measured with a Yokogawa OSA with a resolution bandwidth of 50 pm. The measured spectra at different drive currents are shown in Figure 3.13 together with the fits of the maxima and minima. The net gain can now be found through the relation

$$\Gamma G = \frac{1}{2\pi R} ln \left(\frac{\sqrt{\frac{P_{max}}{P_{min}}} + 1}{\sqrt{\frac{P_{max}}{P_{min}}} - 1} \right) + \alpha_c, \tag{3.21}$$

where α_c is the distributed coupling loss as described in Equation 3.2. Plotting these values for different injection levels, gives the result shown in Figure 3.14. The gain peaks at a wavelength between 1555 and 1560 nm, which is again in good agreement with the simulation results. From this plot also an estimation of the internal loss can be obtained, which is given by the modal gain value at longer wavelengths where the different curves saturate. This indicated in Figure 3.14 by the black arrow. Because of the large (20 μm) radius of the microdisk laser used for these measurements, it can be assumed that the scattering loss is 0. The influence of the coupling loss α_c was less than 1 cm^{-1} for this large microdisk, but was also already included by shifting the gain spectrum as described in Equation 3.21. Therefore, the loss found in Figure 3.14 can be attributed to the

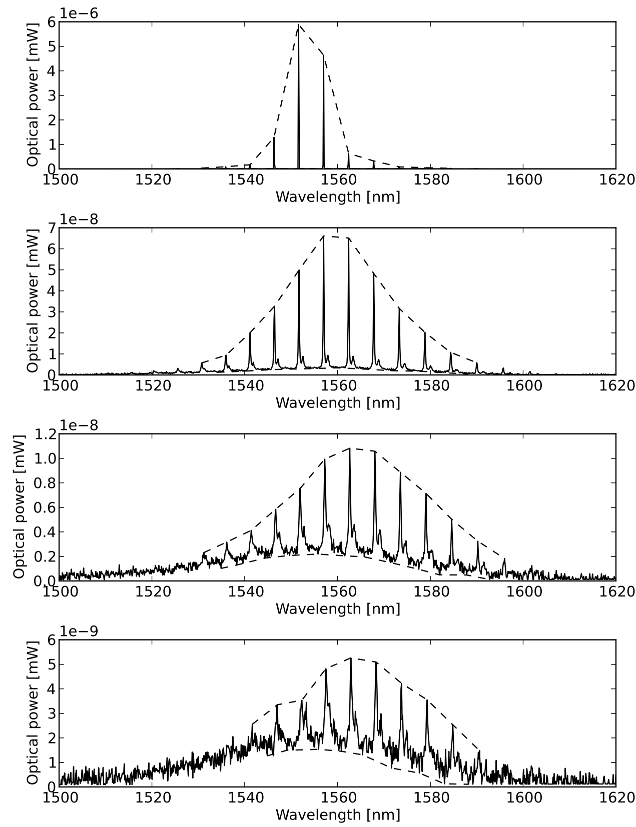

Figure 3.13: Measured spontaneous emission spectra for different drive currents.

internal loss caused by intervalence band absorption from (mainly) the quantum wells and the p-type layer of the tunnel junction. The intervalence band absorption is independent of disk diameter and therefore the value obtained here can also be used for fitting the losses in smaller microdisk cavities, where any additional loss can be attributed to scattering loss.

3.5.3 Static laser performance

With the qualitative agreement of the simulated spontaneous emission and gain spectrum with the measurements, we can continue with the evaluation of the static laser performance. As the $k \cdot \mathbf{p}$ model used here is still under development, we were not yet able to obtain an accurate fit with measurement results with respect to threshold current and slope efficiency. That is, the results from the model are in

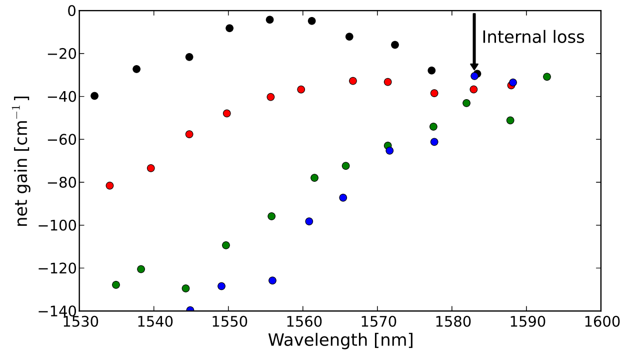

Figure 3.14: Obtained gain spectra for different drive currents from a Hakki-Paoli measurement.

the same order as experimentally obtained values, but in order to have a reliable fit one needs to be able to reproduce the results not only at room temperature but also at elevated temperatures. If only room temperature is considered, several solutions with different parameters will give similar results, while if also higher temperatures are considered a significant number of solutions can be ruled out. The simulation results obtained here, were compared with the measurements of LI curves at elevated temperatures such as in Figure 4.28, but could not yet be fitted over the whole temperature range. Nevertheless, a good understanding of the microdisk laser behavior can be obtained. Here we will first analyze the microdisk laser behavior, after which we will look at the performance of slightly modified designs.

Conduction band offset

The influence of the conduction band offset on the LI curve at room temperature is shown in Figure 3.15. The lowest threshold current is obtained for the highest conduction band offset, which is a result of the higher confinement of electrons. The influence of the conduction band offset on the slope efficiency is limited. However, at higher temperatures the slope efficiency decreases dramatically for lower conduction band offsets as can be seen in Figure 3.16 where the LI curves are plotted for the same conduction band offsets, but at 70 $^\circ C$. At this temperature the vertical leakage clearly dominates in case of a low conduction band offset. Based on these simulations we find that the conduction band offset for the microdisk laser presented here should lie around 0.5 ΔE_g, which is among the lower values in literature for this material system, but still higher than the commonly used InGaAsP/InP material system.

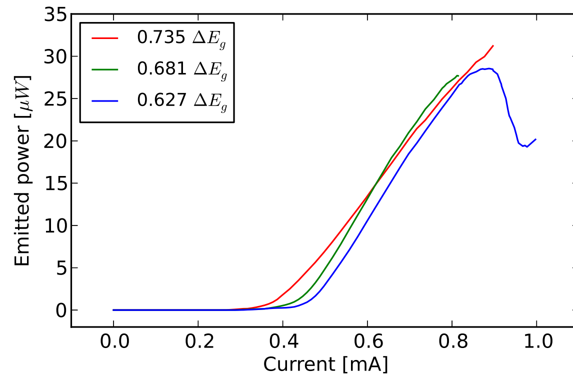

Figure 3.15: Effect of the conduction band offset on the LI curve at room temperature.

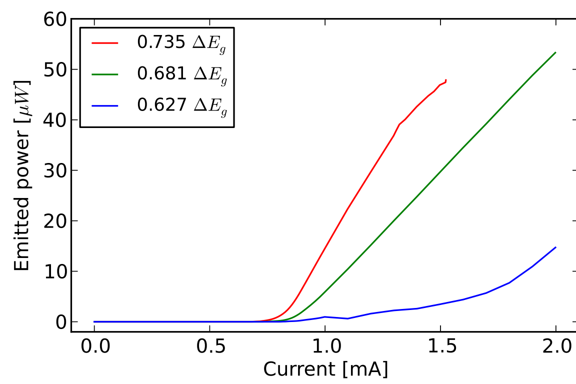

Figure 3.16: Effect of the conduction band offset on the LI curve at 70 $^\circ C$.

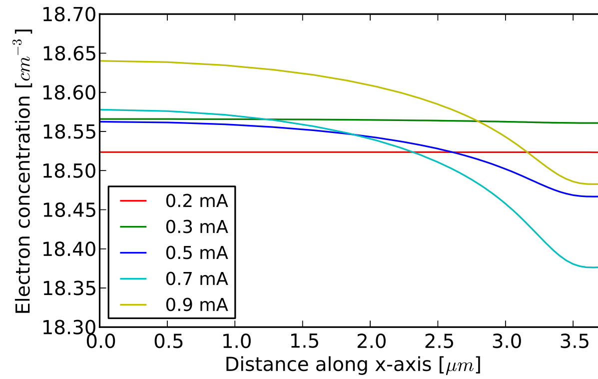

Figure 3.17: Electron density within the center quantum well along the radial axis for different injection currents. The outer part gets depleted of electrons due to the strong stimulated emission. The threshold current is 0.3 mA for this laser. The y-axis is a log scale where the digits before and after the decimal point represent the exponent and the base, respectively.

Carrier distribution

When threshold is reached the carrier density in the active region is often assumed to be clamped. However, when current is injected uniformly over a microdisk structure this might not be true. Light is only propagating at the periphery of the microdisk and this is thus also the only area where stimulated emission takes place. The carriers injected in the center of the microdisk can only contribute to stimulated emission if there is a drift and/or diffusion current towards the outer edge. Figure 3.17 shows a 1D plot of the electron density in the center quantum well for different injection currents, where the threshold current lies at 0.3 mA. It can be seen that below threshold there is a uniform carrier density in the quantum well and thus we can conclude that the injection scheme is indeed uniform. However, at larger currents the carrier density becomes non-uniform due to the strong stimulated emission at the outer edge of the microdisk structure. This has some consequences for the performance of the microdisk laser.

First of all, let us consider the effect on the total loss and gain, which are plotted in Figure 3.18 versus injected current.

At a current of 0.26 mA the modal gain clamps to the total loss thereby reaching the lasing threshold. It can also be seen that the total loss itself increases and reaches a maximum around 0.34 mA after which it starts to decrease again. The increase in total loss before reaching threshold can be explained by the increasing intervalence band absorption due to the higher carrier density. However, the total loss decreases after threshold indicating that the carrier density is not completely

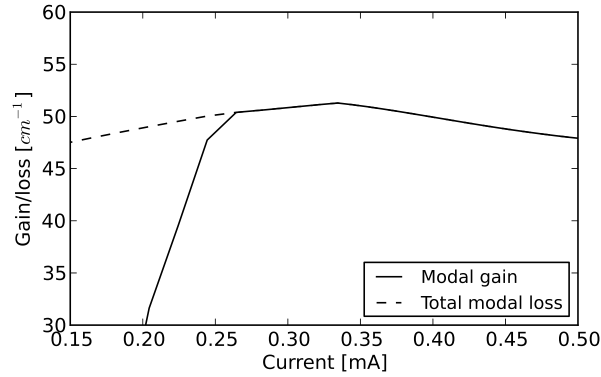

Figure 3.18: Total loss and optical gain as function of injected current.

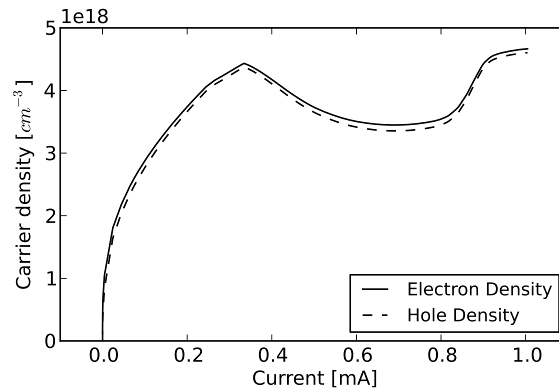

Figure 3.19: Carrier density in the active region as function of injected current.

clamped. It actually implies that the carrier density is decreasing after threshold, which is obviously a rather strange behavior.

In Figure 3.19 the electron and hole density in the active region are plotted against the injected current. Indeed, the carrier density appears to peak just above threshold after which it starts to decrease again. Around 0.6 mA the carrier density seems to saturate, but then above 0.8 mA it again rapidly increases. In principle one would expect that when the carrier density decreases, this would also become visible in the LI curve because the stimulated emission normally would decrease. However, although the LI curve indeed shows a dip around 0.9 mA as can be seen in Figure 3.20, it continues to grow while the carrier density is already decreasing albeit with a decreasing slope efficiency.

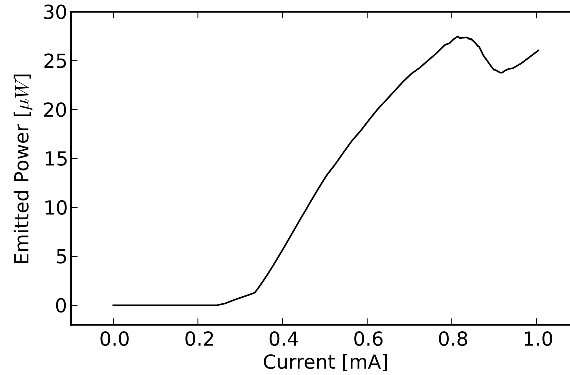

Figure 3.20: Simulated LI curve of the microdisk laser.

By looking at the electron and hole current densities, displayed in Figure 3.21 it can be seen that there is indeed a strong current flowing in the quantum wells from the center of the microdisk towards the edge. Therefore, the process in the microdisk can be understood as follows. First carriers are injected uniformly over the microdisk structure. Below threshold the dominating recombination effect is Auger recombination which is uniform over the active region and thus the carrier density remains uniform. Then, when threshold is reached strong stimulated emission at the periphery of the microdisk makes the recombination process non-uniform across the active region. At first, there is a strong current from the center of the microdisk towards the edge, feeding the stimulated emission. However, this is clearly not sufficient to sustain the stimulated emission rate and the area at the edge gets depleted from carriers. As a result, the slope efficiency starts to degrade and eventually a dip in the LI curve is observed. At that point the total carrier density in the quantum wells can again increase, after which the stimulated emission also starts to increase again.

Modified designs

Because of the uniform injection scheme the whole active region needs to be pumped to the threshold current density in order to achieve lasing, which is obviously not very efficient. It is expected that the threshold current can be reduced by using more efficient injection schemes. Two obvious and relatively easy to implement possibilities are either to etch a hole completely through the stack in the center of the microdisk or to etch away the tunnel junction in the center.

The first option also confines the carriers better in the active region, but this might come at the cost of higher surface recombination because the surface to

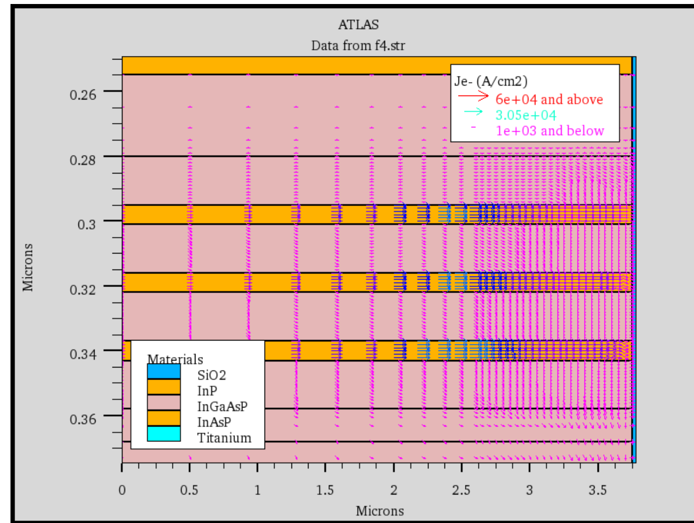

Figure 3.21: 2D vector plot showing the electron current density in the active region that flows from the center towards the edge.

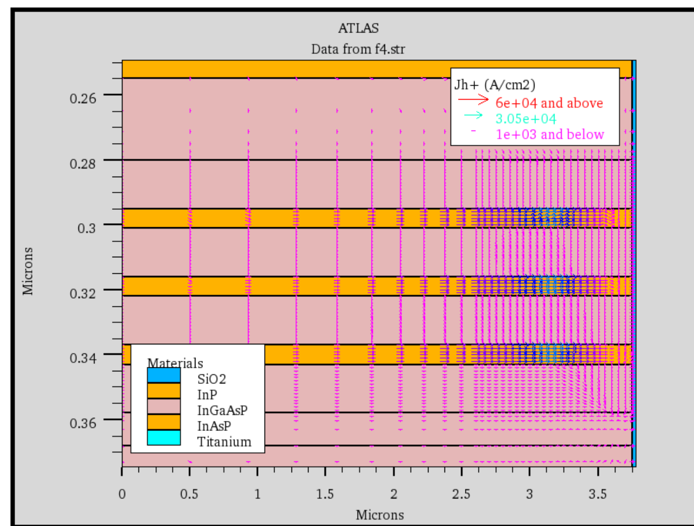

Figure 3.22: 2D vector plot showing the hole current density in the active region that flows from the center towards the edge.

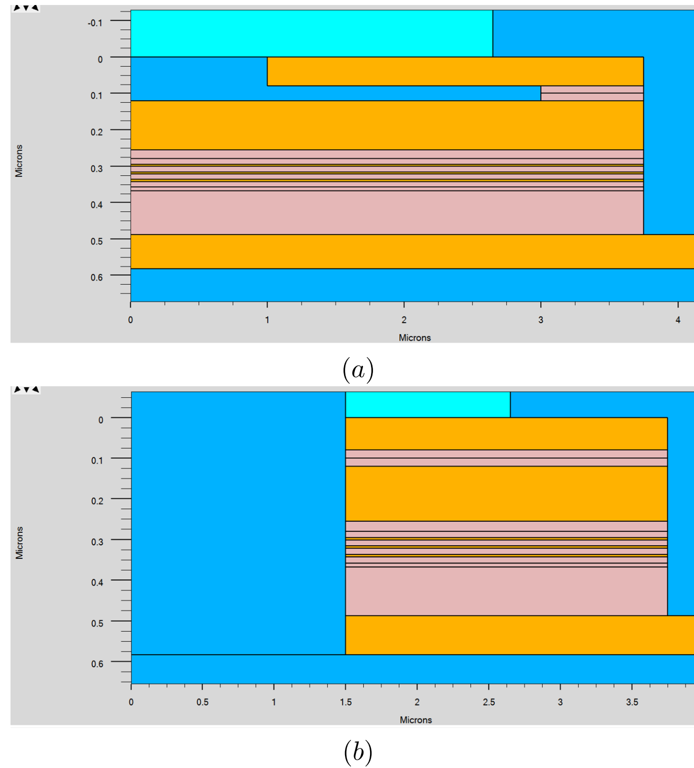

Figure 3.23: Schematic overviews of alternative microdisk laser designs where in (a) the tunnel junction is etched from the center and in (b) a center hole is etched through the whole stack.

volume ratio increases in this case. Furthermore, the top contact becomes smaller which might result in higher series resistance and increased self-heating.

The second approach would require a wet etch, where the tunnel junction is etched from the center such that the carriers can only tunnel at the periphery. In this case, no extra etch through the active region is required. On the other hand, there might be a lateral leakage current in the active region from the edge towards the center, because no carriers are injected in that region. Schematic overviews of these alternative designs are shown in Figure 3.23.

A simulation was performed to investigate these alternatives. For the first option a center hole diameter of 3 μm was used and for the second option a center hole diameter of 2 μm was etched in the top InP layer and the tunnel junction was then etched from the center towards the edge such that 0.75 μm of the tunnel junction is left. In all three designs the same material parameters were used, with Auger coefficients C_n and C_p both set to $2e-29cm^6/s$, free carrier absorption

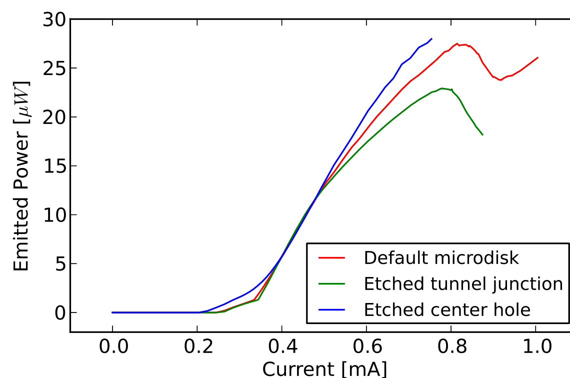

Figure 3.24: LI curves for 3 different microdisk laser designs: default design (red line), etched tunnel junction (green line) and etched center hole (blue line).

parameters k_n set to $1e-18cm^2$ for all materials and k_p set $30e-18cm^2$ in InGaAsP and InP and $40e-18cm^2$ in InAsP. SRH lifetimes of 350 ns were used for all materials. The resulting LI curves of the default microdisk laser and the two alternative options are shown in Figure 3.24.

It can be seen that the performance of these three designs are actually quite similar and no major improvement is obtained for the alternative designs. The best performance is obtained for the design where a center hole is etched through the hole stack. In this case a slightly lower threshold current is obtained and the output power tends to saturate at higher currents compared to the other designs. The design with the etched tunnel junction performs even slightly worse compared to the default design. The threshold current is still similar but the slope efficiency saturates faster due to lateral leakage in the active region.

It should be noted that the simulation with a center hole was also performed for a microdisk laser with a diameter of 40 μm and in this case a significant improvement was obtained, where the threshold current decreased from 7.2 to 4.5 mA. The center hole had a diameter of 28 μm in this case. The result is shown in Figure 3.25.

3.6 Fabrication

As the fabrication process of the microdisk laser is carried out simultaneously with the detector, the description of this process is described in Chapter 5 which deals with the detectors.

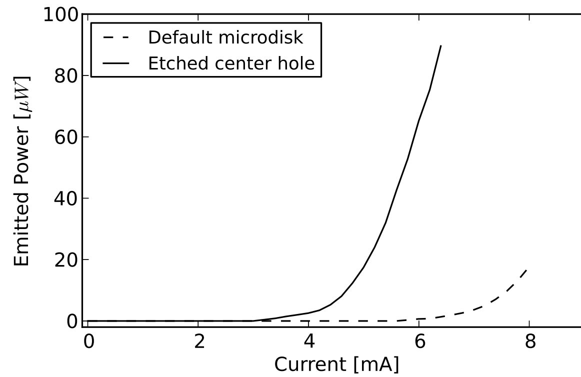

Figure 3.25: LI curves for a 40 μm diameter microdisk with (green line) and without (red line) center hole.

3.7 Conclusions

In this chapter a physical model of the microdisk laser has been presented using the device simulator Atlas from Silvaco. First the electrical behavior of the microdisk laser was analyzed and the contribution of different parts of the microdisk laser to the series resistance was investigated.

This was followed by a full laser simulation where first the simulated spontaneous emission and gain spectrum were compared with experimental results and showed a good qualitative agreement. However, we were not yet able to make an accurate fit with measured LI curves under elevated temperatures. The transparency carrier density was found to be quite high in the simulations and therefore some benchmark simulations are required to further test and calibrate the $k \cdot \mathbf{p}$ model.

Nevertheless, the model can be used to investigate the carrier distribution in microdisk lasers and it was found that the carrier density is not completely clamped above threshold, which is a consequence of the uniform injection scheme. This results in a strong carrier flow in the active region from the center towards the edge of the microdisk and these carriers are used to feed the stimulated emission. However, this scheme cannot sustain and results in saturation of the output power. Two alternative designs where either a center hole is etched in the microdisk or the tunnel junction is etched from the center were also investigated and it was found that a minor improvement could be obtained for the design with the center hole in case of small microdisks (3.75 μm radius). For larger devices (20 μm radius) the improvement tends to be more significant.

References

[1] Alexander W Fang, Hyundai Park, Oded Cohen, Richard Jones, Mario J Paniccia, and John E Bowers. *Electrically pumped hybrid AlGaInAs-silicon evanescent laser.* Optics express, 14(20):9203–10, October 2006.

[2] Alexander W Fang, Erica Lively, Ying-Hao Kuo, Di Liang, and John E Bowers. *A distributed feedback silicon evanescent laser.* Optics express, 16(7):4413–9, March 2008.

[3] Shahram Keyvaninia, Gunther Roelkens, Dries Van Thourhout, Christophe Jany, Marco Lamponi, Alban Le Liepvre, Francois Lelarge, Dalila Make, Guang-Hua Duan, Damien Bordel, and Jean-Marc Fedeli. *Demonstration of a heterogeneously integrated III-V/SOI single wavelength tunable laser.* Optics express, 21(3):3784–92, February 2013.

[4] Stevan Stankovic. *Hybrid III-V / Si DFB Lasers Based on Polymer Bonding Technology*. PhD thesis, Ghent University, 2013.

[5] Martin T. Hill, Yok-Siang Oei, Barry Smalbrugge, Youcai Zhu, Tjibbe de Vries, Peter J. van Veldhoven, Frank W. M. van Otten, Tom J. Eijkemans, Jarosaw P. Turkiewicz, Huug de Waardt, Erik Jan Geluk, Soon-Hong Kwon, Yong-Hee Lee, Richard Nötzel, and Meint K. Smit. *Lasing in metallic-coated nanocavities*. Nature Photonics, 1(10):589–594, September 2007.

[6] Martin T Hill, Milan Marell, Eunice S P Leong, Barry Smalbrugge, Youcai Zhu, Minghua Sun, Peter J van Veldhoven, Erik Jan Geluk, Fouad Karouta, Yok-Siang Oei, Richard Nötzel, Cun-Zheng Ning, and Meint K Smit. *Lasing in metal-insulator-metal sub-wavelength plasmonic waveguides.* Optics express, 17(13):11107–12, June 2009.

[7] Shinji Matsuo, Akihiko Shinya, and Takaaki Kakitsuka. *High-speed ultra-compact buried heterostructure photonic-crystal laser with 13 fJ of energy consumed per bit transmitted*. Nature Photonics, 4(September):648–654, 2010.

[8] Bryan Ellis, MA Mayer, Gary Shambat, and Tomas Sarmiento. *Ultralow-threshold electrically pumped quantum-dot photonic-crystal nanocavity laser*. Nature Photonics, 5(April):297–300, 2011.

[9] K Takeda, T Sato, A Shinya, and K Nozaki. *Few-fJ/bit data transmissions using directly modulated lambda-scale embedded active region photonic-crystal lasers*. Nature Photonics, 7(July):569–575, 2013.

[10] J.Y. Hsing, T.E. Tzeng, K.Y. Chuang, T.S. Lay, M.Y. Kuo, Y.Y. Tsai, K.S. Hsu, and M.H. Shih. *Lasing in compact microdisks with InAs quantum dots in a well structure*. Journal of Crystal Growth, 323(1):457–459, May 2011.

[11] Yoon-Ho Kim, Soon-Hong Kwon, Jung Min Lee, Min-Soo Hwang, Ju-Hyung Kang, Won Il Park, and Hong-Gyu Park. *Graphene-contact electrically driven microdisk lasers.* Nature communications, 3:1123, January 2012.

[12] Roger Chen, TTD Tran, KW Ng, and WS Ko. *Nanolasers grown on silicon*. Nature Photonics, 5(March):170–175, 2011.

[13] Linus C. Chuang, Roger Chen, Forrest G. Sedgwick, Wai Son Ko, Kar Wei Ng, Thai-Truong D. Tran, and Connie Chang-Hasnain. *InGaAs QW Nanopillar Light Emitting Diodes Monolithically Grown on a Si Substrate*. In Conference on Lasers and Electro-Optics 2010, page CMFF6, Washington, D.C., 2010. OSA.

[14] Jian Wang, Di Liang, Yongbo Tang, Daoxin Dai, and John E Bowers. *Realization of an ultra-short silicon polarization beam splitter with an asymmetrical bent directional coupler.* Optics letters, 38(1):4–6, January 2013.

[15] G Vecchi, F Raineri, I Sagnes, a Yacomotti, P Monnier, T J Karle, K-H Lee, R Braive, L Le Gratiet, S Guilet, G Beaudoin, a Taneau, S Bouchoule, a Levenson, and R Raj. *Continuous-wave operation of photonic band-edge laser near 1.55 microm on silicon wafer.* Optics express, 15(12):7551–6, June 2007.

[16] MH Shih, Adam Mock, M Bagheri, and NK Suh. *Photonic crystal lasers in InGaAsP on a SiO (2)/Si substrates and its thermal impedance*. Optics express, 15(1):227–232, 2007.

[17] Katsuaki Tanabe, Masahiro Nomura, Denis Guimard, Satoshi Iwamoto, and Yasuhiko Arakawa. *Room temperature continuous wave operation of InAs/-GaAs quantum dot photonic crystal nanocavity laser on silicon substrate.* Optics express, 17(9):7036–42, April 2009.

[18] Y Halioua, A Bazin, P Monnier, T J Karle, G Roelkens, I Sagnes, R Raj, and F Raineri. *Hybrid III-V semiconductor/silicon nanolaser.* Optics express, 19(10):9221–31, May 2011.

[19] Yannick de Koninck, Fabrice Raineri, Alexandre Bazin, Rama Raj, Gunther Roelkens, and Roel Baets. *Experimental demonstration of a hybrid III-V-on-silicon microlaser based on resonant grating cavity mirrors.* Optics letters, 38(14):2496–8, July 2013.

[20] Joris Van Campenhout. *Thin-Film Microlasers for the Integration of Electronic and Photonic Integrated Circuits*. PhD thesis, Ghent University, 2007.

[21] Di Liang, Marco Fiorentino, Tadashi Okumura, Hsu-Hao Chang, Daryl T Spencer, Ying-Hao Kuo, Alexander W Fang, Daoxin Dai, Raymond G Beausoleil, and John E Bowers. *Electrically-pumped compact hybrid silicon microring lasers for optical interconnects.* Optics express, 17(22):20355–64, October 2009.

[22] LA Coldren and SW Corzine. *Diode lasers and photonic integrated circuits*. Wiley-Interscience, 2012.

[23] Joachim Piprek. *Semiconductor optoelectronic devices: introduction to physics and simulation*. Academic Press, 2003.

[24] A Katz, BE Weir, and W.C Dautremont-smith. *Au/Pt/Ti contacts to p-In0. 53Ga0. 47As and n-InP layers formed by a single metallization common step and rapid thermal processing*. Journal of Applied Physics, 68(3):1123–1128, 1990.

[25] M Yamamoto, N Yamamoto, and J Nakano. *MOVPE growth of strained InAsP/InGaAsP quantum-well structures for low-threshold 1.3-m lasers*. IEEE Journal of Quantum Electronics, 30(2):554–561, 1994.

[26] H Oohashi, T Hirono, and S Seki. *1.3 μm InAsP compressively strained multiplequantumwell lasers for hightemperature operation*. Journal of applied physics, 77(April), 1995.

[27] M Sotoodeh, AH Khalid, and AA Rezazadeh. *Empirical low-field mobility model for IIIV compounds applicable in device simulation codes*. Journal of applied physics, 87(6):2890–2900, 2000.

[28] Manish Mehta and Danny Feezell. *Electrical design optimization of single-mode tunnel-junction-based long-wavelength VCSELs*. IEEE Journal of Quantum Electronics, 42(7):675–682, 2006.

[29] Silvaco. *www.silvaco.com*, 2013.

[30] I. Vurgaftman, J. R. Meyer, and L. R. Ram-Mohan. *Band parameters for IIIV compound semiconductors and their alloys*. Journal of Applied Physics, 89(11):5815, 2001.

[31] Basil W. Hakki and Thomas L. Paoli. *Gain spectra in GaAs double-heterostructure injection lasers*. Journal of Applied Physics, 46(3):1299, 1975.

4
Characterization of microdisk lasers

In this chapter the characterization of the microdisk lasers will be discussed. We will first focus on microdisk lasers completely fabricated in the CMOS pilot line at CEA Leti. Two different design runs were executed in this CMOS pilot line. Then, the results from a fabrication run performed in the clean room of Ghent University will be discussed.

Run 1 was executed at the very beginning of this work and therefore none of the obtained results discussed in Chapter 2 and 3 were included in these designs. In the second run the results from the simulations to reduce metal losses were included as well as some early results on the coupling conditions between the microdisk laser and the access waveguide. The final run also includes the latest results on optimal coupling conditions. The experimental data from the second and final run was used to build the model discussed in Chapter 3. The complete mask layouts used throughout these different designs runs as well as more detailed layouts of the microdisk laser and detector designs can be found in Appendix C.

4.1 Run 1 results: First generation CMOS

In this section the measurement results of the first batch of microdisk lasers that were processed completely in a CMOS pilot line are discussed. Several wafers were processed at CEA Leti, Grenoble, France, with several different processing parameters for testing purposes. The design contains microdisk lasers with three different diameters: 7.5, 20 and 40 μm. We received samples from three different

wafers, but on one wafer different etch parameters were used that resulted in high surface roughness and no lasing was observed for the devices from this wafer. The waveguide width of the access waveguide under the microdisk laser was 1 μm in all cases. The results are arranged by diameter.

The generated light from the microdisk lasers that is coupled to the waveguide is coupled out vertically through a grating coupler and is then collected by a single mode fiber. Such a grating coupler is basically a one dimensional diffraction grating etched in the silicon and light will diffract under a certain angle. The maximum efficiency of these fiber grating couplers or fiber couplers (FCs) is typically around 30% and the 1 dB bandwidth is approximately 40 nm. When measuring micro lasers with a large FSR it is important to know the efficiency at the lasing wavelength to be able to determine the correct output power. Therefore, before characterizing the microdisk lasers, the performance of the fiber couplers was measured through a transmission measurement. The maximum coupling efficiency was found to be 25% at a wavelength of 1581 nm, while as we will see, lasing was obtained at wavelengths between 1535 and 1565 nm with coupling efficiencies around 10% and 20%, respectively.

4.1.1 7.5 μm diameter microdisk lasers

To characterize the microdisk lasers, LIV measurements were performed. The results of several microdisk lasers are shown in Figure 4.1(a). The IV curves indicate good electrical performance and the different devices show all similar behavior. From the slope of the IV curves at higher currents the series resistance was found to be in the order of 50 Ohms. However, measurements in later runs revealed that a burn-in treatment changed the behavior of the contacts from a Schottky like behavior to an Ohmic like behavior. As this influences the slope of the IV curve, the values found here should be seen as an under estimation of the actual series resistance. From the LI curves it can be seen that there is only spontaneous light emission and no lasing behavior for these devices, despite the good IV curves. The maximum output power collected by the fiber is 36 nW, which corresponds with at least 144 nW in the waveguide. The maximum output power is reached at a current of 3.5 mA after which the output power decreases again due to thermal roll-over. The optical spectrum of one of the devices is shown in Figure 4.1(b). Four broad peaks can be seen with a spacing of 30.1 nm, which corresponds with the FSR of the fundamental modes. The fact that there are no other peaks present, indicates that higher order modes are either very leaky due to the bottom contact slab or are suppressed by the presence of the metal top contact. As this was the first attempt to fabricate microdisk lasers in a CMOS pilot line, the designs were kept rather conventional. Given the good electrical injection, lasing operation was expected. SEM and cross-section images were made with the FIB to inspect to devices and

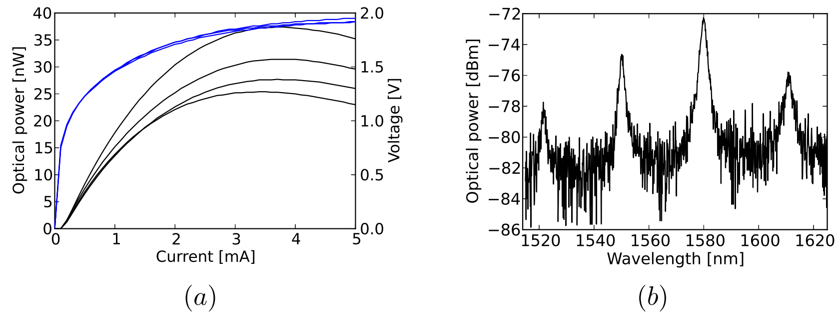

Figure 4.1: (a) LIV curves of several microdisk lasers with a diameter of 7.5 μm. The IV curves (blue lines) are all very similar and show good electrical behavior, but the LI curves (black lines) indicate that there is only spontaneous emission. (b) The optical spectrum observed for these microdisk lasers. 4 Azimuthal modes can be recognized and the FSR is 30 nm.

a cross-section image is shown in Figure 4.2. It was found that all layers with critical alignment were well within range, which could be expected because of the 248 nm DUV lithography. However, from the cross-section an object was found around the periphery of the microdisk as indicated in Figure 4.2, where only oxide around the microdisk was expected. Based on these findings EDX measurements were performed at Leti and the material around the microdisk was identified as Titanium. Most likely it was a residue of the heater layer for which Titanium was full sheet deposited and then dry etched. As the distance between the microdisk and the Titanium ring was only about 200 nm, it is likely that it causes extra optical absorption. To estimate the losses induced by the Titanium we simulated the structure with the FEM model described in Section 2. From the simulation it was found that for a 7.5 μm diameter microdisk the losses induced by the Titanium are around 20 cm^{-1}. It is likely that the gain is not sufficient to compensate for these extra losses.

4.1.2 20 μm diameter microdisk lasers

The LIV curve of a 20 μm diameter microdisk is shown in Figure 4.3(a). Clearly, lasing is observed in this device with a threshold current of 3 mA and a maximum output power measured in the fiber of 15 μW at a bias of 11 mA. The spectrum of this device at a bias of 11 mA is shown in Figure 4.3(b). At this particular current the output is single mode with a lasing wavelength of 1567 nm and a side mode suppression ratio (SMSR) of 22 dB. The FSR is around 11 nm, which corresponds with the fundamental azimuthal modes. This indicates that the top contact size is large enough to suppress higher order radial modes. Due to thermal effects, the

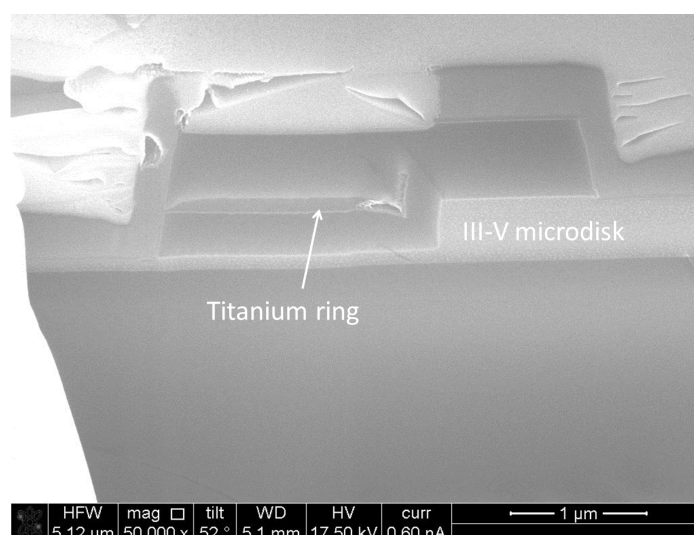

Figure 4.2: SEM image of a cross-section of a microdisk laser. Next to the microdisk a Titanium layer can be observed, which is a residue of the heater layer and is likely to cause significant absorption.

lasing wavelength varies from 1534 nm at low drive currents to 1567 nm at 11 mA after which thermal roll-over starts and the output power starts to decrease. Although also for these larger devices a Titanium ring was found around the disk, the influence of this ring was lower because of the higher confinement of the light due to the larger bend radius. Just as in the case of the 7.5 μm diameter devices, the shape of the IV curve looks as expected, except for the fact that the series resistance is with 30 Ohms slightly higher for these larger disks. Normally one would expect lower series resistance because of the larger contact areas. The light output however, shows very chaotic behavior. Reflections from for instance the grating couplers or possible discontinuities in the titanium ring are possible causes of this chaotic behavior.

The tunnel junction resistance ensures that the injected carriers are uniformly distributed over the disk cavity. However, as the optical mode is propagating near the edge of the disk, carriers injected in the center of the disk will not contribute to stimulated emission, except for the carriers that move towards the periphery by diffusion. By etching a hole in the center of the disk, the area that does not contribute to the lasing is reduced, which could result in a lower threshold current and higher slope efficiency. Therefore, devices were designed with a center hole with different diameter ranging from 4 to 14 μm. However, the yield of these microdisk laser was too low to extract any information. Microdisk lasers with 40 μm diameter and center holes were also fabricated and these will be discussed in

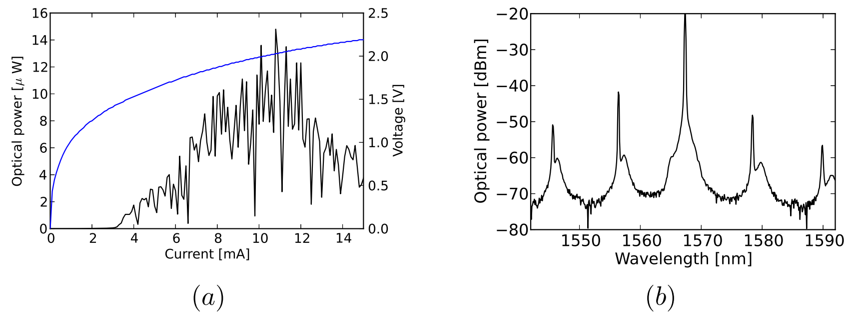

Figure 4.3: (a) Typical LIV curve of microdisk lasers with a diameter of 20 μm on this run. The IV curve shows good electrical behavior, and from the LI curve a threshold current of 3 mA is found. The optical output power reaches a maximum of 15 μW at an 11 mA drive current. The chaotic behavior is believed to be caused by external reflections. (b) The optical spectrum observed at a bias current of 11 mA.

the next section.

4.1.3 40 μm diameter microdisk lasers

The highest yield was obtained for the largest devices. One of the best LIV curves measured for a 40 μm diameter microdisk is shown in Figure 4.4. The maximum output power in the fiber is 33 μW and the threshold current is 6 mA. Most of the devices were found to have a maximum output power between 10 and 15 μW and a threshold current between 6 and 10 mA. From the LI curve in Figure 4.4 it seems that the device shows bistable behavior in combination with self switching, because of the sharp transitions and constant regions. In this case the degeneracy of the clockwise and counterclockwise mode is lifted and instead of bidirectional output, unidirectional output is observed where either the clockwise or counterclockwise mode is suppressed. However, in order to confirm this, also the other output from the microdisk laser is needed and this was not possible in this design. In general, most of the devices showed a more chaotic behavior similar to the 20 μm diameter devices. The spectrum of the laser measured at a drive current of 24 mA is shown in Figure 4.5. The lasing wavelength is 1566 nm and the SMSR is 27 dB. Again, the FSR is in agreement with the expected value of 5 nm for this diameter ensuring only the presence of fundamental modes. The inset in Figure 4.5 shows a close up of the lasing peak. While the resolution bandwidth of the spectrum analyzer was set to 100 pm, the linewidth of the lasing peak was measured to be 240 pm. Such a large linewidth is unusual for lasers as typical values are in the order of only a few picometer, well below the highest resolution bandwidth of spectrum analyzers. The large linewidth might be an indication of coherence col-

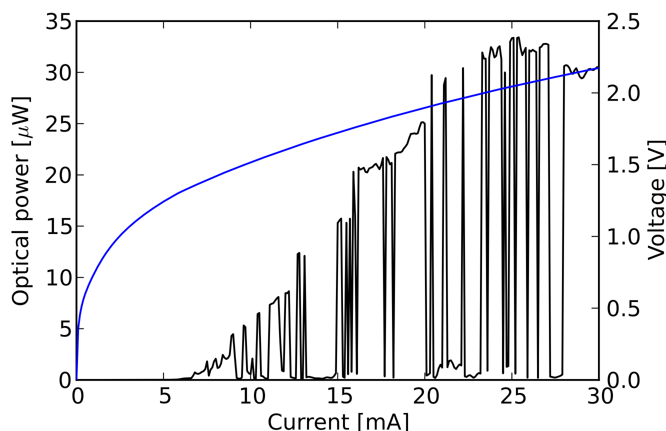

Figure 4.4: LIV curve of a 40 μm diameter microdisk laser. The threshold current is 6 mA and the peak output power is 33 μW. The sharp transitions are an indication of bistable operation.

lapse in the laser. Coherence collapse is caused by strong reflections and results in the appearance of satellite modes separated from the main mode by the relaxation oscillation frequency [1]. The Titanium ring around the disk or reflections from fiber couplers might play a role in this.

The influence of a center hole was also studied for these largest devices. Figure 4.6 and 4.7 show LIV curves versus hole diameter for two different samples, referred to as sample 1 and 2. The different hole diameters were 8, 16 and 24 μm, corresponding to the red, green and blue curves, respectively. For sample 1 we find threshold currents of 6.67, 7.05 and 7.18 mA while for sample 2 we find values of 7.94. 8.53 and 9.41 mA. In both cases the lowest threshold is obtained for the microdisks with the largest central hole, while the microdisks with the smallest central hole have the highest threshold. However, by etching a central hole in the microdisk the area available for the top contact reduces and leads to a higher series resistance, which increases the thermal resistance of the microdisks. This is indeed also observed in these devices as the microdisks with the largest hole diameters have IV curves with the highest slope. Despite the low number of devices available we can conclude that there is indeed some correlation between the center hole diameter and the threshold current and series resistance of these microdisks.

When the optical spectrum is analyzed as function of the drive current, mode hopping is observed. This is illustrated in Figure 4.8 where the optical spectrum is plotted for different drive currents. In principle one would expect that the lasing mode will hop to longer wavelengths as the drive current is increased because the

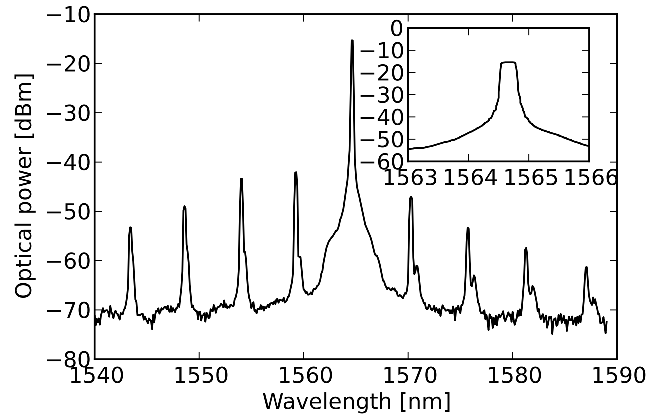

Figure 4.5: Optical spectrum of a 40 μm diameter microdisk laser. The inset shows a close up of the lasing peak recorded with a 0.1 nm resolution bandwidth. The wide peak might be an indication of coherence collapse due to external reflections.

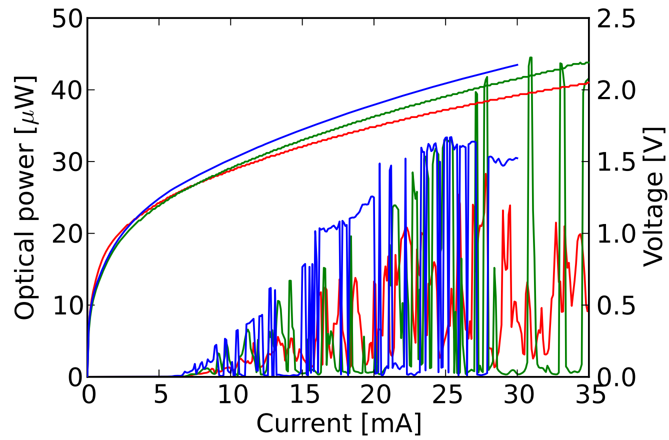

Figure 4.6: LIV curves of 40 μm diameter microdisk lasers with different center hole diameter on sample 1. The red, green and blue line correspond with a 8, 16 and 24 μm hole diameter, respectively.

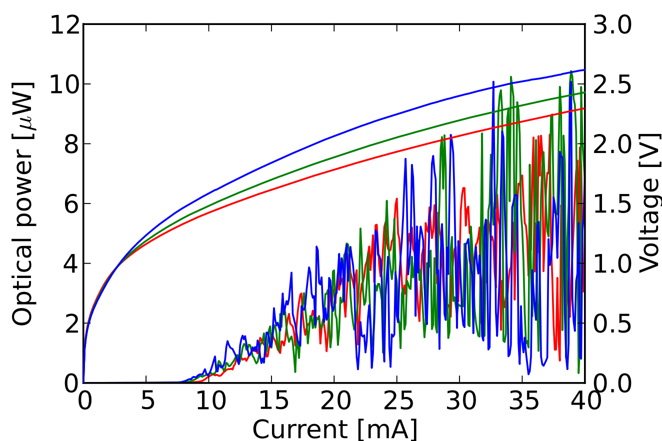

Figure 4.7: LIV curves of 40 μm diameter microdisk lasers with different center hole diameter on sample 2. The red, green and blue line correspond with a 8, 16 and 24 μm hole diameter, respectively.

gain spectrum will red shift as a result of the self heating. Although the general observed trend is a shift to longer wavelengths, a lot of other mode hops are observed which cannot be explained by the red shift of the gain spectrum. In the first plot, where the drive current is 5 mA, only spontaneous emission is observed. The second plot shows the recorded spectrum around threshold. At a current of 10 mA the modes at 1529 and 1534 nm are lasing. Next, at 12.5 mA the mode around 1529 nm is still lasing while the mode at 1534 nm is suppressed and the one at 1540 nm start to lase. If the current is increased only a little bit further to 13 mA, the four modes between 1525 and 1540 nm are lasing. This process of mode hopping continues even for larger currents but at a drive current of 23.9 mA the device becomes single mode as here only the mode around 1553 nm is lasing. At a current of 25.7 mA, the device is multimode again as modes around 1544 and 1559 nm are lasing. This behavior is observed for all the microdisks.

Although, no lasing was obtained in the small devices and the light output versus current for larger devices showed quite a chaotic behavior in this first run, the feasibility of processing these microdisk lasers completely in a CMOS pilot line is demonstrated.

4.2 Run 2 results: Second generation CMOS

Due to some delays in the processing of the first CMOS run, the second run had to be designed before the results of the first run were available. Therefore, the results

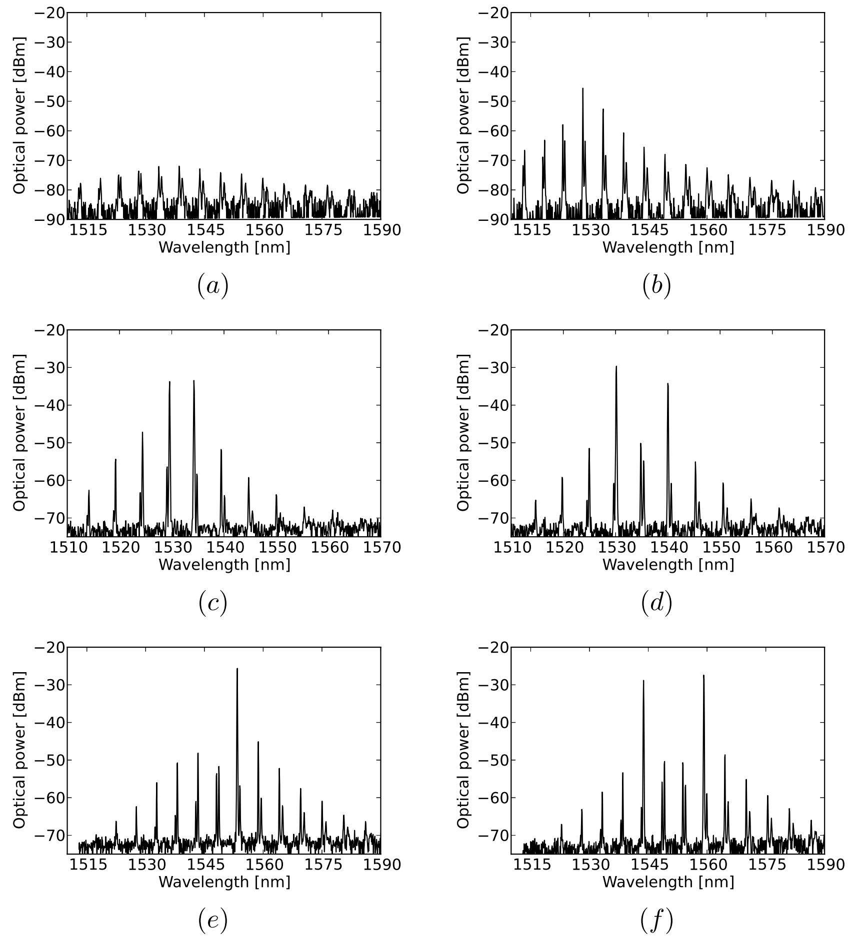

Figure 4.8: Optical spectra of a 40 μm diameter microdisk laser recorded at different drive currents, showing the intense mode hopping in these devices. (a) 5 mA: below threshold, (b) 6.5 mA: around threshold, (c) 10 mA: two lasing modes around 1529 and 1534 nm, (d) 12.5 mA: two lasing modes around 1529 and 1540 nm, (e) 23.9 mA: single mode lasing at 1553 nm and (f) 25.7 mA: two lasing modes at 1544 and 1559 nm.

discussed above could not be used in the design process of the devices discussed in this section. The focus of the design for this run was mainly on optical interconnects and Optical Networks-on-Chip (ONoCs), which is the topic of Chapter 6. Next to these designs, also some stand-alone microdisk lasers were included to be able to test their performance. Microdisks ranging from 5 to 40 μm diameter were designed. No lasing was obtained in the 5 μm diameter devices, larger diameter devices all showed lasing behavior. The width of the access waveguides was adjusted depending on the microdisk radius to achieve better phase matching of the optical modes.

4.2.1 Burn-in treatment

During the first initial measurements of the devices on this second run it was observed that a burn-in treatment improved the performance of the microdisk lasers considerably. This burn-in treatment was executed by pumping the device at a high current for several minutes. The IV curves were recorded at different time instances and are shown in Figure 4.9 for a microdisk laser with a 7 μm diameter. The dash-dotted black curve is recorded immediately without burn-in treatment, the red dashed line is recorded after 5 minutes and the solid blue line after 10 minutes. Clearly, the shape of the IV curves changes significantly during the burn-in treatment. It appears that the contact was slightly rectifying as deposited and became ohmic after the burn-in treatment. Furthermore, it was observed that the maximum optical output power increased by a factor of 5 and the threshold current decreased by a factor of 2. This result indicates that an annealing procedure is actually required for this Ti/TiN/AlCu metal stack that was described in Section 5.3.1. However, as no annealing was performed on any of the received samples, a burn-in treatment of 5 min. was performed on all measured devices.

4.2.2 Pulsed measurements

To measure the performance of the microdisk lasers first pulsed measurements were performed to avoid self heating effects. The microdisk lasers were electrically pumped by an ILX Lightwave LDP-3811 and the optical power and spectra were recorded with an HP 81532A power sensor and an Agilent 86140B optical spectrum analyzer, respectively. The result obtained for a microdisk laser with a diameter of 7 μm and an access waveguide width of 650 nm, driven by a signal with a pulsewidth of 100 ns and a duty cycle of 2% is shown in Figure 4.10. The black solid line corresponds with the optical output from the clockwise mode measured at the left fiber coupler and the red dashed line with the output from the counterclockwise mode measured at the right fiber coupler. It is clear from this figure that the output is unidirectional as only the clockwise mode shows lasing behavior and almost no light is emitted in the opposite direction. Because the curve

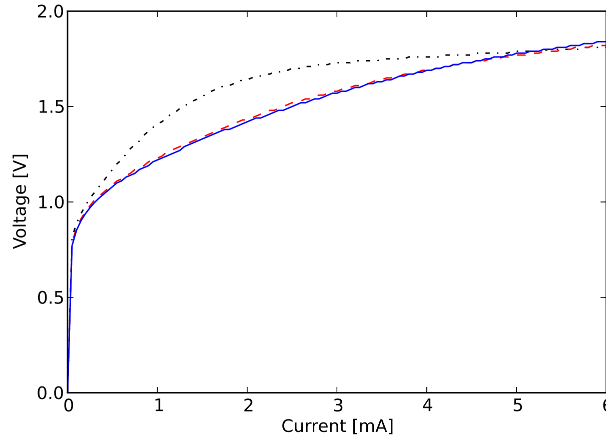

Figure 4.9: IV curves of a 7 μm diameter microdisk laser before (black dash-dotted line), after 5 min. (red dashed line) and after 10 min. burn in (blue line).

is unidirectional directly above the threshold current we believe this is caused by a stronger external reflection from one side than from the other, rather than being caused by intrinsic bistable behavior as reported in [2]. A threshold current of 600 μA and, after correction for the duty cycle, a peak optical power of 15.5 μW were measured in the fiber at an 8 mA drive pulse. Under these pulsed driving conditions the laser was lasing around a wavelength of 1536 nm. At this wavelength the fiber coupler efficiency was around 10% and therefore the peak optical power in the waveguide can be calculated to be 155 μW.

4.2.3 CW performance

The performance of the microdisk lasers was also measured under Continuous Wave (CW) operation where a Keithley 2400 was used as current source instead of the ILX Lightwave LDP3811. The LI curves of the 7 μm diameter microdisk discussed above but now under CW drive conditions are shown in Figure 4.11. Again, the black solid line corresponds with the left fiber coupler and the red dashed line corresponds with the right fiber coupler. The maximum output power observed in CW operation for this laser is 6.25 μW measured in the fiber for a drive current of 4 mA. If the drive current is increased further, thermal roll-over is observed. The large jump in the LI curve around a drive current of 3.7 mA is also an indirect result of self heating. As the temperature in the cavity increases and the gain spectrum shifts towards longer wavelengths, mode hopping will occur. Spectra at two different drive conditions are shown in Figure 4.12. The laser first lases around a wavelength of 1535 nm, but when the drive current is increased it hops to the next

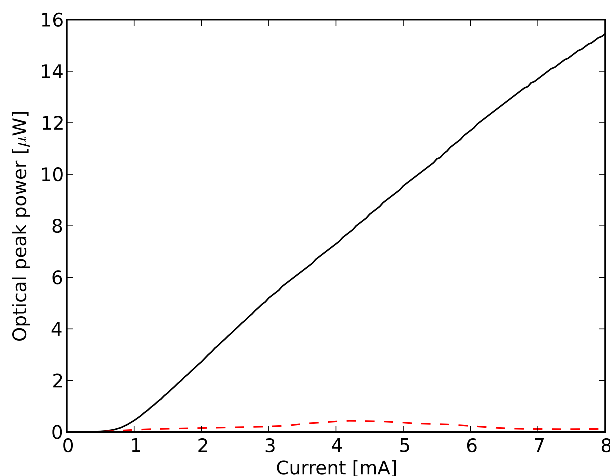

Figure 4.10: LI curve that shows unidirectional operation measured in pulsed mode. Black solid line represents the left output and the red dashed line the right output of the microdisk laser. The power is the fiber coupled output power.

azimuthal mode around a wavelength of 1565 nm. The fiber coupler efficiency was 10% around 1535 nm and 20% around 1565 nm. As the fiber coupler efficiency is higher in the latter case, it results in higher power in the fiber. The maximum output power of 6.25 μW in the fiber thus corresponds with 31 μW in the silicon waveguide. The side mode suppression ratio is $>$25 dB at lower drive currents and $>$21 dB at drive currents above 3.7 mA.

In all LI curves under CW operation, strong oscillations are observed, where the oscillations of the left and right output are complementary. These oscillations between the clockwise and counterclockwise mode are caused by output light of the microdisk laser that is reflected back at e.g. the fiber couplers and interferes either constructively or destructively at the microdisk cavity. The reflection from the fiber couplers used here is in the order of -20 dB [3]. The variation in interference is a result of the change in optical path length in the microdisk cavity under the influence of self-heating and the thermo-optic effect. When the drive current is changed, the microdisk cavity heats up and the refractive index of the cavity material changes and thereby also the resonance wavelength will shift. The temperature in the silicon waveguide and hence its refractive index are hardly affected and this causes variation in the interference. The oscillations are larger than that of similar microdisks reported earlier in [4]. This is due to stronger interference with the reflected light from the fiber couplers as a result of the higher coupling efficiency between the disk and the waveguide. This higher coupling efficiency is

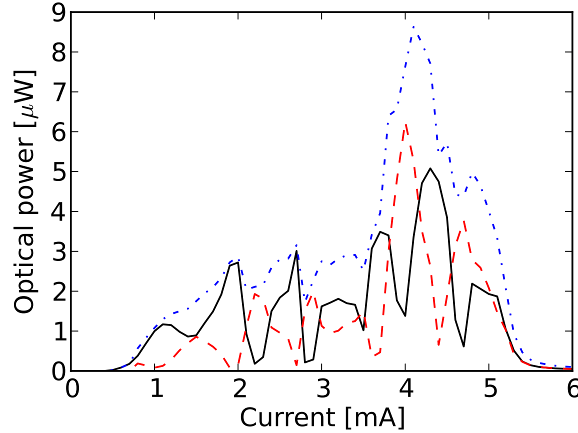

Figure 4.11: LI curve of both the left (black solid line) and right (red dashed line) output of a 7 μm diameter microdisk laser under CW operation. The blue dash dotted line represents the sum of the left and right output power.

a consequence of the better phase matching because of the adapted access waveguides and the thinner epitaxial stack of the microdisk compared to the microdisk reported in [4].

The threshold current density and external differential quantum efficiency η_d can easily be determined from the LI curve, assuming the lasing wavelength is known. However, both parameters depend on the length of the laser cavity. Obviously, it is desirable to deduce parameters from measurements that are independent of the geometry. Typically, in the case of stripe lasers, this is achieved by measuring devices of different length and using linear regression. The internal quantum efficiency η_i and the internal loss α_i, can be found this way by plotting the inverse external differential quantum efficiency versus cavity length. Through the relation

$$\frac{1}{\eta_d} = \frac{1}{\eta_i}\left(1 + \frac{\alpha_i}{ln(1/R)}L\right), \tag{4.1}$$

where R is the mirror reflectivity and L the length of the cavity, the internal quantum efficiency can be found from the intersect point with the y-axis and the internal loss corresponds with the slope of the fitted line. In using this method it is assumed that η_i and α_i do not change with cavity length. In a similar way a threshold current density independent of geometry J_0, can be determined by plotting the threshold current density versus the inverse cavity length, and looking up the intersect point of the linear fitted line with the y-axis. This will give the threshold current density of an 'infinitely long laser' and this value can be used to compare different laser designs.

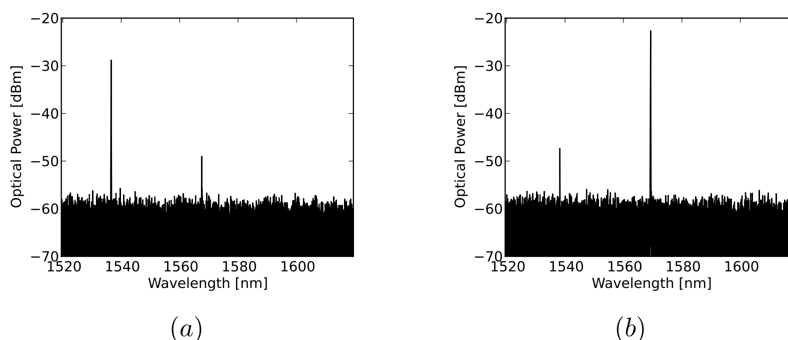

Figure 4.12: Optical spectrum recorded at a drive current of 2.9 mA (a) and 4 mA (b). Due to self heating effects the lasing mode hops to the next azimuthal mode at a longer wavelength.

In order to make a comparison between microdisk lasers of different diameter it would be desirable to follow a similar approach. However, in case of small microdisk lasers also the scattering loss and surface recombination need to be taken into account. These parameters are very difficult to extract and therefore the standard approach used for stripe lasers was also used here. The threshold current densities and the inverse external differential quantum efficiencies are plotted in Figure 4.13 versus (inverse) radius.

From Figure 4.13(a) it can be seen that the threshold current density varies between 1250 and 2310 A/cm^2. Although there is a linear trend for the smallest microdisks (largest 1/R), the threshold current density seems to saturate around 1400 A/cm^2 and thus, no clear linear relation can be found to deduce J_0. The linear trend seen in stripe lasers, shows a decreasing threshold current density with increasing length. This is a direct result of the decrease in distributed mirror loss. In case of microdisk cavities however, other loss factors indeed seem to play a role. As already mentioned, there is next to a change in distributed coupling loss, also a change in scattering loss. As seen in Section 2.3.3, the scattering loss increases rapidly with decreasing diameter. Secondly, possible surface recombination also increases with decreasing diameter. As these two effects both work in the same direction as distributed mirror loss, i.e. they decrease with increasing radius, this should result in a very steep slope for the J_{th} versus inverse radius plot in Figure 4.13(a). When the radius increases the influence of these effects decreases, which could be an explanation for the saturation.

Also for the inverse differential quantum efficiency plotted in Figure 4.13(b), the result is different from what is typically seen in stripe lasers. A linear trend with a positive slope is what one expects from stripe lasers. The trend of $1/\eta_d$ in Figure 4.13(b) has a negative slope, which means the slope efficiency of the

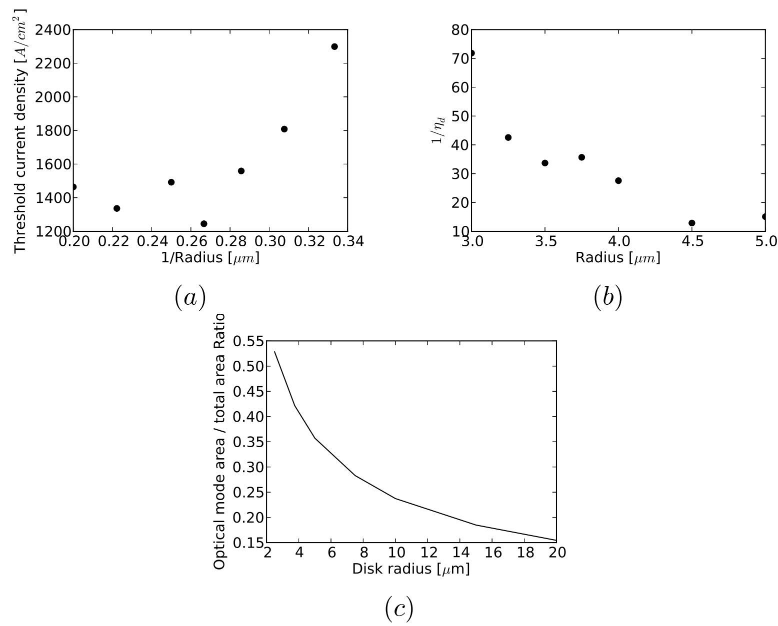

Figure 4.13: Comparison of the performance between microdisk lasers with different diameter. (a) Threshold current density versus inverse microdisk radius, (b) Inverse differential quantum efficiency η_d versus microdisk radius and (c) the ratio of the optical mode area over the total microdisk area versus microdisk radius.

microdisks increases with radius. As explained above, in microdisks it is not only the distributed coupling loss that changes with radius but also the scattering loss. This loss factor becomes smaller for larger microdisks, enhancing η_d. However, at the same time the injection efficiency is expected to decrease for increasing radius due to the smaller ratio of the area where the light is propagating versus the area of the center of the disk (Figure 4.13(c)) . The increase in η_d for larger microdisks might be an indication that surface recombination also has a significant impact as this carrier loss mechanism decreases with increasing radius.

It should also be noted that it is questioned in literature [5] whether the assumption of constant η_i and α_i still holds for short cavities. The distributed mirror loss increases rapidly at shorter cavity lengths and therefore, higher carrier densities are required to overcome the losses. However, the absorption coefficient of free carrier and intervalence band absorption rises proportionally with the carrier concentration.

By etching a center hole in the microdisk cavity as discussed in the previous section for large microdisks, the area that does not contribute to the laser action can be decreased. However, by doing so the sidewall surface area of the active region becomes larger thereby increasing the surface recombination. Furthermore, when a hole is etched the area for the top contact metal decreases and this results in higher series resistance and therefore increasing self heating. However, improving the specific contact resistance of the metal-semiconductor interface can help to keep the series resistance at an acceptable level. Another interesting approach to improve the injection efficiency would be to use proton implantation in the center of the microdisk thereby forcing the carriers to the periphery of the microdisk, as is also done in some stripe lasers [6].

4.2.4 Self heating

By comparing the pulsed and CW LI curves from the previous section and from the early thermal roll-over in output power under CW operation, it already became clear that self heating of microdisk lasers has a significant influence on the performance. Therefore, a more detailed analysis on the temperature dependence of microdisk lasers was performed. First the performance of microdisk lasers under elevated ambient temperatures was studied. Then, the thermal resistance, which is a measure of the increase in temperature as a function of dissipated power.

Temperature dependence

To determine the temperature sensitivity of microdisk lasers, the sample was heated by means of a Peltier element. Pulsed drive conditions with a duty cycle of 2% and a pulse width of 200 ns where used to suppress the influence of self heating. The temperature was increased from 25 to 70 degrees Celsius with the following

steps 25, 30, 40, .., 70 °C. The LI curves recorded at the different ambient temperatures for a microdisk laser with a diameter of 7 μm are displayed in Figure 4.14. First of all, it is interesting to note that at elevated temperatures under pulsed driving conditions the LI curve remains relatively smooth and unidirectional, in contrast to the case where CW drive conditions were applied and the temperature increases by self heating. Most likely this is because when the ambient temperature is changed under pulsed drive conditions, it affects both the silicon waveguide and the InP-based microdisk cavity, while the self heating effect in CW mode mainly heats up the disk cavity. As the thermo-optic coefficients for these materials are similar [7, 8], the phase difference between the output from the microdisk and the reflected light from the fiber coupler remains more or less constant and hence no oscillations are observed. As expected, the threshold current increases gradually with increasing temperatures, as can be seen in more detail in the inset of Figure 4.14, while the slope efficiency drops. Several different physical mechanisms, such as Auger recombination, thermionic emission and optical gain reductions [5], lie behind the temperature sensitivity of lasers, but in general the temperature dependence of the threshold current and the slope efficiency show an exponential relation. For the threshold current this dependence is written as

$$I_{th} = I_0 e^{T/T_0}, \tag{4.2}$$

where I_0 is a constant and T_0 is a characteristic temperature, which is often used as an indicator of the temperature sensitivity of the device. A low T_0 indicates strong temperature sensitivity. Similarly, the temperature dependence of the slope efficiency can be written as

$$I - I_{th} = I_\eta e^{T/T_1}, \tag{4.3}$$

where I_η is a constant and T_1 is an above threshold characteristic temperature. The parameters in Equation 4.2 and 4.3 can be found by using the data from the LI curves in Figure 4.14 and by plotting the natural logarithm of the threshold current or slope efficiency versus the ambient temperature and applying a linear fit. Figure 4.15(a) shows the linear fit for the threshold current and based on this fit a characteristic temperature T_0 of 66.33 °C and a value of 0.446 mA for I_0 are obtained. The value found for T_0 is comparable to typical values for InGaAsP based long-wavelength lasers which are in the order of 50-70 °C [9]. However, compared to other material systems these values are quite low indicating strong temperature sensitivity. Figure 4.15(b) shows the linear fit for the slope efficiency. Here a value of 28.33 °C was found for the above threshold characteristic temperature T_1 and for I_η 0.269 mA was obtained. Typically the value found for T_1 is higher than T_0, but here this is not the case. It could be that at higher temperatures the microdisk laser lases at a longer wavelength, because of the shift of the gain spectrum. As

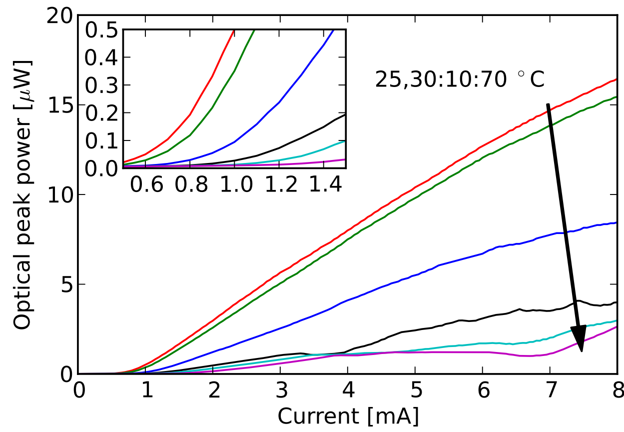

Figure 4.14: LI curves measured under pulsed operation at elevated temperatures. The slope efficiency decreases and the threshold current (inset) increases at higher temperatures. The power is the fiber coupled peak output power.

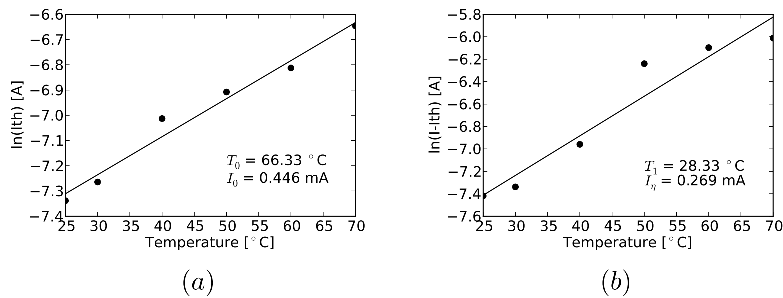

Figure 4.15: Extraction of characteristic temperatures T_0 and T_1 for a 7 μm diameter microdisk laser.

the efficiency of the fiber couplers is known to be higher at longer wavelengths for this sample, this results in overestimation of output power at these higher temperatures. Unfortunately, the spectrum was only recorded in a small wavelength span during these measurements, and therefore the reason for this low T_1 value remains unclear.

Thermal resistance

It is important to get rid of generated heat in the device in an efficient way. The heat flux from the device to the heat sink can be characterized by a thermal resis-

tance R_{th} which is expressed in terms of Kelvin per Watt. Knowing the thermal resistance and the heat generated in the device, the temperature increase simply follows from

$$\Delta T = R_{th} P_{heat}. \quad (4.4)$$

Here P_{heat} is the heat dissipated in the device. The thermal resistance depends on the thermal conductivity of the materials used, but also on the geometry of the device, just as a thin electrical wire has a higher electrical resistance as compared to a thick wire. Heterogeneously integrated lasers typically have high thermal resistance because they are bonded on SOI, and often also cladded by SiO_2 or BCB, which both have poor thermal conductivity. On top of this, the small footprint of microdisk lasers also has a negative influence on the thermal resistance. The thermal resistance can be determined by measuring the wavelength as a function of ambient temperature $(d\lambda/dT)$ in pulsed mode and the wavelength change as a function of injected power $(d\lambda/dP)$ in CW mode. By assuming that almost all power is dissipated as heat, the thermal resistance can then simply be calculated by

$$R_{th} = (\frac{dT}{d\lambda})(\frac{d\lambda}{dP}). \quad (4.5)$$

The results of these optical spectrum measurements are shown in Figure 4.16, where the wavelength dependence on ambient temperature is shown in Figure 4.16(a) and the dependence on dissipated power is shown in Figure 4.16(b). The abrupt change in wavelength in Figure 4.16(b) is a result of mode hopping to longer wavelengths at higher temperatures. The linear fits result in a value of 88.5 pm/K for $d\lambda/dT$ and a value of 0.69 nm/mW for $d\lambda/dP$. Using Equation 4.5 this leads to a thermal resistance R_{th} of 7.84 K/mW, which is about 20% lower compared to the microdisk lasers reported earlier in [10], most likely because of the lower electrical resistance and the higher thermal conductivity of oxide compared to BCB. However, the thermal resistance is e.g. still at least a factor of 3 higher compared to VCSELS of comparable dimensions on a GaAs substrate [11]. Therefore, in future devices special attention should be paid to improve the heat flux from the microdisk laser to the silicon substrate or another heat sink structure. A method that is simple to implement is for instance adding a heat spreading layer as proposed in [2]. However, this approach could not be used in the fabrication process here, as the metal contacts were all defined in a single processing step.

4.2.5 Small-signal behavior

In order to make efficient optical links the bandwidth of the microdisk laser should be sufficiently large such that the dissipated energy per bit is low. In order to assess

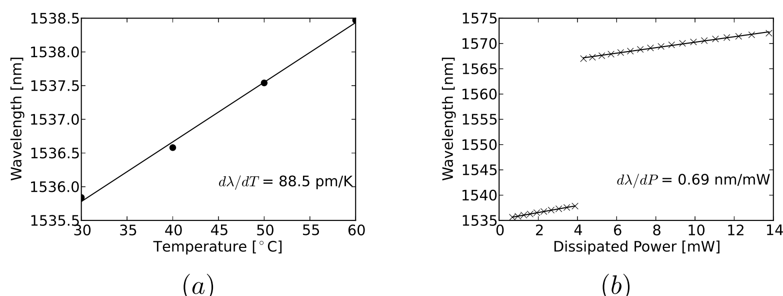

Figure 4.16: Plots to deduce the thermal resistance of the microdisk lasers. Impact on lasing wavelength as a function of ambient temperature (a) and as function of dissipated power (b) for a 7 μm diameter microdisk laser.

the bandwidth of the microdisk lasers, the small-signal response was measured using an HP 83420A Lightwave test system. The result is shown in Figure 4.17. The microdisk laser was biased at 1, 1.5 and 1.9 mA with a Keithley 2400 and it was lasing around a wavelength of 1532 nm. As can be seen from the figure, a 3 dB bandwidth of 7.8 GHz was achieved for a bias of 1.9 mA.

Because the output power in the fiber is relatively low due to the off-target peak efficiency of the fiber couplers, the large signal modulation could not be measured for these devices. However, it is likely that the reflections from the fiber couplers will have a negative effect. The temperature in the microdisk cavity will slowly fluctuate depending on the length of trailing ones and zeros and, as explained above, result in switching between the clockwise and counterclockwise mode. This will become visible as amplitude noise in the output signal.

4.2.6 Multi-wavelength lasers

Wavelength Division Multiplexing (WDM) is a well known technique to increase the bandwidth in an optical link or to supply additional flexibility in routing schemes. This technique can also be applied to on-chip optical links. Obviously, this requires multi-wavelength lasers (MWLs). It has been proposed and demonstrated [12, 13] to use integrated microdisk lasers to make a multi-wavelength laser by simply cascading microdisks on the same bus waveguide. As the lasing wavelength in microdisk lasers is determined by the radius of the microdisk, cascading microdisks of different radius on the same bus waveguide results in a multi-wavelength laser. In [13] a 4-channel laser on SOI was demonstrated using ebeam lithography. Here the goal was to make an MWL integrated on SOI consisting of 8 microdisk lasers on a single silicon waveguide by using Deep UV lithography. To avoid mode overlaps of the desired lasing modes with higher order azimuthal modes the radii of the microdisks are chosen such that the lasing wavelengths are uniformly distributed

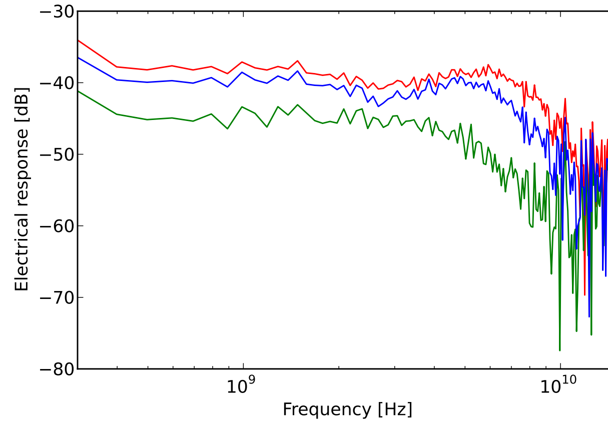

Figure 4.17: Small signal response of a 7 μm diameter microdisk laser for three different bias currents: 1 mA (green curve), 1.5 mA (blue curve) and 1.9 mA (red curve).

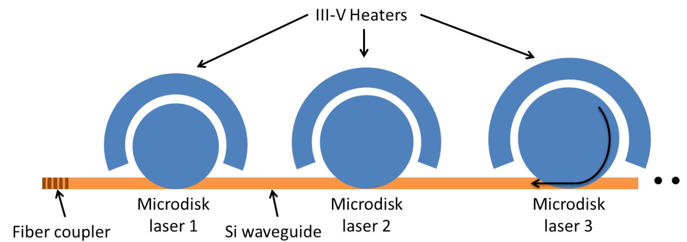

Figure 4.18: Schematic representation of a multi-wavelength laser based on microdisk lasers. The MWL consists of a single silicon bus waveguide on which multiple microdisk lasers of different diameter are cascaded. III-V ring heaters around the microdisks can be used to trim the output wavelengths of microdisk lasers.

over the FSR. The FSR of microdisks with a 3.75 μm radius is around 32 nm and this leads to a channel spacing of 4 nm in the case of 8 microdisk lasers. To achieve this, the difference in radii between the different microdisks should be 11.7 nm, which is obviously challenging from a processing point of view. By incorporating III-V ring heaters in the design for wavelength tuning, as proposed in [14] and schematically shown in Figure 4.18, this challenge can be somewhat relaxed.

III-V ring heaters

The III-V ring heaters, schematically shown in Figure 4.18, are defined together with the microdisk lasers and thus no extra processing steps are required to make

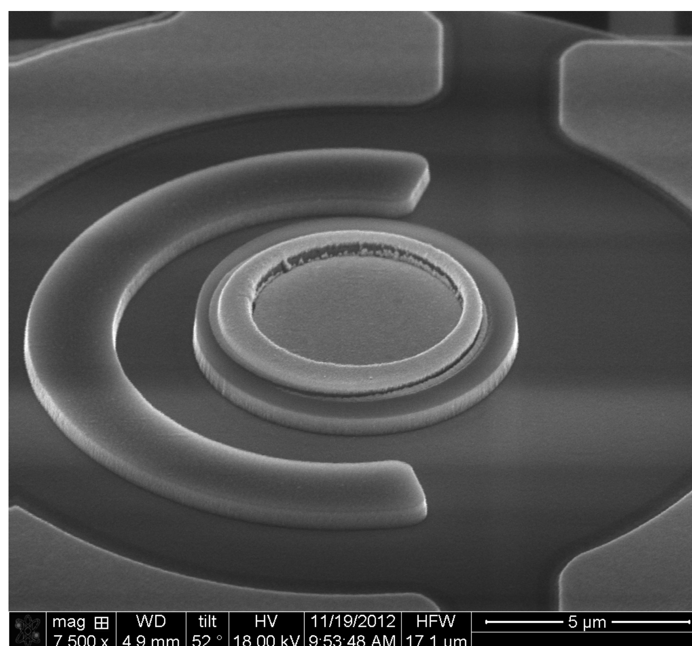

Figure 4.19: SEM image of a processed III-V ring heater around a microdisk laser.

these heaters. As bottom contact for the III-V heater the same contact as the microdisk laser is used, while at the top a separate contact is used. By injecting current in the III-V heater it will heat up the neighboring area including the microdisk, changing the refractive index of the microdisk material and results in a change in lasing wavelength. The distance between the heater and the microdisk should be chosen carefully. Bringer the heater closer to the microdisk will make the heater more efficient, but it cannot be placed too close as otherwise it will induce optical loss. The optimum distance depends on the radius of the microdisk. For the microdisks discussed here, the distance between the microdisk and the heater was set to 1.5 μm which was also the width of the heater itself. In Figure 4.19 a microscope image of a processed microdisk laser with III-V ring heater is shown.

Using the heater the microdisk laser can be trimmed around a certain azimuthal mode or it can be forced to work in a higher order azimuthal mode if the heater power is increased further. Figure 4.20(a) shows the optical spectrum of a microdisk laser as a function of heating power. In this particular case the laser was biased at a current of 1.4 mA. It can be seen that the lasing wavelength gradually shifts towards longer wavelengths when the heater power is increased. When a current of 3 mA is applied to the heater, the laser hops to the next azimuthal mode

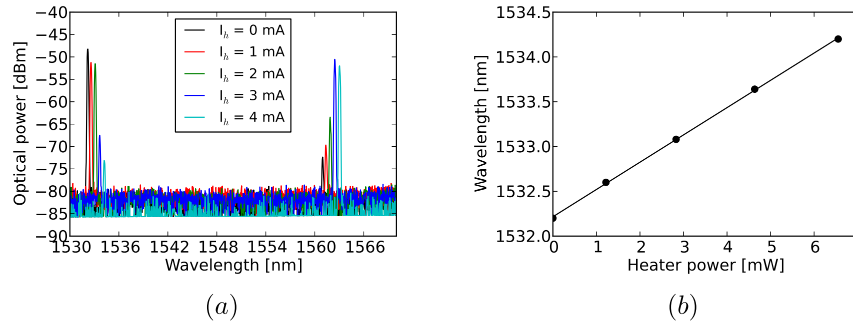

Figure 4.20: Influence of the III-V ring heater. (a) Optical spectrum of the microdisk laser for different drive currents of the heater. When the heater current is above 2 mA the lasing mode hops to the next azimuthal mode. (b) Plot of lasing wavelength versus heater power, the slope indicates an efficiency of 0.32 nm/mW.

about 30 nm further. The efficiency of the heater can be deduced from Figure 4.20(b) where the wavelength is plotted versus the heater power. From this figure it can be concluded that the efficiency of the heater is around 0.32 nm/mW.

MWL results

The complete spectrum of an MWL consisting of 8 lasers is shown in Figure 4.21. Obviously, the result is not as expected. First of all, the lasing wavelengths are not uniformly distributed over an FSR. This is most likely caused by rounding errors as the mask was designed on a 5 nm grid. Second, there is a clear degradation in output power of the laser array. The first laser, which is closest to the fiber coupler, has the highest output power. While the further the laser is positioned in the array, the lower is its output power. It appears that part of the light is coupled to higher order modes of subsequent disks. This was also reported in [13], but here the power loss is even stronger. The output power of laser 8 did not even come above the noise level of the spectrum analyzer, while laser 4 was electrically open circuited.

In order to verify the hypothesis that output light from a certain microdisk in the array is coupled to a higher order mode of a subsequent microdisk, the optical spectrum of one microdisk laser was recorded while the heaters around neighboring microdisks were tuned. When the heaters of neighboring disks are turned on, the resonances in these particular cavities will shift which should result in an increase or decrease in the measured output power of the laser that is turned on. Referring to Figure 4.18, the measurement scheme can be explained as follows: a measurement was performed where laser 3 was turned on, while laser 1 and 2 were turned off. Then, the heaters around laser 1 and 2 were turned on, while

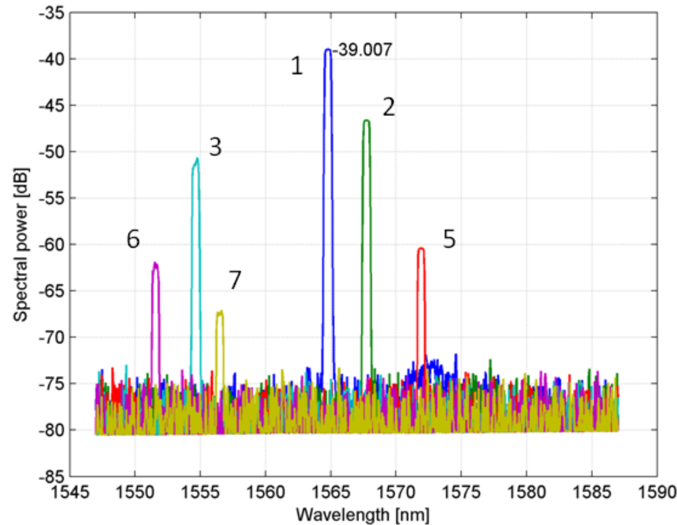

Figure 4.21: Optical spectrum of a multi-wavelength laser. Lasing wavelengths are not on a uniform grid and the output power collected at the fiber coupler decreases for microdisk lasers further in the array.

the output spectrum on the left FC was recorded. The output spectrum of laser 3, with heaters 1 and 2 turned off is shown in Figure 4.22(a). The maximum output power measured in the fiber was -74.1 dBm. If indeed some output light from laser 3 is coupled into a higher order mode of laser 1, then a change in output power should be observed when the heater of laser 1 is turned on, because the resonance in the cavity of laser 1 will shift. This is indeed the case as is shown in Figure 4.22(b). The output power of laser 3, measured in the fiber, has increased by 4.7 dB. The same situation, but now with heater 2 turned on, is shown in Figure 4.22(c). In this case the output power has increased by 4.8 dB. Finally, Figure 4.22(d) shows the output spectrum when both the heaters were turned on, which results in an increase of output power of 9.5 dB. Note that the wavelength of the active laser remains unchanged as no heating is applied to this laser. The current applied to the heaters to achieve maximum output power was 20 and 16 mA for heater 1 and heater 2 respectively. These high currents applied to the heaters to get maximum output indicate that a large wavelength shift is required. This can be expected because the higher order modes have much higher losses than the fundamental modes and are therefore undercoupled, which results in broader resonance dips. The result obtained here was actually the trigger for the detailed analysis on microdisk-waveguide coupling discussed in Chapter 2. The results from these simulations where used in the new design discussed in next section.

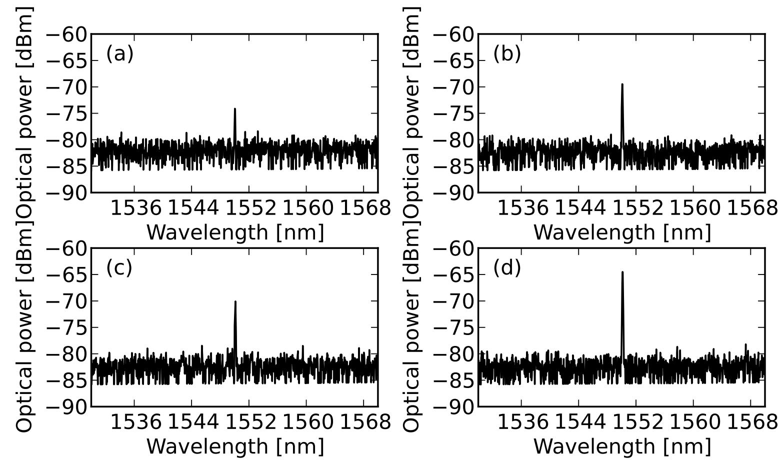

Figure 4.22: Optical spectrum of laser 3 in an array configuration of 8 microdisks to demonstrate the influence of coupling to higher order modes of neighboring microdisks. Output spectrum of laser 3 when the heaters 1 and 2 are turned off (a), when heater 1 is driven by a current of 20 mA (b), when heater 2 is driven by a current of 16 mA (c), when heater 1 is driven by a current of 20 mA and heater 2 by a current of 16 mA (d).

4.3 Run 3 results: UGent clean room

The results discussed in this section are based on samples processed in the clean room of Ghent University. The focus of this run was to fabricate both microdisk lasers and detectors on a single sample to establish an optical link on a silicon photonics platform. The results on the detectors and optical interconnects will be discussed in Chapter 5 and 6, respectively. Here, we will focus on the stand-alone performance of the microdisk lasers from this run.

An adhesive bonding method that allows for ultra-thin bonding layers was used on SOI dies with planarized top oxide. This made it possible to fabricate 2 samples with uniform bonding layer thicknesses of 170 and 250 nm. The details of this fabrication process will be covered in the next chapter about detectors as the microdisk laser is fabricated simultaneously with this detector.

As already became clear from the results in the previous sections, reflections from the fiber couplers have a significant impact on the performance of microdisk lasers. To minimize the influence of reflections from the fiber couplers, a new type of fiber coupler, designed by Vermeulen and coworkers [15], was used in this run. These fiber couplers were optimized to have minimum reflections, while maintaining the coupling efficiency of standard fiber couplers. However, the design used here was one of the first tests of these low reflection fiber couplers and due to a

mistake in the simulations no significant reduction of reflections was observed for the fiber couplers used here. The efficiency was with 16% also significantly lower than standard fiber couplers. It should be noted that these low reflection fiber couplers were further optimized and reflections lower than -40 dB have been shown experimentally [16].

Finally, it should be mentioned that the results discussed here are all obtained from the sample with 250 nm bonding layer thickness. The sample with 170 nm bonding layer thickness was exposed to an overetch of the disk cavity, resulting in too thin slab thicknesses and high series resistance. However, because the etch rate was not entirely uniform across the sample, good lasing behavior was obtained for microdisk lasers on specific areas on the sample, but no lasing was obtained in the stand-alone microdisk laser section which are the devices discussed here.

4.3.1 Pulsed performance

We again start by examining the performance of the microdisk lasers under pulsed drive conditions. The same experimental setup is used as for the devices discussed in the previous section. Here we compare 4 microdisk lasers, all with 7.5 μm diameter, but with minor differences in the design. The LI curves obtained for these 4 microdisk lasers are shown in Figure 4.23 and the design parameters which are different for each of these devices are written in the plots. The waveguide offset was designed to be the same for all these devices with a value of -300 nm. It was confirmed by a XSEM, that the waveguide offset was indeed the same, although a general misalignment of +120 nm was observed.

Threshold currents are very similar for all 4 devices with values in the order of 300 μA. A small kink is observed in the LI curves of device (a) and (c) which seems to originate from the pulsed current source as it does not occur in the CW measurements. The dashed output, corresponding with the output on the right side of the microdisk laser, is the highest in all cases. For a better comparison of the slope efficiencies, the left and right outputs of each microdisk laser are added together. This is also useful for fitting the simulation results obtained with Silvaco Atlas with the experimental results, as in the simulation clockwise and counterclockwise modes cannot be taken into account. The results for all 4 devices are shown in Figure 4.24. From this Figure it is clear that the slope efficiencies are also very similar, but the highest value is obtained for device (b) which has the smallest top contact. Simulations discussed in Section 2.3.2 on the influence of the top contact size on the optical losses showed that such a small contact should not cause any substantial losses. Therefore, it is more likely that the higher output power is due to the existence of multiple modes that are not suppressed by this small top contact. This will be analyzed in more detail in the next section on CW operation. The small variations in waveguide width seem to have almost no effect

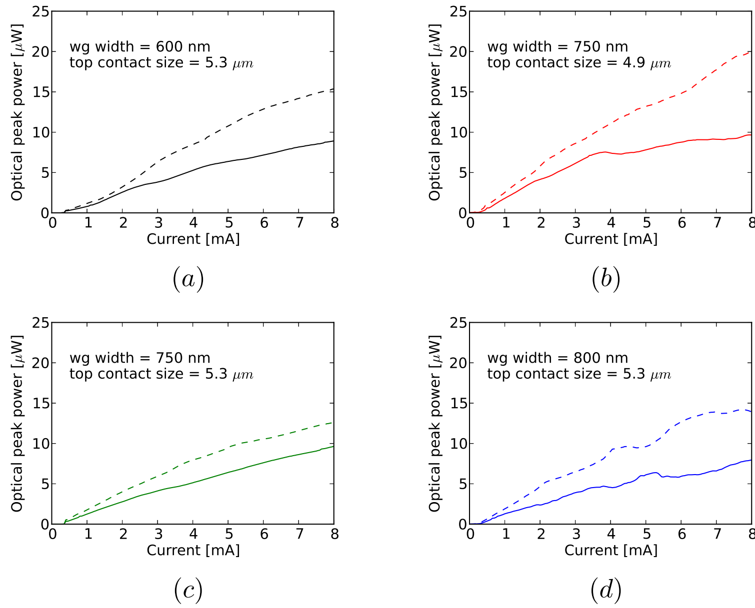

Figure 4.23: Measured LI curves for 4 different microdisk lasers under pulsed drive conditions. Solid lines represent the left output and dashed lines the right output. The power is the fiber coupled peak output power.

on the slope efficiency, which is in agreement with the results discussed in Chapter 2, where it was found that the coupling between the fundamental WGM and the fundamental waveguide mode does not change significantly for small waveguide variations.

It is also interesting to note that the physical distance between device (a) and (d) on the sample is 2 mm, and yet still quite uniform performance is obtained in terms of threshold current and slope efficiency. This indicates that the bonding layer thickness is uniform across the sample.

4.3.2 CW performance

The CW performance of the microdisk lasers is shown in Figure 4.25. Just as in the case of pulsed drive conditions we find that the output on the right side is the highest in all cases and just as for the CW results of the devices in the second CMOS run, oscillations in the LI curves are observed. The consequent higher output power from the right side could be an indication that there was a problem in collecting the light from the fiber coupler on the left side, e.g. a slightly different fiber angle, resulting in a wavelength shift of the transmission spectrum and thus a lower coupling efficiency at the lasing wavelength. The threshold currents are

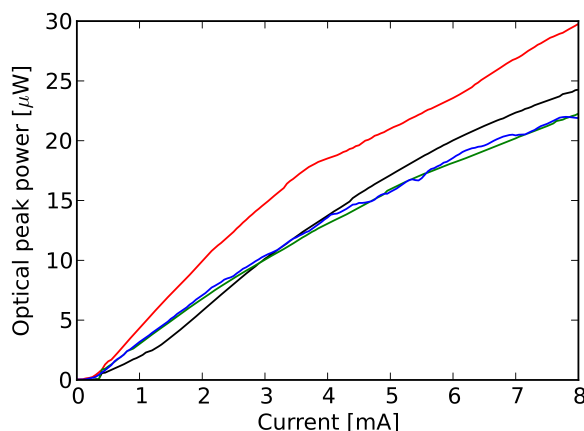

Figure 4.24: Measured LI curves for 4 different microdisk lasers under pulsed drive conditions where the left and right output are added together. The power is the fiber coupled peak output power.

with values between 350 and 450 μA slightly higher than the values obtained under pulsed drive conditions.

When we compare the IV curves of the different microdisk lasers, we see a clear trend of decreasing series resistance from device (a) to (d). This result reflects the non-uniform etching process of the microdisk laser cavity. The microdisk cavities are not completely etched through the III-V stack, such that a thin bottom contact slab is left for electrical injection. Obviously the resistance of this bottom contact slab increases with decreasing thickness. Due to the non-uniform etching process the bottom contact slab thickness varies across the sample. Device (a) is positioned most left on the sample and for devices in this region high series resistance is observed, while device (d) is positioned most to the right where lower contact resistances are observed. The series resistance also has a clear impact on the LI curves, as the self heating is more severe when the series resistance is higher. This effect is most clear when we again plot the combined output collected at the left and right side for all the devices as shown in Figure 4.26. In order the analyze whether the output power for device (b) is higher due to lower losses induced by the metal or is caused by the existence of multiple modes, the optical spectra need to be analyzed.

Influence of top contact size

For the fabrication of the top contact, a new self-aligned process was developed, which results in perfect alignment. This process will be described in Section 5.3.2.

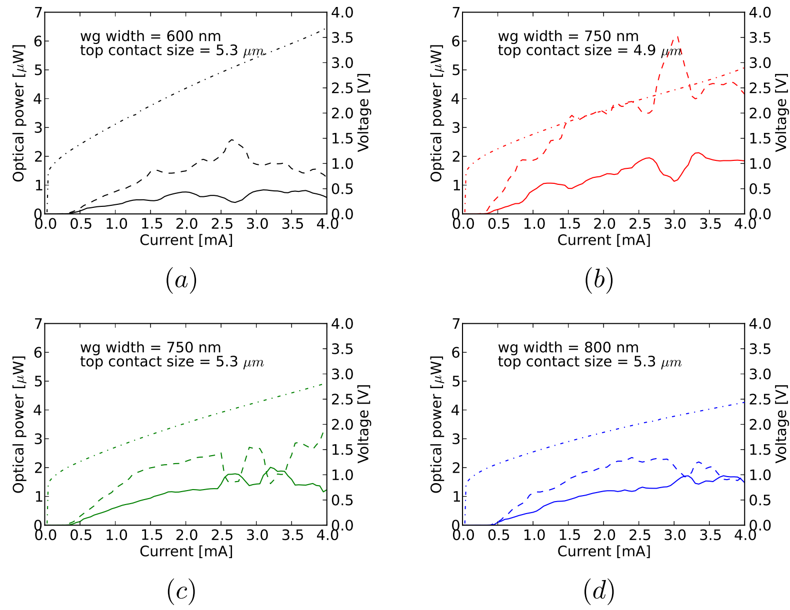

Figure 4.25: Measured LI curves for 4 different microdisk lasers under CW drive conditions. Solid lines represent the left output and dashed lines the right output. The power is the fiber coupled output power.

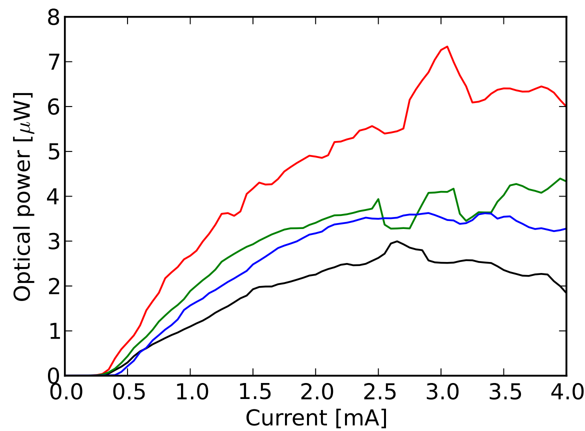

Figure 4.26: Measured LI curves for 4 different microdisk lasers under CW drive conditions where the left and right output are added together. The devices and corresponding colors are the same as in Figure 4.25. The power is the fiber coupled output power.

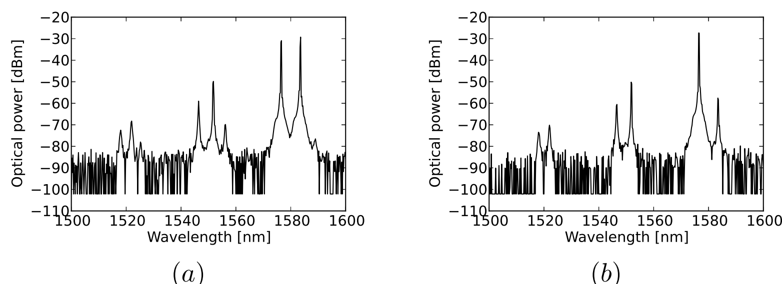

Figure 4.27: Measured optical spectra for a microdisk laser with a 4.9 μm (a) and a 5.3 μm (b) top contact. Suppression of higher order modes is not sufficient in case of the smaller top contact as the device is multimode.

However, the size of the top contact was a little bit smaller than intended, due to the slightly positive angle of the photoresist and the hard mask, that was not taken into account during the design. Therefore, losses induced by the top metal are expected to be negligible, but on the other hand the suppression of higher order modes might not be sufficient. The spectra of device (b) and (d) were recorded at a drive current of 1.5 mA under CW operation and are shown in Figure 4.27. In both spectra three azimuthal mode orders can be recognized separated by an FSR of 32 nm. Next to the different azimuthal modes, there are also other higher order modes visible in both spectra indicating that the top contact size is indeed not sufficient to suppress higher order modes. In Figure 4.27(a), which corresponds with device (b) that has the smallest top contact, 3 peaks are visible around each azimuthal mode order, while for the device with a slightly larger top contact, device (d), shown in Figure 4.27(b) only 2 peaks are visible per azimuthal mode order. Clearly, the device with the small top contact is multimodal as the power of the two neighboring modes is almost equal. This explains the higher output power observed in the LI curves for this microdisk laser. The device with the larger top contact is in the single mode regime at this drive current as the side mode suppression ratio (SMSR) is > 20 dB.

On the same run there were also microdisk lasers included with a diameter of 10, 15 and 20 μm. In all cases lasing was obtained where the threshold currents were in the order of 0.55, 1 and 1.8 mA, respectively. The single sided slope efficiencies were in the order of 1, 1.3 and 0.25 $\mu W/mA$, respectively.

4.3.3 Temperature dependence

As there are a few differences in the design of the microdisk lasers compared to the devices processed in the CMOS pilot line discussed in the previous section, a thermal analysis was performed again to be able to make a comparison. First of all, the cladding and bonding material used in this run is BCB, while in the

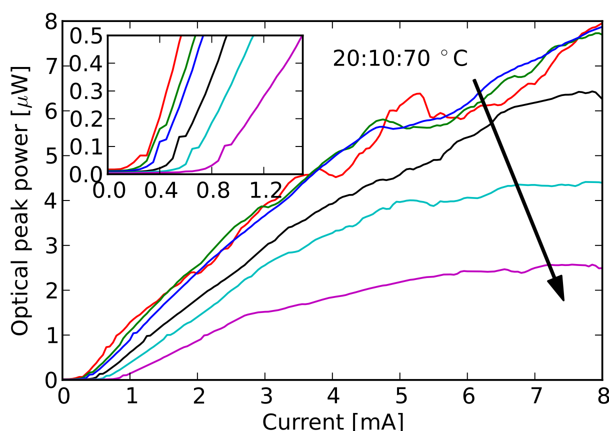

Figure 4.28: LI curves measured under pulsed operation at elevated temperatures. The slope efficiency decreases and the threshold current (inset) increases at higher temperatures. The power is the fiber coupled peak output power.

CMOS run silicon oxide was used. The thermal conductivity of BCB is about a factor of 4 lower compared to silicon oxide, which obviously has a negative influence on the thermal resistance. Second, a Ti/Pt/Au metal stack was used in this run, while in the CMOS run a Ti/TiN/AlCu metal stack was used as Au is not allowed in a CMOS environment. To reduce the thermal resistance in this run an extra layer of Au with a thickness of 600 nm covering a larger area was deposited over the top contact to spread out the heat as proposed and demonstrated in [2]. Figure 4.28 shows the LI curves of a 3.75 μm radius microdisk laser measured under pulsed drive conditions at different ambient temperatures, ranging from 20 to 70 degrees C. As can be seen there is still laser action at a temperature of 70 degrees C, but the maximum output power decreased from 8 to 2.5 μW, while the threshold current increased from 0.3 to 0.8 mA. From the threshold currents and the slope efficiencies in this plot the characteristic temperatures T_0 and T_1 can be determined as described in the previous section. The resulting fits are shown in Figure 4.29.

The characteristic temperature T_0 was found to be 43.73 °C and is considerably lower than the value of 66.33 °C found for the devices from the CMOS run. The devices here seem to be significantly more sensitive to temperature variations. On the other hand, the value of T_1 appears to be significantly higher compared to the devices from the CMOS run, implying the slope efficiency is less temperature sensitive. This seems to be a bit contradictory. In an attempt to clarify this, another measurement on the same sample, but now on a 5 μm radius microdisk laser, was

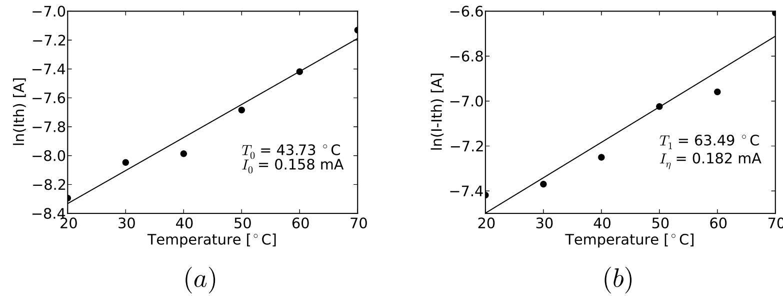

Figure 4.29: Extraction of characteristic temperatures T_0 and T_1 for a 7.5 μm diameter microdisk laser.

performed which yielded values of 44.07 and 34.70 °C for T_0 and T_1, respectively. The value found for T_0 is in good agreement with the result obtained for the 3.75 μm radius microdisk laser, while T_1 is almost twice as low. Based on this result it was concluded that the values found for T_1 are not reliable. Nevertheless, the temperature dependence of the threshold current for these devices is clearly larger than for the devices from the CMOS run.

Using spectral measurements versus drive current and temperature, the thermal resistance of the microdisk lasers was determined. The wavelength shift versus temperature was found to be 103 pm/K, as can be in Figure 4.30(a). This value is slightly larger compared to that found in the CMOS run, which was 88.5 pm/K. Most likely this is because of the higher mode confinement due to a thinner bottom contact layer. The wavelength shift versus dissipated power is shown in Figure 4.30(b) and has a slope of 0.593 nm/mW. This leads to a thermal resistance of 5.76 K/mW and this is considerably lower as compared to the value of 7.84 K/mW found for the devices in the CMOS run. For the 5 μm radius microdisk laser the wavelength shift versus current was measured to be 0.525 nm/mW, while the wavelength shift versus temperature was not measured for this device. However, assuming a value between 88.5 and 103 pm/K based on the previous results, this leads to a thermal resistance between 5.10 and 5.93 K/mW. It can be concluded that the heat spreader layer reduced the thermal resistance by more than 25%.

4.3.4 Multi-wavelength laser

In this run we again included a multi-wavelength laser based on an array of microdisk lasers. In the previous run, a strong degradation in output power was observed for microdisk lasers further away from the fiber coupler. This was attributed to coupling to higher order modes of subsequent microdisks. For the design in this run we made use of the simulation results on the coupling between a

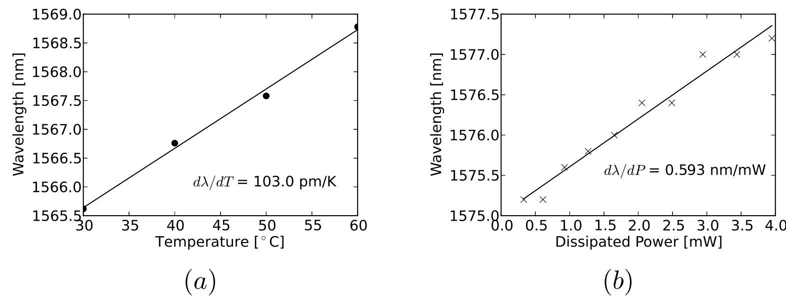

Figure 4.30: Plots to deduce the thermal resistance of the microdisk lasers. Impact on lasing wavelength as a function of ambient temperature (a) and as function of dissipated power (b) for a 7.5 μm diameter microdisk laser.

microdisk laser and a silicon waveguide as discussed in Section 2.4. The coupling was optimized to have only efficient coupling between the fundamental WGM and the fundamental waveguide mode. An array of 8 microdisk lasers with slightly different radii that are coupled to a single silicon waveguide was designed. The waveguide width was designed to be 750 nm. The optical spectrum of the MWL is shown in Figure 4.31, where all the microdisk lasers are driven at a 1 mA current. Microdisk laser number 8 appeared to be short-circuited. The microdisk lasers are not single mode, which is due to the top contact that is slightly undersized. The arrows above the figure indicate the modes of interest. As can be seen, there is no clear correlation anymore between the position of the microdisk laser in the array and the output power. The largest amount of difference in output power is between the red and yellow mode and is around 7 dB. It is not clear whether this is still caused by coupling to another higher order mode or a lower efficiency of this particular microdisk laser. Nevertheless, in terms of output power uniformity the result obtained here is significantly better then the result obtained in the second CMOS run.

However, again no uniform wavelength spacing is obtained. This was somewhat expected because also this mask was designed on a 5 nm grid and in this fabrication process contact lithography was used to define the microdisk patterns, which is known to have limited resolution. Electron beam patterning, which is known to have very high resolution, was originally planned for this design run. However, due to issues with the alignment structures this was not possible. To get the microdisk lasers on the targeted grid III-V ring heaters were included in the design. Unfortunately, it was found that all heaters were open-circuited, most likely due to a too short etch for opening the contact windows in the cladding. Therefore, the output power of the microdisk lasers was altered by changing the current, such that through self-heating the wavelength shifts to the desired position

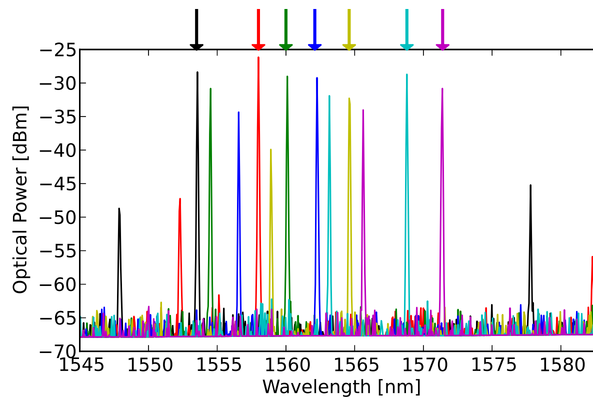

Figure 4.31: Measured optical spectrum of a multi-wavelength laser based on 7 microdisk lasers, coupled to a single waveguide. All microdisks are driven at a 1 mA current, no clear degradation in output power versus the distance to the fiber coupler is observed.

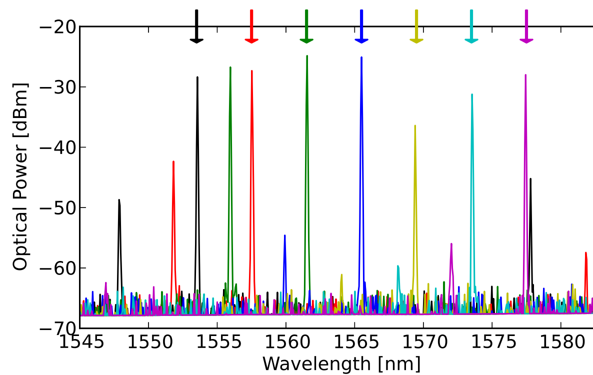

Figure 4.32: Measured optical spectrum of a multi-wavelength laser based on 7 microdisk lasers, coupled to a single waveguide. The applied current to each microdisk laser is adapted such that a uniform wavelength spacing is obtained.

in the spectrum. The result is shown in Figure 4.32. This method obviously comes at the cost of higher non-uniformity in terms of output power. By using a mask designed on a 1 nm grid, it is expected that an array of 8 microdisk lasers becomes more feasible.

Device	*on silicon*	*Size*	I_{th}	P_{max}	*Slope efficiency*	*Bandwidth*
CMOS run 1	Yes	D=40 μm	6 mA	132 μW	0.006 W/A	-
CMOS run 2	Yes	D=7 μm	0.6 mA	38.5 μW	0.05 W/A	7.8 GHz
UGent CR run 3	Yes	D=7.5 μm	0.45 mA	290 μW	0.11 W/A	7.6 GHz
PICMOS microdisk laser [4]	Yes	D=7.5 μm	0.5 mA	10 μW	0.02 W/A	3.5 GHz
Microring laser [17]	Yes	D=50 μm	10 mA	1.2 mW	0.1 W/A	-
PhC laser [18]	No, InP	$4 \times 0.3\ \mu m$	4.8 μA	8.75 μW	0.1 W/A	12 GHz

Table 4.1: Comparison of the (CW) performance at room temperature of microdisk lasers from different runs together with some important results found in literature.

4.4 Comparison between generations

In order to compare the results between the different generations we here briefly summarize the main characteristics of the microdisk lasers in Table 4.1. As a reference some other electrically injected micro lasers are are included as well. These are the microring laser on silicon demonstrated by Liang and co-workers [17], the microdisk laser on silicon developed in the EU FP6 PICMOS project [4] and the Photonic Crystal laser on InP demonstrated by [18].

For the microdisks and -ring, the size is specified by the outer diameter and the maximum output power and slope efficiency are determined by combining the output from both sides. The devices from CMOS run1 and PICMOS are an exception, as only data was available from one side.

Clearly, the smallest laser also having the lowest threshold current and the highest modulation bandwidth is the PhC laser. However, this laser is fabricated on an InP platform, while the other lasers are on a silicon platform. When comparing the microdisk lasers fabricated in this work, we observe an improvement in performance from the first CMOS run, where only the large microdisks showed lasing, to the second CMOS run, where microdisks down to 6 μm in diameter showed lasing. With these runs we demonstrated the feasibility to fabricate these lasers on 200 mm waferscale with standard CMOS technology. The best performing microdisk lasers were obtained in the last run and were fabricated on individual samples in the clean room of Ghent University. The slope efficiency of these lasers is similar to that of the microring laser and the PhC laser on InP. As mentioned in the introduction of this chapter, the CMOS fabrication runs were executed in the first and second year of this PhD. Therefore, these runs do not include all optimizations found from the simulations discussed in Chapter 2. Furthermore, the development of the CMOS fabrication process itself for these III-V structures was also part of the WADIMOS project. For the final run on the other hand, we were able to include all the results from the simulations in the designs and optimizations in the fabrication process could be implemented more quickly. Therefore, this run yielded the best results.

4.5 Conclusions

We discussed the experimental results of microdisk lasers fabricated on a 200 mm wafer scale in a CMOS pilot line and on individual samples fabricated in the clean room of Ghent University. The first CMOS run only resulted in a limited number of working microdisk lasers due to a Titanium ring residue around the microdisk cavities causing excessive absorption. Therefore, only the larger microdisks were lasing.

In the second CMOS run, microdisk lasers with diameters between 6 and 40 μm showed lasing. The best performance was obtained for microdisk lasers with diameters around 7 μm. Threshold currents of 0.6 mA were measured for these devices, together with a (total) slope efficiency of 0.05 W/A. A maximum small-signal modulation bandwidth of 7.8 GHz was obtained. Strong oscillations were observed in the LI curves under CW operation and are attributed to external reflections from the fiber couplers. On this run also multi-wavelength lasers were fabricated, but the output power of the microdisk lasers degraded significantly for microdisks further away in the array. This was attributed to coupling to higher order modes of neighboring microdisks. This was the trigger for the analysis on the coupling between microdisks and access waveguides discussed in Chapter 2.

In the fabrication run in the UGent clean room two individual samples were fabricated with different bonding layer thicknesses. However, due to a strong over etch of the bottom contact layer, individual microdisk lasers could only be characterized on 1 sample. However, the microdisk lasers with integrated detectors were working on both samples and this still allowed us to analyze the performance of microdisk lasers on both samples. These results will be discussed in Chapter 6. Because the best microdisk laser performance was measured on structures with integrated detectors, this result was used in the overview table in the previous section. This run also contained multi-wavelength laser designs where the coupling conditions were adjusted based on the simulations discussed in Chapter 2. It is shown that with these optimized coupling conditions the output power of the microdisk lasers no longer depend on the position of the microdisks in the array, which is a significant improvement over the result obtained in the second CMOS run.

References

[1] R Tkach and AR Chraplyvy. *Regimes of feedback effects in 1.5-m distributed feedback lasers*. Lightwave Technology, Journal of, LT-4(11):1655–1661, 1986.

[2] Liu Liu, Rajesh Kumar, Koen Huybrechts, Thijs Spuesens, G. Roelkens, E.J. Geluk, T. De Vries, Philippe Regreny, D. Van Thourhout, Roel Baets, and G Morthier. *An ultra-small, low-power, all-optical flip-flop memory on a silicon chip*. Nature Photonics, 4(3):182–187, 2010.

[3] Dirk Taillaert, Frederik Van Laere, Melanie Ayre, Wim Bogaerts, Dries Van Thourhout, Peter Bienstman, and Roel Baets. *Grating Couplers for Coupling between Optical Fibers and Nanophotonic Waveguides*. Japanese Journal of Applied Physics, 45(No. 8A):6071–6077, August 2006.

[4] J Van Campenhout, P Rojo Romeo, P Regreny, C Seassal, D Van Thourhout, S Verstuyft, L Di Cioccio, J-M Fedeli, C Lagahe, and R Baets. *Electrically pumped InP-based microdisk lasers integrated with a nanophotonic silicon-on-insulator waveguide circuit.* Optics express, 15(11):6744–9, May 2007.

[5] Joachim Piprek. *Semiconductor optoelectronic devices: introduction to physics and simulation*. Academic Press, 2003.

[6] Stevan Stankovic. *Hybrid III-V / Si DFB Lasers Based on Polymer Bonding Technology*. PhD thesis, Ghent University, 2013.

[7] G. Ghosh. *Handbook of thermo-optic coefficients of optical materials with applications*, volume 5. Academic Press, 1998.

[8] F.G. Della Corte, Giuseppe Cocorullo, Mario Iodice, and Ivo Rendina. *Temperature dependence of the thermo-optic coefficient of InP, GaAs, and SiC from room temperature to 600 K at the wavelength of 1.5 m.* Applied Physics Letters, 77(11):1614, 2000.

[9] LA Coldren and SW Corzine. *Diode lasers and photonic integrated circuits*. Wiley-Interscience, 2012.

[10] Joris Van Campenhout. *Thin-Film Microlasers for the Integration of Electronic and Photonic Integrated Circuits*. PhD thesis, Ghent University, 2007.

[11] AN Al-Omari and KL Lear. *Low current density, inverted polarity, high-speed, top-emitting 850 nm vertical-cavity surface-emitting lasers*. Opto-electronics, IET, 1(5):221–225, 2007.

[12] SJ Choi, Zhen Peng, and Qi Yang. *Eight-channel microdisk CW laser arrays vertically coupled to common output bus waveguides*. Photonics Technology Letters, IEEE, 16(2):2–5, 2004.

[13] Joris Van Campenhout, Liu Liu, Pedro Rojo Romeo, Dries Van Thourhout, Christian Seassal, Philippe Regreny, Lea Di Cioccio, Jean-Marc Fedeli, and Roel Baets. *A Compact SOI-Integrated Multiwavelength Laser Source Based on Cascaded InP Microdisks*. IEEE Photonics Technology Letters, 20(16):1345–1347, August 2008.

[14] Liu Liu, Thijs Spuesens, Günther Roelkens, D. Van Thourhout, Philippe Regreny, and P. Rojo-Romeo. *A Thermally Tunable IIIV Compound Semiconductor Microdisk Laser Integrated on Silicon-on-Insulator Circuits*. Photonics Technology Letters, IEEE, 22(17):1270–1272, 2010.

[15] D Vermeulen, Y De Koninck, Y Li, E Lambert, W Bogaerts, R Baets, and G Roelkens. *Reflectionless grating couplers for Silicon-on-Insulator photonic integrated circuits*. Optics express, 20(20):1919–1921, 2012.

[16] Yanlu Li, Steven Verstuyft, Gunay Yurtsever, Shahram Keyvaninia, Gunther Roelkens, Dries Van Thourhout, and Roel Baets. *Heterodyne laser Doppler vibrometers integrated on silicon-on-insulator based on serrodyne thermo-optic frequency shifters.* Applied optics, 52(10):2145–52, April 2013.

[17] D Liang, M Fiorentino, S Srinivasan, S.T Todd, G Kurczveil, John E. Bowers, and Raymond G Beausoleil. *Optimization of Hybrid Silicon Microring Lasers*. IEEE Photonics Journal, 3(3):580–587, 2011.

[18] K Takeda, T Sato, A Shinya, and K Nozaki. *Few-fJ/bit data transmissions using directly modulated lambda-scale embedded active region photonic-crystal lasers*. Nature Photonics, 7(July):569–575, 2013.

5 Detectors

In the previous sections we focused on the design of a microdisk laser as a compact source for an optical interconnect. In this chapter we will have a closer look at the design of a compact detector. Also the fabrication process that allows for simultaneous fabrication of microdisk lasers and detectors will be explained.

5.1 Detectors on Silicon

Silicon is transparent for wavelengths in the telecommunication window. It is therefore not a suitable material to make detectors at these wavelength ranges. In Section 1.4, we have already seen that other materials are combined with silicon to be able to integrate lasers and detectors. For detector integration on silicon at telecommunication wavelengths, the most suitable materials are Ge and InGaAs.

Next to the detector material also different types of detectors exist. The most commonly used types are so called pin diodes and metal-semiconductor-metal (MSM) Schottky barrier diodes. A pin diode consists of an undoped absorbing region that is sandwiched between a p-doped and n-doped region. Typically the doped regions are heavily doped such that ohmic contacts can be formed with the contact metals. Because of the doped regions, a build-in electric field exists over the intrinsic region. A photon entering the intrinsic region of the photodiode will generate an electron-hole pair and due to the electric field the photogenerated electron is swept to the n-side region, while the photogenerated hole is swept to the p-side. This results in a drift current that flows in the reverse direction. By ap-

plying a reverse bias to the diode the depleted region can be increased somewhat, resulting in a slightly higher responsivity and a reduced junction capacitance and thereby a reduced RC time constant.

An MSM detector consists of an absorbing layer on which interdigitated electrodes are placed to form two back-to-back contacted Schottky diodes. When the two Schottky diodes are not biased the structure is symmetrical and hence no electric field exists. Photogenerated electron-hole pairs are trapped in a potential well and no photocurrent is generated. When a large enough voltage is applied, the potential barrier for the photogenerated electron-hole pairs disappears and the electric field will have the same direction over the structure and a photocurrent will flow. An MSM detector is typically easier to fabricate because of its planar structure, but there can be some difficulties with the reliability of the contacts. It also has a smaller capacitance per unit area compared to PIN detectors, making it possible to achieve high bandwidths. The responsivity is typically lower due to the absorption by the metal contacts.

For the integration of photodetectors on silicon, there are basically three coupling schemes that can be used to couple the light from the silicon waveguide into the detector. First there is the vertical coupling scheme. In this case a diagonal mirror or a diffractive structure is etched in the silicon such that the light is reflected or diffracted upwards. When a III-V detector is used, which has a vertical diode structure, a trade-off has to be made between responsivity and bandwidth. The second approach is a butt-coupling scheme. Here a recess is etched in the silicon such that the detector can be placed in the same vertical plane as the waveguide. The last option is an evanescent coupling scheme as also used for the microdisk laser. In this case the detector needs to be brought sufficiently close to the waveguide. Both for the butt-coupled and evanescently coupled detector a lateral or vertical diode structure can be used. As the light propagates through the detector in the longitudinal direction, no trade-off between bandwidth and responsivity needs to be taken into account.

5.1.1 State-of-the-art

In recent years several detectors on silicon have been successfully demonstrated. In 2007 Vivien and coworkers demonstrated a Ge MSM detector with a high responsivity of 1 A/W together with a bandwidth of 25 GHz [1]. The dark current of this detector was with 130 μA very high. In 2008 Luxtera presented a Ge PIN detector with a responsivity of 0.85 A/W and a bandwidth in excess of 20 GHz [2]. Also in this case the dark current was in the μA range. However, this was the world's first demonstration of a monolithic high-speed optical receiver based on Ge waveguide photodetectors. A Ge detector with a dark current below 1 μA was demonstrated by Intel [3]. More recently several high-speed Ge detectors that also

have low dark current have been reported [4, 5].

Also several III-V based detectors on silicon have been demonstrated. An evanescent MSM detector was demonstrated by Brouckaert et al. A responsivity of 1 A/W and a dark current of 4.5 nA was obtained [6]. Another example of an InGaAs MSM photodetector is reported in [7]. This detector has a responsivity of 0.94 A/W and a dark current of 20 nA. It is capable of receiving data at a rate of 10 Gbps. An evanescent PIN detector was developed by Binetti and coworkers [8]. For this detector light was coupled from a silicon waveguide to an InP waveguide that had an InGaAs absorbing section at the end of this InP waveguide. This device had a responsivity of 0.45 A/W and a bandwidth of 33 GHz, while the dark current was as low as 1.6 nA.

In order to be able to make flexible optical interconnects, it is desirable to be able to place the optical transmitters and receivers anywhere on the chip in a compact area. If for instance a bidirectional link is required, a compact transceiver block consisting of a laser and optionally a modulator and detector is needed. This asks for an integration scheme that allows these different structures to be processed in close proximity. The Ge based detectors discussed above can be integrated with silicon modulators [9], but it becomes more complicated when also the lasers need to be integrated. In principle an off-chip laser approach can be used, but this comes at the cost of extra coupling losses and when multiple links across the chip are required waveguide routing issues might be encountered. Some III-V detectors that can be co-integrated with lasers have also been proposed [10, 11], but either the bandwidth or the responsivity is low in these cases.

5.1.2 Proposed integration scheme

Here we propose to use an epitaxial material stack that contains both quantum well layers for the laser as well as a bulk region to make efficient detectors. In this configuration the detector layers are stacked on top of the laser. This approach has the advantage that both lasers and detectors can be processed right next to each other in this material stack and allows for very compact integration of transceivers on silicon. Figure 5.1 shows the proposed integration scheme next to the approach where separate III-V dies are used for the laser and detector. The spatial limitation in case of separate dies is overcome with the proposed scheme.

5.2 Design and simulations

A schematic representation of the proposed detector is shown in Figure 5.2. It consists of a 400 nm i-InGaAs layer sandwiched between a 100 nm heavily doped p-type InGaAs top contact layer and an 80 nm n-type InP bottom contact layer that also serves as the top contact of the laser. It has a waveguide type design where,

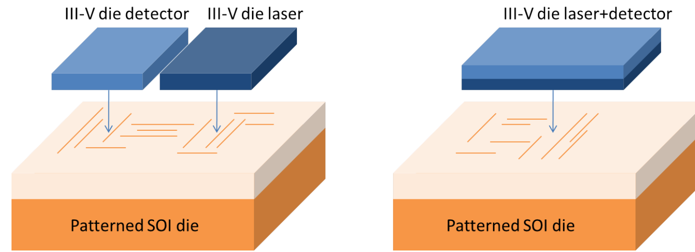

Figure 5.1: Schematic representations showing the spatial limitation when using separate III-V dies for the laser and detector (a) and the proposed design to overcome this limitation (b).

similar to the microdisk laser, an evanescent coupling scheme is used to couple light from the underlying SOI waveguide to the detector. For the waveguide under the detector 500 nm and 3 μm wide variants were designed. The height of the waveguide is 220 nm. Detector lengths vary between 20 and 80 μm and mesa widths of 3.5 and 5 μm were designed. The length variation was applied to find an optimum for both the responsivity and dark current. A longer detector will have higher responsivity, but at the same time the increased sidewall surface area will result in higher dark current.

5.2.1 Epitaxial structure

The details of the epitaxial structure are depicted in Table 5.1. The thickness of the laser and detector layers is only 583 nm and 580 nm, respectively. Note that because the top contact layer of the laser and the bottom contact of the detector are shared the total thickness of the stack is only 1083 nm. If a laser is required at a certain position on the sample the detector layers can simply be removed by a wet etching step. On the other hand, if a detector is required the laser layers remain intact under the detector.

5.2.2 Optical modes

The detector is based on a waveguide type design where light is coupled from the waveguide to the detector through an evanescent coupling scheme. The phase matching condition is, compared to the microdisk laser, easier to satisfy for the detector because the light does not necessarily need to couple to a specific mode. As the stack is a few micrometer wide and also about 1 μm high, a large amount of optical modes can exist in the detector. The main requirements for the coupling are that the detector modes have sufficient overlap with the silicon waveguide mode to ensure efficient coupling from waveguide to detector and that the detector modes to which the light is coupled have sufficient overlap with the absorption section of

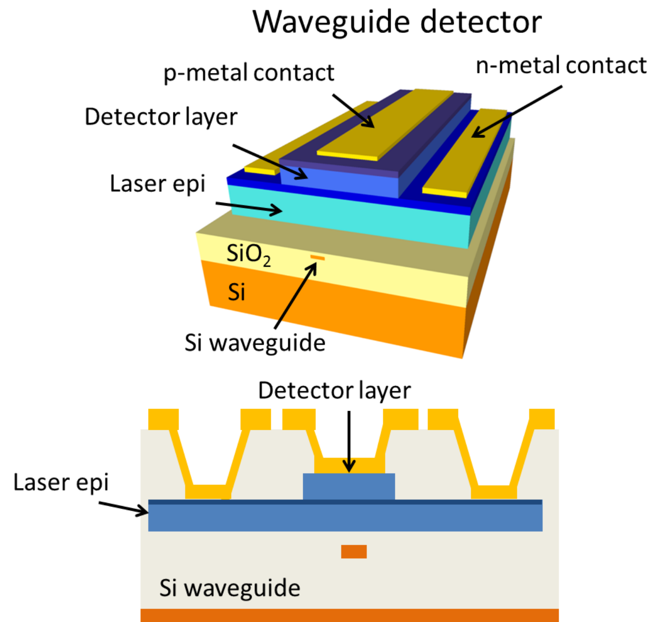

Figure 5.2: Schematic overview of the detector design, where (a) shows a 3D impression and (b) shows the cross section of the detector.

Layer	*Composition*	*Doping*	*Thickness*
Detector P	InGaAs	P++ $1 \times 10^{19} cm^{-3}$	100 nm
Detector nid	InGaAs	nid	400 nm
Detector/laser N	InP	N+ $5 \times 10^{18} cm^{-3}$	80 nm
Tunnel junction	Q1.3	N++ $1 \times 10^{19} cm^{-3}$	20 nm
Tunnel junction	Q1.3	P++ $2 \times 10^{19} cm^{-3}$	20 nm
Laser diode P	InP	P+ $1 \times 10^{18} cm^{-3}$	135 nm
SCH	Q1.2	nid	25 nm
3x barrier	Q1.2	nid	3x15 nm
3x QW	InAsP	nid	3x6 nm
SCH	Q1.2	nid	25 nm
Laser diode N	Q1.2	N+ $1 \times 10^{18} cm^{-3}$	120 nm
Laser N contact	InP	N+ $5 \times 10^{18} cm^{-3}$	95 nm

Table 5.1: Epitaxial structure containing the layers for both the laser and detector.

Material	*Refractive index*	*Absorption coefficient [cm^{-1}]*	*Reference*
$In_{0.53}Ga_{0.47}As$	3.595	7820	[12]
$InAs_{0.65}P_{0.35}$ QW	3.633	4000	[13]
InP	3.18	-	-
$In_{0.8}Ga_{0.2}As_{0.44}P_{0.56}$	3.328	-	-
Ti	3.69	374560	[14]
Si	3.48	-	-
SiO_2	1.44	-	-

Table 5.2: Material parameters used for the detector simulation.

the detector. Concerning the first requirement it is obvious that the bonding layer thickness should be as thin as possible as this will increase the overlap between the waveguide and detector modes. However, when both lasers and detectors need to be integrated a trade-off needs to be made to have acceptable coupling for both. The coupling conditions for a microdisk laser are much more critical compared to the coupling conditions for the detector. Therefore, we choose to optimize the coupling for the microdisk laser and adapt the detector design to this coupling gap.

In order to calculate the different optical mode profiles, the detector structure was simulated using the commercial software package Fimmwave. As the complete epitaxial structure contains quite some layers which have similar refractive index but e.g. different doping levels, the structure was slightly simplified for the simulation where the layers with similar refractive indices were grouped together. Furthermore, the top metal was taken over the full width of the detector mesa, thereby overestimating the influence of the metal layer. The height of the detector mesa is fixed by the epitaxial structure and is 1083 nm, while the mesa width can be optimized. However, from a processing point of view a mesa width of a few micrometer is desirable. We here assume a mesa width of 3.5 μm. The refractive indices of the materials used are given in Table 5.2.

Given these geometrical parameters and the refractive indices of the III-V materials, it is already clear that phase matching with the silicon waveguide mode will occur for higher order modes in the detector. Therefore, first an extensive modelist of the detector structure was build. From this list it was found that there exists a third order vertical hybrid mode with an effective index of 2.81, which is close to the effective index of the silicon slab mode which is 2.82. Thus, by using a silicon waveguide of at least 2 μm wide, phase matching can be obtained. The confinement factors of this mode for the quantum well and absorbing layer of the detector are calculated to be 1.2% and 8.5%, respectively. Another variant of the third order vertical mode, but now also higher order in the horizontal direction is found to have an effective index of 2.59, coming close to that of a 500 nm wide silicon waveguide. The mode profiles of these two modes are shown in Figure 5.3. When the detector mesa width is varied between 2 and 5 μm, it has almost no

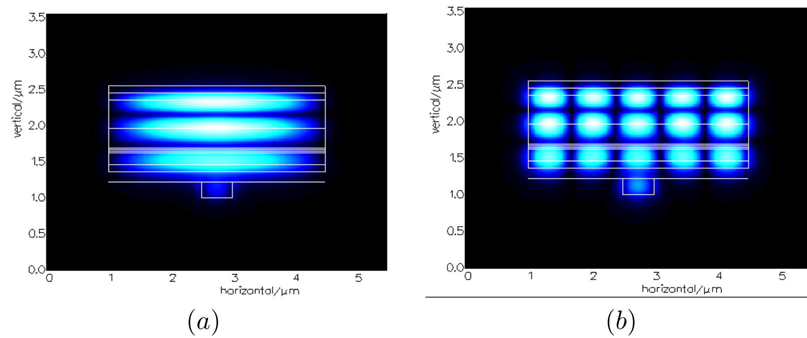

Figure 5.3: Detector mode profiles that have both overlap and approximate phase matching with the silicon waveguide mode.

influence on the third order vertical mode and so the effective index is insensitive for these mesa width variations. The other mode which is higher order in the horizontal direction is obviously confined by the mesa width and therefore, this mode is more sensitive to width variations of the mesa. However, as many modes, of which some have very similar effective index, can exist in the detector structure, it is difficult to tell to which mode the light will couple. More insight can be obtained by performing a propagation simulation.

5.2.3 Optical absorption versus length

Based on the mode profiles obtained with Fimmwave, the coupling from the silicon waveguide mode to the detector modes and the absorption in the detector was analyzed with Fimmprop, the propagation module of Fimmwave. Light is injected from the left side in a silicon waveguide of 1 μm length followed by the detector structure. Figure 5.4(a) shows the intensity profile in the detector after 2 μm, when light is injected in a 500 nm wide silicon waveguide. The bonding layer thickness was set to 150 nm in this case. It can be seen that the light couples mainly to the 3th order vertical mode in the detector. Figure 5.4(b,c) shows the propagation and the absorption of the light where (b) is a top view of the detector with averaged intensity and (c) is the sideview. From this Figure it can be seen that a large part of the injected power is already absorbed within the first 20 μm of the detector.

The light absorbed in the detector over a given length also depends on the coupling efficiency between the waveguide and the detector. This coupling efficiency has an exponential dependence on the bonding layer thickness. It is therefore interesting to compare the absorbed power fraction versus detector length for different bonding layer thicknesses. However, in the detector configuration used here, the absorption in the laser QWs and the top metal also contribute to the total absorption. To trace the influence of these layers multiple simulation runs were

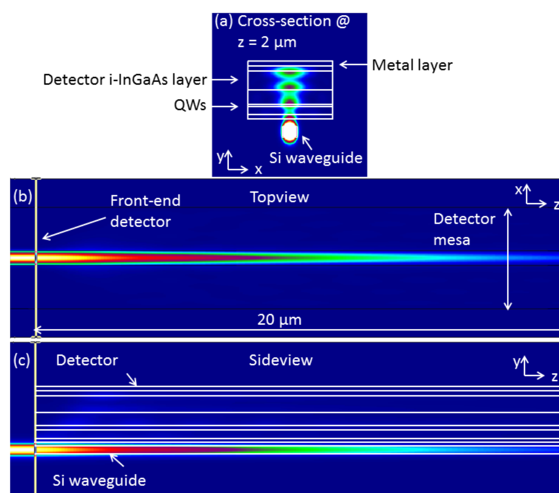

Figure 5.4: (a) Detector mode profile at 2 μm, which shows coupling to the 3th order vertical mode. Topview (b) and side view (c) of the mode propagation and absorption in the detector.

performed, where the absorption in specific layers was turned off.

The absorbed power fraction versus detector length based on a 500 nm wide silicon access waveguide is shown in Figure 5.5 for different bonding layer thicknesses. It can be seen that for a bonding layer thickness of 150 nm already 89% of the injected optical power is absorbed within the first 20 μm of the detector, which is in agreement with Figure 5.4(b,c). After 50 μm length nearly all the light is absorbed in this case. Clearly, when the bonding layer thickness increases the length required to obtain a similar amount of absorption increases considerably. For a bonding layer thickness of 250 nm still only 83% is absorbed in a 80 μm long detector. The influence of the laser QW layers can also be found from Figure 5.5 by comparing the absorbed power fraction versus detector length with and without QW absorption. When the absorption in the QW layers is turned off, the total absorption after 20 μm for a 150 nm bonding layer thickness is still 87 % which indicates that the absorption in the QWs is very limited.

The absorbed power fraction versus length was also evaluated for a 3 μm wide silicon waveguide and the result is shown in Figure 5.6(a) together with the result of a 500 nm wide waveguide for comparison. The bonding layer thickness was again taken to be 150 nm. The results obtained for the 500 nm and 3 μm waveguide are quire similar as in both cases a detector length of 50 μm is required to reach nearly complete absorption. The absorbed power fraction for a detector with a 500 nm wide waveguide appears to ramp up a little bit faster, but at a length of 20 μm

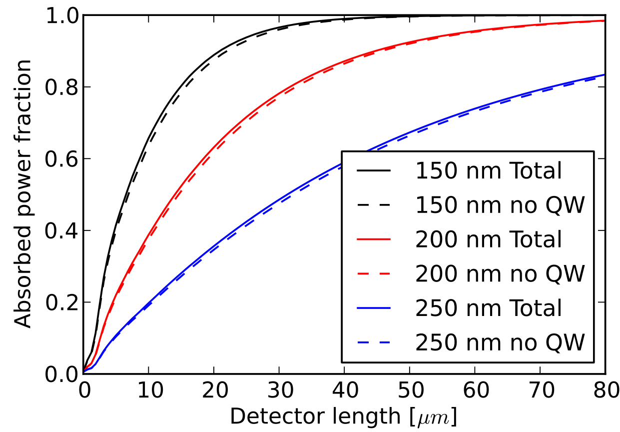

Figure 5.5: Simulation result of the absorption versus detector length for 3 different bonding layer thicknesses with (solid lines) and without (dashed lines) laser quantum well absorption.

the absorbed power fraction only differs by 2%. Based on these results the detector with a 500 nm wide waveguide is preferred as there is no need for a taper structure to change the waveguide width.

Determining the exact influence of the top metal structure is not straightforward because when the absorption in the InGaAs detector layer is set to zero, the metal absorption will be strongly overestimated as now all the light will reach the metal layer, while this is obviously not the case in a real structure. On the other hand, when the absorption in the metal is taken to be zero, this will change the mode profiles significantly because Titanium has both a large real and imaginary part of the refractive index. By neglecting the imaginary part it will result in different mode solutions which makes it difficult to make comparisons. In order to approximate the influence of the metal we performed a simulation where we replaced the top metal layer with silicon oxide. In this situation the mode profiles found in the structure are similar as when an top metal layer is included, due to the large index contrast. The result for a detector without a metal top contact is shown in Figure 5.6(b) together with a detector where all absorbing layers are present. As expected, the absorbed power fraction is slightly lower without the top metal layer. For a detector length of 20 μm the absorbed power is 10% lower when no metal absorption is included. As the top metal layer was taken over the complete mesa width, the loss induced by the top metal is slightly overestimated because in practice it will not cover the full mesa width. Nevertheless, based on these simulations we can conclude that although in this configuration about 10% of the injected

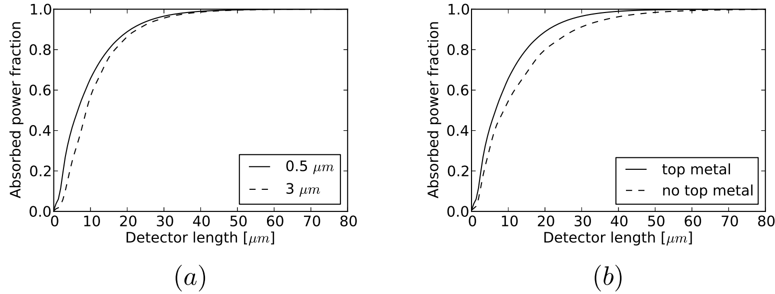

Figure 5.6: Simulation result of the absorption versus detector length for two different waveguide widths (a) and with and without top metal contact (b).

optical power will be lost in the top metal and the laser quantum wells, there is also sufficient coupling to the absorption layer of the detector, which makes an efficient photodetector feasible.

5.2.4 Bandwidth

For optical interconnects having a detector with good responsivity is not sufficient. The detector should also be able to follow the variations of the incident optical power as the data is intensity modulated on the optical signal and should be recovered by the detector. The bandwidth of the detector is a measure of how fast it can respond to these changes. The main factors that determine the speed of the detector are the RC constant and the transit time of the detector. Here we will analyze the effect of the detector design on the RC constant and transit time, and hence, on the detector bandwidth.

Transit time

When light enters the absorbing (InGaAs) layer in the detector, carriers are generated in the form of electrons and holes. The carriers will drift towards the electrodes as a result of the built-in potential over the depleted area of the diode and a possibly additional applied electric field. The time required for the carriers to drift out of the depletion layer is called the carrier-transit time. The 3 dB electrical frequency, i.e. the frequency where the generated photocurrent has decreased by $\sqrt{2}$ is limited by this carrier-transit time and thus related to the carrier-transit distance D [15] by

$$f_{tr} \cong \frac{3.5\bar{v}}{2\pi D} \tag{5.1}$$

$$\frac{1}{\bar{v}^4} = \frac{1}{2}\left(\frac{1}{v_e^4} + \frac{1}{v_h^4}\right). \tag{5.2}$$

Here v_e and v_h are the electron and hole saturation velocities, respectively. The saturation velocities for InGaAs are $6.5 \times 10^6 cm/s$ for v_e and $4.8 \times 10^6 cm/s$ for v_h [16] and the thickness of the intrinsic InGaAs layer in the proposed detector structure is 400 nm resulting in an electrical bandwidth of 74 GHz.

RC constant

Electrically the detector can be seen as a lumped element structure. Therefore, the RC constant can also be a limiting factor of the detector bandwidth. The RC limited bandwidth can be written as

$$f_{RC} = \frac{1}{2\pi C(R_s + R_L)}, \tag{5.3}$$

where C is the capacitance of the detector, R_s is the series resistance of the detector and R_L is the load resistance. The series resistance of the detector is mainly determined by the contact resistance and the thin lateral layer that serves as bottom contact. In good detectors this is typically only a few Ohms and the total resistance is dominated by the load resistance which is 50 Ω in a high speed system. The capacitance of the detector can be found by using the relation for a parallel plate capacitor

$$C = \epsilon_0 \epsilon_r \frac{A}{d}, \tag{5.4}$$

where ϵ_0 is the permittivity in vacuum and ϵ_r the dielectric constant, A the area and d the thickness of the intrinsic layer. Assuming a mesa width of 3.5 μm and a detector length between 20 and 80 μm for the proposed detector structure, results in a capacitance between 20 and 80 fF.

If we also assume a series resistance of the detector of 10 Ohms in combination with a 50 Ohm load, a theoretical bandwidth between 132 and 33 GHz is found for a 20 and 80 μm long detector, respectively. Based on these values we can conclude that the 20 μm long detector would be transit time limited with a bandwidth of 74 GHz, while the 80 μm long detector would be RC limited with a bandwidth of 33 GHz. However, under the influence of other parasitic resistors and capacitors and non optimal contact resistance, these values might be lower in practical systems. Our aim is to make an optical interconnect with a bandwidth $>$10 GHz and based on these calculations this should be feasible for the proposed detector.

5.3 Fabrication process for microdisk lasers with detectors

This section covers the fabrication process of the detector structure and the microdisk laser. All fabrication steps, except for the definition of the detector mesa, are carried out simultaneously, therefore the fabrication process for both the detector and microdisk laser is described as one single fabrication process.

The devices were processed on 200 mm wafers in a CMOS pilot line by our project partners at CEA Leti in Grenoble, France as well as on smaller samples in the clean room of Ghent University. These fabrication processes are slightly different and will therefore be treated separately in the next sections. The III-V epitaxial structure used in both these fabrication processes was grown at INL, Lyon, France, which was also a project partner in the EU FP7 WADIMOS project. The epitaxial structure for the laser and detector was grown at 490 °C using solid source molecular beam epitaxy (SSMBE) on a two inch wafer. InGaAs and InP layers were included as protective sacrificial layers.

5.3.1 CMOS pilot line process

A schematic overview of the fabrication steps performed in the CMOS pilot line is shown in Figure 5.7. This process was developed and carried out at CEA Leti and will therefore only be roughly explained.

Patterning of the SOI wafer

The first step is the patterning of the SOI wafer. The process starts from a 200 mm SOI wafer with a 2 μm buried oxide layer and a 220 nm thin silicon layer. Patterns are written by a 193 nm deep-UV lithography tool. To be able to make both rib and strip waveguides and e.g. shallow gratings, two different etch depths are used: a 220 nm full etch and a 70 nm shallow etch.

Molecular bonding

After the SOI wafer has been patterned it has to be planarized for the molecular bonding process. This is done by depositing silicon dioxide on the wafer, the deposited silicon dioxide layer is then planarized through a chemical-mechanical polishing (CMP) process.

InP and InGaAs sacrificial layers on the III-V wafer are removed through wet chemical etching in hydrochloric acid (HCl) and a sulfuric acid based solution (H_2SO_4/H_2O_2/H_2O). A thin $\tilde{1}0$ nm layer of silicon oxide is deposited on the III-V wafer for the actual bonding process. The silicon oxide surfaces are then plasma-activated and brought into contact, followed by an annealing step at 300 °C.

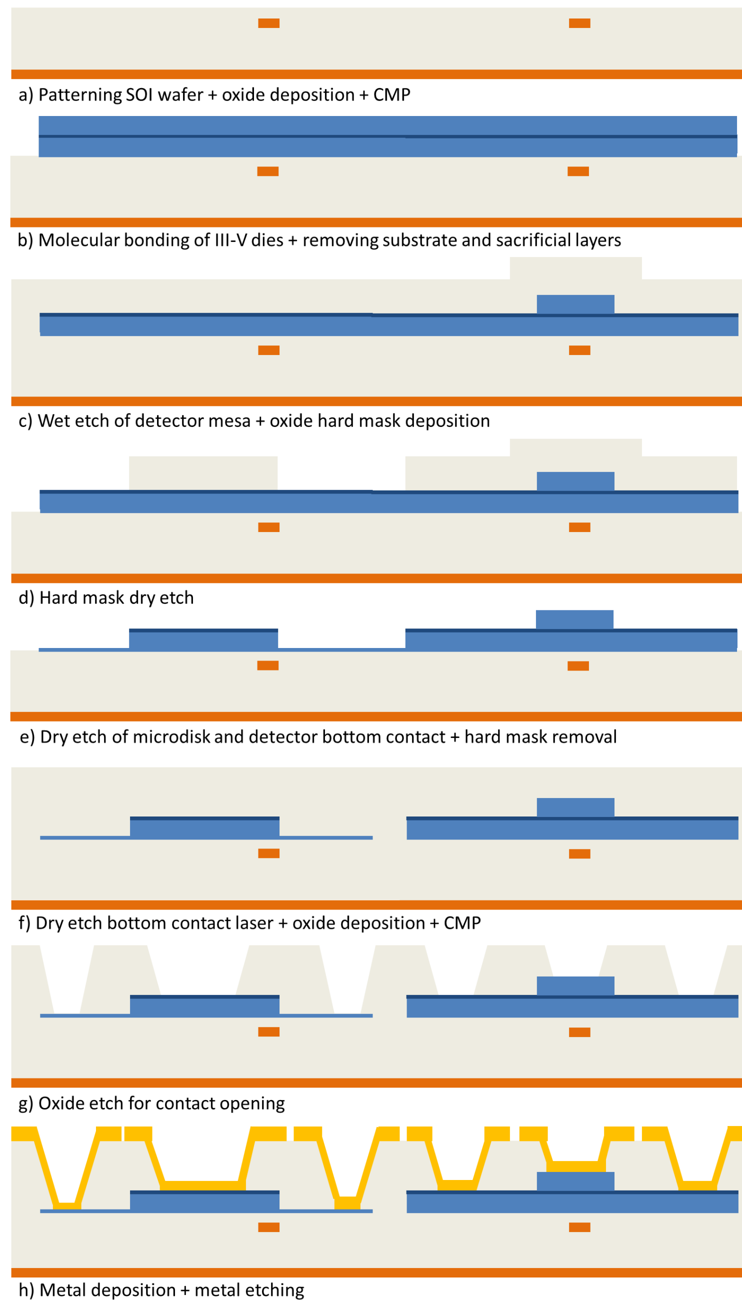

Figure 5.7: Fabrication process for microdisk lasers and detectors in a CMOS pilot line.

After bonding the InP substrate and sacrificial layers are removed through mechanical grinding and wet chemical etching.

Detector mesa definition

The wafer is coated with photoresist and 248 nm deep-UV lithography (all litho processes from this point on are based on 248 nm DUV) is used to define the detector mesa. A sulfuric acid based solution is then used to etch the InGaAs detector mesa. The selectivity to InP for this chemical solution is high, but still care has to be taken for the etching time as a too long etch will result in large undercut, thereby reducing the mesa width.

Disk definition

The microdisk structure requires a dry etch process. Therefore, first a 100 nm thick SiO_2 hard mask is deposited. The wafer is again coated with photoresist and exposed, after which the hard mask is etched and the photoresist stripped. Next, a partial dry etch of the III-V is performed using reactive ion etching (RIE) with a CH_4/H_2 plasma. Note that in this step next to the microdisk structure also the island of the detector is defined. Care has to be taken in this step as a 100 nm layer of III-V should remain for the microdisk bottom contact. Finally, the SiO_2 hard mask is removed.

Island definition

After the previous step a 100 nm n-doped InP bottom contact layer is left. The distance from this layer to the silicon waveguide is determined by the bonding layer thickness and can be very small. To avoid free carrier absorption in the silicon waveguides induced by this doped layer, it should be removed in areas away from the microdisk laser where it is not needed. This process step is called the island definition and is similar as the disk definition. In this case a 50 nm thick SiO_2 hard mask is deposited however.

Metal heaters

Metal heaters were included to tune passive wavelength selective devices. First, a 400 nm SiO_2 layer that also functions as passivation layer for the active devices is deposited after which a 100 nm Titanium layer is full-sheet deposited. The heater structures are then defined and a metal dry etch is performed.

Contact window opening

In the fabrication process of III-V components it is common to use polymers to planarize the samples. However, this is not very common in a CMOS process.

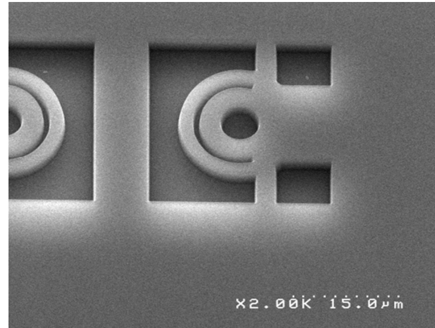

Figure 5.8: SEM image showing the planarized top oxide and the etched contact openings.

Therefore, to obtain a flat surface for the metal contacts, a process thick oxide deposition and CMP was developed.

A 1600 nm thick SiO_2 layer is deposited and this step is followed by CMP to planarize the top oxide. This is a critical step and care has to be taken that the CMP stops above the detector layer, which is done using ellipsometry. Then, contact window openings are defined for all three contact levels (top detector, top laser+bottom detector and bottom laser) and the SiO_2 is dry etched until the III-V of the laser island is reached. Because the distance from the top of the SiO_2 layer to e.g. the top of the detector is much smaller compared to the distance to the bottom layer of the laser, this means that the top contact layer of the detector is strongly over etched. It was found however, that this had no negative influence on the contacts. An SEM image of the planarized top oxide and the contact openings is shown in Figure 5.8.

Metallization

Typical metal stacks used to contact III-V material are e.g. Ti/Pt/Au and AuGe/Ni/Au. As Au is strictly forbidden in a CMOS environment and lift-off processes are not common in a CMOS foundries a new contact metal stack and etch process needed to be developed. It was found that Ti/TiN/AlCu gave the best results [17].

A Ti/TiN/AlCu 10/40/1000 nm metal stack is full sheet deposited. Contact pads with a size of 80 x 80 μm are defined after which the metal layer is dry etched. As the contact window openings and the metallization both use a single step approach the total number of processing steps is significantly reduced. A disadvantage is that it is not possible to use large area top contacts to spread the heat as proposed and demonstrated in [18], because in that case the top metal covers part of the bottom metal area and a two step metallization approach is required.

Cross-section SEM images of the microdisk laser and detector are shown in Figure 5.9.

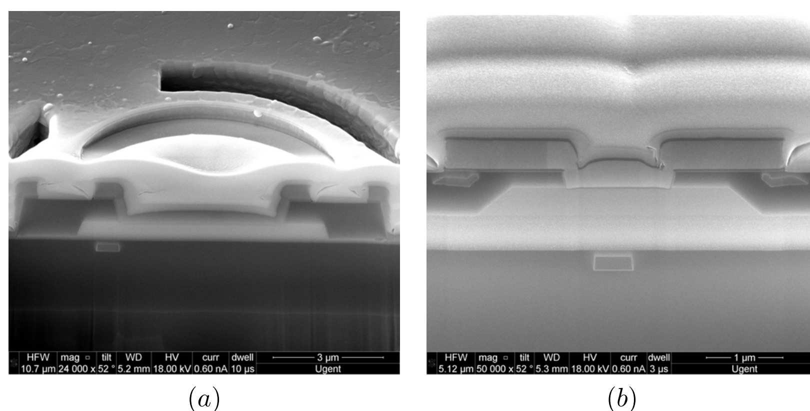

Figure 5.9: Cross-section SEM images of the microdisk laser (a) and the detector (b).

5.3.2 UGent process

A schematic overview of the fabrication steps performed in the clean room of Ghent University is shown in Figure 5.10. Processing was performed on die level rather then on wafer level in this process. In this section the main process flow will be discussed. More detailed processing parameters can be found in Appendix B.

Patterning of the SOI wafer

In this process patterned SOI wafers were received from the multi project wafer (MPW) shuttle runs offered through ePIXfab [19]. The fabrication steps for these wafers are similar as discussed above.

Adhesive bonding

In the UGent process an adhesive bonding method based on BCB is used rather than a molecular bonding approach and in principle no perfect planarized surface is required as the BCB polymer works as a planarization layer. However, there might still be some non-uniformity in bonding layer thickness over the sample, depending on the design of the silicon layer, especially when thin bonding layers are required. This non-uniformity can be problematic, in particular for the structures that require accurate control of bonding layer thickness to tune the coupling efficiency, such as microdisk lasers. Therefore we here also used wafers which were covered by a planarized top silicon oxide layer. In the MPW runs from imec the thickness of the silicon oxide layer is fixed to 1.25 μm above the waveguide level, which is obviously too much for efficient coupling. Therefore the top silicon oxide layer is etched back using a buffered fluoric acid (BHF) wet etch until the thickness of the silicon oxide layer is reduced to the desired thickness. In fact,

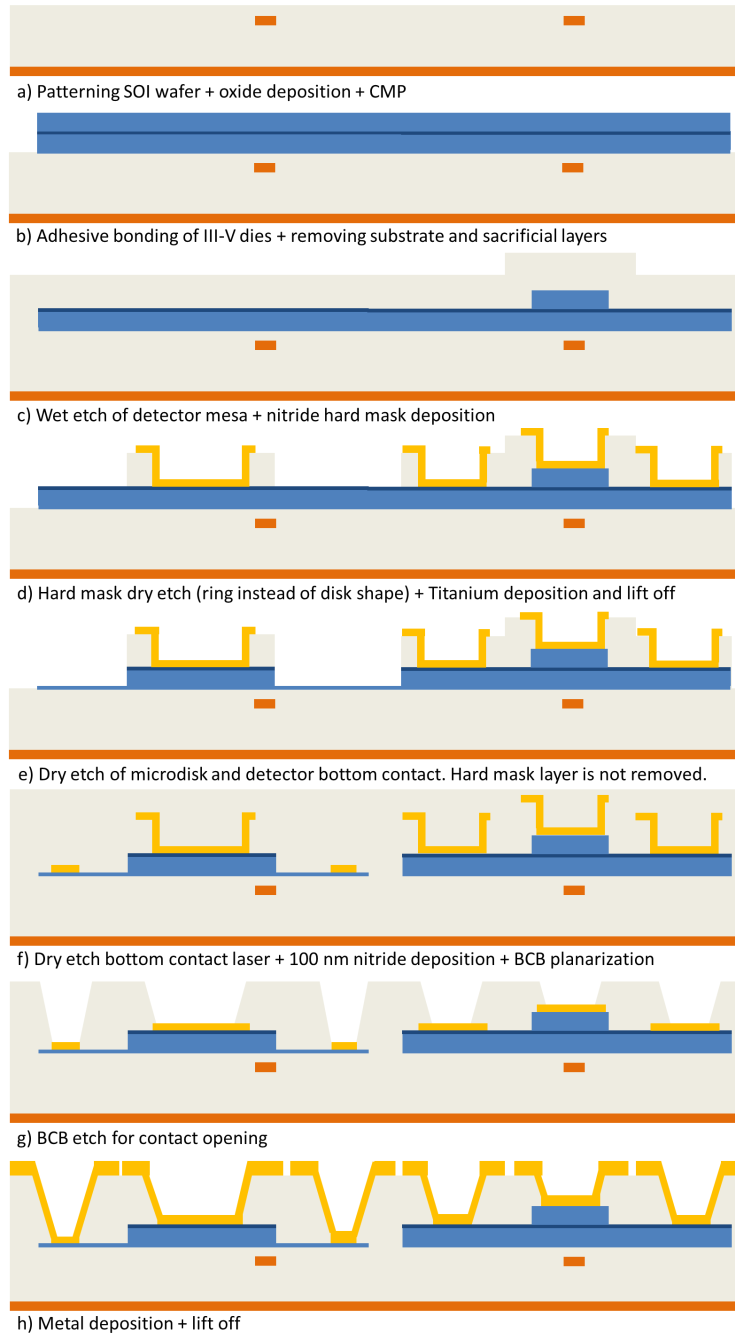

Figure 5.10: Fabrication process for microdisk lasers and detectors as performed in the UGhent clean room.

this etch back step is used to control the gap between the silicon waveguide and the microdisk structure, while a fixed BCB solution is used that results in a thin reproducible layer of 40nm. By keeping the BCB layer thin and using planarized SOI, very high uniformity can be obtained.

First a standard clean 1 (SC-1) is performed on the SOI samples to remove particles and organic contaminants before the etch back step. This is a crucial step as particles on the surface will work as an etching mask resulting in a non-uniform surface after etching and thereby impeding the bonding process.

The III-V stack contains InP and InGaAs sacrificial layers to protect the actual layers required for the devices. These sacrificial layers are removed just before the bonding process by wet chemical etching. The InP layer is removed in a hydrochloric acid (HCl) solution while the InGaAs layer is removed in a sulfuric acid based solution ($H_2SO_4/H_2O_2/H_2O$). It is well known that the adhesion of BCB to III-V material is very low [20]. Therefore, immediately after removal of the sacrificial layers, a thin 10 nm layer of silicon dioxide is deposited on the III-V wafer by Plasma Enhanced Chemical Vapor deposition (PECVD) to ensure good adhesion and high bonding yield.

The actual bonding process used here is based on an adhesive 'cold' bonding method developed by Keyvaninia and co-workers [21]. This process goes as follows; first, a highly diluted BCB:Mesithylene (1:8) solution is spincoated on the SOI sample. Then, the sample is heated to 150 °C for 10 minutes such that the Mesithylene evaporates. Now, the sample is cooled down slowly and the BCB solidifies. The III-V die can be positioned on the SOI die easily after which the stacked dies are put into a Karl Suss CB6L machinebonder. The BCB is cured at a temperature of 250 °C for 1 hour, but the temperature is ramped up slowly (1.6 °C per minute) from 150 to 250 °C. This process results in a reproducible uniform BCB layer of 40 nm.

After bonding, the InP substrate is removed through mechanical grinding and wet chemical etching with HCl. The final step is again removing InGaAs and InP sacrificial layers. However, due to the anisotropic etching of InP in HCl, ridges will remain on two sides of the III-V die. These ridges have about the same height as the thickness of InP after grinding 60 μm and cause problems during the following lithography steps. Therefore, these ridges are manually removed with a scalpel before removing the sacrificial layers to avoid particle contamination of the actual III-V stack.

Detector mesa definition

The sample is coated with AZ ECI 3027 photoresist through spincoating. This photoresist is optimized for wet etching processes and thus ensures good adhesion, while the sidewall slope typically has a less perfect angle. The mesas are defined with contact lithography using a Karl Suss MA6 maskaligner. A sulfuric

acid based solution ($H_2SO_4/H_2O_2/H_2O$) is used to transfer the pattern from the photoresist into the InGaAs layer. The selectivity for InP to this chemical solution is high, but still care has to be taken for the etching time as a too long etch will result in large undercut, thereby reducing the mesa width.

Disk definition

In the UGent clean room only contact lithography is available and the alignment accuracy is limited to about +/- 250 nm at best. Top contact misalignment might therefore cause excessive optical absorption. To avoid this, a self-aligned process was developed for the top contact such that it is always perfectly aligned with respect to the microdisk. This process starts by depositing a 500 nm thick silicon nitride layer using PECVD. This layer will serve as hard mask for the microdisk and simultaneously the bottom contact for the detector. MIR701 photoresist is spincoated on the sample to define the patterns. This resist is optimized for dry etching, having a steep sidewall profile opposed to ECI3027 resist and being more thermally stable. It allows definition of sub-micron feature sizes. If needed a primer can be used to enhance the adhesion.

Now, for the self-aligned process a ring pattern is defined in the resist instead of the normal disk pattern. This pattern is transferred to the hard mask by dry etching the silicon nitride using Reactive Ion Etching (RIE). Next, the top metal needs to be defined. This top metal not only serves as electrical contact for the microdisk laser but also completes the mask for the microdisk as this top metal in combination with the nitride ring forms a disk pattern. To define the top metal AZ5214E photoresist is spincoated on the sample. Image reversal lithography is performed such that openings with negative sidewalls are obtained in the resist at the top contact area of the microdisk and the contact areas of the detector. A 60 nm Titanium layer is then evaporated on the sample. A lift-off process using Dimethyl Sulfoxide (DMSO) is used to remove the resist together with the metal on top of it. DMSO is used rather then acetone, as it was found that it is a better lift-off processor especially in the case of small feature sizes.

Now that the hard mask consisting of the nitride ring and Titanium disk is defined, a partial dry etch of the III-V is performed using inductively coupled plasma etching (ICP) with a CH_4/H_2 plasma. In this step both the microdisk and the detector island are etched in the III-V. Care has to be taken in this step as a 100 nm layer of III-V should remain for the microdisk bottom contact and therefore laser interferometry is used to monitor the etch depth. After this etch step a III-V microdisk with a perfectly aligned top contact is obtained, as can be seen in Figure 5.11.

Finally it should be noted that TI prime from MicroChemical should be avoided in this step. TI prime contains Titanium and it was found that this primer is not completely removed during development. As titanium acts as a mask when etching

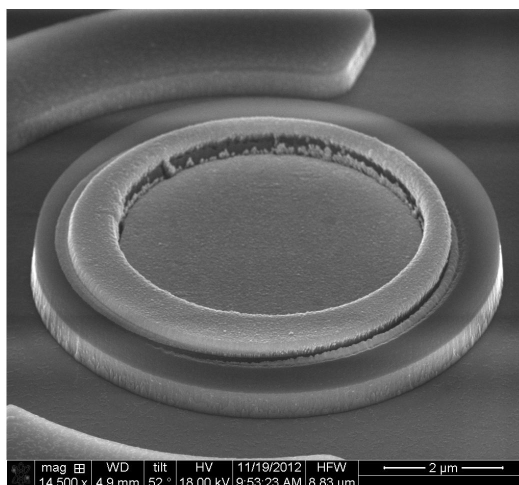

Figure 5.11: SEM image of an etched microdisk with a self aligned top contact. It can be seen that the Titanium layer itself is misaligned, but the metal area that contacts the disk is perfectly in the center because of the nitride ring.

III-V with a CH_4/H_2 gas mixture, remainder of the TI primer causes micromasking resulting in the formation of small pillars in the III-V material. This problem is illustrated in Figure 5.12. If adhesion promotor is required HDMS can be used instead.

Contact metalization

For the contact metalization again an image reversal lithography step is performed using AZ5214E photoresist. Before metal evaporation a short BHF dip is performed to slightly etch the Titanium top contact to ensure a clean surface before metalization. Now, a Ti/Pt/Au (25/50/100 nm) metal stack is deposited using an Ebeam evaporator. The Platinum layer acts as a difussion barrier to the gold thereby avoiding gold spiking into the III-V. In this step contacts on all three levels are defined (top detector / top laser + bottom detector / bottom laser). Again DMSO is used as lift-off processor.

Island definition

For the island definition again MIR701 photoresist was used to define the pattern. If there is any misalignment in this step then the deposited metal will also act as a mask and ensures that III-V will be present everywhere under the metal contacts. The etch process of the island layer is similar as for the microdisk layer.

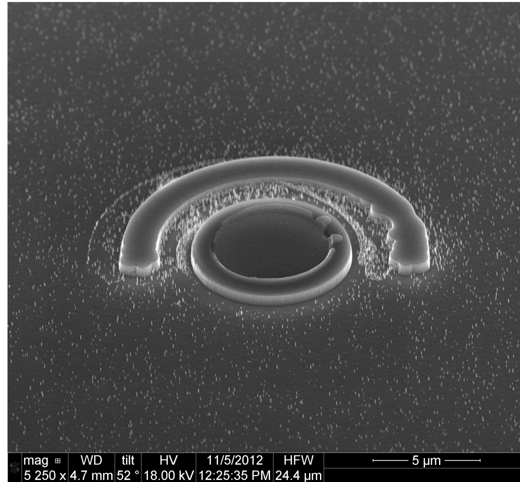

Figure 5.12: SEM image of an etched microdisk where TI prime is used, resulting in the formation of small pillars in the III-V.

Contact window opening

The active devices are passivated with a 100 nm silicon nitride layer that is deposited using PECVD. Next, a 1 μm thick BCB layer is spincoated on the sample for planarization. An image reversal lithography step using AZ5214E is done to define the contact window openings after which an RIE etch with SF_6/O_2 plasma is used to open the contacts. Because the gas mixture for etching BCB contains a lot of oxygen, the photoresist will also be etched quite fast. As a result the contact openings widen during etching. To avoid, too large openings that can result in short circuits after metalization, this process is done in two steps. In the first steps all contacts are opened until the top contact of the detector is reached with a short over etch. In the second step this process is repeated for the top and bottom laser contacts as these lie deeper compared to the detector top layer. It should also be noted that due to variations in the BCB thickness across the sample, not all contact windows will open at the same time. Therefore careful inspection under the microscope is required to ensure that all contact windows are open. Microscope images of the microdisk laser and detector after opening of the contact windows are shown in Figure 5.13.

Metalization

Finally, to be able to contact the devices again an image reversal lithography step is performed to define the contact pads for the devices. A 20 nm thin Titanium layer is sputtered for increased adhesion followed by a 500 nm thick Gold layer for

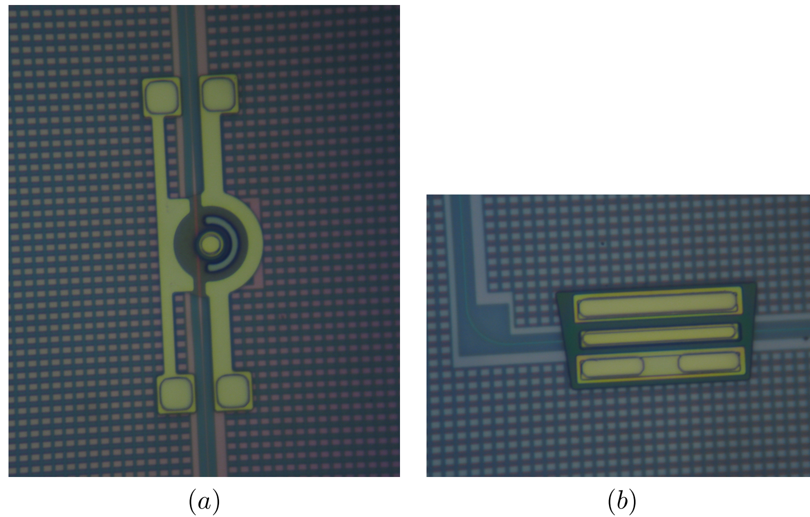

(a) (b)

Figure 5.13: Microscope images of the microdisk laser (a) and the detector (b) after opening the contact windows in the BCB.

contacting and heat spreading. This is the final step in the process and microscope images of the completed microdisk laser and detector are shown in Figure 5.14.

5.4 Characterization of photodetectors

In this section we will focus on the characterization of the fabricated photodetectors. The results of two different processing runs will be presented. First, we will have a look at the performance of devices fabricated in the CMOS pilot line from CEA Leti. Then, the results from a batch fabricated in the UGent clean room will be discussed.

5.4.1 Run 1: CMOS pilot line

In this run photodetectors with various lengths ranging from 20 to 80 μm were fabricated. Besides the detector length also two different waveguide dimensions of 500 nm and 3 μm were used to analyze possible differences in coupling efficiencies. The detector mesa was kept fixed to 3.5 μm. A bonding layer thickness of 130 nm was measured from a cross-section SEM (XSEM). In order to be able to calculate the responsivity of the photodetectors, it is important to know the optical power in the silicon waveguide that reaches the detector. Therefore, fiber-to-fiber transmission measurements were performed of a reference waveguide on the chip. The coupling efficiency was found to be 15% at a wavelength of 1550 nm.

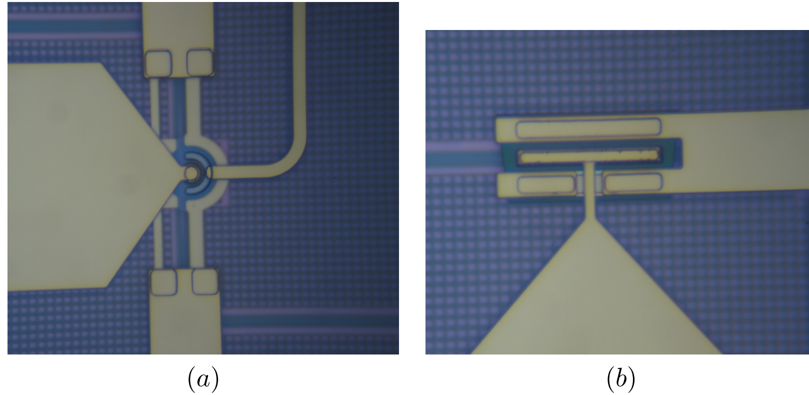

(a) (b)

Figure 5.14: Microscope images of the microdisk laser (a) and the detector (b) after contact metalization.

Dark current and Responsivity

First the IV curves of several photodetectors were measured with and without illumination. From this data, the dark current and responsivity of the photodetectors can be determined. Figure 5.15 shows the IV curves of photodetectors with lengths varying from 20 to 80 μm when no light is injected in the waveguide. The dark current measured at a reverse bias of 1.5 V varies from 230 nA to 10.7 μA and increases with increasing detector length. Typically the dark current for etched InGaAs based detectors is in the range of a few nano Amperes [22], so the measured dark current is more than two orders of magnitude larger than the typical value for this material. Most likely this is caused by not timely passivating the structure, resulting in a lot of surface states and therefore high surface recombination. By careful passivation the dark current is expected to reduce. An assessment of the temperature dependency of the dark current has not been performed, but in general the dark current approximately doubles for every 10 °C increase in temperature.

To measure the responsivity of the photodetectors light from a tunable laser was injected into the silicon waveguides via the fiber couplers. The optical power was measured just before the fiber coupler and the power coupled into the waveguide was then calculated by using the fiber coupler efficiency. As the efficiency depends on the alignment of the fiber with respect to the fiber coupler, there is some uncertainty about the actual optical power in the waveguide. However, the fiber was positioned using active alignment by real time monitoring the photocurrent of the detector and therefore, the uncertainty is expected to be negligible.

The measured responsivities for different detector lengths and two different silicon waveguide widths are shown in Figure 5.16. The shortest detectors with a length of 20 μm have responsivities of 0.70 and 0.58 A/W for 500 nm and 3

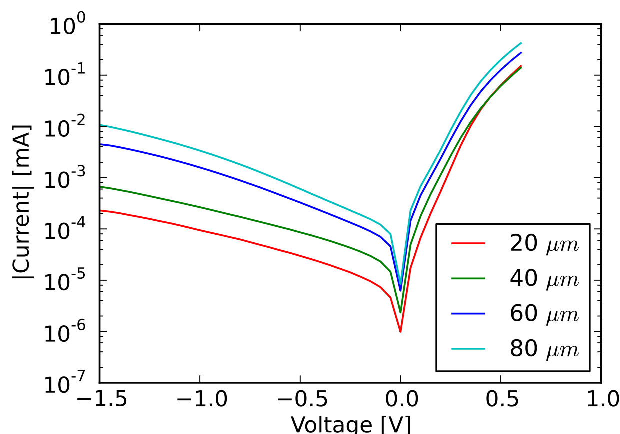

Figure 5.15: Measured IV curves for different detector lengths. The dark current increases for longer detectors.

μm wide waveguides, respectively. When the detector length increases a slow increment in responsivity is seen for the 500 nm wide waveguide, while in case of the 3 μm wide waveguide the responsivity makes a large jump from 20 to 40 μm followed by a slow increase for longer detector lengths. The reason for the large jump might be that light is coupled to a different mode as found in the simulation, thereby requiring a longer coupling length to couple light from the waveguide to the detector. For both waveguide widths maximum responsivity was obtained for the longest detectors, with values of 0.82 and 0.88 A/W for the 500 nm and 3 μm wide waveguides, respectively. Furthermore, from the experimental results it was found that the responsivity of the detectors with a 500 nm wide waveguide is slightly lower compared to the detectors with a 3 μm wide waveguide, while the simulations showed similar results for both waveguide widths at detector lengths above 20 μm. However, in general the experimental results show reasonable agreement with the simulation results. Based on the absorption values from the simulations, slightly higher responsivities could be expected. This discrepancy could be because in the real device light couples to other modes then found in the simulation, which have smaller overlap with the absorbing InGaAs layer of the detector. Another reason could be that the losses from the top metal and the quantum wells are larger than expected. Finally, the simulations only account for optical absorption and not for electrical efficiency. Recombination of generated carriers could also lower the responsivity.

It should also be noted that the best responsivities measured were 0.71 A/W for a 20 μm length and 0.97 A/W for a 80 μm long detector, both with a waveguide

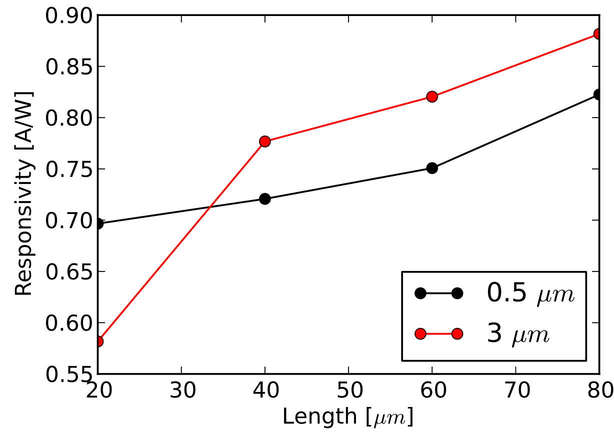

Figure 5.16: Measured responsivity versus detector length for a 500 nm and 3 μm wide access waveguide.

width of 500 nm. However, these results were measured on different samples and therefore this data was not used in Figure 5.16.

Bandwidth

The frequency response of the detectors was measured with an Agilent N4373B Lightwave Component Analyzer (LCA). The modulated optical output from the LCA was coupled into the SOI waveguide via a fiber coupler, while the electrical input from the LCA was connected to the detector through a bias-tee to measure electrical RF response. A Keithley 2400 voltage source was used to apply a reverse bias and to monitor the average photocurrent. Figure 5.17 shows the frequency response for a 20 and 80 μm long detector. The 3dB bandwidth under a reverse bias of -1.5 V was 9 GHz for the 80 μm long detector and around 16 GHz for the detector with a length of 20 μm. The lower bandwidth for the 80 μm long detector can be explained by the larger capacitance following from an increased mesa area. In principle the series resistance should be lower for the longer detector as the contact area increases, thereby compensating for the higher capacitance, but for both detectors a series resistance of 100 +/- 10 Ohms was measured. The relatively high resistance is most likely caused by the fact that no annealing was performed on these samples. Even in the case of good contact resistance, the bandwidth of the longer detector would still be lower as the load resistance would then be the limiting factor.

It should be noted that the ripple in Figure 5.17 is similar for both detectors. This is most likely caused by a not perfect calibration of the network analyzer and

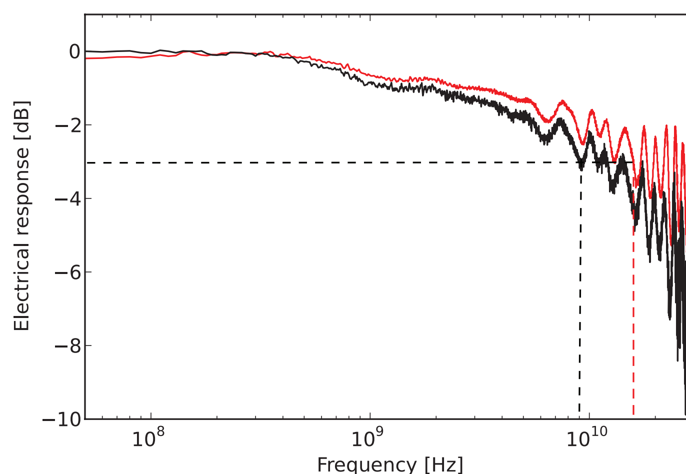

Figure 5.17: Electrical response of a 20 (red curve) and 80 (black curve) μm long detector with a 3 dB bandwidth of 9 and 16 GHz, respectively.

therefore not perfect de-embedding of the electrical cables and the bias-tee. From the measured series resistance and 3 dB bandwidth we find that the capacitance of the detector including the pads is 90 fF for the 20 μm long detector and 175 fF for the 80 μm long detector. These values are higher than the calculated values for the parasitic capacitance of the detector which are 20 and 80 fF for the 20 and 80 μm long detector, respectively. However, in the calculation only the capacitance over the intrinsic layer was taken into account, other parasitic effects were omitted.

Nevertheless, based on the experimental results on dark current, responsivity and bandwidth, we can conclude that this detector can be used for realizing compact optical interconnects on silicon with speeds exceeding 10 Gb/s.

5.4.2 Run 2: UGent clean room

In this run the focus was mainly on the realization of a complete interconnect based on a microdisk laser with the compatible detector proposed here. As, the detector itself was already demonstrated in the CMOS pilot line run, only detectors with a length of 40 and 60 μm were included in this design. The silicon waveguide underneath the detector structure had a width of 500 nm. Two different samples were fabricated, one with a bonding layer thickness of 250 nm (referred to as sample 1) and another with with a thickness of 170 nm (referred to as sample 2).

Fiber-to-fiber transmission measurements were performed on reference waveguides on the chips. The efficiency of the fiber couplers was measured to be 25% at a wavelength of 1550 nm for both samples.

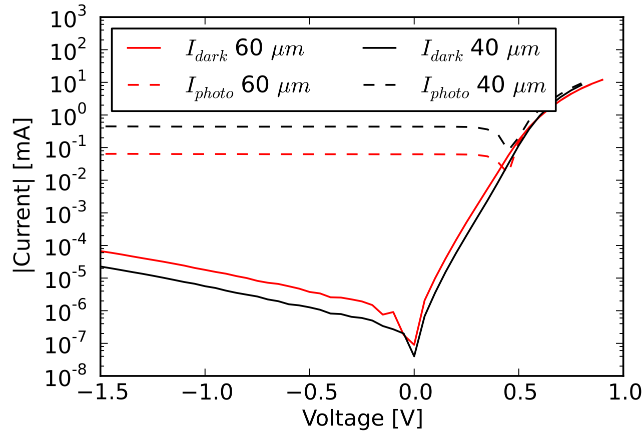

Figure 5.18: Measured IV curves with and without illumination for 40 and 60 μm long detectors on sample 1. It should be noted that different optical input power was used when measuring the 40 and 60 μm long devices. The higher photocurrent for the shorter detector is therefore due to a higher optical input power and not the result of higher responsivity.

Dark current and Responsivity

Again, first the dark current and responsivity of the detectors were characterized. Figure 5.18 shows the IV curves measured on sample 1 with and without illumination. The dark current measured at a reverse bias of 1.5 V was 22 and 67 nA for the 40 and 60 μm long detectors, respectively. These values are significantly lower compared to the values measured on the samples fabricated in the CMOS pilot line discussed in the previous section.

From Figure 5.18 it can be seen that the shorter detector generates a larger photocurrent than the longer detector, which may lead to the impression that the shorter detector has a larger responsivity compared to the longer detector, but this is not the case. The responsivity measurements were performed over different days where different laser sources were used. The injected optical power was not the same during these different measurement sessions. For the 40 μm long detector the optical power in the silicon waveguide was 731 μW, while for the 60 μm long detector, it was only 105 μW. Therefore, the responsivity for these detectors is 0.61 A/W both for the 40 and 60 μm long detector.

The IV curves with and without illumination measured on sample 2 are shown in Figure 5.19. The dark currents were 227 and 205 nA for the 40 and 60 μm long detectors, again measured at a reverse bias of 1.5 V. These values are slightly worse then the other sample fabricated in this batch, but still better than the devices processed in the CMOS pilot line. In the UGent process both samples were

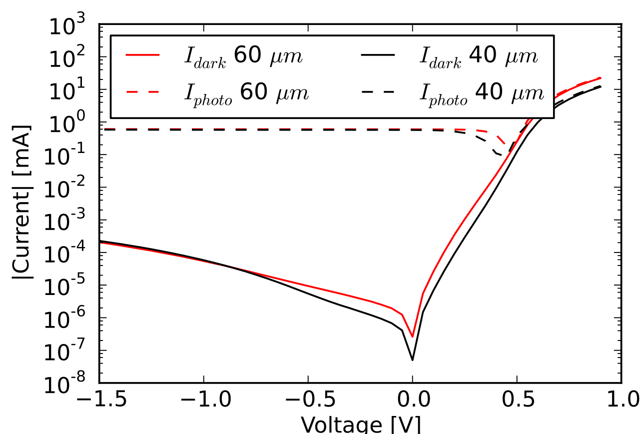

Figure 5.19: Measured IV curves with and without illumination for 40 and 60 μm long detectors on sample 2.

passivated with a 100 nm thin silicon nitride layer, while in the CMOS process the devices were passivated with silicon dioxide. The passivation process should be investigated in more detail to achieve reproducible and low dark currents.

The optical power in the silicon waveguide was 831.5 μW for both detectors on sample 2. From the measured photocurrents we find that the responsivities for the 40 and 60 μm long detectors is 0.69 and 0.73 A/W. The responsivities on sample 2 are slightly higher than the responsivities measured on sample 1. This difference can be attributed to the thinner bonding layer thickness on sample 2, resulting in stronger coupling.

Bandwidth

The 40 μm long detectors were incorporated in a design ready for integration with a CMOS driver chip using a flip-chip approach. This integration approach had some implications for the contact pads and therefore it was not possible to use high-speed measurement probes and thus the bandwidth could not be measured for these devices.

The bandwidth of four 60 μm long detectors was measured with an Agilent N4373D Lightwave Component Analyzer (LCA). Modulated light from the LCA was injected in the detector via the grating coupler and the generated electrical signal was collected via a signal-ground (SG) high speed probe and fed back into the LCA. A bias-T was included to apply a reverse bias to the detector and read out the average photocurrent. The response of these detectors is shown in Figure 5.20 for 0 and -1 V bias. Clearly, very good uniformity is obtained for the different

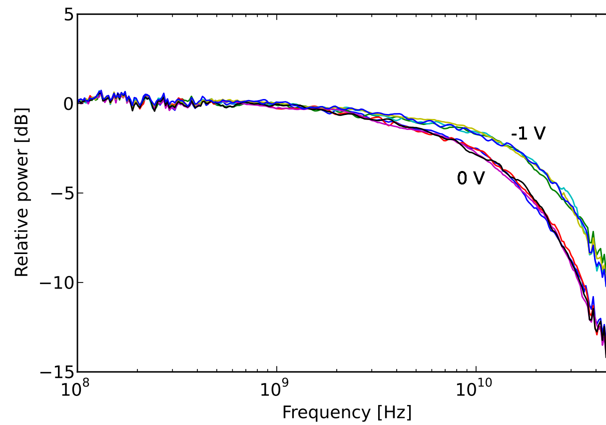

Figure 5.20: Small signal response of four 60 μm long photodetectors for 0 V and -1 V bias, showing very good uniformity. A bandwidth of 12 GHz and 18 GHz was obtained for 0 and -1 V bias, respectively.

detectors. A bandwidth of 12 GHz was obtained for the detectors when no bias was applied, while a bandwidth of 18 GHz was measured for a bias of -1 V. Further increasing the bias did not have any effect, indicating that the depletion width was maximum at 1V reverse bias. The series resistance was measured to be 15 Ohm for these detectors, which is significantly lower compared to the devices from the CMOS run, despite the fact that again no annealing was performed on the samples. This might be the result of a different cleaning step before metal deposition and/or the different metal stack used here. The lower series resistance results in the higher bandwidth measured here.

Large signal response

The large signal response was also measured for these detectors. An Anritsu MP2101A signal generator was used to drive a Lithium Niobate optical modulator from JDSU at a speed of 12.5 Gb/s. A tunable laser source set to a wavelength of 1550 nm was used as optical input for the modulator. The output of the modulator was coupled into the silicon waveguide via the fiber coupler. Again an SG high-speed probe was used to collect the generated photocurrent. A bias-T was included where the DC input/output was used for biasing and monitoring the average photocurrent, while the RF output was fed into an electrical amplifier with a bandwidth of 13.5 GHz before it was collected by a Lecroy WaveExpert 100H 100 GHz sampling scope . The eye diagram at a speed of 12.5 Gb/s is shown in Figure 5.21(a). The optical power in the waveguide is 0 dBm. For this input power an

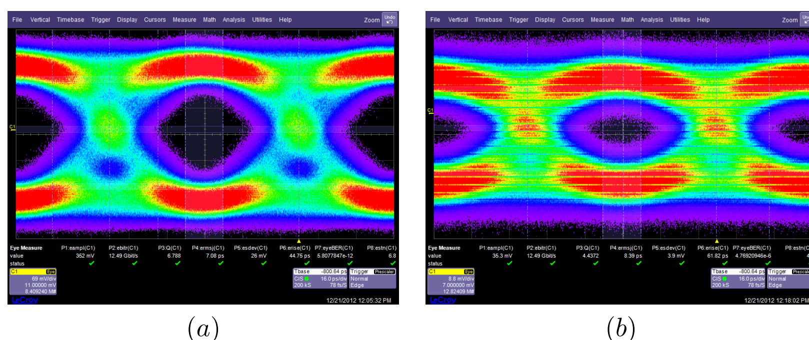

(a) (b)

Figure 5.21: Measured eye diagrams for a 60 μm long detector for an optical input power of 0 dBm (a) and -10 dBm (b).

open eye is obtained. When the optical power is decreased the eye starts to close as can be seen in Figure 5.21(b) where the optical power in the waveguide is 10 dB lower. It should be noted that phase noise is added to the eye pattern, because of issues with the trigger of the scope, while also amplitude noise was added due to issues with the driver of the modulator.

5.5 Conclusions

In this chapter a detector design is proposed that allows for the compact integration of microdisk lasers and detectors. This makes it possible to make compact bidirectional optical links on a silicon chip. The design makes use of a single epitaxial structure that contains the layers for the microdisk laser and the detector. Simulations were carried out to analyze the performance of these detectors and showed that it is possible to achieve both high responsivity and bandwidth.

An efficient fabrication process has been developed both for 200 mm CMOS technology and for smaller scale technology using individual samples. In these processes all fabrication steps for the microdisk laser and detector are carrier out simultaneously, except for the etch step of the detector mesa. In the CMOS process the passivation of the devices was done by PECVD oxide deposition. Due to the conformal nature of the deposition, this also required for the development of a planarization step of the oxide which was done using CMP. Furthermore, as gold is not allowed in a CMOS environment a new Ti/TiN/AlCu metal stack for ohmic contacts was developed. In the fabrication process used in the clean room of Ghent University, the adhesive bonding process was changed such that the thickness control of the gap is no longer determined by the BCB, but by etching back the top oxide on the SOI sample. This allows for better control of the critical gap between the microdisk laser and the waveguide. Furthermore, a self-aligned process was

developed for the critical top contact, resulting in perfect alignment.

Two runs resulted in working detectors: the first CMOS run and the fabrication run in the UGent clean room. The detectors from the CMOS run showed responsivities up to 0.97 A/W for 80 μm long devices, but the dark current was with minimum values in the order of a few hundred nA, quite high. This was attributed to not timely passivating the detectors resulting in a large number of surface states. A maximum small-signal bandwidth of 16 GHz was obtained. The detectors from the UGent clean room run, had lower responsivities up to 0.69 A/W due to the larger gap with the waveguide. Dark currents were an order of magnitude smaller compared to the detectors from the CMOS run and a maximum bandwidth of 18 GHz was obtained.

References

[1] Laurent Vivien, Mathieu Rouvière, Jean-Marc Fédéli, Delphine Marris-Morini, Jean François Damlencourt, Juliette Mangeney, Paul Crozat, Loubna El Melhaoui, Eric Cassan, Xavier Le Roux, Daniel Pascal, and Suzanne Laval. *High speed and high responsivity germanium photodetector integrated in a Silicon-On-Insulator microwaveguide*. Optics Express, 15(15):9843, 2007.

[2] Gianlorenzo Masini, Subal Sahni, Giovanni Capellini, Jeremy Witzens, and Cary Gunn. *High-Speed Near Infrared Optical Receivers Based on Ge Waveguide Photodetectors Integrated in a CMOS Process*. Advances in Optical Technologies, 2008:1–5, 2008.

[3] Tao Yin, Rami Cohen, Mike M. Morse, Gadi Sarid, Yoel Chetrit, Doron Rubin, and Mario J. Paniccia. *31 GHz Ge n-i-p waveguide photodetectors on Silicon-on-Insulator substrate*. Optics Express, 15(21):13965, 2007.

[4] Laurent Vivien, Andreas Polzer, and D Marris-Morini. *Zero-bias 40Gbit/s germanium waveguide photodetector on silicon*. Optics express, 20(2):5905–5907, 2012.

[5] M. Pantouvaki, G. Lepage, J. Van Campenhout, H. Yu, P. Absil, P. Verheyen, J. De Coster, and P. De Heyn. *20Gb/s Silicon Ring Modulator Co-Integrated with a Ge Monitor Photodetector*. 39th European Conference and Exhibition on Optical Communication (ECOC 2013), (1):507–509, 2013.

[6] Joost Brouckaert, Günther Roelkens, Dries Van Thourhout, and Bae. *Compact InAlAsInGaAs metalsemiconductormetal photodetectors integrated on silicon-on-insulator waveguides*. Photonics Technology Letters, IEEE, 19(19):1484–1486, 2007.

[7] Kazuya Ohira, Kentaro Kobayashi, Norio Iizuka, Haruhiko Yoshida, Mizunori Ezaki, Hiroshi Uemura, Akihiro Kojima, Kenro Nakamura, Hideto Furuyama, and Hideki Shibata. *On-chip optical interconnection by using integrated III-V laser diode and photodetector with silicon waveguide.* Optics express, 18(15):15440–7, July 2010.

[8] P R A Binetti, X J M Leijtens, T de Vries, Y S Oei, L Di Cioccio, J.-M Fedeli, C Lagahe, J Van Campenhout, D Van Thourhout, P J van Veldhoven, R Notzel, and M K Smit. *InP/InGaAs Photodetector on SOI Photonic Circuitry*. IEEE Photonics Journal, 2(3):299–305, June 2010.

[9] Long Chen, Kyle Preston, Sasikanth Manipatruni, and Michal Lipson. *Integrated GHz silicon photonic interconnect with micrometer-scale modulators and detectors.* Optics express, 17(17):15248–56, August 2009.

[10] G Roelkens, D Van Thourhout, R Baets, R Nötzel, and M Smit. *Laser emission and photodetection in an InP/InGaAsP layer integrated on and coupled to a Silicon-on-Insulator waveguide circuit.* Optics express, 14(18):8154–9, September 2006.

[11] Hyundai Park, Alexander W Fang, Richard Jones, Oded Cohen, Omri Raday, Matthew N Sysak, Mario J Paniccia, and John E Bowers. *A hybrid AlGaInAs-silicon evanescent waveguide photodetector.* Optics express, 15(10):6044–52, May 2007.

[12] J. Brouckaert. *Integration of Photodetectors on Silicon Photonic Integrated Circuits (PICs) for Spectroscopic Applications*. PhD thesis, Ghent University, 2010.

[13] Silvaco. *www.silvaco.com*, 2013.

[14] E.D. Palik. *Handbook of Optical Constants, Vol.3*. Academic Press, 1998.

[15] Kazutoshi Kato. *Ultrawide-band/high-frequency photodetectors*. IEEE Transactions on Microwave Theory and Techniques, 47(7):1265–1281, 1999.

[16] J. Bowers and C. Burrus. *Ultrawide-band long-wavelength p-i-n photodetectors*. Journal of Lightwave Technology, 5(10):1339–1350, October 1987.

[17] L Grenouillet, AL Bavencove, T Dupont, J Harduin, P Philippe, P Regreny, F Lelarge, K Gilbert, P Grosse, and JM Fedeli. *CMOS compatible contacts and etching for InP-on-silicon active devices*. In Group IV Photonics, 2009. GFP'09. 6th IEEE International Conference on, pages 196–198. IEEE, 2009.

[18] Liu Liu, Rajesh Kumar, Koen Huybrechts, Thijs Spuesens, G. Roelkens, E.J. Geluk, T. De Vries, Philippe Regreny, D. Van Thourhout, Roel Baets, and G Morthier. *An ultra-small, low-power, all-optical flip-flop memory on a silicon chip*. Nature Photonics, 4(3):182–187, 2010.

[19] EPIXfab. *www.epixfab.eu*, 2013.

[20] Www.dowchemical.com. *Processing Procedures for BCB Adhesion*. 2007.

[21] S Keyvaninia and M Muneeb. *Ultra-thin DVS-BCB adhesive bonding of III-V wafers, dies and multiple dies to a patterned silicon-on-insulator substrate*. Optical Materials Express, 34(18):1047–1056, 2013.

[22] Govind P. Agrawal. *Fiber-Optic Communication Systems(Google eBook)*. John Wiley & Sons, 2010.

6

Optical Interconnects on Silicon

In the previous chapters we focused on the active building blocks for realizing optical interconnects on silicon. Here we will focus on the realization of such a complete compact optical interconnect based on these building blocks.

6.1 State-of-the-art on-chip optical links on silicon

Although until now most of the research work focused on the building blocks for realizing optical interconnects, several optical interconnects on silicon have been demonstrated in the literature. Here we will give a brief overview of some important results presented in recent publications.

One of the first optical links on silicon based on silicon Mach-Zehnder modulators and Ge detectors was demonstrated by Luxtera [1]. They demonstrated a 4x10 Gb/s transceiver on a single die that was fabricated through a monolithic integration approach with electronic circuits in a CMOS compatible process. However, the modulators are several millimeters long and have relatively large power consumption. A similar configuration but with ring based silicon modulators is becoming a popular approach. Both the ring modulators and the Ge detectors have small footprints and thus dense integration can be achieved. One of the first demonstrations of this approach was published by Chen and coworkers [2]. They demonstrated 3 Gbps data communication with 0.5 V modulator voltage swing and 1 V detector bias. The total energy consumption was only 120 fJ/bit. More recently, several platforms [3, 4] where silicon modulators and Ge detectors

with bandwidths exceeding 25 GHz have been made available to the community through multi project wafer (MPW) runs. The main drawbacks of using these silicon modulators is that the insertion loss is typically in the order of 6 dB. Therefore, the off-chip laser sources can only be shared over a few modulators. Moreover, because the sources are shared, they cannot easily be turned off and this has a negative impact on the power budget. Furthermore, the optical bandwidth of the ring modulators is small and they need to be tuned to match the wavelength of the source, which requires power hungry heater structures.

When using a III-V heterogeneous integration approach, an obvious and easy solution to make an optical interconnect on silicon is to use the same III-V material stack for the laser and detector. However, efficient lasers are typically based on a (multiple) quantum well approach. When such a material stack is also used for the detector, the small overlap of the optical mode with the quantum wells requires a long detector to achieve an acceptable responsivity. The bandwidth of these long detectors is then limited by the large junction capacitance. Both lasers and detectors processed together on a single sample have been demonstrated using this approach [5], although without an on-chip optical link. The laser could only be operated under pulsed drive conditions and the threshold current was 180 mA for a 500 μm long laser. The detector had a length of 50 μm and a responsivity of 0.23 A/W was obtained. The dark current was around 50 nA at 2V reverse bias.

Another possibility based on a heterogeneous integration approach, is to use separate III-V dies for the lasers and the detectors. This ensures good performance of both the lasers and detectors but they need to be spatially separated ans thus the integration density is limited and compact transceivers cannot be realized. In [6] an optical interconnect is demonstrated that uses a microdisk laser with InAsP quantum wells as a source and an InGaAs based layer stack for the detector. The laser had a low threshold current of 0.6 mA, but the output power was limited to values below 3 μW in the silicon waveguide. The responsivity of the detector was measured to be 0.35 A/W and the reported 3 dB bandwidth of the detector was 33 GHz. The bandwidth of the complete optical link was not measured, but the direct modulation bandwidth of this microdisk laser was reported elsewhere [7] and found to be 5 Gb/s. The bandwidth of the optical link is therefore limited by the bandwidth of the microdisk laser. Another optical link on silicon using a similar approach was demonstrated by Ohira and coworkers [8]. Here, GaInNAs/GaAs laser diodes were integrated directly on the silicon substrate by a flip-chipping approach. The detectors were fabricated by bonding of InGaAs/InP wafers on the SOI. The threshold current of the lasers was around 50 mA and output powers of several mWs were observed. However, the coupling efficiency from the laser to waveguide was estimated to be around 62%. An MSM approach was used for the detector and the responsivity of 0.74 A/W was obtained. For the complete optical link an efficiency of 0.025 mA/mW was obtained and this low value was attributed

to the high waveguide losses of 10 dB. No data was presented on the bandwidth of the optical link.

6.2 Compact integration of microdisk lasers and detectors

Here we will discuss two different link designs: a compact single link design with electrical contacts close to the devices for direct probing and a design containing multiple links, that can be driven by directly flip-chipping a CMOS control chip on top. Both of these designs were fabricated in both the CMOS run and the UGent clean room run, but due to some processing issues no complete interconnects were obtained from the CMOS run. Therefore, the results discussed here are all from the UGent clean room run.

6.2.1 Compact single optical link

This design consists of one microdisk laser, 2 detectors and a silicon waveguide. A microscope image of the fabricated interconnect is shown in Figure 6.1. The diameter of the microdisk laser in the interconnects circuits is 7.5 μm. The detector mesa has a width of 5 μm and a length of 60 μm. The height of the silicon waveguide is 220 nm and the width is 450 nm such that it only supports the fundamental TE mode. For efficient coupling between the fundamental mode of the microdisk and the waveguide mode, the width of the waveguide was tapered to 750 nm around the microdisk-waveguide coupling section. The same is done for the detector where the waveguide width under the detector is 500 nm. In this optical link configuration the metal contact pads were designed such that the signaling and pitch is compatible with high-speed ground-signal-ground (GSG) probes. The waveguide is terminated after the detectors by fiber couplers. In principle a basic optical interconnect would consist of a microdisk laser, ideally operating in the unidirectional regime and only 1 detector. Several approaches are demonstrated in literature to make the microdisk lasers unidirectional. Most approaches rely on using an external reflector in the silicon waveguide, e.g. through a Bragg grating [9] or through a loop mirror [10]. Another approach uses a so called racket-shape where two access waveguides of the microdisk resonator are connected on one side forming a feedback loop and combined using a 3 dB combiner on the other side [11]. This method also allows for selecting specific optical modes by changing the phase in the feedback loop.

Here, detectors on both sides of the microdisk laser were used to gain insight in the influence of external spurious reflections by e.g. fiber couplers. As a single III-V epitaxial structure is used, it becomes possible to make efficient lasers and detectors right next to each other and thus form a compact optical transceiver. This

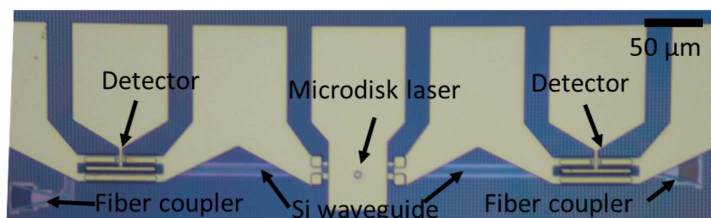

Figure 6.1: Microscope image of the full optical link, where detectors on both sides of the microdisk laser are connected via a silicon waveguide.

is demonstrated in this design by placing the laser and detector only 150 μm apart from each other as can be seen in Figure 6.1.

DC characterization

The fiber couplers on both sides can be used to characterize the detectors separately from the microdisk laser by using an external laser source. This makes it possible to determine the efficiency of the detectors. Once the efficiency of the detectors is known, the performance of the microdisk laser can be determined by measuring the photocurrent from the detectors while pumping the microdisk laser. The performance of these detectors was already discussed in Chapter 5 and here we will further focus on the performance of the optical link and the microdisk laser.

First, the DC characteristics of several optical links were measured where both CW and pulsed drive conditions for the microdisk laser were used. The links were characterized by measuring the generated photocurrent at the detectors while a current sweep was applied to the microdisk laser resulting in a current versus current characteristic. The result of one of the best optical links is shown in Figure 6.2, where the black and red curves correspond with the left and right detector, respectively. The solid lines represent CW operation, while the dashed lines represent pulsed operation. The IV curve of the microdisk laser is also shown in this plot (blue line) and from this the series resistance of the laser is found to be around 130 Ohm. This high contact resistance is a result of the small dimensions of the top contact and not annealing the contacts. A Ti/Pt/Au metal stack was used for these devices as described in Chapter 4 and although these contacts are typically ohmic as deposited, an annealing process can reduce the resistance of such a contact by more than an order of magnitude [12]. However, because of the risk of short

circuiting the devices through such an annealing process, measurements were carried out already before annealing. New measurements after annealing could show slightly better results.

The output from the microdisk laser is bidirectional in pulsed as well as in CW mode. In CW mode, the power is evenly divided between the left and right output up to 2.3 mA drive current. Based on the complementary oscillations in the CW LI curves at higher currents, there is clearly some coupling between the clockwise and counterclockwise mode. The threshold current of the microdisk laser is 0.45 mA and the maximum generated photocurrent (single sided) is slightly above 100 μA at 4 mA drive current. The maximum slope efficiency is 40 $\mu A/mA$. Taking the responsivity of the detector into account, which was found to be 0.69 A/W, this corresponds with a single sided maximum laser output of 145 μW and a maximum slope efficiency of 57 $\mu W/mA$, which is a record high output and efficiency for these microdisks. At a 2 mA laser drive current the generated photocurrent is 61 and 66 μA for the left and right detector, respectively. The power efficiency of the optical link from the microdisk laser to one detector is therefore slightly above 3%. If the microdisk laser would be made unidirectional e.g. by an external reflector as suggested above, the link efficiency could increase to 6%. It is also interesting to note that the LI curve of the microdisk laser is much smoother compared to the microdisk lasers discussed in Chapter 4 where the output of the microdisk was collected via a fiber coupler. It was suggested that the oscillations in the LI curve were attributed to reflections from the fiber coupler. In the present work, the facets from the detectors were designed under a 7 degree angle to avoid reflections from the III-V interface as much as possible. The smoother LI curves obtained here is another confirmation that reflections from the fiber couplers, typically in the order of -20 dB, can disturb the performance significantly. A new grating coupler design with reflections lower than -50 dB proposed by [13], would be better suited to characterize integrated lasers.

As can be seen from Figure 6.1, the microdisk laser design used here has a large top contact functioning as a heat spreader as discussed in Chapter 4. Although, the thermal resistance decreased by more than 25%, it is still obvious by comparing the LI curves under pulsed and CW drive conditions that the microdisk lasers still suffer from self heating effects.

For two optical links the LI curves under pulsed drive conditions were also measured for higher currents and these results are shown in Figure 6.3. Both optical links had the same design parameters and this is reflected in the threshold current and slope efficiency just above threshold which are the same for both links. The optical link represented by the dashed lines, shows relatively constant bidirectional behavior, although there is some small discrepancy in output power at drive currents above 2 mA. The other link represented by the solid lines, shows bidirectional behavior up to about 2.2 mA, after which the left output (black line)

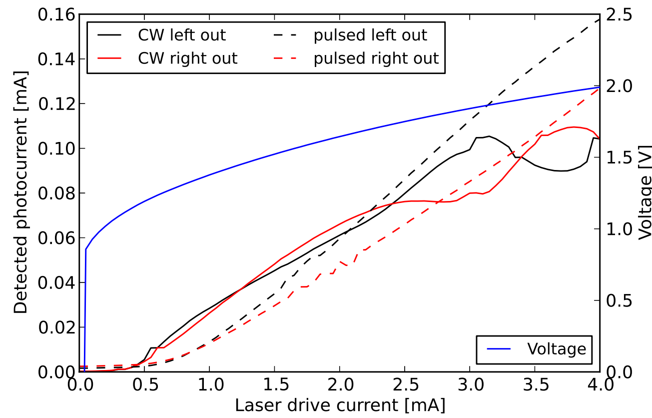

Figure 6.2: Current versus current plot of the optical link. The black and red curves correspond with the left and right detector, respectively. Solid lines represent CW measurements, while dashed lines represent pulsed measurements. The IV curve is indicated by the blue curve.

starts to saturate, while the slope efficiency of the right output (red line) starts to increase. Between 7 and 8 mA this behavior seems to reverse. The average output power over the left and right output however, remains constant in both cases. This indicates coupling between the clockwise and counterclockwise mode for the link represented by the solid lines. Both optical links reach an aggregated peak output current of 560 μA at a drive current of 8 mA. Taking into account the responsivity of the detectors, this comes down to a peak optical output power of the microdisk lasers in these two links of 810 μW. This result clearly indicates that thermal management and structures to make the microdisk laser unidirectional could improve the performance significantly.

Two different samples with identical optical link designs were fabricated. For these samples the gap between the silicon waveguide and the III-V microdisk laser and detector was controlled by etching back the top oxide above the silicon waveguide, as explained in Section 5.3. A slightly different etching time was used for each sample such that it resulted in two different gaps and therefore different coupling conditions. For the first sample a gap of 200 nm was targeted, while for the second sample the target was 250 nm. Based on cross sections made with an FIB it was found that the first sample was slightly under target with a 160 nm gap, while the second sample was on target. Identical optical link designs from these samples were compared as the different gaps are expected to result in different threshold currents and slope efficiencies for the microdisk laser and different responsivities for the detector. The results of the optical link discussed above correspond with

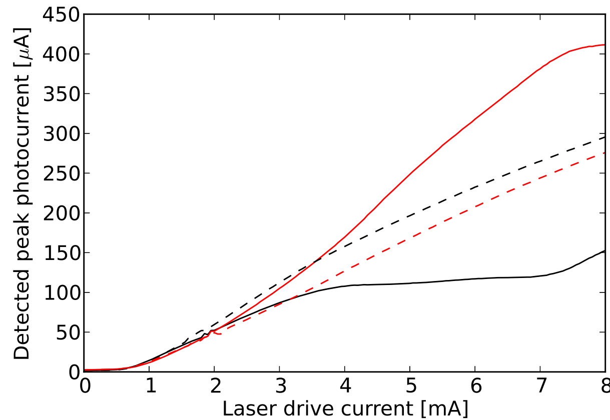

Figure 6.3: Current versus current plot for two different optical links (dashed and solid lines) under pulsed drive conditions. The black and red curves correspond with the left and right detector, respectively.

sample 1. The responsivity of the detectors on sample 2 are expected to be lower because of the larger gap. Indeed, the responsivity of the detectors on sample 2 was found to be 0.56 A/W with dark currents of 20 nA at a reverse bias of 1 V. The results of the full optical links are shown in Figure 6.4 for comparison, where in both cases the microdisk laser is working in CW regime. The solid lines represent the link on sample 1 (which corresponds with the link discussed above), while the dashed lines represent the link of sample 2. The black and red lines correspond with the left and right detectors respectively. The link on sample 2 has a threshold current of 0.22 mA and a maximum slope efficiency of 16 $\mu A/mA$. Correcting for the detector responsivity this yields 29 $\mu W/mA$. In this case a record low threshold current is achieved for these microdisks. If we compare the result from the two samples we find that sample 1 has a better slope efficiency, but at the cost of a higher threshold current. This is as expected because the thinner gap on sample 1 results in stronger coupling, which obviously results in higher output power but also in a larger optical loss factor that needs to be overcome to reach the lasing regime which is reflected in the higher threshold current.

Finally, another interesting result obtained from these optical links is shown in Figure 6.5. Above threshold the microdisk laser is operating in a bidirectional regime, where the total output power is evenly divided between the left and right output. Then, around 2.4 mA there is some oscillation between the left and right output, after which a sharp decrease in output power is observed for the left output and a sharp increase for the right output, thereby entering a unidirectional

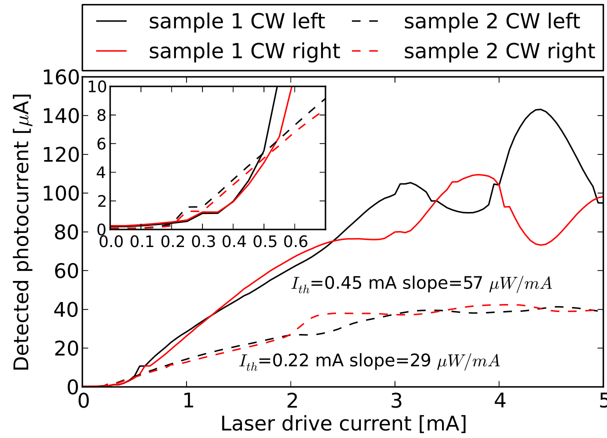

Figure 6.4: Current versus current plot of two identical optical interconnects from sample 1 (solid) and sample 2 (dashed). Black and red lines correspond with left and right outputs. Inset: zoom of the threshold currents.

regime. This behavior showing three different regimes in the LI curve indicates possible bistable operation of the microdisk laser. Bistable operation can be obtained in two mode lasers via gain saturation. A model to describe the occurrence of bistability in microring- and microdisk lasers, that takes into account the carrier reservoir, gain saturation and linear coupling between the clockwise and counter-clockwise mode, was presented by Sorel et al. [14]. Bistability in microdisk lasers with similar parameters as the devices described here has been studied through simulation [15] and was also experimentally demonstrated [16]. However, additional measurements are required for these devices to determine if they indeed show bistable behavior, but this was outside the scope of this thesis.

high-speed characterization

Knowing the CW characteristics, the small signal response of the full optical link was measured using an Agilent N5247A Performance Network Analyzer (PNA). The modulated signal from the PNA was fed into the laser via a ground-signal-ground (GSG) probe. Using an SG probe the detected signal at detector was fed back into the PNA. A bias-T was used for both the laser and the detector, where the detector bias was fixed to -1 V and the laser bias was swept from 1.4 to 1.9 V (1.1 to 3.4 mA) in steps of 0.1 V. The response of the optical link versus laser bias is shown in Figure 6.6 and the inset shows the 3 dB bandwidth versus the square root of the laser output power. As expected an almost linear relation is observed. At a bias of 1.9 V a 3 dB bandwidth of 7.6 GHz was measured. It should be noted that at

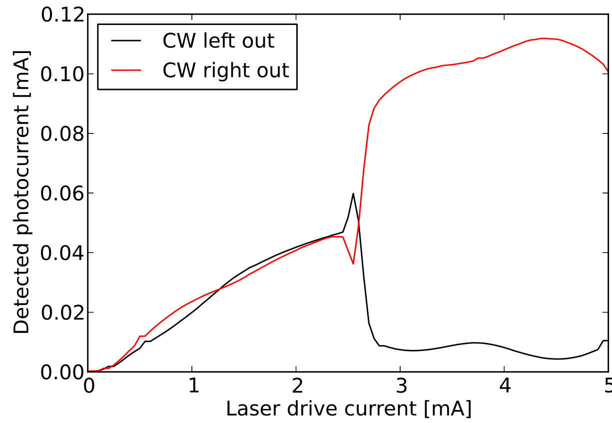

Figure 6.5: Current versus current plot of an optical link showing three different operating regimes: bidirectional output, oscillating output and unidirectional output regime.

higher frequencies the response increases again. As the distance between the laser and detector signal pads is only 120 μm, this is most likely caused by coupling of the microwave signal between the contacts via the sample's substrate. At this point no specific attention was paid to the impedance matching of the laser and detector to a 50 Ohm load. As a result, the return loss for the laser was at best 4 dB, while for the detector it was at best 2 dB indicating significant reflection. Reflection problems could be avoided by using a dedicated laser driver and integrated TIA for the detector.

Finally, a large-signal modulation was applied to the optical link. Similar as for the small signal modulation, a bias-T was used where the laser was biased at 1.9 V while the detector was biased at -1 V. A $2^7 - 1$ PRBS pattern from an Anritsu pattern generator was used to directly modulate the laser. The modulation voltage was set to 0.4 Vpp. The generated photocurrent from the detector was fed into a 13.5 GHz electrical amplifier and collected by a 100 GHz LeCroy scope. The large signal modulation response for a 10 Gb/s data rate is shown in Figure 6.7. A rise time with a mean value of 45 ps was measured, while the mean value of the fall time was rather high with 60 ps. Although the bit pattern can be resolved, the bit error rate is still poor at this point. This is most likely caused by the poor impedance matching in combination with the low power levels associated with microdisk lasers, resulting in a low signal-to-noise ratio. It is therefore expected that the performance can be improved by using a dedicated laser driver and integrated TIA for the detector.

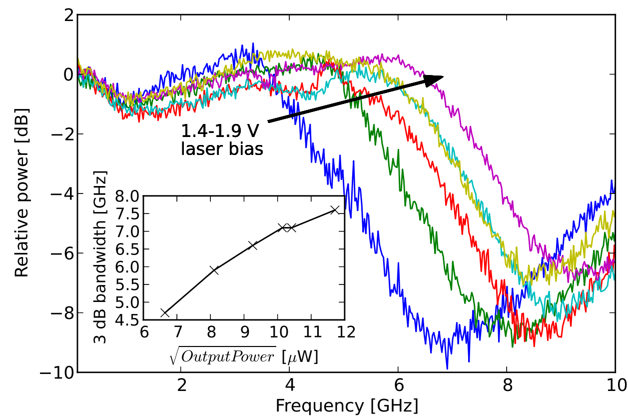

Figure 6.6: Small signal response of the full optical link versus laser bias and the 3dB bandwidth versus the square root of the laser output power (inset).

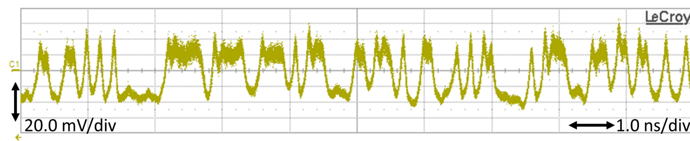

Figure 6.7: Large signal modulation response of the full optical link for a 10 Gb/s $2^7 - 1$ PRBS pattern.

6.2.2 Optical interconnect design for integration with CMOS

Next to the direct single optical link design described in the previous section, also a design consisting of multiple direct links was made. The purpose of this design is to enable data transfer between different points on a CMOS chip and thereby demonstrating a proof-of-concept for optical interconnects. The optical design consists of 4 transceiver blocks that each contain 2 microdisk lasers as sources and 2 detectors as receivers. The two microdisk lasers of a transceiver are both directly connected via a silicon waveguide to a detector of another transceiver. Each transceiver block can thereby communicate with two of the other transceiver blocks. At the other side of the microdisk laser the waveguide is terminated with a fiber coupler. The microdisk lasers are similar to the ones of the single optical links discussed above, except for the fact that in this design III-V heaters were placed around the microdisk cavity for wavelength tunability and no large heat spreading top contact was included. Also the detector designs are similar to the ones discussed in the previous section, although they are with a length of 40 μm a bit shorter. Furthermore, the electrical contacts of the sources and detectors are arranged in such a way that the photonics chip can be integrated with a CMOS chip through a flip-chipping process. A microscope image of the complete design including all the contact pads is shown in Figure 6.8(a). A more detailed image of the optical part of the design is shown in Figure 6.8(b) and Figure 6.8(c) shows a close-up image of a single transceiver block. This design was made in the context of the European FP7 project WADIMOS, where collaborating partners were taking care of the CMOS chip design, processing, flip-chip integration, system level simulations and so on.

Integration with CMOS electronics

The CMOS chip contains digital circuitry to generate the data to be transmitted over the optical link, as well as analog drivers and amplifier structures for the lasers and detectors, respectively. A flip-chip integration approach was foreseen for this demonstrator to connect the CMOS electronics with the photonics chip. In total 3 levels of electrical connections can be identified: first there are the connections between the CMOS and photonics, to drive the sources and read out data from the detectors. Second, there are connections required from the CMOS chip to the outside world, e.g. for power supply and testing of subcircuits such as the phase locked loop. Finally, there are connections required to connect the photonics chip to the outside world, e.g. to drive the heaters to tune the sources. Because of the large number of design rules for the CMOS chip, it was decided to keep the pad layout of the CMOS chip simple and to connect the CMOS chip to the outside world via the photonics chip. Thus, flip-chipping the CMOS die on top of the photonics die as shown schematically in Figure 6.9. The integrated package then

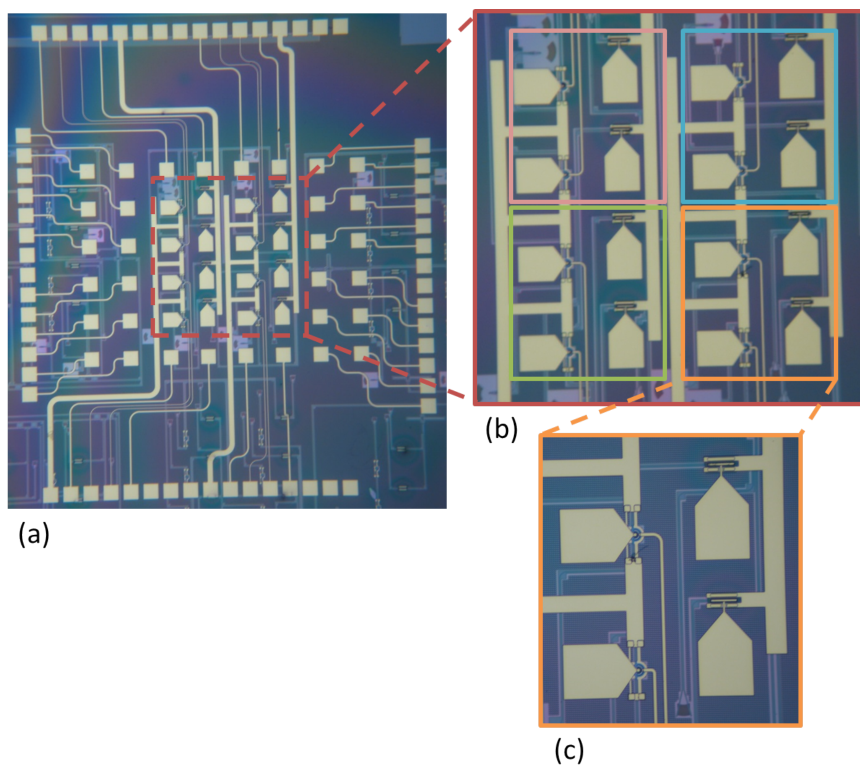

Figure 6.8: Microscope images of the fabricated Optical Interconnects for integration with CMOS. (a) Full overview including all the contact pads, (b) zoom on the 4 transceiver blocks and (c) zoom in on one particular transceiver block showing the 2 microdisk lasers and 2 detectors.

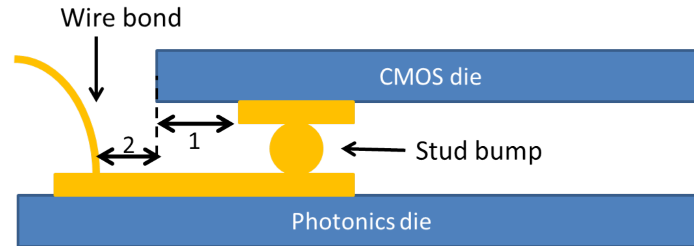

Figure 6.9: Schematic showing the integration approach used here. The CMOS chip is flip-chipped on top of the photonics chip. Stud bumps are used for electrical contacts between the CMOS and photonics chip. Contacts to the outside world are achieved through a wire bonding approach.

needs to be mounted on top of a PCB and all connections to the outside world are then connected to the PCB through a wire bonding approach. Important aspects here are the size of the CMOS die and the space required by the wire bonding tool (indicated in Figure 6.9 by 1 and 2 respectively), as these two parameters determine the pad positions for wire bonding. The final photonics chip layout is shown in Figure 6.8(a) and an image of a flip-chipping demo of two CMOS dies on top of a photonics die is shown in Figure 6.10.

Although this relatively easy flip-chipping integration approach is useful for demonstrating a proof-of-concept of optical interconnects, it is also clear from the large amount of contact pads required, that it is not scalable as the chip area for more complex circuits will go to extreme values. Therefore, other integration approaches such as TSVs and 3D integration are required for more complex circuits.

DC characterization of the optical links

To characterize the optical links a current sweep was applied to the microdisk lasers, just as was done for the compact single optical link discussed in the previous section. On one end of the waveguide the photocurrent generated by the detector is then measured, while at the other end the optical output is collected by a single mode fiber through a fiber coupler. The responsivity of the 40 μm long detectors in these designs was measured to be 0.69 A/W as discussed in Chapter 5. The fiber couplers used in these designs are slightly different from the ones used in the single microdisk laser designs as discussed in Section 4.3. The maximum efficiency of these fiber couplers was measured to be 24% at a wavelength of 1550 nm.

Figure 6.11 shows an example of the obtained results for two different optical links. The result in Figure 6.11(a) corresponds with the optical link from the orange marked transceiver to the pink marked transceiver in Figure 6.8(b) and the result in Figure 6.11(b) corresponds with the optical link from the orange marked

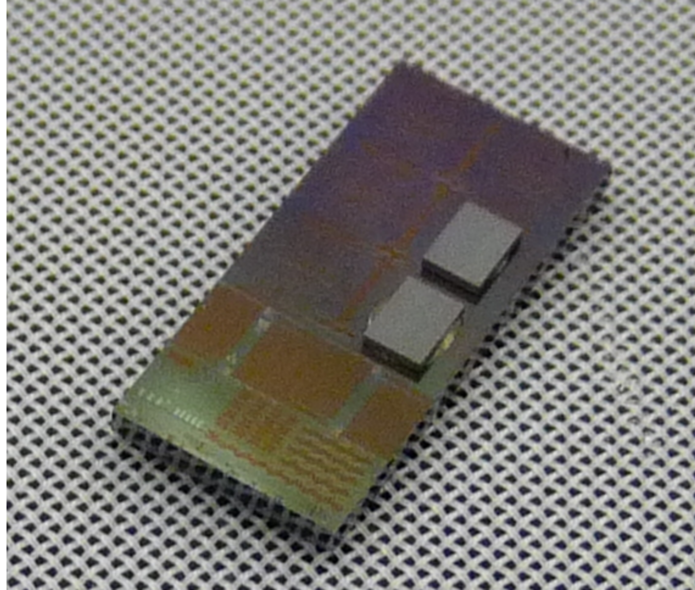

Figure 6.10: Image showing two CMOS chips flip-chipped on top of a photonics chip. Image courtesy of CEA Leti.

transceiver to the blue marked transceiver. For both optical links the threshold current of the microdisk laser is around 0.45 mA. For the link in Figure 6.11(a) the maximum output power collected by the fiber is 12.8 μW and the maximum detected photocurrent is 48 μA. Taking the efficiencies of the fiber coupler and the detector into account, this leads to 53 and 70 μW of optical power in the silicon waveguide. For the link in Figure 6.11(b) we find maximum output values of 8.5 μW and 39 μA, corresponding to 34 and 57 μW in the silicon waveguide.

In these optical links we also again see strong oscillations in the LI (or II) curves. This is in strong contrast to the results of the single optical links where detectors were placed on both sides of the microdisk laser. Although also in that case some oscillations could be observed the effect was much less then for the optical links here. In the design, measures were taken to avoid external reflections by using a bend radius for the silicon waveguides of 10 μm instead of the standard value of 5 μm. Also, low reflection fiber couplers were used instead of the standard fiber couplers. However, as already mentioned in Section 4.3 about the single microdisk laser designs, the low reflection fiber couplers used in this run were based on simulations only and the design was not yet optimized. It is therefore expected that the oscillations are still caused by reflections from the fiber couplers.

Another observation that can be made is that the thermal roll-over in the LI curves of the microdisk lasers is stronger for the devices discussed here, compared

to the single microdisk laser designs discussed in Section 4.3 and the single optical links discussed in the previous section. Both these designs used a large top contact on the microdisk laser that served as a heat spreader. In the design here, III-V ring heaters were placed around the microdisk lasers to be able to tune the wavelength and thus the heat spreading layer was absent resulting in a stronger thermal roll-over.

With this design it is shown that with the integration approach used here it is indeed possible to place microdisk lasers and detectors anywhere on the chip and even side by side if necessary. In the next section we will briefly discuss more complex designs that can be made using this approach.

6.3 Towards Optical Networks on Chip

In the previous section the feasibility of realizing compact optical interconnects using heterogeneously integrated microdisk lasers and detectors was demonstrated. There are no spatial constraints for both the microdisk laser and detector and thus basically any link circuit can be made. The optical links can be extended to form Optical Networks on Chip (ONoC) by including additional building blocks next to the source and detector. Designing such optical networks on chip requires analysis on a (micro)architectural and physical level. On an architectural level the analysis focuses on choosing the best network topology and routing algorithm based on the system requirements. The physical level deals with the actual design of the sources and detectors, waveguide layouts, router implementation and so on. In between the architectural level and the physical level, in literature often denoted as microarchitectural level, decisions need to be made on which parts of the network will be implemented in the electronic or photonic domain, the type of arbitration and flow control. The analysis on the (micro)architectural level is outside the scope of this thesis and here we will focus on building blocks and implementation on the physical level.

Amongst other multiplexing schemes, wavelength division multiplexing (WDM) is an attractive scheme and received a lot of attention as it allows for utilizing the full optical bandwidth of waveguides. In such a scheme, multiple wavelength channels are used and each wavelength channel can be modulated with data. These wavelength channels do not interfere with each other and therefore multiple wavelength channels in a single waveguide can be used such that the integration density can be increased. This WDM ONoC approach requires the implementation of wavelength demultiplexers and routers in the physical layout. Both passive and active solutions exist for these devices, but as power consumption is of prime importance in these on-chip networks, passive solutions are preferred.

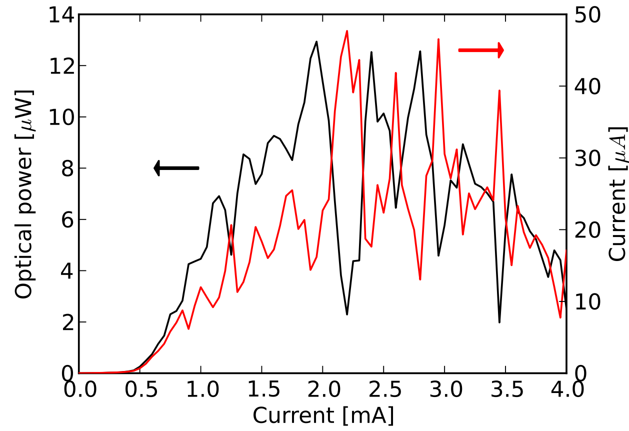

(a)

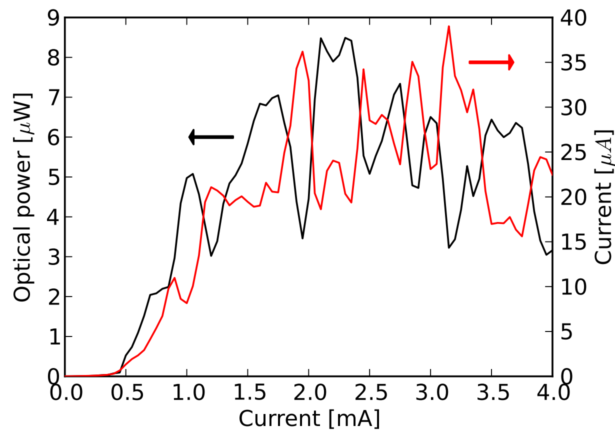

(b)

Figure 6.11: Current and light versus current plot of two optical links in the configuration for integration with CMOS. Threshold currents are 0.45 mA for both optical links. The optical link in (a) has slightly higher output power. Oscillations in the LI curves are much stronger compared to the optical links where detectors were placed on both sides of the microdisk.

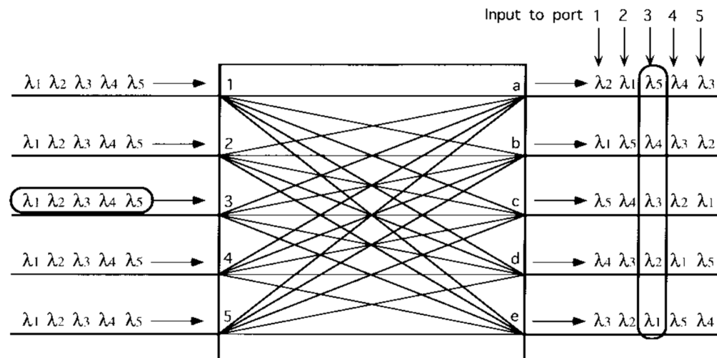

Figure 6.12: Schematic illustration of a wavelength router. Taken from [17]

Wavelength demultiplexer

Wavelength (de)multiplexers are based on structures with wavelength selective elements. When multiple wavelength channels are used in a single waveguide, e.g. by using a multi-wavelength laser, certain channels can be dropped from this waveguide to another waveguide, which could e.g. be connected to a receiver. When a large integration density is required such as for ONoCs, compact structures are preferred and this leads to either Mach-Zehnder interferometers or ring resonators.

Wavelength router

A wavelength router is a device with in general N input and output ports. Such a device basically combines the functionality of a multiplexer and demultiplexer and the principle of operation is schematically depicted in Figure 6.12. Waveguides that contain multiple wavelength channels are connected to the input ports of the wavelength router. Then at each port the different wavelength channels are demultiplexed into individual channels which are directed to the output ports. This is done in such a way that at each output port a single wavelength channel from each input port is collected and multiplexed onto the output waveguides. Thus, from a given input port each output port can be reached by using the designated wavelength.

6.3.1 ONoC demonstrators circuits

In the WADIMOS project several ONoC demonstrator circuits were designed. Unfortunately, due to fabrication and design issues we were not able to demonstrate these circuits. In nearly all cases the fabrication issues occurred in the steps for the active devices. Typical difficulties were the control of the etch depth of the mi-

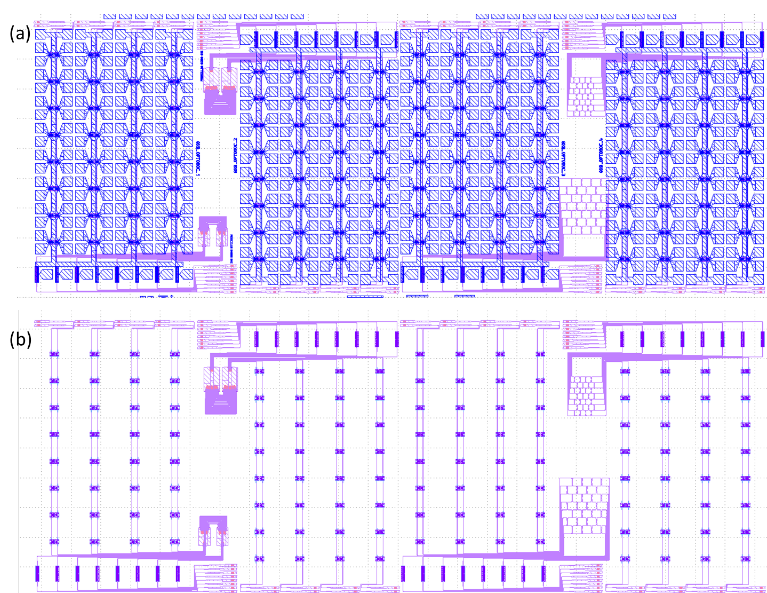

Figure 6.13: Mask layout of 4 8x8 Optical Networks on Chip, where in each design a different wavelength router is used. (a) Including metal contact pads and (b) without metal contact pads showing the possible size reduction.

crodisk laser and the control of the CMP step to planarize the surface after oxide deposition. Nevertheless, we will briefly discuss the designs of these circuits. In a first design, 8 transmitters are connected to an 8x8 wavelength router of which the outputs are connected to 8 receivers. Each transmitter consists of an array of 8 microdisk lasers coupled to one silicon waveguide such that a multi-wavelength laser is formed. The 8 output waveguides from the transmitters are then connected to either an AWG or a ring network that serves as a wavelength router. The detectors discussed in Chapter 5 serve as broadband receivers as no wavelength selective circuit is included at the receiving side. Figure 6.13 shows 4 designs using this approach where each design uses a variation of the wavelength router. Figure 6.13(a) shows the designs including the contact pads, while Figure 6.13(b) shows the same circuits but without contact pads. Comparing Figure 6.13(a) and (b) it is clear that the size of these designs is mainly determined by the contact pads. Therefore, we can conclude that an advanced contacting scheme is required such as e.g. through silicon vias as a flip chip approach is obviously not scalable.

In another design approach the complexity of the optical circuit is reduced and is actually based on the multiple optical interconnects for integration with CMOS discussed in the previous section. However, instead of a direct connection between a microdisk laser and detector, now small wavelength routers and wavelength se-

lective elements are included. Such a design variation is shown in Figure 6.14. Again Figure 6.14(a) shows the schematic that includes all the metal pads, while Figure 6.14(b) only shows the optical circuit, which clearly can be reduced in size. As can be seen from Figure 6.14(a) heaters are included to tune the wavelength routers and wavelength selective elements. The circuit is designed in such a way that each transceiver block can communicate with two other transceiver blocks.

The operation principle is as follows, each transceiver block has 2 lasers operating at a different wavelength. The wavelength routers are tuned in such a way that the ring is in resonance on one of the wavelengths. As a result the different wavelengths will be routed to a different output port. At the receiving side of each transceiver block, two rings are included that are tuned to λ_1 and λ_2, respectively. By including these demultiplexers and two separate detectors at the receiving side, data from two different sources can be received simultaneously. The arrows in Figure 6.14(b) indicate the flow for transmission from the pink transceiver to the blue and orange transceiver.

Figure 6.15(a) shows a circuit that works on the same principle, but in this case the rings in the wavelength routers and the wavelengths selective elements are replaced by Mach-Zehnder interferometers.

Figure 6.15(b) uses a slightly different approach where the transmitters and receivers are connected to a bus waveguide through ring resonators.

6.4 Conclusions

Using the microdisk laser and the detector described in Chapter 5 we here demonstrated a compact optical link on silicon. These optical links were fabricated in the clean room of Ghent University. The optical links were realized on two different samples having a different gap between the active devices and the waveguide. The sample with the 250 nm gap resulted in very low threshold currents of 0.22 mA and a single sided slope efficiency of 29 $\mu W/mA$ for the microdisk laser. While on the sample with the 160 nm gap a threshold current of 0.45 mA and a single sided slope efficiency of 57 $\mu W/mA$ was obtained. Furthermore, it was also observed that by using detectors instead of fiber couplers the LI curves were much smoother. The small-signal bandwidth of the full optical link was measured to be 7.6 GHz and is limited by the bandwidth of the microdisk laser. Large-signal modulation was also performed at a rate of 10 Gb/s and the data could be resolved at the detector.

An optical interconnect design for integration with CMOS electronics, consisting of multiple direct optical links, was also demonstrated. A 2-dimensional contact pad array was included for interfacing with the CMOS electronics through a flip-chipping approach. In this design, fiber couplers were used on one end of the waveguide coming from the microdisk lasers, while on the other end a detector

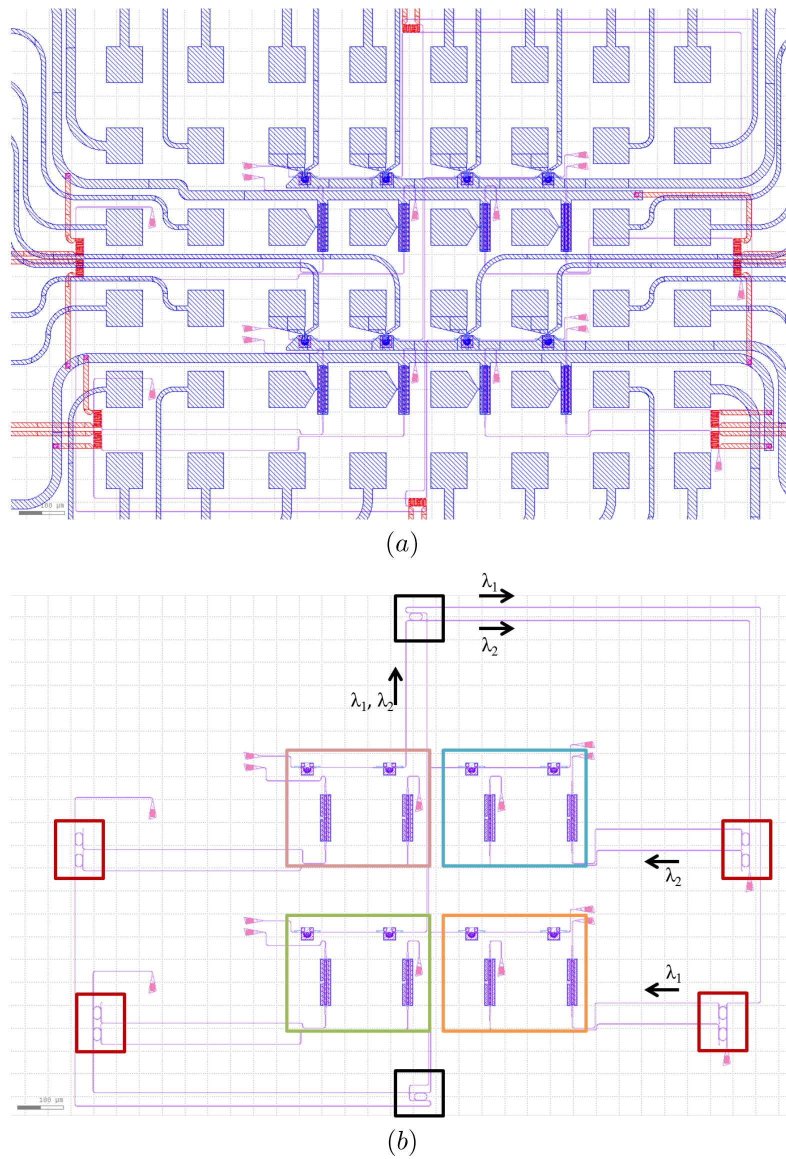

Figure 6.14: Mask layout of a 2x2 Optical Network on Chip. (a) Full layout including metal contact pads and heaters for tuning the wavelength selective elements and (b) without metal contact pads showing the possible size reduction and also the flow of 2 different wavelength channels originating from the pink transceiver block.

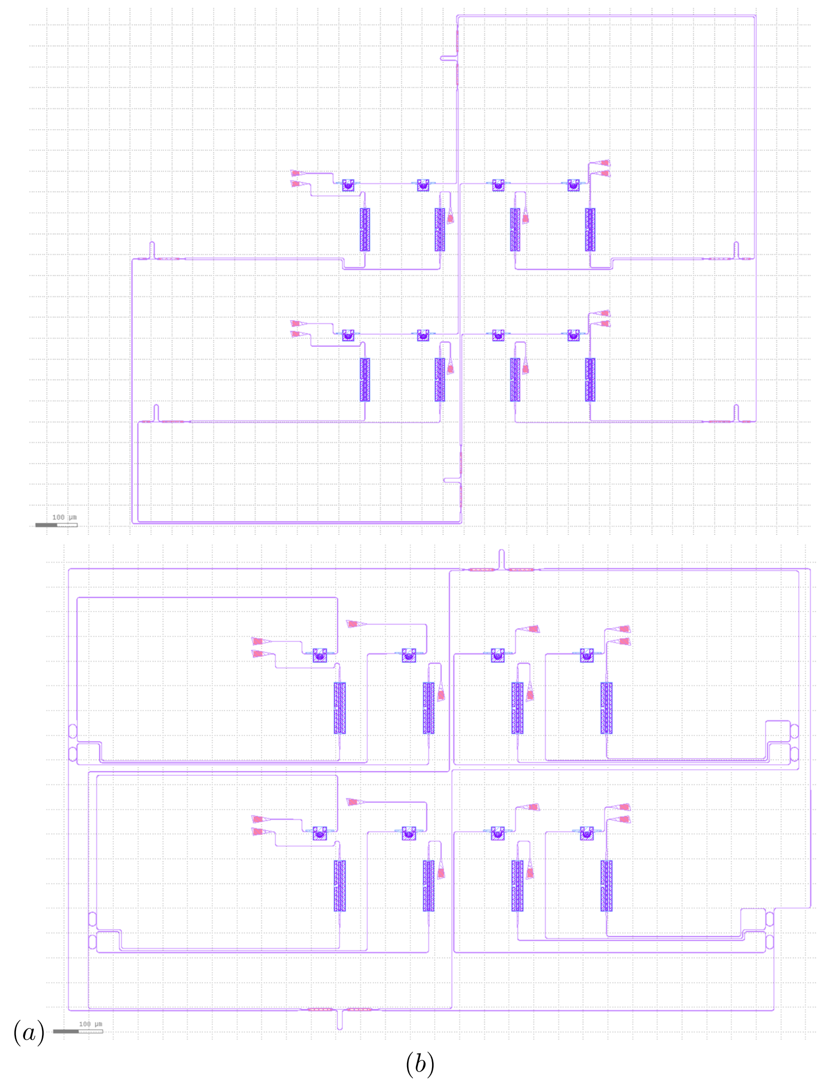

Figure 6.15: 2 variations on the 2x2 Optical Network on Chip shown in the previous Figure, where in (a) MZIs are used as wavelength selective elements instead of rings and in (b) the sources and detectors are connected to a bus waveguide through ring resonators.

was used to form the optical link. Because of the presence of the fiber coupler, again strong oscillations were observed in the LI curves.

By adding wavelength selective elements in the passive silicon layer, the optical links can be extended to form Optical Networks-on-Chip. Several designs have been made to demonstrate such networks, but these could unfortunately not be experimentally demonstrated due to several fabrication errors. Nevertheless, as numerous of these passive wavelength selective elements have already been demonstrated and we here demonstrated the possibility for compact integration of microdisk lasers and detectors on silicon, there is no fundamental issue preventing to realize Optical Networks-on-Chip.

References

[1] Attila Mekis, Steffen Gloeckner, Gianlorenzo Masini, Adithyaram Narasimha, Thierry Pinguet, Subal Sahni, and Peter De Dobbelaere. *A Grating-Coupler-Enabled CMOS Photonics Platform*. IEEE Journal of Selected Topics in Quantum Electronics, 17(3):597–608, May 2011.

[2] Long Chen, Kyle Preston, Sasikanth Manipatruni, and Michal Lipson. *Integrated GHz silicon photonic interconnect with micrometer-scale modulators and detectors.* Optics express, 17(17):15248–56, August 2009.

[3] EPIXfab. *www.epixfab.eu*, 2013.

[4] Ari Novack, Yang Liu, Ran Ding, Michael Gould, Tom Baehr-Jones, Qi Li, Yisu Yang, Yangjin Ma, Yi Zhang, Kishore Padmaraju, Karen Bergmen, Andy Eu-Jin Lim, Guo-Qiang Lo, and Michael Hochberg. *A 30 GHz silicon photonic platform*. In Pavel Cheben, Jií Čtyroký, and Iñigo Molina-Fernandez, editors, SPIE Optics + Optoelectronics, page 878107. International Society for Optics and Photonics, May 2013.

[5] G Roelkens, D Van Thourhout, R Baets, R Nötzel, and M Smit. *Laser emission and photodetection in an InP/InGaAsP layer integrated on and coupled to a Silicon-on-Insulator waveguide circuit.* Optics express, 14(18):8154–9, September 2006.

[6] J. Van Campenhout, PRA Binetti, P.R. Romeo, P. Regreny, C. Seassal, X.J.M. Leijtens, T. De Vries, Y.S. Oei, R.P.J. Van Veldhoven, R. Notzel, L Di Cioccio, J-M Fedeli, M Smit, D Van Thourhout, and R Baets. *Low-footprint optical interconnect on an SOI chip through heterogeneous integration of InP-based microdisk lasers and microdetectors*. Photonics Technology Letters, IEEE, 21(8):522–524, 2009.

[7] Liu Liu, Joris Van Campenhout, Gunther Roelkens, Dries Van Thourhout, Pedro Rojo-Romeo, Philippe Regreny, Christian Seassal, Jean-Marc Fedeli, and Roel Baets. *Ultralow-power all-optical wavelength conversion in a silicon-on-insulator waveguide based on a heterogeneously integrated III-V microdisk laser*. Applied Physics Letters, 93(6):061107, 2008.

[8] Kazuya Ohira, Kentaro Kobayashi, Norio Iizuka, Haruhiko Yoshida, Mizunori Ezaki, Hiroshi Uemura, Akihiro Kojima, Kenro Nakamura, Hideto Furuyama, and Hideki Shibata. *On-chip optical interconnection by using integrated III-V laser diode and photodetector with silicon waveguide.* Optics express, 18(15):15440–7, July 2010.

[9] P Mechet, S Verstuyft, T de Vries, T Spuesens, P Regreny, D Van Thourhout, G Roelkens, and G Morthier. *Unidirectional III-V microdisk lasers heterogeneously integrated on SOI.* Optics express, 21(16):19339–52, August 2013.

[10] Di Liang, Sudharsanan Srinivasan, David A Fattal, Marco Fiorentino, Zhihong Huang, Daryl T Spencer, John E Bowers, and Raymond G Beausoleil. *Teardrop Reflector-Assisted Unidirectional Hybrid Silicon Microring Lasers*. Photonics Technology Letters, IEEE, 24(22):1988–1990, 2012.

[11] F Mandorlo, P Rojo Romeo, Xavier Letartre, R Orobtchouk, and Pierre Viktorovitch. *Compact modulated and tunable microdisk laser using vertical coupling and a feedback loop*. Optics express, 18(19):19612–19625, 2010.

[12] A Katz, BE Weir, and W.C Dautremont-smith. *Au/Pt/Ti contacts to p-In0. 53Ga0. 47As and n-InP layers formed by a single metallization common step and rapid thermal processing*. Journal of Applied Physics, 68(3):1123–1128, 1990.

[13] Yanlu Li, Diedrik Vermeulen, Yannick De Koninck, Gunay Yurtsever, Günther Roelkens, and Roel Baets. *Compact grating couplers on silicon-on-insulator with reduced backreflection.* Optics letters, 37(21):4356–8, November 2012.

[14] M Sorel, G Giuliani, A Scirè, R Miglierina, and Student Member. *Operating Regimes of GaAs AlGaAs Semiconductor Ring Lasers : Experiment and Model*. October, 39(10):1187–1195, 2003.

[15] Y. De Koninck, K. Huybrechts, G. Van der Sande, J. Danckaert, R. Baets, and G. Morthier. *Nonlinear dynamics of asymmetrically coupled microdisk lasers*. In 2009 IEEE LEOS Annual Meeting Conference Proceedings, pages 503–504. IEEE, October 2009.

[16] Liu Liu, Rajesh Kumar, Koen Huybrechts, Thijs Spuesens, G. Roelkens, E.J. Geluk, T. De Vries, Philippe Regreny, D. Van Thourhout, Roel Baets, and G Morthier. *An ultra-small, low-power, all-optical flip-flop memory on a silicon chip*. Nature Photonics, 4(3):182–187, 2010.

[17] Govind P. Agrawal. *Fiber-Optic Communication Systems(Google eBook)*. John Wiley & Sons, 2010.

7
Conclusions and outlook

7.1 Conclusions

With the increasing computational power and bandwidth, electrical interconnects form a bottleneck at shorter and shorter distances. On-chip bandwidths in the order of over 100 Tb/s are expected for 2022 and hence alternatives need to be explored. Optical interconnects are a possible solution. Next to bandwidth, also energy efficiency is a major issue for on-chip links and the available power budget translates into an estimated energy efficiency of 10-30 fJ/bit.

In this work we investigated the feasibility of on-chip optical interconnects on silicon based on a heterogeneous integration approach with III-V material. Compact on-chip optical links on silicon using microdisk lasers as a source in combination with compatible detectors have been successfully demonstrated. Achieving compact integration of sources and detectors is important when one wants to realize bidirectional links. Compact integration is achieved by using a new epitaxial structure that contains the required layers for an efficient detector on top of the thin film required for the laser. This allows lasers and detectors to be fabricated right next to each other.

Simulations were performed to investigate optical loss mechanisms in the microdisk lasers and optimized designs were made based on these results. Next to this, rigorous 2.5 D axi-symmetric electro-optical simulations were performed to get better insight in the charge carrier transport. The simulation was fitted to experimental results, increasing the reliability of the model. It was found that carriers

injected in the center move towards the periphery through a drift and/or diffusion current which enhances the stimulated recombination rate. However, this process cannot sustain and as a result the output power first saturates, then carrier density increases again such that the output power can also increase again.

Microdisk lasers with threshold currents as low as 0.22 mA have been demonstrated and a total peak output power of 860 μW has been obtained under pulsed drive conditions. In CW operation the laser suffers from severe self-heating resulting in early thermal roll-over limiting the total output power to a maximum of 300 μW i.e. 150 μW single sided. A maximum small-signal bandwidth of 7.8 GHz has been measured.

A detector structure on top of the thin film laser structure has been developed and shows good performance compared to the standard III-V integrated detectors on silicon. A maximum responsivity of 0.97 A/W and dark currents down to 20 nA have been demonstrated. Furthermore, a maximum small-signal bandwidth of 18 GHz was achieved. Nevertheless, further improvement of the responsivity and bandwidth would be desirable.

An efficient fabrication process has been developed where all fabrication steps for the microdisk laser and detector are carried out simultaneously, expect for the detector mesa definition. Both the microdisk laser and detector were successfully fabricated on a 200 mm waferscale in a CMOS pilot line facility at CEA-Leti. However, several issues during processing prevented the realization of both microdisk laser and detectors on the same chip. Therefore, no optical link was obtained on these samples.

Optical links on silicon were demonstrated on the samples fabricated in the clean room of Ghent University. The bandwidth of the optical links was found to be limited by the bandwidth of the microdisk laser. Next to single optical links also multiple optical links on a photonics chip were designed and in such a way that they allowed for a flip-chip integration approach with an electronic CMOS chip. From this design it is clear that integration of a large number of interconnects will be limited by the pad size and pitch when a flip chip approach is used. Therefore, Electro-photonic integration schemes need to be further investigated.

Several issues with mainly the sources still exist. The self-heating of the microdisk lasers is a significant problem and has a large impact on the performance. This is in fact a general problem for heterogeneously integrated lasers as they are thermally isolated by the bonding layer. It has been shown that a heat spreader in the form of a large top contact could reduce the thermal resistance by 25%, but this is still not sufficient to prevent early thermal roll-over.

Also the energy efficiency needs to be further improved in order to meet the requirements for on-chip optical interconnects. Mainly at the laser side further improvements are required. By reducing the threshold current the dissipated power can be lowered and also the bandwidth might be enhanced by this and both help in

decreasing the required amount of energy per bit. Therefore, future work should focus on more efficient current injection schemes that can help to reduce the threshold current.

The first iteration of multi-wavelength lasers based on cascaded microdisk lasers showed strong coupling to higher order modes of adjacent microdisks. This problem was further investigated by simulating the coupling between the access waveguide mode and multiple disk modes. Based on these results the coupling was optimized and this was experimentally confirmed with the second generation of multi-wavelength lasers. A remaining issue here is the control of disk diameter to get the lasing wavelengths on the desired grid. However, by using higher resolution lithography like electron beam or immersion lithography in case of mass production, the diameter can be controlled more accurately.

Optical Networks-on-Chip (ONoCs) have been designed but due to processing and design issues no measurement results could be obtained. However, numerous passive circuits in silicon have already been demonstrated and because both the microdisk laser and detector were successfully fabricated in a 200 mm CMOS pilot line, there is no fundamental reason why ONoCs based on passive wavelength selective elements in combination with the microdisk lasers and detectors should not work.

7.2 Outlook

A proof-of-principle of an optical link on silicon has been successfully demonstrated. However, additional work needs to be done...

The energy efficiency of the optical link needs to be improved by at least an order of magnitude in order to be a feasible alternative for electrical interconnects. Especially at the source an improvement is required. With the current devices a uniform injection scheme is used. However, the carriers injected in the center of the microdisk cavity are a large source for non-radiative Auger recombination. The injection scheme therefore needs to be optimized such that carriers are confined to the area where the light is propagating. Possible solutions are proton implant in the center of the microdisk cavity or reducing the size of the tunnel junction by wet etching it from the center. Another possibility would be to use optically transparent contacts that can be placed at the periphery of the microdisk.

Reducing the diameter of the microdisk laser could also yield lower threshold currents and hence improved energy efficiency, but this is limited by bend losses due to the bottom contact layer and scattering losses due to sidewall roughness. Using an optically transparent contact layer such as ITO or Graphene could allow for compact microdisk lasers. However, the efficiency of the current injection should be sufficiently high, as otherwise the high electrical resistance will result in strong self heating of the microdisk laser. Also the dry etch process need to be

optimized to reduce scattering losses.

Through Silicon Vias (TSVs) could potentially be used to make a thermal shunt path to the silicon substrate, such that heat can be evacuated more efficiently.

At the detector side, it might be worthwhile to investigate the possibility of preamplification by the laser stack below the detector. In the present devices, the laser stack under the detector was not electrically contacted, but when this is done preamplification could be achieved. This obviously, would come at the cost of higher power consumption.

For efficient multi-wavelength lasers based on microdisks, the disk diameter should be better controlled such that the lasing wavelengths are on the targeted grid. This can be achieved by using e.g. ebeam lithography. In case of mass-fabrication using CMOS technology improved performance can be expected when a mask grid of 1 nm is used instead of 5 nm. Furthermore, using immersion lithography used in 300 mm CMOS lines, will also allow for better control of the disk diameter.

List of publications

A.1 Publications in International Journals

1. P. Mechet, T. Spuesens, S. Werquin, K.T Vandoorne, N. Olivier, J.M. Fedeli, P. Regreny, D. Van Thourhout, G. Roelkens, G. Morthier, "All-optical low-power 2R regeneration of 10Gb/s NRZ signals using a III-V on SOI microdisk laser", IEEE Photonics Journal, vol. 5(6), p. 7802510, Dec. 2013.

2. P. Mechet, S. Verstuyft, T. De Vries, T. Spuesens, P. Regreny, D. Van Thourhout, G. Roelkens, G. Morthier, "Unidirectional III-V microdisk lasers heterogeneously integrated on SOI", Optics Express, vol. 21(16), pp. 19339-19352, Aug. 2013.

3. T. Spuesens, J. Bauwelinck, P. Regreny, D. Van Thourhout, "Realization of a compact optical interconnect on Silicon by heterogeneous integration of III-V", Photonics Technology Letters, vol. 25(14), pp. 1332-1335, Jul. 2013.

4. P. Mechet, F. Raineri, A. Bazin, Y. Halioua, T. Spuesens, T. J. Karle, P. Regreny, P. Monnier, D. Van Thourhout, I. Sagnes, R. Raj, G. Roelkens, G. Morthier, "Uniformity of the lasing wavelength of heterogeneously integrated InP microdisk lasers on SOI", Optics Express, vol. 21(9), pp. 10622-10631, Mar. 2013.

5. T. Van Vaerenbergh, M. Fiers, P. Mechet, T. Spuesens, R. Kumar, G. Morthier, B. Schrauwen, J. Dambre, P. Bienstman, "Cascadable Excitability in

microrings", Optics Express, vol. 20(18), OSA, pp. 20292-20308, Aug. 2012.

6. T. Spuesens, F. Mandorlo, P. Rojo-Romeo, P. Regreny, N. Olivier, J.M. Fedeli, D. Van Thourhout, "Compact integration of optical sources and detectors on SOI for optical interconnects fabricated in a 200 mm CMOS pilot line", Journal of Lightwave Technology, vol. 30(11), pp. 1764-1770, Jun. 2012.

7. Joan Lloret, G. Morthier, Francisco Ramos, Salvador Sales, D. Van Thourhout, T. Spuesens, Nicolas Olivier, Jean-Marc Fedeli, Jose Capmany, "Broadband microwave photonic fully tunable filter using a single heterogeneously integrated III-V/SOI-microdisk-based phase shifter", Optics Express, pp. 10796-10806, Apr. 2012.

8. J. Lloret, R. Kumar, S. Sales, F. Ramos, G. Morthier, P. Mechet, T. Spuesens, D. Van Thourhout, N. Olivier, J.-M. Fedeli, J. Capmany, "Ultra-compact electro-optic phase modulator based on III-V-on-silicon microdisk resonator", Optics Letters, vol. 37(12), pp. 2379-2381, Feb. 2012.

9. R. Kumar, T. Spuesens, P. Mechet, N. Olivier, J.- M. Fedeli, P. Regreny, G. Roelkens, D. Van Thourhout, G. Morthier, "10Gbit/s all-optical NRZ-OOK to RZ-OOK format conversion in an ultra-small III-V-on-silicon microdisk fabricated in a CMOS pilot line ", Optics Express, vol. 19(24), OSA, pp. 24647-24656, Nov. 2011.

10. R. Kumar, T. Spuesens, P. Mechet, P. Kumar, O.Raz, N. Olivier, J.- M. Fedeli, G. Roelkens, R. Baets, D. Van Thourhout, G. Morthier, "Ultra-fast and Bias-free All-Optical Wavelength Conversion Using III-V on Silicon Technology", Optics Letters, vol. 36(13), OSA, pp. 2450-2452, Jul. 2011.

11. D. Van Thourhout, T. Spuesens, S. Selvaraja, L. Liu, G. Roelkens, R. Kumar, G. Morthier, P. R. -Romeo, , F. Mandorlo, O. Raz, C. Kopp, L. Grenouillet, "Nanophotonic Devices for Optical Interconnect", IEEE JSTQE (invited), vol. 16(5), IEEE, pp. 1363-1375, Sep. 2010.

12. L. Liu, T. Spuesens, G. Roelkens, D. Van Thourhout, P. Regreny, P. Rojo-Romeo, "A thermally tunable microdisk laser built on a III-V/Silicon-on-insulator heterogeneous integration platform", Photonics Technology Letters, vol. 22, p. 1270, May. 2010.

13. L. Liu, R. Kumar, K. Huybrechts, T. Spuesens, G. Roelkens, E.-J. Geluk, T. de Vries, P. Regreny, D. Van Thourhout, R. Baets, G. Morthier, "An ultra-small, low-power, all-optical flip-flop memory on a silicon chip", Nature Photonics, vol. 4(3), pp. 182-187, Jan. 2010.

A.2 Publications in International Conferences

1. G. Morthier, P. Mechet, T. Spuesens, D. Van Thourhout, G. Roelkens, "Asymmetric Heterogeneously Integrated InP Microdisk Lasers on Si for Optical Interconnect and Optical Logic" (invited), Conference on Lasers and Electro-Optics 2014, to be published.

2. P. Mechet, F. Raineri, A. Bazin, T. Spuesens, P. Regreny, P. Monnier, D. Van Thourhout, I. Sagnes, R. Raj, G. Roelkens, G. Morthier, "Extremely uniform lasing wavelengths of InP microdisk lasers heterogeneously integrated on SOI", IEEE Photonics Conference 2013 (IPC), Seattle, United States, p. ME3.2, Sep. 2013.

3. G. Roelkens, S. Keyvaninia, Y. De Koninck, P. Mechet, T. Spuesens, M. Tassaert, S. Stankovic, G. Morthier, R. Baets, D. Van Thourhout, G. Duan, J.M. Fedeli, M. Smit, "Heterogeneous III-V/silicon photonic integrated circuits" (invited), Asia Communications and Photonics Conference 2013, to be published.

4. P. Mechet, T. Spuesens, N. Olivier, J.-M. Fedeli, P. Regreny, D. Van Thourhout, G. Roelkens, G. Morthier, "All-optical, low-power 2R regeneration of 10Gb/s NRZ signals using a III-V on SOI microdisk laser", 18th OptoElectronics and Communications Conference held jointly with 2013 International Conference on Photonics in Switching (OECC/PS), Kyoto, Japan, pp. paper TuPO-4, Jun. 2013.

5. G. Morthier, P. Mechet, T. Spuesens, G. Roelkens, D. Van Thourhout, "Heterogeneously integrated InP microdisk lasers" (invited), the 7th International Conference on Nanophotonics (ICNP) The 3rd Conference on Advances in Optoelectronics and Micro/Nano Optics (AOM)2013, Hong Kong , China, p. 111, May. 2013.

6. T. Spuesens, P. Regreny, D. Van Thourhout, "Improved fabrication process for III-V based Optical Interconnects on Silicon", Group IV Photonics 2013, to be published.

7. T. Van Vaerenbergh, M. Fiers, P. Mechet, T. Spuesens, R. Kumar, G. Morthier, K.T Vandoorne, B. Schneider, B. Schrauwen, J. Dambre, P. Bienstman, "Characterization of cascadable excitability in a silicon-on-insulator microring", Proceedings of the 2012 Annual Symposium of the IEEE Photonics Society Belenux Chapter, Mons, Belgium, pp. 119-122, Nov. 2012.

8. T. Van Vaerenbergh, M. Fiers, P. Mechet, T. Spuesens, R. Kumar, G. Morthier, K.T Vandoorne, B. Schneider, B. Schrauwen, J. Dambre, P. Bienst-

man, " Self-pulsation and excitability mechanism in silicon-on-insulator microrings ", 2012 Asia Communications and Photonics Conference (ACP), OSA, Guangzhou, China, p. ATh4B.5, Nov. 2012.

9. T. Spuesens, Y. De Koninck, D. Van Thourhout, "Efficient vertical coupling between a silicon waveguide and an InP-based microdisk", 16th European Conference on Integrated Optics (ECIO 2012), Barcelona, Spain, p. paper 212, Apr. 2012.

10. R. Kumar, T. Spuesens, P. Mechet, N. Olivier, J.- M. Fedeli, P. Regreny, G. Roelkens, D. Van Thourhout, G. Morthier, "10Gbit/s Bias-free and Error-free All-optical NRZ-OOK to RZ-OOK Format Conversion Using a III-V-on-silicon Microdisk Resonator ", The Optical Fiber Communication Conference and Exposition (OFC) and The National Fiber Optic Engineers Conference (NFOEC) 2012, United States, p. JW2A.77, Mar. 2012.

11. Joan Lloret, F. Ramos, S. Sales, J. Capmany, G. Morthier, D. Van Thourhout, T. Spuesens, N. Olivier, J.-M. Fedeli, "Fully tunable microwave photonic phase shifter for broadband signals based on a single heterogeneously integrated III-V-on-SOI microdisk resonator", 16th European Conference on Integrated Optics (ECIO 2012), Barcelona, Spain, p. paper 158, Feb. 2012.

12. R. Kumar, T. Spuesens, P. Mechet, J.- M. Fedeli, N. Olivier, P. Regreny, G. Roelkens, D. Van Thourhout, G. Morthier, "All-optical de-multiplexing of 10Gbps data using III-V/SOI microdisk resonators", Annual Symposium of the IEEE Photononics Benelux Chapter, Belgium, Oct. 2011.

13. G. Morthier, P. Mechet, R. Kumar, G. Roelkens, T. Spuesens, T. De Vries, E. J. Geluk, P. Regreny, R. Baets, D. Van Thourhout, "Progress in heterogeneously integrated silicon-InP laser diodes for on-chip all-optical networks and signal processing" (invited), Frontiers in Optics 2011, OSA, San Jose, California, United States, p. paper FWBB4, Oct. 2011.

14. R. Kumar, T. Spuesens, P. Mechet, J.- M. Fedeli, N. Olivier, P. Regreny, G. Roelkens, D. Van Thourhout, G. Morthier, "Proof-of-concept Demonstration of an All-Optical De-multiplexer Using III-V/SOI Microdisk Resonator Fabricated in a CMOS Pilot Line", IPC2011, Arlington, Virginia, pp. 127-128, Oct. 2011.

15. G. Roelkens, S. Stankovic, S. Keyvaninia, P. Mechet, R. Kumar, T. Spuesens, G. Morthier, R. Baets, D. Van Thourhout, M. Lamponi, G. Duan, Y. Halioua, F. Raineri, R. Raj, "Laser sources on a heterogeneous III-V/silicon platform" (invited), IEEE Photonics 2011 (IPC 2011), Arlington, Virginia, United States, pp. 395-396, Oct. 2011.

16. R. Kumar, T. Spuesens, P. Mechet, P. Regreny, J.- M. Fedeli, N. Olivier, G. Roelkens, D. Van Thourhout, G. Morthier, ”All-optical de-multiplexing using III-V/SOI microdisk resonators”, European Semiconductor Laser Workshop (ESLW), Lausanne, Switzerland, Sep. 2011.

17. R. Kumar, T. Spuesens, P. Mechet, P. Regreny, N. Olivier, J.-M. Fedeli, G. Roelkens, D. Van Thourhout, G. Morthier, ”10Gbps bias-free all-optical wavelength conversion using InP-microdisk resonators heterogeneously integrated onto SOI ”, ECOC, Geneva, Switzerland, p. paper We.9.LeSaleve.3, Sep. 2011.

18. T. Spuesens, D. Van Thourhout, P. Rojo Romeo, P. Regreny, J.M. Fedeli, ”CW operation of III-V microdisk lasers on SOI fabricated in a 200 mm CMOS pilot line”, Group IV Photonics 2011, pp. 199-201, Sep. 2011.

19. W. Bogaerts, S. Selvaraja, H. Yu, T. Spuesens, P. Mechet, S. Stankovic, S. Keyvaninia, J. Van Campenhout, P. Absil, G. Roelkens, D. Van Thourhout, R. Baets, ”A Silicon Photonics Platform with Heterogeneous III-V Integration” (invited), Integrated Photonics Research, Silicon and Nano-Photonics (IPR), Optical Society of America, Toronto, Canada, p. IWC2, Jun. 2011.

20. T. Spuesens, L. Liu, D. Vermeulen, J. Zhao, P. Rojo Romeo, P. Regreny, L. Grenouillet, J.M. Fedeli, D. Van Thourhout, ”Integration of photodetectors with lasers for optical interconnects using 200 mm waferscale III-V/SOI technology”, The Optical Fiber Communication Conference and Exposition (OFC) and The National Fiber Optic Engineers Conference (NFOEC) 2011, Mar. 2011.

21. Fedeli, J.-M., L. Liu, Grenouillet, L., Bordel, D., Mandorlo, F., Olivier, N., T. Spuesens, Regreny, P., Grosse, P., Rojo-Romeo, P., Orobtchouk, R., D. Van Thourhout, ”Towards optical networks-on-chip with 200mm hybrid technology”, OFCNFOEC 2011 (Optical Fiber Communication Conference and Exposition/National Fiber Optic Engineers Conference), Los Angeles, California, United States, p. paper OMM3 (3 pages), Mar. 2011.

22. P. Mechet, L. Liu, R. Kumar, K. Huybrechts, T. Spuesens, G. Roelkens, E.-J. Geluk , T. De Vries , P. Regreny , D. Van Thourhout, R. Baets, G. Morthier, ”Heterogeneously Integrated Microdisk Lasers for Optical Interconnects and Optical Logic” (invited), SPIE Photonics West 2011, vol. 7913, San Francisco, California, United States, p. 791319, Feb. 2011.

23. T. Spuesens, D. Van Thourhout, ”Analysis of loss contributions in InP-based microdisk lasers heterogeneously integrated with SOI”, Annual Symposium of the IEEE Photononics Benelux Chapter, Netherlands, pp. 209-212, Nov. 2010.

24. K. Huybrechts, L. Liu, R. Kumar, T. Spuesens, G. Roelkens, E.J. Geluk, T. De Vries, P. Regreny, D. Van Thourhout, R. Baets, G. Morthier, "All-Optical Flip-Flops using Electrically Pumped Microdisk Lasers Integrated on Silicon " (invited), IEEE Photonics Society Annual Meeting, Denver, United States, Oct. 2010.

25. L. Liu, T. Spuesens, D. Van Thourhout, G. Morthier, Grenouillet, Laurent, Olivier, Nicolas, Fedeli, Jean-Marc, Rojo-Romeo, Pedro, Regreny, Philippe, Mandorlo, Fabien, Oroubtchouck, Regis, "200mm Wafer Scale III-V/SOI Technology for All-Optical Network-on-Chip and Signal Processing" (invited), Group IV Photonics 2010, Beijing, China, p. WB1, Sep. 2010.

26. G. Roelkens, D. Vermeulen, L. Liu, T. Spuesens, R. Kumar, P. Mechet, K. Huybrechts, S. Keyvaninia, S. Stankovic, M. Tassaert, P. De Heyn, K. Komorowska, S. Selvaraja, D. Van Thourhout, G. Morthier, R. Baets, R. Halir, "III-V/silicon photonic integrated circuits for FTTH and optical interconnect" (invited), IB2COM, Malaga, Spain, Aug. 2010.

27. G. Morthier, L. Liu, R. Kumar, P. Mechet, K. Huybrechts, G. Roelkens, T. Spuesens, T. de Vries, E.J. Geluk, P. Regreny, R. Baets, D. Van Thourhout, "Heterogeneous InP on SOI integration for the realization of all-optical logic devices" (invited), Integrated Photonics Research, Silicon and Nano Photonics (IPR), Photonics in Switching (PS), Monterey, California, United States, p. IWF2.pdf (3 pages), Jul. 2010.

28. D. Vermeulen, T. Spuesens, P. De Heyn, P. Mechet, R. Notzel, S. Verstuyft, D. Van Thourhout, G. Roelkens, "III-V/SOI photonic integrated circuit for FTTH central office transceivers in a PTP network configuration", ECOC, Torino, Italy, p. Tu.5.C.2, May. 2010.

29. K. Huybrechts, L. Liu, R. Kumar, T. Spuesens, G. Roelkens, E.-J. Geluk, T. de Vries, M. Smit, P. Regreny, P. Rojo-Romeo, D. Van Thourhout, R. Baets, G. Morthier, "Digital photonics using InP microdisk lasers heterogeneously integrated on Silicon-on-Insulator" (invited), European Conference on Integrated Optics (ECIO), Cambridge, United Kingdom, p. WeF1, Apr. 2010.

30. R. Kumar, K. Huybrechts, L. Liu, T. Spuesens, G. Roelkens, E.-J. Geluk, T. de Vries, P. Regreny, D. Van Thourhout, R. Baets, G. Morthier, "An ultra-small, low-power all-optical flip-flop memory on a silicon chip", The Optical Fiber Communication Conference and Exposition (OFC) and The National Fiber Optic Engineers Conference (NFOEC) 2010, San Diego, CA, United States, p. OTuN7, Mar. 2010.

31. G. Roelkens, L. Liu, T. Spuesens, T. De Vries, P. Regreny, D. Van Thourhout, R. Baets, "Progress in III-V/SOI photonic integrated circuits" (invited), The 22nd Annual Meeting of the IEEE Photonics Society, vol. TuN1, Antalya, Turkey, pp. 240-241, Oct. 2009.
32. T. Spuesens, L. Liu, T. De Vries, P. Rojo-Romeo, P. Regreny, D. Van Thourhout, "Improved design of an InP-based microdisk laser heterogeneously integrated with SOI", 6th IEEE International Conference on Group IV Photonics, San Francisco, United States, p. FA3, Sep. 2009.
33. L. Liu, G. Roelkens, T. Spuesens, R. Soref, P. Regreny, D. Van Thourhout, R. Baets, "Low-Power Electro-Optical Switch Based on a III-V Microdisk Cavity on Silicon-on-Insulator Circuit", ACP, pp. 76310P-76310P-6, Jun. 2009.
34. T. Spuesens, L. Liu, D. Van Thourhout, "Towards efficient microdisk lasers heterogeneously integrated with SOI", CMOS Photonics, 5th Optoelectronic and Photonic Winter School, Trento, Italy, Mar. 2009.

A.3 Publications in National Conferences

1. T. Spuesens, D. Van Thourhout, "Microdisk lasers as integrated sources for optical interconnects", 10e Ugent-Firw Doctoraatssympoisum , Gent, Belgium, Dec. 2009.

B

Process flow

B.1 Bonding

B.1.1 III-V preparation

Protection
Spincoat AZ5214E 2000 RPM, 40s
Softbake 100 C 3m
Cleaving
Cleave samples in desired size using the scriber microscope or by hand
Strip resist
Strip resist with acetone
Immediately rinse with IPA (don't let the acetone vaporize)
blow dry with N2
Sacrificial layer removal, !Next step should follow immediately!
InP: dip in HCl watch color change.
InGaAs: dip in H2SO4:H2O2:H2O 1:3:1 watch color change
Oxide deposition
PECVD

B.1.2 SOI preparation

Strip resist
Strip resist with acetone
Immediately rinse with IPA (don't let the acetone vaporize)
blow dry with N2
Cleaning
Particle lift-off standard clean 1 (SC-1) NH4OH:H2O2:H2O 1:1:5 70 C 15m
Optional: etch back top oxide
Wet: BHF +/- 8m30s. Etch rate is +/- 122 nm/min. Duration depends on desired thickness.

B.1.3 Bonding

Ultra thin +/- 50 nm above top oxide
Spin adhesion promoter AP3000 3000 RPM ACL 10, 40s
Spin BCB:Mesithylene 1:8 2000 RPM ACL 10, 40s
Bake 157 C 15m
Slow cool down to 80 C by turning off hotplate
Thin +/- 180 nm above waveguide
Spin adhesion promoter AP3000 3000 RPM ACL 10, 40s
Spin BCB:Mesithylene 3:2 2000 RPM ACL 10, 40s
Bake 157 C 5m
Bake 180 C 15m
Slow cool down to 80 C by turning off hotplate
Loading in CB6L
Recipe Thijs_v7_2

B.1.4 InP substrate removal

Protection
Spincoat AZ5214E 2000 RPM, 40s
Softbake 100 C 3m
Grinding
Mount sample on glass with purple wax
Grind till +/- 60-70 μm is left
Remove sample from glass with wax remover @ 120 C
Strip resist
Strip resist with acetone
Immediately rinse with IPA (don't let the acetone vaporize)

blow dry with N2
Wet etch
HCl +/- 8m until bubbling stops.
Sacrificial layer removal ! next step should follow shortly!
InGaAs: dip in H_2SO_4:H_2O_2:H_2O 1:3:1 watch color change
InP: dip in HCl watch color change

B.2 Detector mesa

ECI 3027 litho detector mesa
Spincoat ECI 3027 4000 RPM ACL 10, 40s
Softbake 100 C 2m
Expose with MA6 50s
Post Exposure Bake 115 C 1m
Develop MIF726 30s
Hardbake 115 C 1m
Wet etch
H_2SO_4:H_2O_2:H_2O 1:1:18 1m40s watch color change
DI water rinse 2m

B.3 Disk definition

Hardmask deposition
PECVD
MIR 701 litho hardmask ring
Spincoat TI prime
Bake 120 C 2m
Spincoat MIR 701 4000 RPM ACL 10, 40s
Softbake 100 C 1m
Expose with MA6 50s
Post Exposure Bake 110 C 1m
Develop MIF726 20s
Hardbake 130 C 1m
Hardmask etch
RIE
BHF 30s
DI water rinse 2m
AZ5214E IR litho top contact

NO TI prime!
Spincoat AZ5214E 4000 RPM ACL 10, 40s
Softbake 100 C 3m
Expose with MA6 12s
Reversal bake 120 C 3m
Flood exposure 52s
Develop AZ400K:H2O 1:3 15s
Metal deposition
H2SO4:H2O2:H2O 1:1:50 5s
Ebeam evaporator Ti/Siox 60/40 nm
Lift-off in DMSO
Rinse with IPA and blow dry
Disk etching
1% HF dip 2-3s
H2SO4:H2O2:H2O 1:1:30 5s
ICP stop leaving around 100 nm InP

B.4 Metal contacts

AZ5214E IR litho bottom contact
NO TI prime!
Spincoat AZ5214E 2000 RPM ACL 10, 40s
Softbake 100 C 3m
Expose with MA6 12s
Reversal bake 120 C 3m
Flood exposure 52s
Develop AZ400K:H2O 1:3 15s
Metal deposition
RIE siox etch 1 m @ 35 C
H2SO4:H2O2:H2O 1:1:30 10s Ebeam evaporator Ti/Pt/Au 25/50/100 nm
Lift-off in DMSO
Rinse with IPA and blow dry

B.5 Island

MIR 701 litho island
NO TI prime!
Spincoat MIR 701 2000 RPM ACL 10, 40s

Softbake 100 C 1m30s
Expose with MA6 60s
Post Exposure Bake 110 C 1m
Develop MIF726 20s
Hardbake 130 C 1m
island etching
ICP etch
Strip resist
O2 plasma 600W 30m

B.6 Passivation and planarization

BHF dip 10s
PECVD oxide+nitride 100nm
Spincoat AP3000 4000 RPM ACL 10, 40s
Spincoat BCB 3022-35 4000 RPM ACL 10, 40s
Cure in oven standard recipe 260 C 1h

B.7 Open contacts

AZ5214E IR litho vias
Spincoat AZ5214E 2000 RPM ACL 10, 40s
Softbake 100 C 3m
Expose with MA6 10s
Reversal bake 120 C 3m (higher temperature for less undercut)
Flood exposure 50s
Open vias
RIE BCB Look under microscope RIE sinx

B.8 Contact metal

AZ5214E IR litho vias
Spincoat AZ5214E 2000 RPM ACL 10, 40s
Softbake 100 C 3m
Expose with MA6 10s
Reversal bake 120 C 3m
Flood exposure 52s
Metal deposition

Univex Ti/Au 40/500 nm
Lift-off in DMSO
Rinse with IPA and blow dry
Anneal 420 C 30s

C
Mask layouts

Here we will briefly discuss the different mask layouts used throughout this work.

C.1 Layouts run 1

An overview of the complete mask layout for the first run is shown in Figure C.1. The two areas indicated in the figure contain the microdisk lasers and detectors that were described in Section 4.1 and 5.4.1, respectively. Figure C.2 shows a close-up of the mask layout of the microdisk laser and detector used in this run. For the microdisk laser a large bottom contact area was used. The bottom contact slab was also extended over the waveguide with a sharp angle, to avoid reflections that could occur if an abrupt change would be used. In this run all metals are defined in a single metalization step and therefore an opening in the bottom contact is required to be able to route the top contact. The detector design still contained an abrupt junction at the interface between the waveguide and the bottom contact in this run.

C.2 Layouts run 2

This run focused on the design of Optical Networks-on-Chip. 6 different layouts for 2x2 ONoCs were made that allow for flip-chip integration with CMOS electronics. 4 different layouts were made for 8x8 ONoCs, with higher complexity in

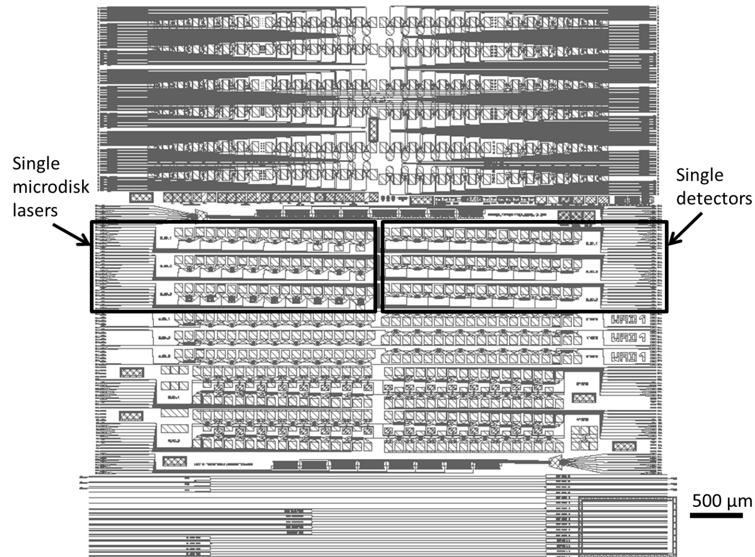

Figure C.1: Overview of the mask layout for the first fabrication run.

the optical level but without the possibility for flip-chip integration with electronics. An overview of this mask layout is shown in Figure C.3. Next to the ONoC circuits, individual microdisk lasers were designed of which an example is shown in Figure C.4. In this microdisk laser design the bottom contact layer was reduced in size compared to the design in run 1, resulting in a significant decrease in device dimensions. Based on preliminary simulation results on microdisk-waveguide coupling, the width of the waveguide in the coupling section was adjusted. Furthermore, the simulation results on metal losses were used to optimize the size of the contacts.

C.3 Layouts run 3

This final run contained several 2x2 ONoC designs, multi-wavelength lasers based on microdisk laser arrays, compact optical links and individual microdisk lasers. An overview of the complete mask is shown in Figure C.5. It should be noted that only 1 2x2 ONoC is displayed here, because the designs were interleaved to reduce the cost of the SOI samples. During post-processing it was decided which of the designs was processed further. A detailed overview of the mask layout of the microdisk laser and detector is shown in Figure C.6. In this process two separate steps were used to define metals and therefore the top and bottom metal contacts can overlap. For the microdisk laser this results in more uniform carrier injection.

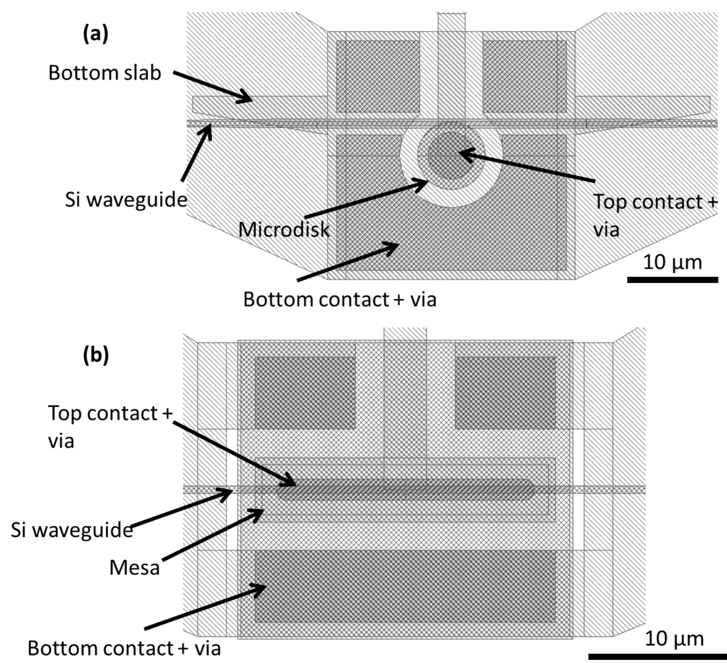

Figure C.2: Detailed overview of the mask layout for the microdisk laser and detector in the first fabrication run.

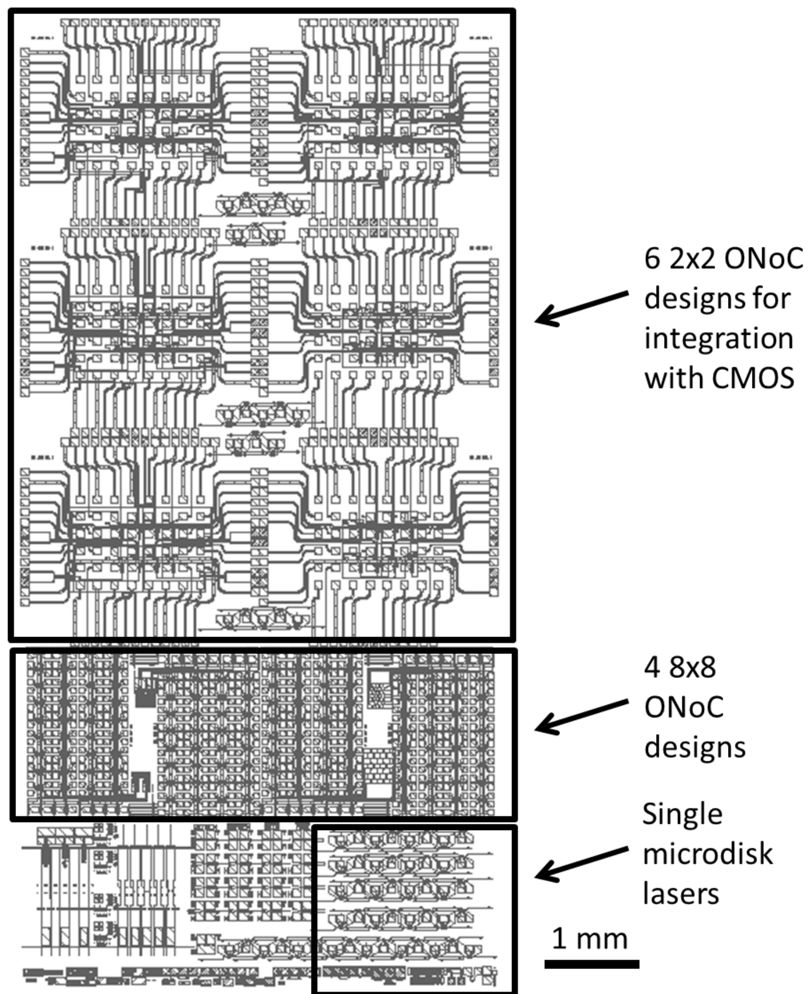

Figure C.3: Overview of the mask layout for the second fabrication run.

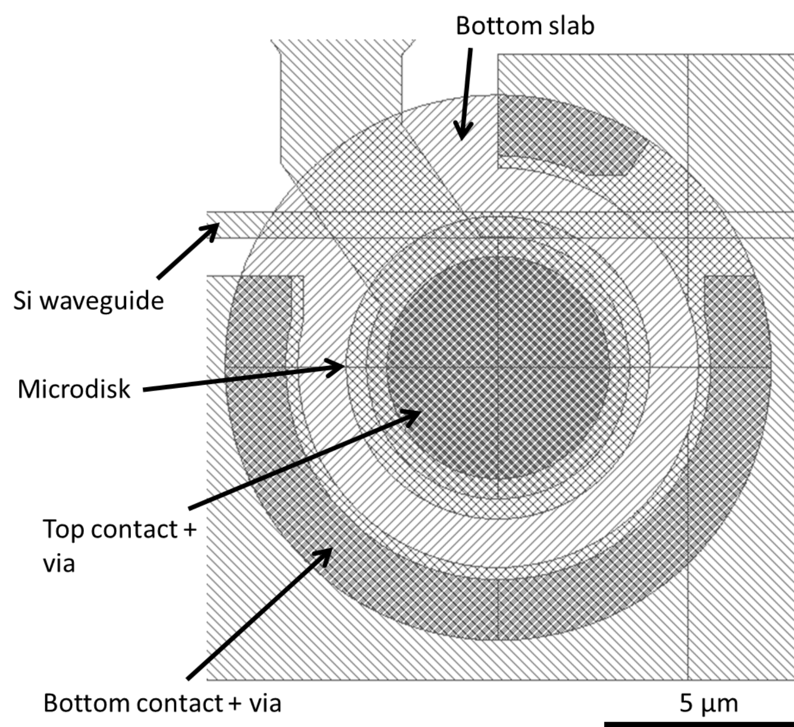

Figure C.4: Detailed overview of the mask layout for the microdisk laser in the second fabrication run.

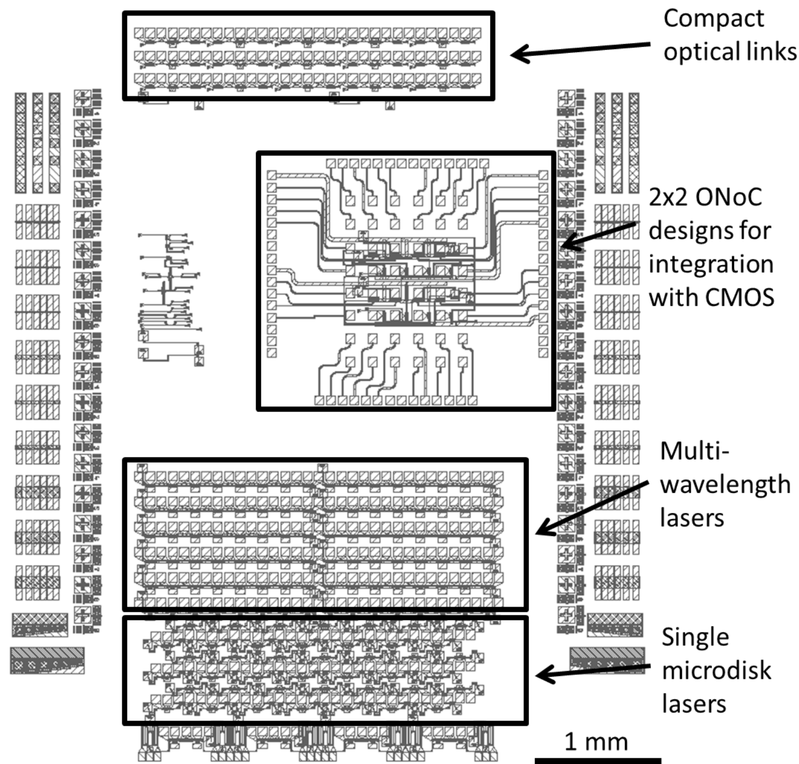

Figure C.5: Overview of the mask layout for the third fabrication run.

This also allows for the use of a large top contact which can act as a heat spreader. In the detector design the bottom contact layer is now angled to avoid reflections at the interface between the waveguide and the detector structure. Because contact lithography was used in this process the mesa width was increased from 3.5 to 5 μm. From simulations it was found that the effect on the performance is negligible.

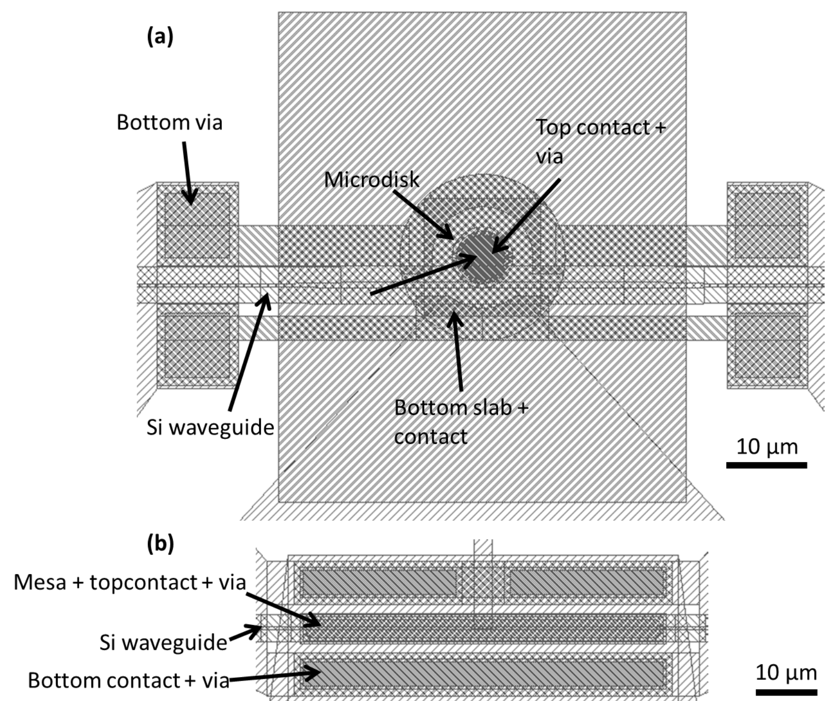

Figure C.6: Detailed overview of the mask layout for the microdisk laser and detector in the third fabrication run.